The role of leaf plasmodesmata in C$_4$ photosynthesis

Florence Reyes Danila

May 2019

A thesis submitted for the degree of
Doctor of Philosophy of
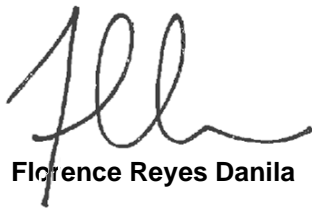The Australian National University

For Mama and Papa

DECLARATION

_____

This thesis contains research undertaken at the Australian National University, Canberra, ACT. Except where otherwise indicated, this thesis is my own original work, performed under the supervision of Distinguished Professor Susanne von Caemmerer, Professor Robert T Furbank, Dr Rosemary G White, and Professor William Paul Quick.

Florence Reyes Danila

May 2019

ACKNOWLEDGEMENTS

_____

ABSTRACT

_____

In a C_4 leaf, numerous plasmodesmata in the wall interface between the mesophyll and bundle sheath cells provide symplastic transport for exchange of C_4 acids and metabolites during photosynthesis. Despite their importance in understanding the function and efficiency of C_4 photosynthesis, quantification studies of the plasmodesmata that exist between these two photosynthetic cells are very few. The main reason for this is the difficulty involved in capturing the plasmodesmata that occur as clusters or pit field units particularly in leaves.

In this work, this problem was overcame through the development of a new and more robust method to accurately quantify plasmodesmata in leaves without resorting to serial sectioning (Chapter 3). This was achieved by combining scanning electron microscopy and three-dimensional laser confocal fluorescence microscopy (e.i. PEA-CLARITY). This new method allowed empirical quantification of plasmodesmata per cell interface area, and consequently, estimation of plasmodesmata flux when these values are combined with photosynthetic measurements (Chapter 3).

The new plasmodesmata quantification method provided the opportunity to examine a diversity of grass species within the non-C_4 BEP clade and PACMAD clade including representative species from C_3, C_3-C_4 intermediate, and all the C_4 biochemical subtypes, nicotinamide adenine dinucleotide phosphate – malic enzyme (NADP-ME), nicotinamide adenine dinucleotide – malic enzyme (NAD-ME), and phosphoenolpyruvate carboxykinase (PCK) (Chapter 4). Results showed that C_3 species, regardless of clade, have fewer plasmodesmata than C_4 species. _Panicum milioides_, a C_3-C_4 intermediate species, had plasmodesmata density within the C_4 species range. Within the C_4 species, there was a substantial variation of plasmodesmata densities at the mesophyll-bundle sheath cell interfaces among the subtypes, where NAD-ME subtype had the greatest value, NADP-ME had the least, and PCK had the largest variability. The greater plasmodesmata density in C_4 leaves was a result of having larger pit fields and an increased number of plasmodesmata per pit field area. Conversely, plasmodesmata densities at the mesophyll-mesophyll cell interfaces were similar in C_3 and C_4 species. Other C_4 evolution-related anatomical traits such as bundle sheath cell size, interveinal distance, and bundle sheath surface area per leaf area (S_b) were also measured. Results revealed that S_b and, to a lesser extent, interveinal distance, but not bundle sheath cell size, were statistically different between C_3 species and C_4 species.

In addition to plasmodesmata density survey, the new method developed here was also applied to investigate the response of plasmodesmata formation in C_4 grasses to changes in photosynthetic capacity. Results showed that when C_4 plants were subjected to different growth light environments (Chapter 5) or

when the initial carbon fixation enzyme, phosphoenolpyruvate carboxylase (PEPC) was downregulated reducing photosynthetic capacity in these plants (Chapter 6), plasmodesmata connection between the mesophyll and bundle sheath cells were altered. Low growth irradiance caused fewer plasmodesmata connection to form between mesophyll and bundle sheath cells in leaves of both *Setaria viridis* and *Zea mays* compared to the high light-grown plants, albeit manifested at different plant ages (Chapter 5). On the other hand, an increased number of pit fields in the mesophyll-bundle sheath cell interface of the leaf resulted from impaired C_4-associated PEPC gene expression in *S. viridis* (Chapter 6).

From these results it can be concluded that increased plasmodesmata density between the mesophyll and bundle sheath cells is an essential anatomical feature of C_4 photosynthesis and is responsive to changes in photosynthetic capacity in C_4 plants.

TABLE OF CONTENTS

_____

LIST OF FIGURES

_____

LIST OF TABLES

_____

ABBREVIATIONS AND SYMBOLS

_____

2D	two-dimensional
3D	three-dimensional
pCO_2	carbon dioxide partial pressure
Γ_*	chloroplast carbon dioxide partial pressure
^{o}C	degrees Celsius
A	carbon dioxide assimilation rate
ANOVA	analysis of variance
BEP	bambusoideae, ehrhartoideae, and pooideae
bp	base pair
BS	bundle sheath
CF	carboxyfluorescein
CFDA	5,6-carboxyfluorescein diacetate
C_i	intercellular carbon dioxide partial pressure
ci	cell interface
cia	cell interface area
C_m	mesophyll carbon dioxide partial pressure
CO_2	carbon dioxide
dA/dC_i	initial slope of the carbon dioxide response curve of carbon dioxide assimilation rate versus intercellular carbon dioxide partial pressure
DCDP	3,3-dichloro-2-(dihydroxyphosphinoylmethyl) propenoate
DRM	detergent-resistant membrane
DT	desmotubule
FESEM	field emission scanning electron microscopy
g_{bs}	bundle sheath conductance to carbon dioxide diffusion
GFP	green fluorescent protein
g_m	mesophyll conductance to carbon dioxide diffusion
GPI	glycosylphosphatidylinositol
g_t	total conductance to carbon dioxide diffusion from the intercellular air space to the site of rubisco carboxylation in the bundle sheath
h	hour
H_2O	water
HG	homogalacturonan
IVD	interveinal distance
K_c	Michaelis-Menten constant of rubisco for carbon dioxide

xiv

K_o	Michaelis-Menten constant of rubisco for oxygen
K_p	Michaelis-Menten constant for carbon dioxide
L	litre
LED	light-emitting diode
M	mesophyll
MPC	melinidinae, panicinae, and cenchrinae
mRNA	messenger ribonucleic acid
NAD-ME	nicotinamide adenine dinucleotide-malic enzyme
NADPH	reduced nicotinamide adenine dinucleotide phosphate
NADP-ME	nicotinamide adenine dinucleotide phosphate-malic enzyme
O_2	oxygen
p	phloem
PACMAD	panicoideae, aristoideae, chloridoideae, micrairoideae, arundinoideae, and danthonioideae
PCK	phosphoenolpyruvate carboxykinase
PD	plasmodesmata
PEA-CLARITY	plant enzyme-assisted-clear lipid-exchanged acylamide-hybridised rigid imaging/in situ hybridization compatible tissue-hydrogel
PEP	phosphoenolpyruvate
PEPC	phosphoenolpyruvate carboxylase
pfa	pit field area
PM	plasma membrane
PPP	phloem-pole pericycle
PSI	photosystem I
PSII	photosystem II
R_d	leaf mitochondrial respiration in the light
RG	rhamnogalacturonan
R_m	mesophyll mitochondrial respiration in the light
RNAi	ribonucleic acid interference
rubisco	ribulose-1,5-biphosphate carboxylase/oxygenase
S_b	bundle sheath surface area per unit leaf area
SBF-SEM	serial block face-scanning electron microscopy
$S_{c/o}$	rubisco carbon dioxide to oxygen specificity
SDS	sodium dodecyl sulfate
SE	sieve element
SEL	size exclusion limit
SEM	scanning electron microscopy

TBST	tris-buffered saline with Tween 20®
TEM	transmission electron microscopy
TR	texas red
V_{cmax}	maximum rubisco carboxylation rate
V_{pmax}	maximum phosphoenolpyruvate carboxylase rates
x	xylem

1
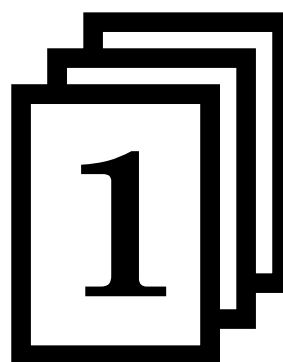
GENERAL INTRODUCTION

1.1 C$_4$ photosynthesis

C$_4$ photosynthesis is a biochemical pathway that concentrates CO$_2$ inside the leaf in specialized cells where rubisco (ribulose-1,5-biphosphate carboxylase/oxygenase) is localized (Furbank and Hatch, 1987; Hatch, 1971; von Caemmerer and Furbank, 2003). This CO$_2$-concentrating mechanism decreases photorespiration which limits the carbon-capture capacity and efficiency of C$_3$ photosynthesis under ambient CO$_2$ (Sharkey, 1988). It operates across two cell types, the mesophyll cell and the bundle sheath cell, which are connected by numerous plasmodesmata (Berry et al., 1970; Hatch, 1971; Hatch and Osmond, 1976). This unique blend of biochemical and anatomical specialization has driven the evolution of two-cell C$_4$ photosynthesis (Edwards et al., 2001; Furbank, 2016; Hatch, 1987).

1.1.1 Biochemical subtypes

Unique to the C$_4$ leaf is the compartmentation of photosynthetic carbon assimilation and photosynthetic carbon reduction into mesophyll and bundle sheath cells, respectively (Berry et al., 1970; Hatch, 1987; Hatch and Osmond, 1976). Radiotracer kinetics experiments performed by Hatch and Slack (Hatch, 1971; Hatch and Slack, 1966; Karpilov, 1960) provided unequivocal evidence of the existence of two component pathways operating in C$_4$ leaves, ultimately leading to the conclusion that mesophyll cells contain enzymes of C$_4$ acid synthesis and bundle sheath cells contain the enzymes of C$_4$ acid decarboxylation and of the C$_3$ cycle (Fig. 1.1; reviewed in Hatch and Osmond, 1976).

Within the mesophyll cells, key enzymes such as the C$_4$-associated carbonic anhydrase and phosphoenolpyruvate carboxylase (PEPC) were found to be exclusively and highly expressed whereas the primary enzyme of carbon fixation in the carbon reduction cycle, rubisco, was absent (Berry et al., 1970; Björkman and Gauhl, 1969; Edwards et al., 1970; Slack et al., 1969). This is a crucial aspect of the C$_4$ photosynthesis pathway. This allows the mesophyll cells, which have immediate access to atmospheric CO$_2$, to perform the initial step of CO$_2$ fixation. This is a two-step process. First, carbonic anhydrase converts atmospheric CO$_2$ to bicarbonate, which is then used by PEPC along with its primary substrate PEP to form a four-carbon acid oxaloacetate.
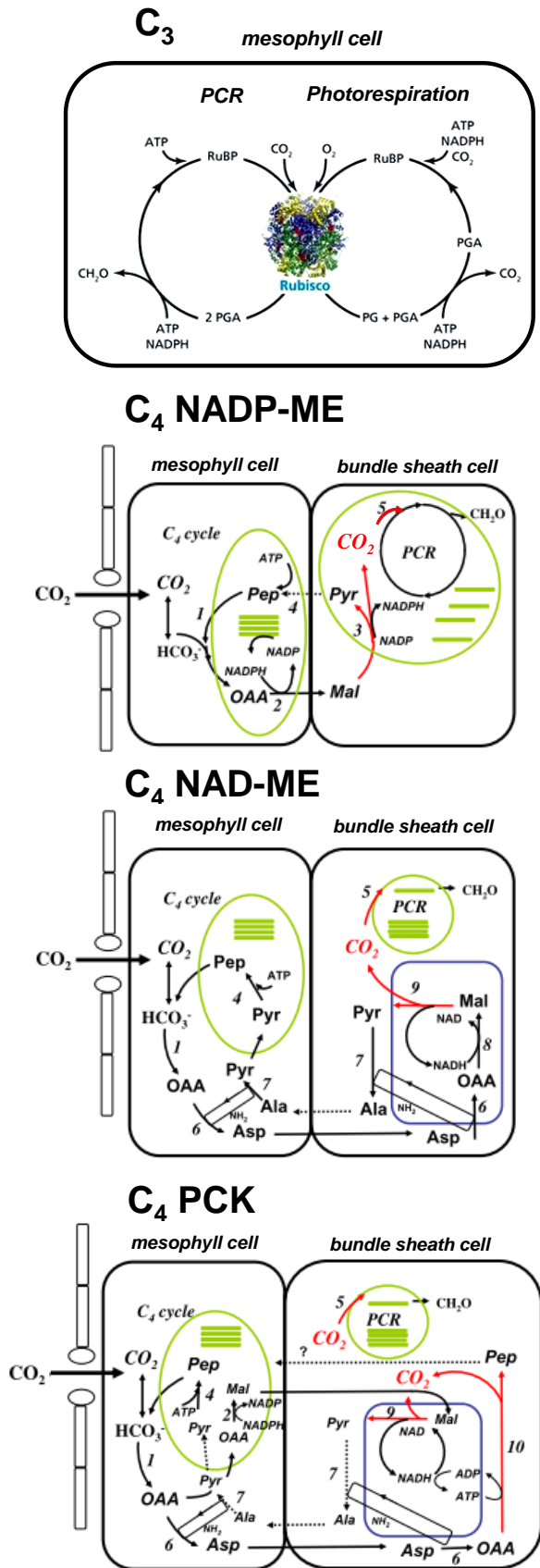
Figure 1.1 The photosynthetic pathways of C_3 and C_4 subtypes. Diagrams for the C_4 subtypes were adapted from Furbank (2011). PCR, photosynthetic carbon reduction; RuBP, ribulose-1,5-biphosphate; PGA, phosphoglyceric acid; PG, phosphoglycolic acid; Pep, phosphoenolpyruvate; Pyr, pyruvate; OAA, oxaloacetate; Ala, alanine; Mal, malate; Asp, aspartate. Chloroplasts and thylakoids are coloured green, mitochondria blue, and the decarboxylation reactions are coloured red. Enzymes in the pathways are numbered as follows: **(1)** phosphoenolpyruvate (PEP) carboxylase; **(2)** NADPH-malate dehydrogenase; **(3)** NADP-malic enzyme; **(4)** pyruvate Pi-dikinase; **(5)** rubisco; **(6)** aspartate aminotransferase; **(7)** alanine amino-transferase; **(8)** NAD-malate dehydrogenase; **(9)** NAD-malic enzyme; **(10)** phosphoenol pyruvate (PEP) carboxykinase.

Although this initial step is universal to all the C_4 species, the subsequent steps are not. The C_4 pathway can be categorized into three classical subtypes depending on whether the oxaloacetate will be converted into malate or aspartate, the organelles involved in the process, and most importantly, the decarboxylating enzymes in play (Fig. 1.1) (Edwards et al., 1971; Furbank, 2011; Hatch and Kagawa, 1976). A great proportion of C_4 species fall under the nicotinamide adenine dinucleotide phosphate – malic enzyme (NADP-ME) subtype. C_4 species belonging to this category are malate-formers; oxaloacetate moves into the mesophyll chloroplast where it is converted into malate through the NADP malate dehydrogenase enzyme and the malate then moves to the bundle sheath cell. On the other hand, C_4 species belonging to the NAD-ME and phosphoenolpyruvate carboxykinase (PCK) subtypes are aspartate-formers, converting oxaloacetate along with glutamine into aspartate via aspartate aminotransferase within the mesophyll cytoplasm, and aspartate moves to the bundle sheath.

Bundle sheath cells house the C_3 photosynthetic pathway, where rubisco fixes CO_2 released from the mesophyll-generated C_4 acids (Kagawa and Hatch, 1974). The C_4 acid decarboxylating enzymes are central to this process. When malate enters the bundle sheath cells of an NADP-ME leaf, it moves into the chloroplasts where it is decarboxylated via NADP-ME producing pyruvate and CO_2 (Fig. 1.1). On the other hand, when aspartate enters the bundle sheath cells, aspartate aminotransferase in the mitochondria of an NAD-ME leaf or in the cytoplasm of a PCK leaf regenerates the oxaloacetate, which is then either converted into malate producing pyruvate and releasing CO_2 from the mitochondria into the cytoplasm via NAD-ME or directly decarboxylated to PEP in the case of PCK catalysis. Once CO_2 is released, it is captured by the rubisco within the bundle sheath chloroplasts to produce 3-phosphoglyceric acid via the Calvin cycle which is then used for the production of sucrose and starch (Bassham et al., 1950). Pyruvate or alanine is transported from the bundle sheath cell back into the mesophyll cell where pyruvate Pi-dikinase regenerates PEP for the next cycle (Hatch and Osmond, 1976). The C_4 cycle operates to concentrate CO_2 in the bundle sheath cells, reducing photorespiration and increasing the efficiency of the C_3 cycle (e.i. Calvin cycle) in C_4 plants.

1.1.2 Compartmentation in C_4 photosynthesis

In monocots, C_4 photosynthesis is almost always associated with the presence of Kranz anatomy in the leaf. Kranz anatomy is characterised by two chloroplast-containing cells, mesophyll cells

abutting bundle sheath cells forming a wreath-like structure around the vascular bundles (Haberlandt, 1904; Laetsch, 1974). Consistent in leaves of all C_4 grasses is the occurrence of two to three layers of mesophyll cells between bundle sheath cylinders rather than six or more as in C_3 leaves (Dengler et al., 1994) (Fig. 1.2A). It is thought that this arrangement of leaf cells provided the opportunity for direct communication between mesophyll and bundle sheath facilitating the cellular cooperation necessary for C_4 photosynthesis to evolve.

1.1.3   Dimorphic chloroplasts

In contrast to C_3 species which have few chloroplasts in their bundle sheath cells, C_4 species contain well-developed chloroplasts in both their mesophyll and bundle sheath cells. Among the C_4 subtypes, NADP-ME species have leaves with dimorphic chloroplasts (Dengler et al., 1994; Hodge et al., 1955; Rhoades and Carvalho, 1944) (Fig. 1.2B). Mesophyll chloroplasts in both C_3 and C_4 species are rich in photosystem II, show extensive granal development and generally perform linear electron flow (Johnson, 2011; Munekage and Taniguchi, 2016). In C_3 species and in grass species belonging to NAD-ME and PCK subtypes, similar chloroplast morphology is present for both mesophyll and bundle sheath cells (Dengler et al., 1994) (Fig. 1.2B). Bundle sheath chloroplasts of NADP-ME subtype, on the other hand, generally have few grana, are rich in photosystem I, and predominately perform cyclic electron flow (Andersen et al., 1972; Majeran and van Wijk, 2009; Woo et al., 1970). During cyclic electron flow only ATP is produced (Kanai and Edwards, 1999). The production of NADPH in the bundle sheath chloroplast of NADP-ME subtype happens during the decarboxylation step (Andersen et al., 1972; Woo et al., 1970).

1.1.4   Structural features of the mesophyll-bundle sheath cell interface

In C_3 grasses, the bundle sheath is thought to perform a role akin to vascular parenchyma cells and cellular communication with the mesophyll is likely limited to sugars moving to the phloem (Leegood, 2008). As discussed above, the C_4 pathway requires a large flux of C_4 acids and C_3 compounds across the interface between mesophyll and bundle sheath. As this is also the surface where CO_2 can diffuse back to the mesophyll, the mesophyll-bundle sheath cell interface is of major significance to the efficient operation of C_4 photosynthesis.
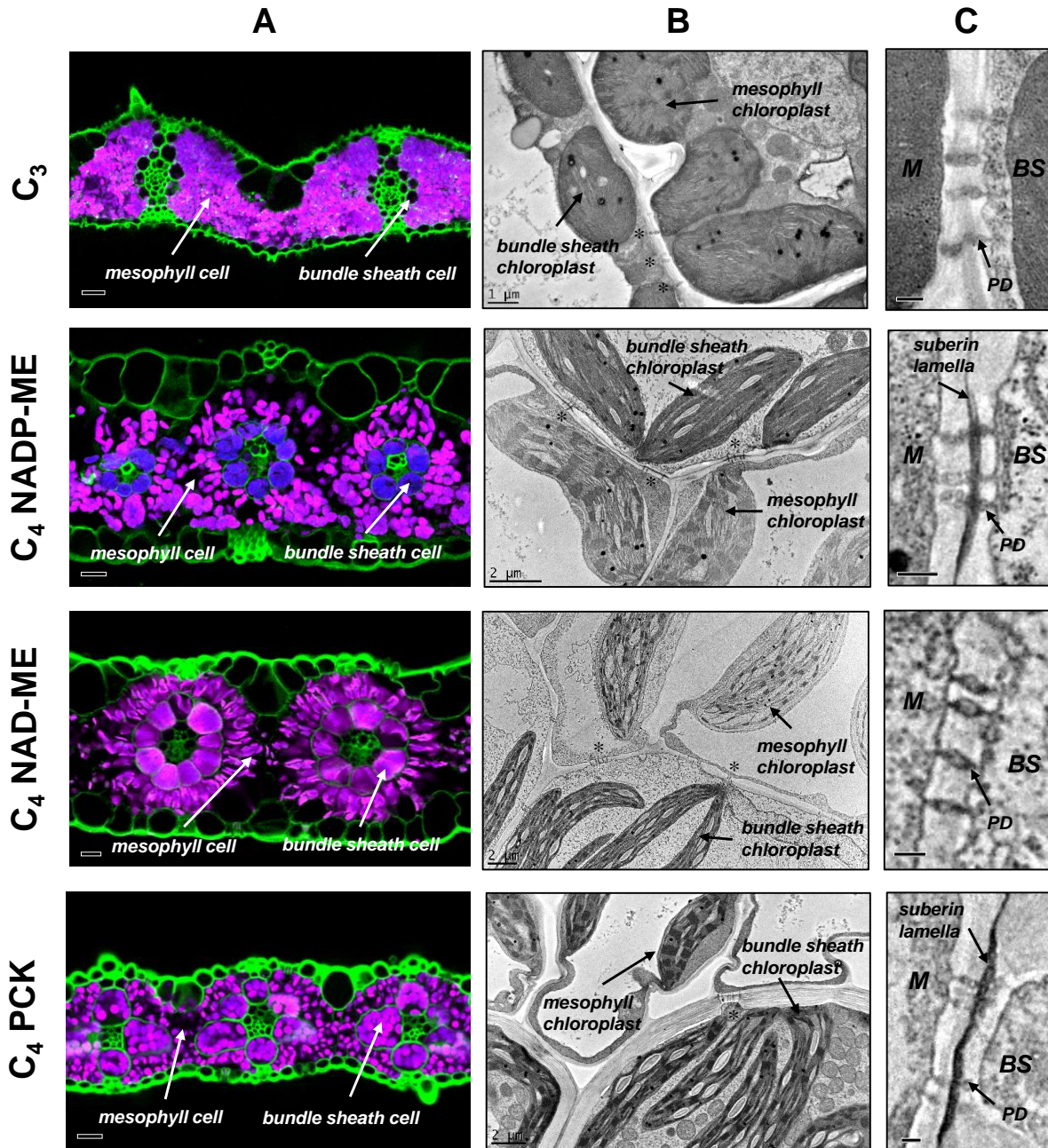
Figure 1.2 Anatomical attributes of the C$_3$ and C$_4$ subtypes in grasses. **(A)** Laser confocal fluorescence micrograph of fresh hand-cut transverse leaf section of *Oryza sativa* (C$_3$), *Setaria viridis* (C$_4$ NADP-ME), *Panicum coloratum* (C$_4$ NAD-ME), and *Megathyrsus maximum* (C$_4$ PCK). For cell wall (green), excitation wavelength: 405 nm; emission wavelength: 420-480 nm. For chloroplasts, excitation wavelength: 633 nm; emission wavelength for photosystem II (magenta): 650-720 nm; emission wavelength for photosystem I (blue): 720-800 nm. Bars = 20 μm. **(B)** Electron micrographs of mesophyll and bundle sheath chloroplasts. Bundle sheath chloroplasts in C$_4$ NADP-ME lack photosystem II due to absence of grana which explains the blue pseudo-color in **(A)**. Asterisk marks presence of a pit field in the mesophyll-bundle sheath cell interface. **(C)** Electron micrographs of the mesophyll (M)-bundle sheath (BS) cell interface showing presence of plasmodesmata (PD) and suberin lamella. Bars = 200 nm.

In a C_4 leaf, mesophyll cells are thin-walled cells loosely arranged between the veins. This loose arrangement creates intercellular airspaces that allow maximum capture of CO_2 entering the leaf from the atmosphere (Laetsch, 1974). The bundle sheath cells, on the other hand, have thickened cell walls and are stacked together forming a cylinder surrounding the vasculature limiting intercellular airspaces (Laetsch, 1974). Moreover, suberin lamellae were found in bundle sheath cell walls of both NADP-ME and PCK subtypes (Hattersley and Browning, 1981) (Fig. 1.2C). Suberin shares many common monomers with epidermal cutin (Hatch and Osmond, 1976; Mertz and Brutnell, 2014; Pollard et al., 2008) and can act as a substantial barrier to the diffusion of CO_2 and photosynthetic intermediates across the cell walls of neighbouring mesophyll and bundle sheath cells (Laetsch, 1974; O'Brien and Carr, 1970). Together, these features provide a CO_2-tight space between the mesophyll and bundle sheath cells of a C_4 leaf. Physiological manifestations of this include the near zero CO_2 compensation point (Hesketh, 1963; Moss, 1962) and low carbon isotope discrimination ratio ($\delta^{13}C$ value) (Farquhar et al., 1989; Henderson et al., 1992) measured in C_4 plants. The presence of suberin in bundle sheath cell walls, however, is not considered to be critical for the C_4 pathway. This is evidenced by observations that suberisation of the bundle sheath cell wall is only observed in C_4 monocots but not in C_4 eudicots (Hatch and Osmond, 1976) and within C_4 monocots, grass species belonging to the NAD-ME subtype generally lack suberin lamellae in their bundle sheath cell walls (Dengler et al., 1994; Prendergast et al., 1987) (Fig. 1.2C).

Another important structural feature of the mesophyll-bundle sheath cell interface is the presence of numerous plasmodesmata (Fig. 1.2C). Because of the apoplastically-impermeable anatomical attributes of the C_4 bundle sheath cells and the need for rapid exchange of photosynthetic metabolites for the C_4 pathway, it has been concluded that the exchange of photosynthetic intermediates between the mesophyll and bundle sheath cells occurs exclusively within the symplast and is facilitated by plasmodesmata (Hatch and Osmond, 1976). The extent of plasmodesmatal connection between the mesophyll and bundle sheath cells must, therefore, be sufficient to support the required higher rates of metabolite exchange for C_4 photosynthesis.

1.2 Plasmodesmata connections between cells

1.2.1 Discovery of plasmodesmata

Knowledge about plasmodesmata has progressed significantly since their first discovery by Eduard Tangl in 1879 using a light microscope (Tangl, 1879). Plasmodesmata were originally known as protoplasmic threads that were seen to connect the protoplasts into a symplastic continuum (Robards, 1976). In 1901, Strasburger coined the term "*plasmodesma*" (in Greek, *plasma* means form and *desma* means bond) to describe these structures and it has been in wide use since then (Robards, 1976). There have been many hypotheses on the importance of plasmodesmata in cell-to-cell communication in plants, particularly their potential role in intercellular transport owing to their localisation in the cell wall (Gunning, 1976; Hatch and Osmond, 1976). Under a light microscope, pit fields or clusters of plasmodesmata can be seen as puncta embedded in the cell wall (Overall, 1999). Initially, limitations to resolution of microscopic imaging technology hindered further investigation of plasmodesmatal ultrastructure. The advent of electron microscopy in the 1940s paved the way towards the understanding of plasmodesmata ultrastructure (Overall, 1999; Robards, 1976), which then gave significant insights into the elucidation of their origin, formation, and biological roles (reviewed in Beebe and Turgeon, 1991; Cilia and Jackson, 2004; Crawford and Zambryski, 1999; Ehlers and Kollman, 2001; Faulkner and Oparka, 2016; Maule, 2008; Maule et al., 2001; Oparka and Roberts, 2001). We now know that plasmodesmata are nanostructures with internal diameters ranging from 20 nm to 100 nm. This diameter range includes values obtained from measurements of both root plasmodesmata (Gunning and Robards, 1976; Nicolas et al., 2017; Overall et al., 1982) and leaf plasmodesmata (Botha, 1992; Evert et al., 1977). Chapter 2 of this thesis is a published current review on the biological roles of plasmodesmata (New Phytologist, Viewpoint, https://doi.org/10.1111/nph.15130).

1.2.2 Formation of plasmodesmata

Plasmodesmata can be primary or secondary. Primary plasmodesmata are formed during the cytokinesis phase of cell division while secondary plasmodesmata are formed *de novo* in completed walls usually within the vicinity of existing primary plasmodesmata (Ehlers and Kollmann, 2001). Both types of plasmodesmata are composed of similar structural features and

therefore can appear identical (Ehlers and Kollmann, 2001). Both can undergo modifications from simple, linear strands to very complicated branched forms (Burch-Smith and C. Zambryski, 2016; Ehlers and Kollmann, 1996; Faulkner et al., 2008). The distinction between these two types of plasmodesmata depends solely on their origin (Ehlers and Kollmann, 2001; Gunning and Robards, 1976; Robards and Lucas, 1990).

Primary plasmodesmata are initiated during early telophase of cell division (Fig. 1.3). Vesicles carrying cell wall precursors from Golgi bodies associate with the phragmoplast microtubules and accumulate in the plane designated by the pre-prophase band of microtubules (Fig. 1.3A) (Hepler, 1982). These vesicles fuse together forming a large, membrane-enclosed, disk-like structure known as the cell plate (Fig. 1.3B). The cell plate contains polysaccharides that form the matrix of the new cell wall. Two daughter cells arise when the cell plate expands outward, meets the parental plasma membrane, and the edges of the cell plate fuse with the parental cell walls (Fig. 1.3C). During the development of the cell plate, strands of tubular endoplasmic reticulum can become entrapped resulting in incomplete vesicle fusion and formation of plasmodesmata between the two daughter cells (Fig. 1.3C) (Hepler, 1982; Overall et al., 1982). Once formed, primary plasmodesmata appear as simple, unbranched strands embedded in the young cell wall, interconnecting the sister cells (Fig. 1.3D) (Ehlers and Kollmann, 2001). During growth, when cells expand and cell wall thickening occurs, the primary plasmodesmata can undergo modification to perform various functions which may or may not include the addition of cell connections (Ehlers and Kollmann, 2001). Modified primary plasmodesmata can appear as either simple elongated structures or in various branched forms (Ehlers and Kollmann, 1996). The mechanisms potentially involved in the formation of various modified primary plasmodesmata during cell wall expansion and thickening are illustrated in Figure 1.4.

Conversely, in most cells which expand considerably after cell division, symplastic continuity does not rely on the few primary plasmodesmata inserted in the cell plate, but is achieved through formation of secondary plasmodesmata. Secondary plasmodesmata are formed *de novo* in completed walls usually within the vicinity of existing primary plasmodesmata (Giannoutsou et al., 2013; Gunning and Robards, 1976; Robards and Lucas, 1990). Secondary plasmodesmata can be simple, twinned, or branched (Faulkner et al., 2008), can appear very similar to primary plasmodesmata, and therefore can only be differentiated based on their origin. Proposed models for secondary plasmodesmata formation are outlined in Figure 1.5.
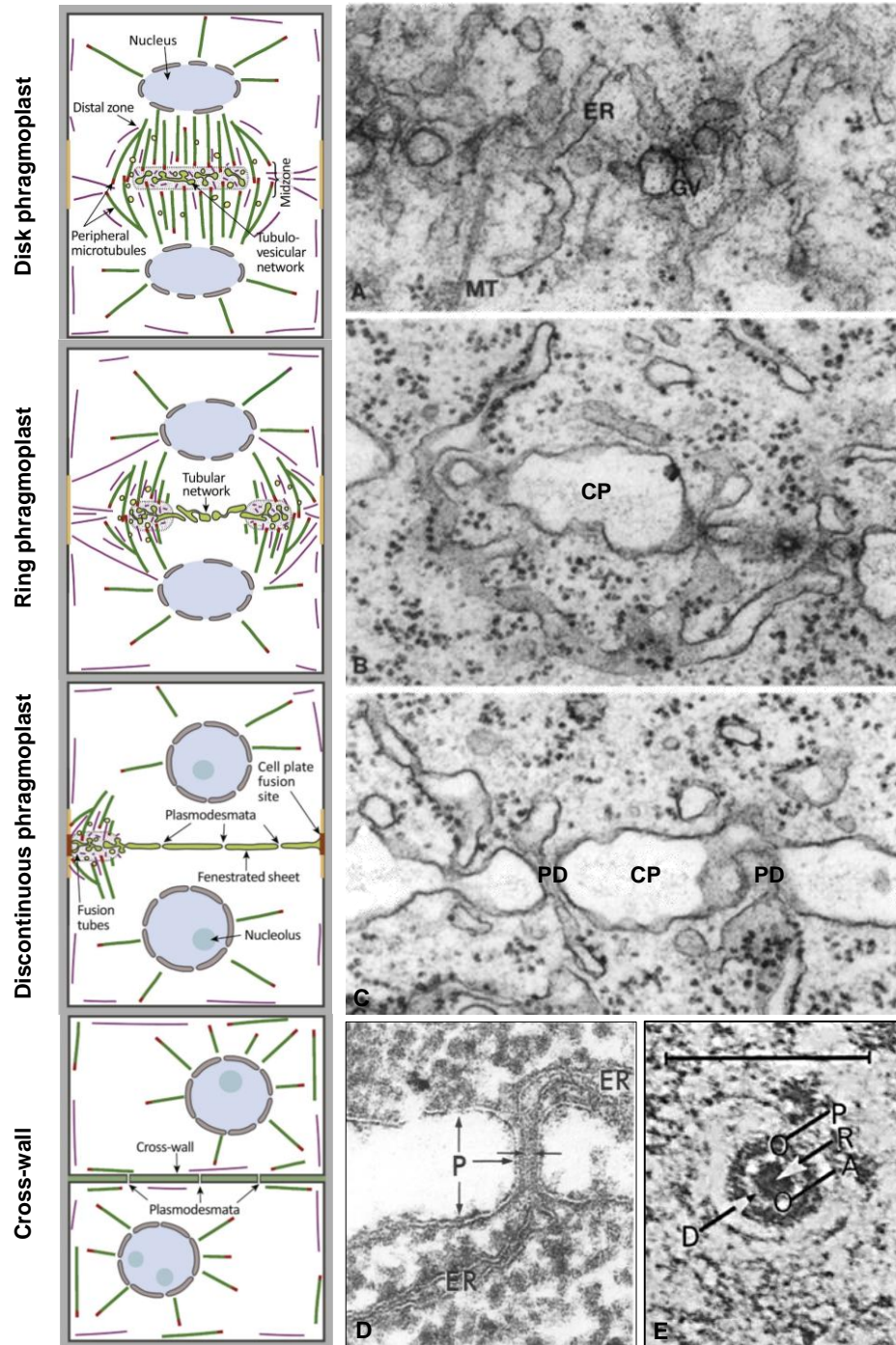
Figure 1.3 (A-C) Formation of plasmodesmata during the cytokinesis phase of plant cell division. Plasmodesmata (PD) are formed when parts of the endoplasmic reticulum (ER) are trapped in the developing cell plate (CP) of a dividing cell. The structural components of fully formed primary plasmodesmata are shown in both longitudinal **(D)** and transverse **(E)** orientations. GV, Golgi vesicles; MT, microtubule; A, cytoplasmic sleeve; D, desmotubule; P, plasma membrane; R; central rod. Bar in **(E)** = 100 nm. Diagram, (Smertenko et al., 2017); **(A-C)**, (Ehlers and Kollmann, 2001); **(D)**, (Overall et al., 1982); **(E)**, (Gunning and Robards, 1976).
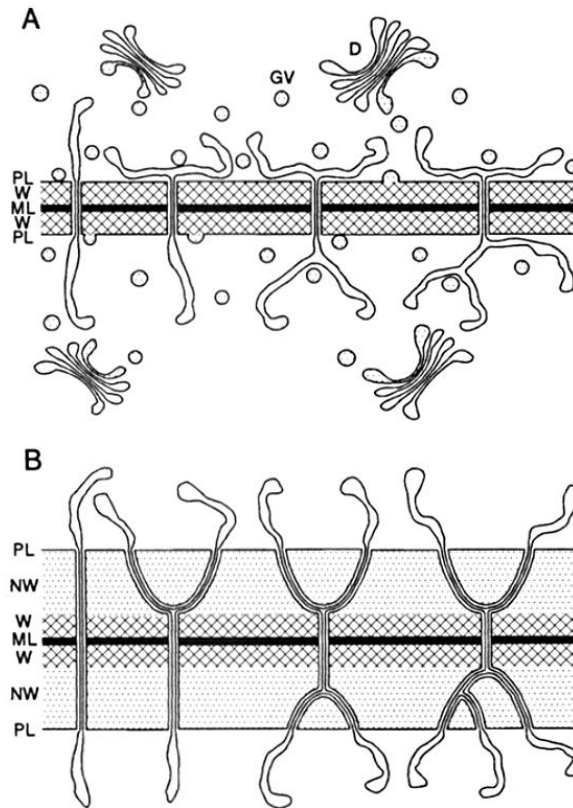
Figure 1.4 Modification of primary plasmodesmata during cell wall thickening. **(A)** Unbranched primary plasmodesmata in young, thin cell wall. **(B)** Variations of modified primary plasmodesmata that arise from **(A)** as a result of Golgi vesicles (GV) and dictyosomes (D) associations during cell wall thickening. PL, plasmalemma; W, cell wall; ML, middle lamella. Adapted from Ehlers and Kollman (1996).

1.2.3   Structure of plasmodesmata

Electron microscopy has consistently revealed that each plasmodesma embedded within the cell wall between two adjacent cells is made up of three basic cellular components: an outer plasma membrane covering, a central axial tubular endoplasmic reticulum strand termed the desmotubule, and a cytoplasmic sleeve in between (Fig. 1.3E). Moreover, recent genetic analysis (Vatén et al., 2011) and proteomic studies (Fernandez-Calvino et al., 2011) have revealed that the cell wall surrounding the plasmodesmata is also important for defining their function and regulation.
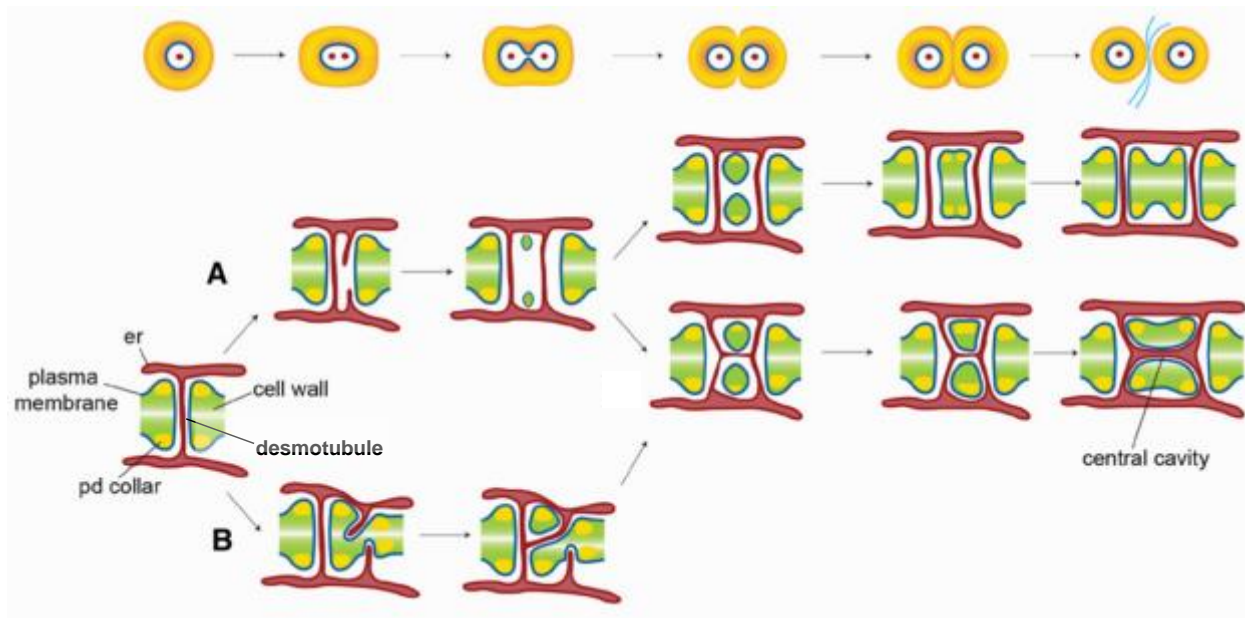
Figure 1.5 The models of secondary plasmodesmata formation. **(A)** Fission model. A second desmotubule is inserted into an enlarging plasmodesma (pd) pore creating a transitory structure containing two desmotubules, which eventually become separated as new wall material is deposited during cell wall expansion forming either twin or branched plasmodesmata. **(B)** *De novo* pore formation. Localised erosion of the cell walls allowed insertion of new endoplasmic reticulum (er) strand resulting to the formation of a new plasmodesma pore, which eventually connects with the original pore forming a complex structure. Adapted from Faulkner et al. (2008).

1.2.3.1 Plasma membrane

Each plasmodesma pore in the cell wall is lined with plasma membrane, which is derived from the original Golgi membrane vesicles forming the cell plate (Ehlers and Kollmann, 2001). The plasma membrane is an essential component of plasmodesmata as it dictates the general structure and shape of the plasmodesmata, and plays a major role in both plasmodesmata function and plasmodesmata regulation. Given its origin, the plasmodesmata plasma membrane is expected to be broadly similar to the adjacent cell plasma membrane, but proteomic analysis of isolated plasmodesmata from *Arabidopsis thaliana* (Arabidopsis) revealed that the plasmodesmata plasma membrane lacks H^+-ATPase, an otherwise ubiquitous plasma membrane transport protein (Fernandez-Calvino et al., 2011). Biological membranes, particularly the plasma membrane, are no longer considered as bilayers composed of homogenously distributed lipids and proteins. Instead, plasma membranes appear to be comprised of a mosaic of microdomains or membrane rafts with specialised compositions and properties (Mongrand et al., 2010) (Fig.

12
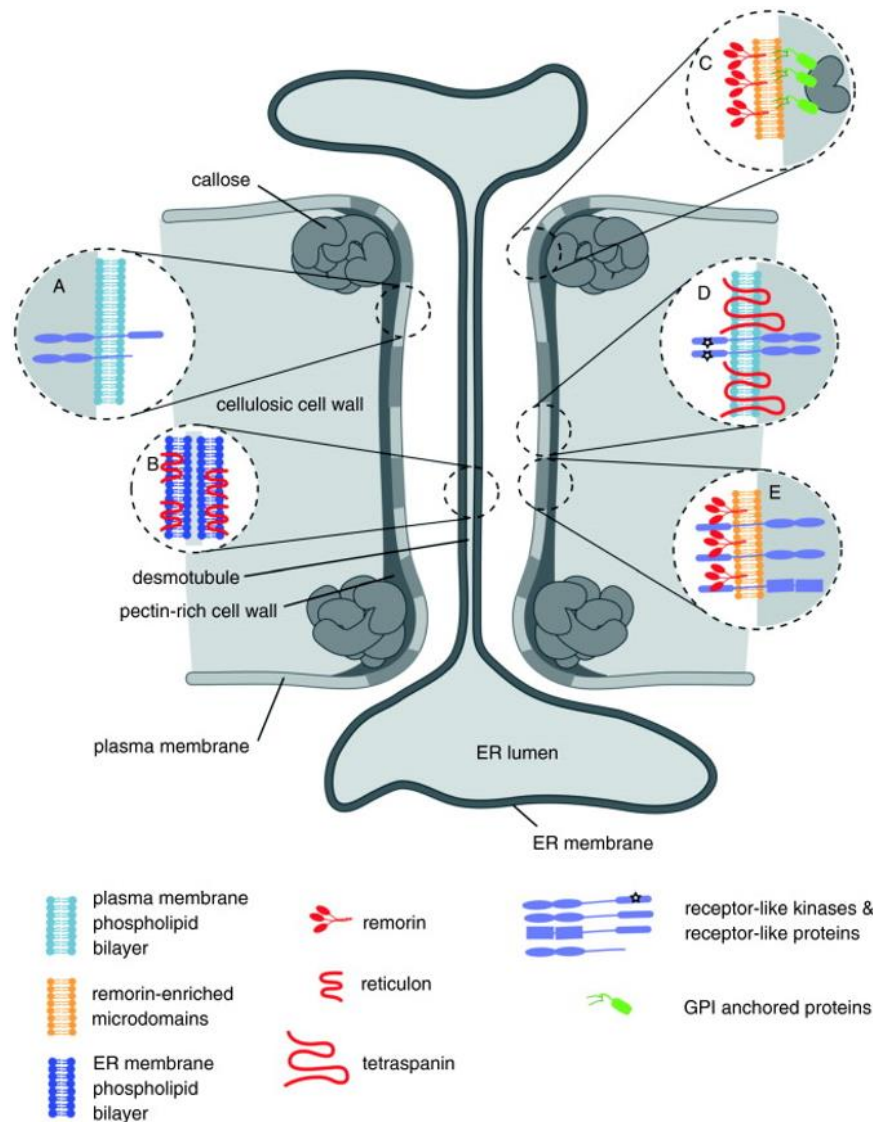
Figure 1.6 Diagrammatic representation of the molecular composition of the membrane components of plasmodesmata in plants. ER, endoplasmic reticulum. Adapted from Maule et al. (2011).

1.6). Membrane rafts are small (10-200 nm), heterogeneous, highly dynamic, sterol- and sphingolipid-enriched domains that compartmentalize cellular processes (Mongrand et al., 2010). In plant plasma membranes, the biochemical equivalent of membrane rafts are called detergent-resistant membranes (DRMs) (Borner et al., 2005; Mongrand et al., 2004; Peskan et al., 2000) which are also found in the plasmodesmata plasma membrane. Cell biological and biochemical characterization of the plasmodesmata plasma membrane in tomato (Raffaele et al., 2009) showed the association of clusters of remorin proteins, a *bona fide* DRM marker. This is an

important discovery considering the potential role of the plasmodesmata plasma membrane in protein sorting and targeting for trafficking through plasmodesmata as these rafts usually incorporate receptor-like kinases and receptor-like proteins and are frequently associated with glycosylphosphatidylinositol (GPI)-anchor proteins associated with plasmodesmata (Maule et al., 2011). These findings suggest that the plasmodesmata plasma membrane may be highly specialized and can function similarly to or autonomously from the bulk plasma membrane.

1.2.3.2 Cytoplasmic sleeve

It is the cytoplasmic sleeve that is believed to be responsible for the majority of molecular cell-to-cell transport because it is directly connected to the cytoplasms of the cells on either side. In leaves of C_4 grasses, plasmodesmata connections along the phloem-loading pathway (mesophyll to phloem) are typically unbranched (Fig. 1.7) (Evert et al., 1977, 1978; Robinson-Beers and Evert, 1991a; Russin et al., 1996). This observation is true in both developing and mature leaves (Evert et al., 1996). However, this does not mean that these plasmodesmata lack complexity. From structural studies of C_4 leaves, a wide variety of plasmodesmata morphologies at various cell wall interfaces has been well documented (Evert et al., 1977, 1978; Robinson-Beers and Evert, 1991a; Russin et al., 1996). Particularly in maize, structural variations observed along the different cell wall interfaces involve modification of the cytoplasmic sleeve. Internal sphincters found at the end of plasmodesmata on the mesophyll-cell side of cell walls do not obstruct the continuity of the desmotubule and may be a gating mechanism to regulate transport through the cytoplasmic sleeve (Fig. 1.7A and B) (Evert et al., 1977). At wall interfaces involving bundle sheath cells, where the plasmodesmata pass through the suberin lamellae, plasmodesmata have a constricted cytoplasmic sleeve; this constriction may also have regulatory functions (Fig. 1.7B-D) (Evert et al., 1977; Russin et al., 1996). On the other hand, plasmodesmata between adjacent vascular parenchyma cells have neither sphincters nor constricted cytoplasmic sleeves but have distinct neck constrictions and appear structurally similar on both sides of the wall interface (Fig. 1.7E) (Evert et al., 1978). Although these observations were based purely on static images and may not truly represent the dynamic nature of plasmodesmata, the existence of different plasmodesmal morphologies in the wall interfaces from the mesophyll cell-side to the vascular parenchyma-cell side indicates that plasmodesmata play an important role in cellular communication and transport during photosynthesis (Beebe and Russin, 1999).

Mesophyll cell

A

Mesophyll cell

B

Bundle sheath cell

C

Bundle sheath cell

D

Vascular parenchyma cell

E

Vascular parenchyma cell
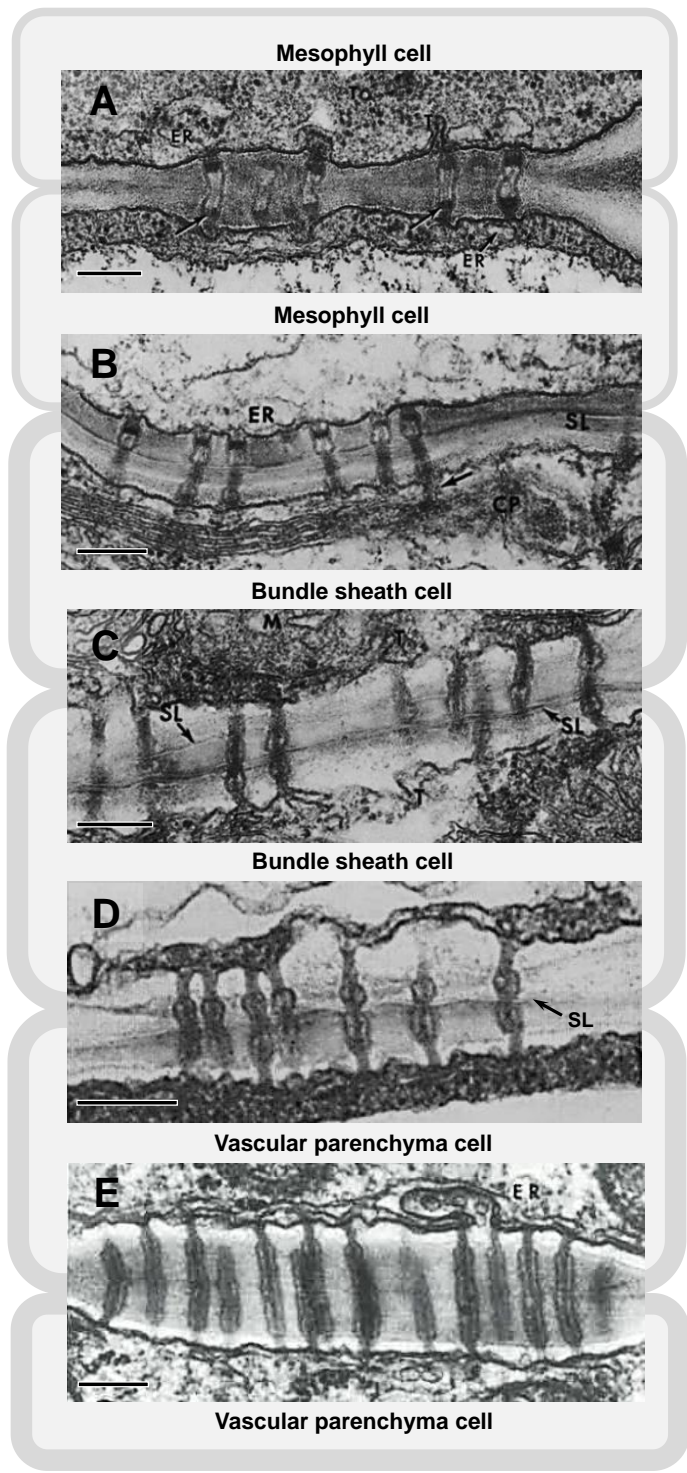
Figure 1.7 Morphologies of plasmodesmata at different cell interfaces along the phloem-loading pathway in a maize leaf. **(A)** Plasmodesmata in the wall between mesophyll cells. Arrows point to the internal sphincters which are found at both ends of the plasmodesmata (Evert et al., 1977). **(B)** Plasmodesmata in the mesophyll-bundle sheath cell wall. Internal sphincters are associated with the mesophyll-cell side of the plasmodesmata. On the bundle sheath-cell side, the cytoplasmic sleeves are constricted by a wide suberin lamellae (SL). Arrow points to desmotubule connected to a chloroplast (CP) (Evert et al., 1977). **(C)** Plasmodesmata in wall between bundle sheath cells. Cytoplasmic sleeves of the plasmodesmata are constricted in regions where SL are present (Evert et al., 1977). **(D)** Plasmodesmata in the bundle sheath-vascular parenchyma cell interface (Russin et al., 1996). **(E)** Plasmodesmata between adjacent vascular parenchyma cells. Note the constricted desmotubules, subtle neck constrictions, and lack of sphincters (Evert et al., 1978). ER, endoplasmic reticulum. Bars = 0.2 μm.

1.2.3.3 Desmotubule

Desmotubules arise from the endoplasmic reticulum trapped during cell plate assembly and are generally believed to be continuous with the endoplasmic reticulum in the adjoining cells (Hepler, 1982; Overall et al., 1982). Observations from electron micrographs of chemically-fixed tissue showed that the tubule of endoplasmic reticulum becomes tightly furled and that the inner leaflet of the endoplasmic reticulum is transformed into a rod (Hepler, 1982; Overall et al., 1982) (Fig. 1.3E). Reticulon proteins are now thought to be responsible for the formation of the desmotubule (Knox et al., 2015). Reticulons are integral membrane proteins that induce curvature of the endoplasmic reticulum to form tubules (Hu et al., 2008; Voeltz et al., 2006). Evidence of their association with the desmotubule (Fig. 1.6) was demonstrated in both plasmodesmata proteomic (Fernandez-Calvino et al., 2011) and colocalisation (Knox et al., 2015) studies. It was once widely accepted that no transport could take place in the desmotubule given the virtually closed cylindrical bilayer structure of endoplasmic reticulum with a central rod diameter of only 2.8 nm providing little or no open pathway for transport (Overall et al., 1982). However, more recent proposals suggest that the desmotubule may allow transport in association with the vacuolar-tubular network, as observed in trichomes of chickpea (Lazzaro and Thomson, 1996). Other studies have also claimed that dyes and proteins inserted into the endoplasmic reticulum membrane can apparently move through the desmotubule, either along the membrane or through the lumen, at least under some conditions (Cantrill et al., 1999; Guenoune-Gelbart et al., 2008; Martens et al., 2006). These observations were also supported by electron micrographs of plasmodesmata generated from rapid-frozen and freeze-substituted material where a more open structure of the desmotubule was seen (White and Barton, 2011).

1.2.3.4 Cell wall

In addition to callose, which is widely known to be associated with the cell wall surrounding the plasmodesmata, cell wall composition analysis revealed that major cell wall components such as pectin and cellulose were also differentially deposited around plasmodesmata (Faulkner et al., 2008; Giannoutsou et al., 2013).

1.2.3.4.1 Callose

The two ends of the plasmodesmata are constricted, each constriction known as the neck region. As a result of the balance between activities of the enzymes β-1,3-glucanases and callose synthases, polysaccharide molecules (β-glucan or callose) can accumulate and form a collar around this neck region (Maule et al., 2012) (Fig. 1.8). Among the β-1,3-glucanase gene families, only the members of GPI-anchored glycosyl hydrolase (family 17) were found to be associated with plasmodesmata (Levy et al., 2007) while Arabidopsis callose synthase 10 or glucan synthase-like 8 (Guseman et al., 2010) and callose synthase 7 (Xie et al., 2011) were shown to be responsible for callose synthesis at plasmodesmata in epidermal cells and phloem, respectively. Callose formation can be induced when plants are subjected to both physical and chemical stresses, which include mechanical wounding, herbivory, pathogen infection, and perception of aluminium and abscisic acid. The degree of callose formation is believed to play a major role in the control of plasmodesmata aperture, and therefore flux. The formation of more callose places a physical constraint on the plasmodesmata neck regions resulting in a lower size exclusion limit (SEL) defined as the maximum size of the molecules that can pass through. Studies involving callose biosynthesis at plasmodesmata have demonstrated the importance of callose in numerous plant developmental processes such as auxin symplastic transport, stomatal patterning (Guseman et al., 2010), lateral root formation (Benitez-Alfonso et al., 2013; Vatén et al., 2011), leaf vein development (Slewinski et al., 2012), and turgor-driven cotton fiber elongation (Ruan et al., 2001).
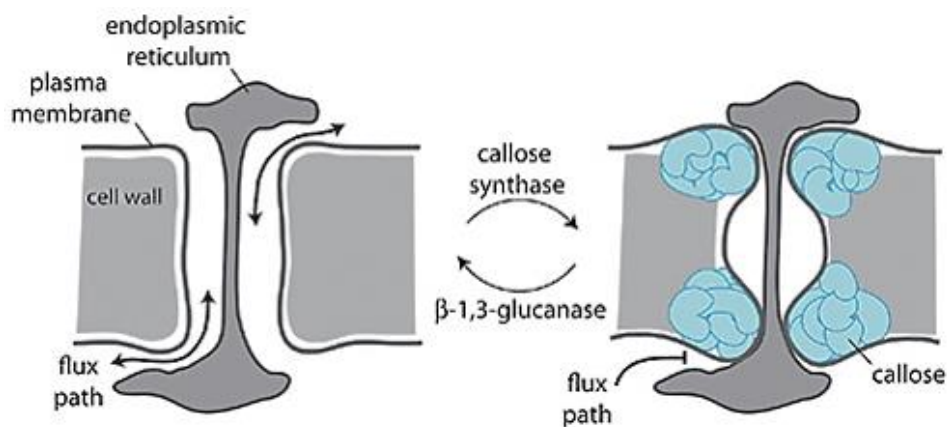
Figure 1.8 The mechanism of plasmodesmatal closure through callose formation. Adapted from Maule et al. (2012).

1.2.3.4.2 Pectin

Immunoassays in different tissues of various plant species have revealed enrichment in pectic polysaccharides in the cell wall regions around plasmodesmata (Faulkner et al., 2008; Giannoutsou et al., 2013; Orfila and Knox, 2000; Roy et al., 1997). Pectin composition can influence the stiffness of cell walls because pectins can interlink to form pectic supramolecules (Knox and Benitez-Alfonso, 2014). Two of the major components of pectin, homogalacturonan (HG) and rhamnogalacturonan-I (RG-I), were found to be preferentially localized at pit fields or plasmodesmata (Faulkner et al., 2008; Giannoutsou et al., 2013; Orfila and Knox, 2000; Roy et al., 1997). RG-I has two side chains; the arabinan domain is known to be associated with flexibility while the galactan domain is typically found in stiffer cell walls (Burton et al., 2010). In the cell wall surrounding plasmodesmata, $(1\rightarrow5)$-α-L-arabinan domains were found while $(1\rightarrow4)$-β-galactan was absent (Faulkner et al., 2008; Giannoutsou et al., 2013; Orfila and Knox, 2000; Roy et al., 1997). It is believed that this differential composition of pectin in the plasmodesmata region plays a role in the stabilization and/or regulation of plasmodesmatal structure.

1.2.3.4.3 Cellulose

Cellulose is the major component of most plant cell walls, and the microfibrils of cellulose constitute the reinforcing rods of the cell wall (Burton et al., 2010). The strength of the microfibrillar complexes is attributed to their unbranched and unsubstituted β-1,4-glucan chains. Both immunoassay and calcofluor white staining of freeze-fractured tobacco trichomes revealed a reduction in cellulose content in the cell wall surrounding plasmodesmata (Faulkner et al., 2008). This makes the surrounding wall more flexible for movement to accommodate oscillations of plasmodesmata apertures (Knox and Benitez-Alfonso, 2014).

1.2.4 Pit fields

Plasmodesmata in leaves occur in clusters, one unit of which is a pit field. It is highly likely that the primary plasmodesmata formed during cytokinesis are the pit field initials. A study of leaf development in maize revealed that the walls between mesophyll cells consistently maintained plasmodesmata at successive stages of mesophyll cell differentiation, and that the callose-bound aniline blue signal increased as the mesophyll cells matured (Giannoutsou et al., 2013). The differential deposition of pectin (Faulkner et al., 2008; Giannoutsou et al., 2013; Orfila and Knox,

2000; Roy et al., 1997) and cellulose (Faulkner et al., 2008) in the wall surrounding plasmodesmata and the insertion of additional plasmodesmata during modification and/or secondary plasmodesmata formation within the vicinity of existing plasmodesmata (Ehlers and Kollmann, 2001) also support this idea.

1.3   What is known about plasmodesmata in C$_4$ leaves?

Structurally, eudicot leaves have more complicated plasmodesmata, containing branches of different shapes and sizes, while plasmodesmata in monocot leaves are generally unbranched (reviewed in Beebe and Russin, 1999). Because of the limitations of using electron micrographs in plasmodesmata frequency studies in leaves (discussed in detail in Section 1.5), only a handful of species has been examined in monocots and most of these studies were done in grasses (Nelson and van Bel, 1998). Among the few C$_4$ grass species examined were maize (Evert et al., 1977, 1978; Evert et al., 1996), sugarcane (Robinson-Beers and Evert, 1991a; Robinson-Beers and Evert, 1991b), and African grasses, *Themeda triandra* (Botha, 1992; Botha and Evert, 1988), *Panicum maximum* (Botha, 1992), and *Eragrostis plana* (Botha, 1992). Consistently, the frequency of plasmodesmata, expressed as percent plasmodesmata per μm vein and plasmodesmata per μm cell wall interface, for C$_4$ leaves decreases as plasmodesmata get closer to the vasculature (Botha and van Bel, 1992). These values are commonly illustrated in plasmodesmograms, which are diagrammatic representations of plasmodesmata frequencies of cell interfaces from the mesophyll to the sieve tube elements derived from different studies (Botha and Evert, 1988; Botha and van Bel, 1992; Robinson-Beers and Evert, 1991a; Russin and Evert, 1985; van Bel et al., 1988). The plasmodesmata frequencies, however, do not always reflect the level of intercellular communication between cells (van Bel and Oparka, 1995). In eudicots, fewer plasmodesmata in wall interfaces closer to the vasculature is thought to be compensated by the presence of more complex and specialized plasmodesmata (Gamalei and Pakhomova, 1982) while a variety of plasmodesmata morphologies were found in different cell interfaces in monocots (Beebe and Russin, 1999; Evert et al., 1977, 1978; Russin et al., 1996).

1.4   The C$_4$ rice project

A major focus in agronomy is increasing crop yields for the increasing global population, which by year 2050 would require doubling of crop productivity per hectare of land available for agriculture (Ray et al., 2013). One of the main targets for increasing yield is improving photosynthetic efficiency, i.e. how efficiently the energy of sunlight is converted into usable biological compounds by plants. Increasing the rate of photosynthesis can lead to enhanced plant growth and better yield (Kromdijk et al., 2016; López-Calcagno et al., 2018; Parry et al., 2013; Whitney et al., 2015; Zhu et al., 2010), and there is a range of strategies to improve the rate of photosynthesis in important crops (Long et al., 2015; Ort et al., 2015). Several large projects are exploring how C$_4$ photosynthesis could be added into key C$_3$ crops, one of which is the C$_4$ Rice Project (https://c4rice.com).

The working goal of the C$_4$ Rice Project is to create a functional C$_4$ rice by modifying both the anatomical structure and biochemical machinery of rice. The reference C$_4$ model is the NADP-ME C$_4$ subtype (Kajala et al., 2011) which occurs widely in the grasses particularly in agricultural crops like setaria, sorghum, and maize. Among other C$_4$ subtypes such as NAD-ME and PCK, the NADP-ME subtype was also found to have greater mechanistic flexibility, energetic consequences, and environmental plasticity (Furbank, 2011). Cell specific expression of known C$_4$ enzymes and associated proteins in rice is underway (Kajala et al., 2011; Lin et al., 2016).

The transport of photosynthetic intermediates between the mesophyll and bundle sheath cells in C$_4$ plants has both apoplastic and symplastic attributes. The apoplastic pathway encompasses transport through the cell wall and intercellular spaces outside the cell plasma membranes, whereas the symplastic pathway involves transport from cell to cell within the contiguous cell plasma membranes, via the plasmodesmata. Although some genes potentially associated with C$_4$ leaf anatomy have been identified in sorghum (Rizal et al., 2015) and maize (Wang et al., 2017) mutants, it is still uncertain whether the existing C$_3$ symplastic transport mechanism between the mesophyll and bundle sheath cells of rice will be sufficient to support the expected increase in cell-to-cell metabolite flux that the C$_4$ photosynthetic pathway will impose. This is an important consideration because an increase in photosynthetic efficiency gained by introducing C$_4$ photosynthesis into a C$_3$ plant cannot be fully achieved if the transport of assimilates is hampered. Therefore, empirical quantification of the symplastic transport channels – the plasmodesmata, between the mesophyll and bundle sheath cells in leaves of C$_3$ and C$_4$ plants is

crucial to gain knowledge on the necessary structural changes that must be incorporated to create a functional C$_4$ rice.

1.5   Quantification of plasmodesmatal connection in leaves

1.5.1   Transmission electron microscopy

Transmission electron microscopy or TEM has commonly been used for plasmodesmata studies due to its high intrinsic resolution, and therefore its ability to capture and resolve the substructure of individual plasmodesma at the nanometer scale. It proved very useful in elucidating the origin, formation, and substructure of plasmodesmata (reviewed in (Beebe and Turgeon, 1991; Cilia and Jackson, 2004; Crawford and Zambryski, 1999; Ehlers and Kollmann, 2001; Faulkner and Oparka, 2016; Maule, 2008; Maule et al., 2011; Oparka and Roberts, 2001). However, the two-dimensional nature of the electron micrographs and very small area of capture per image impose a significant limitation in quantifying the plasmodesmatal connection at a tissue or organ level. To accurately quantify plasmodesmal frequency and dimensions (i.e., cross-sectional area) would require serial sectioning, preferably with the cell wall sectioned *en face*, and meticulous data analysis including three-dimensional reconstructionSerial sectioning and three-dimensional reconstruction are both labour-intensive and time-consuming activities which nowadays can be achieved through serial block face scanning electron microscopy (Hughes et al., 2014). The first attempt at plasmodesmata quantification used *Azolla pinnata* roots (Gunning, 1978). Gunning (1978) argued that when randomly distributed plasmodesmata are cut longitudinally, the number of cylindrical profiles seen per unit length of wall, multiplied by a proportionality constant, is equal to their frequency per unit area. Consequently, from electron micrographs of *Azolla* root plasmodesmata one can estimate plasmodesmata density by implementing the Gunning constant $1/(t+1.5R)$ where t is the section thickness and R is the average radius of plasmodesmata (Gunning, 1978). Although this proportionality constant provided good estimates of *Azolla* root plasmodesmata density, it is not appropriate for quantifying plasmodesmata density in higher plant tissues (Gunning, 1978). In contrast to the randomly distributed plasmodesmata in *Azolla* roots, pit fields or clusters of plasmodesmata are common in higher plant root (Seagull, 1983) and leaf tissues (Botha, 1992; Botha and Evert, 1988; Sage and Sage, 2009). These pit fields add another layer of complexity to quantification because their sizes and shapes are variable (Olesen, 1975). Moreover, the pattern of distribution of pit fields in leaves, whether the pit fields are in

clusters or evenly distributed on the cell wall interfaces, is still unknown for almost all leaf tissues. Despite this, a number of studies have attempted to quantify plasmodesmata density between leaf cells using TEM either with (Sowiński et al., 2007; Sowiński et al., 2003) or without (Botha and Cross, 1997; Botha, 1992; Botha and Evert, 1988; Seagull, 1983) incorporating the Gunning constant in their calculations. Most of these studies analysed monocots, comparing a C_3 photosynthetic leaf to a C_4 counterpart with minimal replication. Of particular interest is the work of Botha (1992) which showed that leaves of C_4 grasses have more plasmodesmatal connection than C_3 grasses. While this result was consistent with a C_4 mechanism, Botha's measurements, although empirical, are limited because the measurements are based on cell wall length or wall interface length rather than on the three-dimensional wall interface area. Consequently, numerical values from these measurements (Botha, 1992) would be very difficult to convert to an estimate of plasmodesmata per wall or interface area. Similarly, using these two-dimensional estimates per wall length for semi-quantification of plasmodesmata density in plasmodesmograms (Botha and van Bel, 1992) cannot reflect the plasmodesmata density throughout a whole leaf.

1.5.2 Scanning electron microscopy

One way to circumvent the problem of localized patches of plasmodesmata is to capture pit fields in leaves using scanning electron microscopy or SEM. Especially with monocot leaves where cells are arranged in parallel, random tearing of the leaf after critical point drying or high pressure freezing can expose cell interfaces and allow capture of whole pit fields (Sage and Sage, 2009) and thus, provide a measure of plasmodesmata frequency within pit fields. An earlier study combined TEM and SEM to quantify plasmodesmata density between the mesophyll and bundle sheath cells of a C_4 leaf (Olesen, 1975). However, similar to TEM, SEM can only capture a very small area representative of the whole tissue and would still require hundreds of images to obtain sufficient data for true quantification of plasmodesmata density for each cell interface in a tissue or organ.

1.5.3 Fluorescence microscopy

The genes involved in plasmodesmata development are not yet known but the close association of callose with plasmodesmata allows indirect labelling, quantification, and characterization of plasmodesmata in plant tissues. Aniline blue staining and β-1,3-glucan antibody hybridization permit plasmodesmata-associated callose localization using fluorescence microscopy. However,

because fluorescence microscopes can only resolve objects as small as pit fields, this imaging technique cannot be used to quantify individual plasmodesmata within cell walls. As noted above, SEM can capture individual plasmodesma within whole pit fields, so in combination with fluorescence microscopy, which can capture pit fields over a large surface area, we can obtain a better estimate of plasmodesmata density in leaves. Although we can tear open critical-point-dried leaves to observe plasmodesmata in pit fields, it is very difficult to obtain fluorescence images from bundle sheath cells deep within leaves. The main limitation is the reduced light penetration due to leaf pigments and light scattering by the cell wall and cell contents. With the exception of the almost pigment-free epidermal layer, cutting the leaf into thin sections would appear necessary to see the succeeding tissue layers inside the leaf.

1.5.4 Plant Enzyme-Assisted (PEA)-CLARITY

Fortunately, during the initial stage of this study, a new technique for three-dimensional micro-visualisation of plant organs, PEA-CLARITY was published (Palmer et al., 2015). Clear Lipid-exchanged Acrylamide-hybridised Rigid Imaging/Immunostaining/In situ hybridization-compatible Tissue-hYdrogel or CLARITY is a whole tissue clearing method followed by fluorescence immunolocalisation that was first developed to image and map connections within an intact mouse brain (Chung et al., 2013). It involves fixing and binding tissues within an acrylamide gel prior to extraction of optically interfering lipids with detergent. This results in an optically transparent tissue suitable for deep imaging using confocal microscopy. Adapting the CLARITY method with an additional enzyme digestion step to permeabilise the cell wall sufficiently to allow entry of antibodies and clearing agents led to a plant-based technique called Plant Enzyme-Assisted-CLARITY or PEA-CLARITY (Palmer et al., 2015). PEA-CLARITY has been used to localise rubisco throughout an intact leaf segments producing three-dimensional reconstructions for both monocot and eudicot leaves without resorting to sectioning (Palmer et al., 2015). These advantages make PEA-CLARITY a valuable technique with great potential for application in quantification of plasmodesmata in intact leaf tissue.

1.6 Research questions

Given the importance of the mesophyll-bundle sheath cell plasmodesmata to the C_4 photosynthetic mechanism, more information about plasmodesmata at the interface is required

to understand the function and efficiency of C_4 photosynthesis. To address this in this thesis, two research questions were proposed. First, *is increased plasmodesmata density between mesophyll and bundle sheath cells in leaves an anatomical enabler of C_4 photosynthesis?* This question relates to a previous report where reduction in distance between bundle sheaths was regarded as one of the anatomical enablers of the evolution of C_4 photosynthesis in grasses (Christin et al., 2013). Similarly, there is a need to know if it is also likely that increased plasmodesmata density between mesophyll and bundle sheath cells is an anatomical requirement for C_4 photosynthesis. Second, *does plasmodesmata density between mesophyll and bundle sheath cells respond to changes in photosynthetic capacity in C_4 species?* This question was prompted by a publication that suggested a direct correlation between plasmodesmata density and photosynthetic capacity in grasses (Sowiński et al., 2007).

1.7   Thesis overview

This thesis by compilation outlines the progressive work that has been done from the development of a new plasmodesmata quantification method (Chapter 3) to the generation of a comprehensive dataset of plasmodesmata densities in a wide selection of C_3 and C_4 grasses (Chapter 4), and how these quantitative values can be used in combination with photosynthetic measurements to get estimates of plasmodesmatal flux in leaves (Chapter 3). The plasmodesmata quantification technique developed from this study was also used to reinvestigate the effect of different growth light environments on plasmodesmata development in leaves of C_4 grasses (Chapter 5) and also, to evaluate the effect of perturbing C_4 metabolism on plasmodesmata development between the mesophyll and bundle sheath cells in *Setaria viridis* (Chapter 6). Synthesis of the results obtained from the experiments performed and how these results contributed in answering the two research questions are discussed in Chapter 7.

2
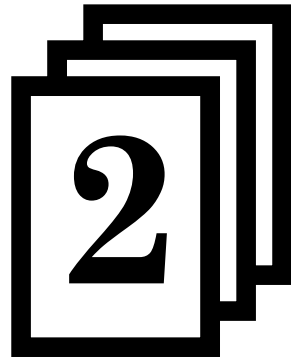
PUBLICATION 1

Peeking at a plant through the holes in the wall – exploring the roles of plasmodesmata

Statement of Contribution

This thesis is submitted as a Thesis by Compilation in accordance with https://policies.anu.edu.au/ppl/document/ANUP_003405

I declare that the research presented in this Thesis represents original work that I carried out during my candidature at the Australian National University, except for contributions to multi-author papers incorporated in the Thesis where my contributions are specified in this Statement of Contribution.

Title and authors: **Peeking at a plant through the holes in the wall – exploring the roles of plasmodesmata.**
Kuan-Ju Lu, Florence R. Danila, Yueh Cho, and Christine Faulkner.

Current status of paper: **Published** (New Phytologist. First published 25 March 2018. https://doi.org/10.1111/nph.15130)

Contribution to paper: **K-J.L., F.R.D., Y.C., and C.F. conceived the idea. K-J.L. led the writing with significant contributions from F.R.D., Y.C., and C.F. K-J.L. and C.F. finalized the manuscript.**
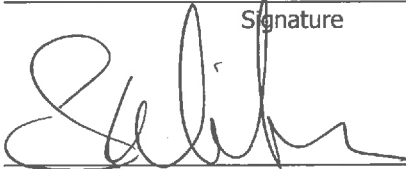
Senior author or collaborating author's endorsement:

Christine Faulkner		11/5/18
Senior author – Print Name	Signature	Date

Florence R. Danila		1/8/18
Candidate – Print Name	Signature	Date

Endorsed

Susanne von Caemmerer	S van Caemmerer	1/8/18
Chair of Supervisory Panel – Print Name	Signature	Date

Spencer Whitney		2/8/18.
Delegated Authority – Print Name	Signature	Date

Viewpoints

Peeking at a plant through the holes in the wall – exploring the roles of plasmodesmata

Summary

Plasmodesmata (PD) are membrane-lined pores that connect neighbouring plant cells and allow molecular exchange via the symplast. Past studies have revealed the basic structure of PD, some of the transport mechanisms for molecules through PD, and a variety of physiological processes in which they function. Recently, with the help of newly developed technologies, several exciting new features of PD have been revealed. New PD structures were observed during early formation of PD and between phloem sieve elements and phloem pole pericycle cells in roots. Both observations challenge our current understanding of PD structure and function. Research into novel physiological responses, which are regulated by PD, indicates that we have not yet fully explored the potential contribution of PD to overall plant function. In this Viewpoint article, we summarize some of the recent advances in understanding the structure and function of PD and propose the challenges ahead for the community.

Introduction

Intercellular communication is a foundation for growth, development and environmental responses in all multicellular organisms (Long *et al.*, 2015). In plants, the cytoplasm of neighbouring cells is connected by membrane-lined pores called plasmodesmata (PD). While PD were originally considered to be mere 'holes in the cell wall' we now understand them to be highly regulated channels that underpin many aspects of plant responses. Studies of PD function have addressed their structure, the control of their functional aperture (or size exclusion limit, SEL), how PD connect cells to the phloem and thereby facilitate long-distant transport of molecules, and how PD respond to internal or external cues (Fig. 1). It is well established that a range of molecules, from small metabolites to macromolecules such as nucleic acids and proteins, can pass through PD (Fig. 1a), but the significance of this transport is not yet fully understood. Recent work has widened our understanding of the contexts in which PD play a fundamental role and raised important questions regarding how PD function and facilitate cell-to-cell communication. Following a workshop in which plasmodesmal researchers came together to discuss the most recent findings

in the field, we will detail some of the outstanding questions that were presented and discussed. We will address fields of plant biology where a role for PD has been poorly considered, and the methods that will enable the field to pursue novel questions. The way we think about PD function is changing and the aim of the workshop and this discussion is to encourage new research ideas that will enable a better understanding of the complexity of PD and the extent of biological roles they play.

Re-evaluating PD structure and function

The basic structure of PD is accepted as a plasma membrane (PM)-lined pore that contains a tubule of compressed endoplasmic reticulum (ER), named the desmotubule (DT). Within the PD, the space between the DT and PM is called the cytoplasmic sleeve and is considered the main passage for molecules between cells (Fig. 1a,g). The cytoplasmic sleeve can be constricted by callose accumulation in the cell wall, and loosened by callose degradation and this controls the PD SEL to regulate transport of small, soluble molecules through PD (Fig. 1f; Otero *et al.*, 2016). It is easy to understand how a soluble molecule can pass through an open PD pore, but this model was recently challenged by electron tomography of PD in *Arabidopsis* root columella initial cells that identified PD with no cytoplasmic sleeve (Fig. 1g). According to our current understanding of the cytoplasmic sleeve we would expect these PD to have a small SEL, but PD in these walls still allow the transport of the Green Fluorescent Protein (GFP) (27 kDa; Nicolas *et al.*, 2017). This result suggests our understanding of PD structure and their functional SEL is too simplistic.

Long-distance transport of molecules between source and sink tissues is vital for plant development. Molecules are loaded into enucleated phloem sieve elements (SEs) via companion cells and are unloaded in sink tissues (Fig. 1b). It is known that the unloading of molecules occurs at the protophloem cells in the *Arabidopsis* root (Oparka *et al.*, 1994), but this model assumed unloading occurs via companion cells. A recent study identified that the phloem-pole pericycle (PPP), and not companion cells, act as a recipient for molecules delivered via the phloem (Fig. 1g; Ross-Elliott *et al.*, 2017). These authors also observed that proteins undergo batch unloading, in which proteins with high molecular weight (above 27 kDa) transport in pulses rather than at a constant rate as expected from passive movement through a pore. Detailed ultrastructural analysis by serial block face-scanning electron microscopy (SBF-SEM) revealed funnel-shaped PD at the PPP–SE interface that are wider on the SE side than the PPP side (Fig. 1g). Mathematical modelling indicated that this structure can sustain the high fluxes of solutes that occur in the unloading zone and that the combination of diffusion with batch unloading makes the unloading of solutes into PPP cells a more likely route for phloem unloading.

These recent findings highlight that we have not yet identified all the forms in which PD occur, or the way different structures underpin the mechanisms of cell-to-cell movement of molecules via the symplast. New methods for imaging PD, such as SBF-SEM, will facilitate advances in understanding PD with respect to PD ultrastructure, positioning, and distribution (Kremer *et al.*, 2015; Ross-Elliott *et al.*, 2017). An example of this is the use of the Plant-Enzyme-Assisted (PEA)-CLARITY immunofluorescence-based method which has been used to provide empirical PD densities and thus quantify PD on larger surface areas of different cellular interfaces in leaves (Danila *et al.*, 2016). These quantitative values can now be used in combination with photosynthetic measurements to get estimates of PD flux in leaves (Danila *et al.*, 2016), an important parameter in modelling the metabolites transport in plants to improve photosynthesis (von Caemmerer *et al.*, 2012). Rolling these methods out to different cell types and tissues would create an atlas of PD structures that can be correlated with known PD fluxes to better understand the role of the symplast.

Genome transfer between cells

An intriguing aspect of cell-to-cell communication is the possibility of transferring whole organelles and genomes between cells. In specific cell types, like male meiocytes, the nuclear genome migrates to the neighbouring cells through cytoplasmic channels that are either derived from PD or synthesized *de novo* (Mursalimov *et al.*, 2013). This process is called cytomixis and might be involved in producing pollen with different karyotypes. The work of Mursalimov & Deineko (2017) has defined cytomixis as a nonspecific process in which selection of chromosomes for migration is random (Mursalimov & Deineko, 2017). Cytomixis is therefore considered as a possible mechanism for evolution, however, the mechanisms of transfer and the relationship of cytomytic channels to PD are still unclear.

Grafting has also presented cases of genome transfer between cells. It was observed several years ago that genome-encoded traits had crossed a graft junction (Fig. 1d). The new species generated by grafting was not only fertile but also had conserved many characteristics of the parental species (Fuentes *et al.*, 2014). There is evidence that both nuclear and organelle genomes can cross a graft junction – given that nuclear genomes incorporate multiple chromosomes, there are many questions to be answered about how this transfer occurs. PD exist at graft junctions but their functional aperture would presumably be far too small to allow DNA or organelle transfer. However, it is possible that PD at a graft junction are highly plastic and dynamic, but this remains to be investigated.

Long-distance calcium waves

Calcium acts as a second messenger in various stress responses; in response to a stimulus, the cytosolic calcium concentration can change dramatically and rapidly (Choi *et al.*, 2016). Calcium waves occur in response to stimuli such as salt stress and wounding and can move systemically in a plant. Thus, they can integrate responses

between different parts of the plant body (Fig. 1e; Gilroy *et al.*, 2016). Recent models of intercellular spread of calcium ions (Ca^{2+}) incorporate extracellular production of reactive oxygen species (ROS; Evans *et al.*, 2016) but it is still unclear how the wave moves from cell-to-cell. PD would seem to be an obvious component in the spread of any signal from cell-to-cell and so their role in systemic calcium waves will be an interesting topic of research. It is possible that PD act as a conduit for the movement of Ca^{2+} between cells, the PD PM acts as a scaffold for the propagation of the wave between cells, or the PD act via some other mechanism entirely (Gilroy *et al.*, 2016; Fig. 1e).

Intercellular coordination of the circadian clock

The circadian clock manifests by oscillation of expression of clock genes with a 24-h periodicity. Interestingly, these oscillations occur in both aerial and subterranean tissues; while shoots and roots exhibit synchronized clock gene oscillations, it was recently established that if roots are excised from plants they cannot sustain clock gene oscillations (Takahashi *et al.*, 2015). The shoot apex is the defining tissue in the synchronization of clock gene oscillations in the shoots and roots, suggesting that a mobile signal travels to distal tissues to coordinate the clock across the whole plant (Takahashi *et al.*, 2015). It has been established that sugars influence the circadian clock (Haydon *et al.*, 2013; Takahashi *et al.*, 2015) and therefore PD might play a role in the entrainment of the circadian clock by regulating the transport of clock-related signals and sugars between shoots and roots. PD themselves might also be regulated by the circadian clock to temporally regulate the movement of clock-related signals (Fig. 1c).

Pathogen recognition and symbiotic interactions

Plant cells can perceive invading microorganisms. N-Acetylglucosamine derivatives such as chitin, lipochitooligosaccharides and Nod factors originate from both pathogens and symbionts and are known inducers of intracellular signalling (Zipfel & Oldroyd, 2017). There are numerous plant receptors that are involved in the perception of microorganisms (Zipfel & Oldroyd, 2017) and fungal pathogens. PD have been found to have a specific PD-located receptor for chitin perception and signalling that contributes to defence (Faulkner *et al.*, 2013; Fig. 1f). In symbiotic interactions it has been shown that the symplast is dynamic during the initiation of nodule organogenesis in legumes. This involves the creation of symplastic connections between the phloem and the nodule primordia initial cells (Complainville *et al.*, 2003). Nodule organogenesis is initiated in the cortex and synchronized with rhizobial infection in the root epidermis (generally a root hair), underpinning the importance of precise signalling and communication for successful nodule development and infection. Understanding how PD and the symplast are regulated by all classes of microbes will help in understanding how the fluxes of signalling molecules are differentially regulated to activate or avoid host defence responses.
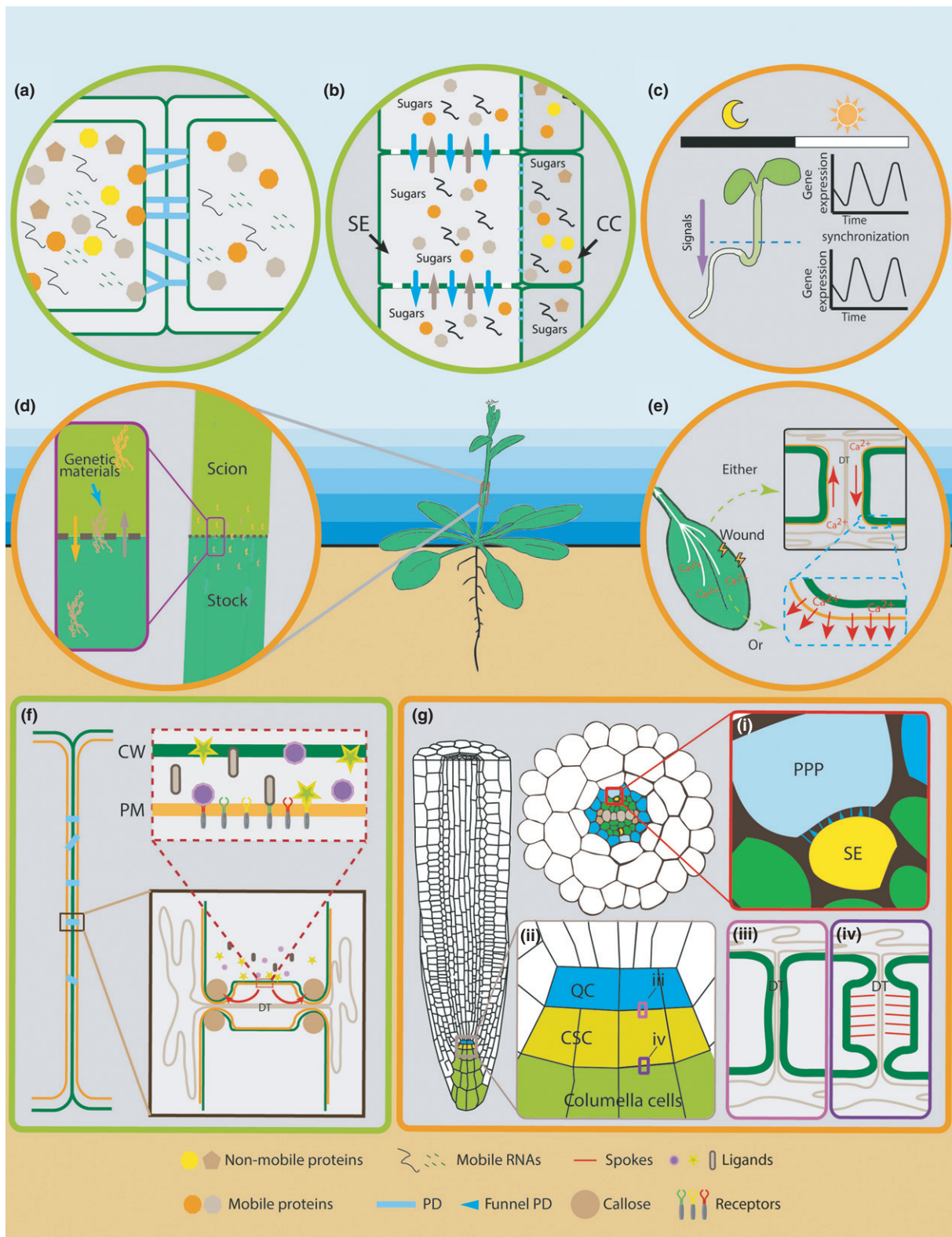
Conclusion

Studies on plant symplastic transport are now becoming multidisciplinary, promoting collaboration between biologists, engineers and computer modellers (Jackson *et al.*, 2017). Current work on both short and long distance symplastic transport in plants in relation to plant–plant, plant–microbe, and plant–environment interactions highlights the usefulness of molecular tools such as the over-active, PD-located callose synthase icals3m (Vatén *et al.*, 2011) and calcium biosensors (Nakai *et al.*, 2001) in root and shoot

Fig. 1 Atlas of known and proposed roles of plasmodesmata (PD). (a) PD allow the cell-to-cell movement of a range of molecules. For macromolecules, such as proteins and RNAs, this movement is proposed to be selective, leading to mobile and nonmobile populations of these molecules. (b) PD connect the phloem companion cells (CCs) to sieve elements (SEs) and thus molecules can travel long distances within the phloem. (c) Circadian rhythms are coordinated between shoots and roots suggesting the existence of circadian signals that travel long distances via the symplast, as well as signals that might regulate the symplast in a circadian-dependent manner. (d) Genetic material has been observed to cross graft junctions. How this occurs is unknown but may include a mechanism in which chromosomes cross between cells via modified PD. (e) Stress-triggered calcium waves move systemically, and PD might play a role in the cell-to-cell transmission of the wave by allowing the flow of calcium from cell to cell, or by providing membrane conduits upon which the wave is propagated between cells. (f) Pathogens and symbionts release ligands that are recognized by host receptors. Some of these regulate symplastic transport by triggering signalling cascades that regulate callose deposition at PD and thus control the size exclusion limit (SEL). CW, cell wall; PM, plasma membrane. (g) Novel PD structures have been identified in roots. (i) Funnel shaped PD were identified at the sieve element–phloem pole pericycle (SE–PPP) interface where they are likely to function in phloem unloading. (ii) In the root meristem, young PD between the quiescent centre cells (QCs) and the columella stem cells (CSCs) were observed with almost no cytoplasmic sleeve (i.e. almost no space between the desmotubule (DT) and the PM, (iii)). (iv) PD spanning the CSCs and columella cells have a visible cytoplasmic sleeve and connections between the DT and PM.

cellular patterning and signalling. As PD are present between almost all cell types in plants, it seems likely that our knowledge of the range of contexts in which PD play a critical role will only increase. The challenge before the community is to translate structural observations into functional understanding of how the interconnected cytoplasm of plants influences localized and systemic responses.

Acknowledgements

Author contributions

K-J.L., F.R.D., Y.C. and C.F. conceived the idea. K-J.L. lead the writing with significant contributions from F.R.D., Y.C. and C.F.K. J.L. designed the artwork. K-J.L. and C.F. finalized the manuscript.

ORCID

Florence R. Danila http://orcid.org/0000-0002-7352-3852

Kuan-Ju Lu[1]*, **Florence R. Danila**[2] , **Yueh Cho**[3,4,5] and **Christine Faulkner**[6]

[1]Laboratory of Biochemistry, Wageningen University, Stippeneng 4, 6708 WE Wageningen, the Netherlands;
[2]ARC Centre of Excellence for Translational Photosynthesis, Research School of Biology, Australian National University, Canberra, ACT 2601, Australia;
[3]Molecular and Biological Agricultural Sciences Program, Taiwan International Graduate Programme, National Chung Hsing University and Academia Sinica, Taipei 11529, Taiwan;
[4]Institute of Plant and Microbial Biology, Academia Sinica, Taipei 11529, Taiwan;
[5]Graduate Institute of Biotechnology, National Chung Hsing University, Taichung 40227, Taiwan;
[6]John Innes Centre, Norwich Research Park, Norwich, NR4 7UH, UK
(*Author for correspondence: tel +31 7 482 868; email kuan-ju.lu@wur.nl)

References

von Caemmerer S, Quick WP, Furbank RT. 2012. The development of C_4 rice: current progress and future challenges. *Science* **336**: 1671–1672.

Choi WG, Hilleary R, Swanson SJ, Kim SH, Gilroy S. 2016. Rapid, long-distance electrical and calcium signaling in plants. *Annual Review of Plant Biology* **67**: 287–307.

Complainville A, Brocard L, Roberts I, Dax E, Sever N, Sauer N, Kondorosi A, Wolf S, Oparka K, Crespi M. 2003. Nodule initiation involves the creation of a new symplasmic field in specific root cells of *Medicago* species. *The Plant Cell* **15**: 2778–2791.

Danila FR, Quick WP, White RG, Furbank RT, von Caemmerer S. 2016. The metabolite pathway between bundle sheath and mesophyll: quantification of plasmodesmata in leaves of C_3 and C_4 monocots. *The Plant Cell* **28**: 1461–1471.

Evans MJ, Choi WG, Gilroy S, Morris RJ. 2016. A ROS-assisted calcium wave dependent on the AtRBOHD NADPH oxidase and TPC1 cation channel propagates the systemic response to salt stress. *Plant Physiology* **171**: 1771–1784.

Faulkner C, Petutschnig E, Benitez-Alfonso Y, Beck M, Robatzek S, Lipka V, Maule AJ. 2013. LYM2-dependent chitin perception limits molecular flux via plasmodesmata. *Proceedings of the National Academy of Sciences, USA* **110**: 9166–9170.

Fuentes I, Stegemann S, Golczyk H, Karcher D, Bock R. 2014. Horizontal genome transfer as an asexual path to the formation of new species. *Nature* **511**: 232–235.

Gilroy S, Bialasek M, Suzuki N, Gorecka M, Devireddy AR, Karpinski S, Mittler R. 2016. ROS, calcium, and electric signals: key mediators of rapid systemic signaling in plants. *Plant Physiology* **171**: 1606–1615.

Haydon MJ, Mielczarek O, Robertson FC, Hubbard KE, Webb AA. 2013. Photosynthetic entrainment of the *Arabidopsis thaliana* circadian clock. *Nature* **502**: 689–692.

Jackson MDB, Xu H, Duran-Nebreda S, Stamm P, Bassel GW. 2017. Topological analysis of multicellular complexity in the plant hypocotyl. *eLife* **6**: e26023.

Kremer A, Lippens S, Bartunkova S, Asselbergh B, Blanpain C, Fendrych M, Goossens A, Holt M, Janssens S, Krols M *et al.* 2015. Developing 3D SEM in a broad biological context. *Journal of Microscopy* **259**: 80–96.

Long Y, Scheres B, Blilou I. 2015. The logic of communication: roles for mobile transcription factors in plants. *Journal of Experimental Botany* **66**: 1133–1144.

Mursalimov S, Deineko E. 2017. Cytomixis in tobacco microsporogenesis: are there any genome parts predisposed to migration? *Protoplasma* **254**: 1379–1384.

Mursalimov SR, Sidorchuk YV, Deineko EV. 2013. New insights into cytomixis: specific cellular features and prevalence in higher plants. *Planta* **238**: 415–423.

Nakai J, Ohkura M, Imoto K. 2001. A high signal-to-noise Ca^{2+} probe composed of a single green fluorescent protein. *Nature Biotechnology* **19**: 137–141.

Nicolas WJ, Grison MS, Trepout S, Gaston A, Fouche M, Cordelieres FP, Oparka K, Tilsner J, Brocard L, Bayer EM. 2017. Architecture and permeability of post-cytokinesis plasmodesmata lacking cytoplasmic sleeves. *Nature Plants* **3**: 17082.

Oparka K, Duckett C, Prior D, Fisher D. 1994. Real-time imaging of phloem unloading in the root tip of Arabidopsis. *Plant Journal* **6**: 759–766.

Otero S, Helariutta Y, Benitez-Alfonso Y. 2016. Symplastic communication in organ formation and tissue patterning. *Current Opinion in Plant Biology* **29**: 21–28.

Ross-Elliott TJ, Jensen KH, Haaning KS, Wager BM, Knoblauch J, Howell AH, Mullendore DL, Monteith AG, Paultre D, Yan D *et al.* 2017. Phloem unloading in Arabidopsis roots is convective and regulated by the phloem-pole pericycle. *eLife* **6**: e24125.

Takahashi N, Hirata Y, Aihara K, Mas P. 2015. A hierarchical multi-oscillator network orchestrates the Arabidopsis circadian system. *Cell* **163**: 148–159.

Vatén A, Dettmer J, Wu S, Stierhof Y-D, Miyashima S, Yadav Shri R, Roberts Christina J, Campilho A, Bulone V, Lichtenberger R *et al.* 2011. Callose biosynthesis regulates symplastic trafficking during root development. *Developmental Cell* **21**: 1144–1155.

Zipfel C, Oldroyd GE. 2017. Plant signalling in symbiosis and immunity. *Nature* **543**: 328–336.

Key words: calcium wave, circadian clock, genome transfer, intercellular communication, pathogen and symbiotic interaction, plasmodesmata.

About *New Phytologist*

- *New Phytologist* is an electronic (online-only) journal owned by the New Phytologist Trust, a **not-for-profit organization** dedicated to the promotion of plant science, facilitating projects from symposia to free access for our Tansley reviews and Tansley insights.

- Regular papers, Letters, Research reviews, Rapid reports and both Modelling/Theory and Methods papers are encouraged. We are committed to rapid processing, from online submission through to publication 'as ready' via *Early View* – our average time to decision is <26 days. There are **no page or colour charges** and a PDF version will be provided for each article.

- The journal is available online at Wiley Online Library. Visit **www.newphytologist.com** to search the articles and register for table of contents email alerts.

- If you have any questions, do get in touch with Central Office (np-centraloffice@lancaster.ac.uk) or, if it is more convenient, our USA Office (np-usaoffice@lancaster.ac.uk)

- For submission instructions, subscription and all the latest information visit **www.newphytologist.com**

3
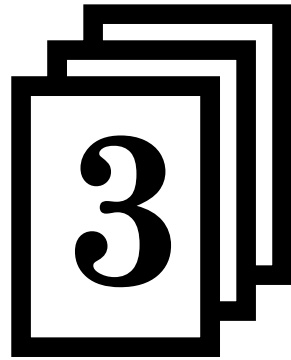
PUBLICATION 2

The metabolite pathway between bundle sheath and mesophyll: quantification of plasmodesmata in leaves of C_3 and C_4 monocots

Statement of Contribution

This thesis is submitted as a Thesis by Compilation in accordance with https://policies.anu.edu.au/ppl/document/ANUP_003405

I declare that the research presented in this Thesis represents original work that I carried out during my candidature at the Australian National University, except for contributions to multi-author papers incorporated in the Thesis where my contributions are specified in this Statement of Contribution.

Title and authors: **The metabolite pathway between bundle sheath and mesophyll: quantification of plasmodesmata in leaves of C₃ and C₄ monocots.**
Florence R. Danila, William Paul Quick, Rosemary G. White, Robert T. Furbank, and Susanne von Caemmerer.
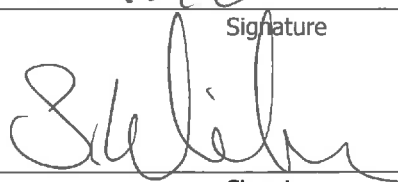
Current status of paper: **Published** (The Plant Cell, Vol. 28: 1461-1471, June 2016. https://doi.org/10.1105/tpc.16.00155)

Contribution to paper: **F.R.D. developed the technique and conducted all the experiments, imaging, quantification, data analysis, and statistics in consultation with S.v.C., R.T.F, R.G.W., and W.P.Q. F.R.D. also prepared the first draft of the manuscript, handled all corrections based on co-authors comments and suggestions, and did all the formatting for journal submission.**

Senior author or collaborating author's endorsement:

Rosemary G. White		3-8-18
Senior author – Print Name	Signature	Date
Robert T. Furbank		1/8/18
Senior author – Print Name	Signature	Date
Susanne von Caemmerer		1/8/18
Senior author – Print Name	Signature	Date
Florence R. Danila		1/8/18
Candidate – Print Name	Signature	Date

Endorsed

Susanne von Caemmerer		1/8/18
Chair of Supervisory Panel – Print Name	Signature	Date
Spencer Whitney		2/8/18
Delegated Authority – Print Name	Signature	Date

The Metabolite Pathway between Bundle Sheath and Mesophyll: Quantification of Plasmodesmata in Leaves of C$_3$ and C$_4$ Monocots[OPEN]

Florence R. Danila,[a,b] William Paul Quick,[b,c] Rosemary G. White,[d] Robert T. Furbank,[a,d,1] and Susanne von Caemmerer[a]

[a] ARC Centre of Excellence for Translational Photosynthesis, Australian National University, Canberra 2601, Australia
[b] International Rice Research Institute, Laguna 4030, Philippines
[c] University of Sheffield, Sheffield S10 2TN, United Kingdom
[d] CSIRO Agriculture, Canberra 2601, Australia

ORCID IDs: 0000-0002-7352-3852 (F.R.D.); 0000-0002-7618-3814 (R.G.W.); 0000-0001-8700-6613 (R.T.F.); 0000-0002-8366-2071 (S.v.C.)

C$_4$ photosynthesis is characterized by a CO$_2$-concentrating mechanism between mesophyll (M) and bundle sheath (BS) cells of leaves. This generates high metabolic fluxes between these cells, through interconnecting plasmodesmata (PD). Quantification of these symplastic fluxes for modeling studies requires accurate quantification of PD, which has proven difficult using transmission electron microscopy. Our new quantitative technique combines scanning electron microscopy and 3D immunolocalization in intact leaf tissues to compare PD density on cell interfaces in leaves of C$_3$ (rice [_Oryza sativa_] and wheat [_Triticum aestivum_]) and C$_4$ (maize [_Zea mays_] and _Setaria viridis_) monocot species. Scanning electron microscopy quantification of PD density revealed that C$_4$ species had approximately twice the number of PD per pitfield area compared with their C$_3$ counterparts. 3D immunolocalization of callose at pitfields using confocal microscopy showed that pitfield area per M-BS interface area was 5 times greater in C$_4$ species. Thus, the two C$_4$ species had up to nine times more PD per M-BS interface area (_S. viridis_, 9.3 PD μm^{-2}; maize, 7.5 PD μm^{-2}; rice 1.0 PD μm^{-2}; wheat, 2.6 PD μm^{-2}). Using these anatomical data and measured photosynthetic rates in these C$_4$ species, we have now calculated symplastic C$_4$ acid flux per PD across the M-BS interface. These quantitative data are essential for modeling studies and gene discovery strategies needed to introduce aspects of C$_4$ photosynthesis to C$_3$ crops.

INTRODUCTION

The superior photosynthetic performance of C$_4$ crop plants is largely due to the biochemical and anatomical specialization that results in concentration of CO$_2$ at the active site of Rubisco, reducing photorespiration and permitting Rubisco to operate close to its catalytic optimum. Separation of the biochemical CO$_2$ pump in the mesophyll (M; where atmospheric CO$_2$ is initially fixed into C$_4$ acids by PEP carboxylase) from the site of decarboxylation and refixation by Rubisco in the bundle sheath (BS) means that C$_4$ acids must move into the BS and C$_3$ products return to the M at rates greater than the net rate of photosynthesis (Hatch and Osmond, 1976; von Caemmerer and Furbank, 2003). Due to the high degree of secondary thickening and often suberization of the BS walls, metabolite movement is limited to the symplasm and abundant plasmodesmata (PD) at this cell interface have been demonstrated (Hatch, 1987).

For accurate modeling of C$_4$ photosynthetic flux, it is essential to quantify the number of PD between the M and BS, which facilitate the bidirectional movement of assimilates. However, due to their minute size (30 to 50 nm), individual PD

can only be seen under the electron microscope (Ding et al., 1992; Robards, 1976). Clusters of PD, called pitfields, are at the limit of detectability for light microscopy (Carr, 1976; Robards, 1976). Transmission electron microscopy (TEM) has been routinely used to study details of PD structure (Robards, 1976; Evert et al., 1977; Ding et al., 1992; Overall and Blackman, 1996), but extracting quantitative data requires careful serial sectioning and reconstruction. There have been very few reports quantifying PD density at the M-BS cell interface in C$_4$ (or C$_3$) plants (Olesen, 1975). This has severely limited our ability to model C$_4$ photosynthetic flux and strategies for determining the genetics and evolution of the anatomical specialization for C$_4$ metabolite flux.

In some cases, estimates of PD frequency via TEM in other plants have employed proportionality constant, originally derived by Gunning (1978). This value is $1/(t + 1.5R)$, where t is the section thickness and R is the average radius of PD. However, the use of the proportionality constant for quantification is limited to randomly distributed, nonclustered PD such as those found in cell plates of _Azolla_ roots, from which the constant was derived (Gunning, 1978). However, in most monocot leaves, PD are clustered in pitfields (Evert et al., 1977; Faulkner et al., 2008; Robinson-Beers and Evert, 1991a, 1991b), making the use of this proportionality constant for PD quantification invalid (Gunning, 1978).

Another common approach to quantify PD density is the plasmodesmogram, in which the total number of PD detected along a given length of cell wall interface is expressed as a PD

---

frequency (Botha and Evert, 1988; Botha, 1992; Botha and van Bel, 1992). The main drawback of this technique is that TEM sections provide only a thin (200 nm at most) 2D slice of a complex 3D cell wall interface, so the number of PD detected is dependent on the angle at which the pitfield was cut. Furthermore, the 2D TEM images capture only a fraction of the total PD within a pitfield and do not allow for the mostly noncircular shape of the pitfields.

In this study, we report a new method that combines scanning electron microscopy and 3D immunolocalization by confocal microscopy to better quantify PD connections in the leaf. Scanning electron microscopy has been used in PD-related studies but not as routinely as TEM due to its inability to capture PD ultrastructural details. With recent advances in high-resolution scanning electron microscopy, capturing the 3D morphology of PD in cell walls of algae, ferns, and vascular plants is now possible (Brecknock et al., 2011; Barton and Overall, 2015). The advantage of scanning electron microscopy to elucidate PD and pitfield distribution on cell surfaces (Botha and Evert, 1988; Faulkner et al., 2008; Sage and Sage, 2009) is that the whole pitfield and all the individual PD within it can be seen in a single image. PD frequency per pitfield area can then be obtained simply by measuring the pitfield area and counting individual PD. In fact, one of the earliest studies that made use of scanning electron microscopy in tandem with TEM looked into the PD frequency at the M-BS cell interface in C_4 species (Olesen, 1975), but these measurements covered only a small portion of the leaf. Scanning electron microscopy alone is impractical for PD quantification because only a small portion of the entire cell interface can be captured at one time.

Confocal microscopy can be used to visualize pitfields using dyes or fluorescent probes known to label proteins or molecules colocalizing with PD (Faulkner et al., 2008). A common method for detecting PD is to use an antibody against callose, a β-1,3-glucan, which is known to be deposited around the PD neck (Turner et al., 1994). However, in intact tissues, the absorption and scattering of light by cell walls and cell contents limits detection of PD to the outer layers such as the leaf epidermis and trichomes (Faulkner et al., 2008). Recent success in 3D confocal imaging of intact plant tissues using a clearing technique (PEA-CLARITY; Palmer et al., 2015) enables the quantification of pitfield distribution and abundance within whole, cleared tissue over large areas of cell interfaces by callose immunofluorescence. By combining details of PD frequency per pitfield by scanning electron microscopy imaging, with the density of pitfields per cell interface derived from 3D confocal imaging, we can more accurately calculate the PD density per cell interface.

Using this improved quantitative method, we report here that C_4 leaves have up to 9-fold higher PD density at the interface between M and BS cells than C_3 leaves. This is due to both an increase in number of PD per pitfield area and an increase in pitfield density at this interface. Quantification of PD at this interface will enable both modeling of C_4 metabolic flux and the design of experiments to determine the genetic regulation and evolution of the symplastic transport mechanisms of C_4 plants.

RESULTS

Leaf Anatomy of Two C_3 and Two C_4 Crop Species

Transverse sections of leaves of the two C_3 species (rice [*Oryza sativa*] and wheat [*Triticum aestivum*]) showed that, as is typical for C_3 plants, the chloroplasts were abundant in M cells with very few or no chloroplasts visible in BS cells (Figures 1A to 1D). In the C_4 photosynthetic leaves, such as *Setaria viridis* and maize (*Zea mays*), both M cells and BS cells have abundant chloroplasts (Figures 1E to 1H). In both C_3 and C_4 species studied, chloroplasts in the M cells were distributed along the cell periphery. Moreover, in the C_4 species studied, the BS cell chloroplasts were positioned centrifugally toward the M cells, characteristic of the
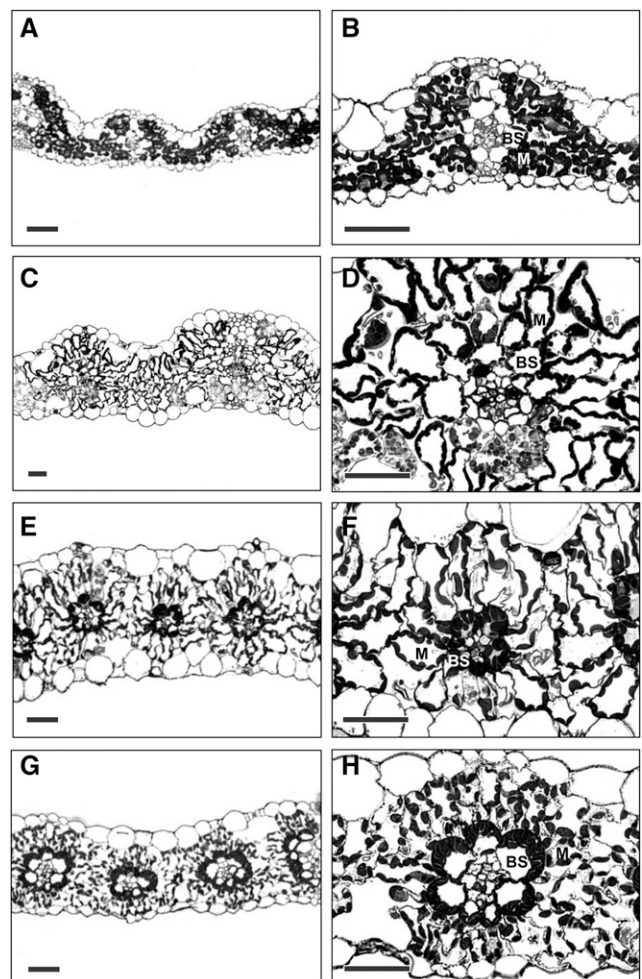
Figure 1. Light Micrographs of Transverse Sections of Leaves of the Two C_3 Species and Two C_4 Species Examined.

(A) and **(B)** Rice, C_3.
(C) and **(D)** Wheat, C_3.
(E) and **(F)** *S. viridis*, C_4.
(G) and **(H)** Maize, C_4.
Bars = 50 μm.
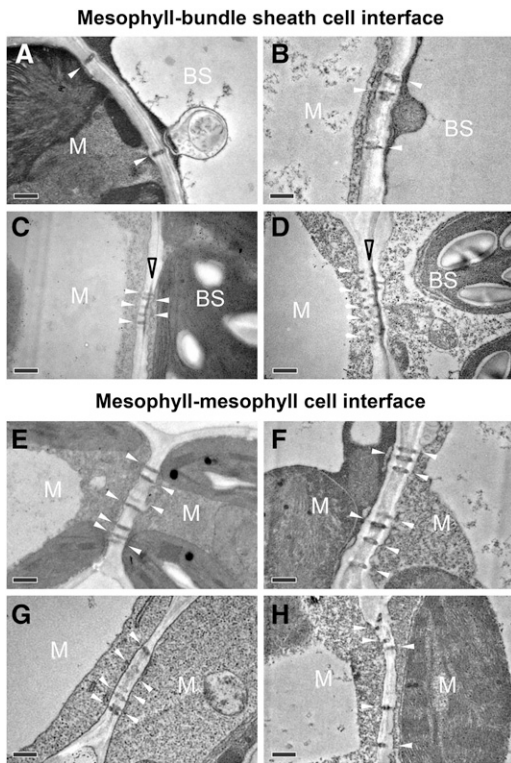
Figure 2. Transmission Electron Micrographs of Plasmodesmata at Cell Interfaces in Leaves of C_3 and C_4 Species.

(A) and **(E)** Rice, C_3.
(B) and **(F)** Wheat, C_3.
(C) and **(G)** *S. viridis*, C_4.
(D) and **(H)** Maize, C_4.
White and open black arrowheads indicate plasmodesmata and suberin lamella, respectively. Bars = 0.5 μm.

NADP-malic enzyme decarboxylation type found in grasses (Hatch, 1987). In the transverse sections shown, the shape of BS cells in both the C_3 and C_4 species was cylindrical with a smooth surface. M cell shape, on the other hand, varied from lobed in rice (Figure 1B) to elongated in *S. viridis* (Figure 1F).

Plasmodesmata of C_3 and C_4 Species Viewed under Transmission Electron Microscope

PD at cell interfaces were readily identified in TEM ultrathin sections (Figure 2), but only a small portion of the total PD within a pitfield could be captured this way. A thicker suberin lamella in the area where PD lie between the M cell and BS cell was observed only in the C_4 species (*S. viridis* and maize; Figures 2C and 2D) but not in the C_3 species (rice and wheat; Figures 2A and 2B). No suberized layer was found between M cells in either C_3 or C_4 species (Figures 2E to 2H). The areas of individual PD were similar in the two C_4 species, *S. viridis* (0.007 ± 0.0002 μm^2) and maize (0.007 ± 0.0002 μm^2) while in C_3 species, a larger PD area was observed in wheat (0.008 ± 0.0002 μm^2) than rice (0.006 ± 0.0001 μm^2).

Quantification of Pitfield Area and Plasmodesmata Frequency per Pitfield Area

Regions of contact between M cells and BS cells that could be visualized with scanning electron microscopy (Figure 3) were exposed by tearing critical point dried leaf tissue parallel to the veins. On closer inspection, clusters of pitfields were seen (Figures 4A, 4C, 4E, and 4G), and within each pitfield, all PD could be counted (Figures 4B, 4D, 4F, and 4H). PD in C_3 species were generally spaced farther apart than PD in C_4 species (Figure 4). C_3 species also had larger pitfield areas on both the M-BS and M-M cell interfaces compared with the C_4 species examined (Figure 5). Because there was considerable variation in pitfield area, we plotted the number of PD as a function of pitfield area and found strong linear correlations for all four species (Figure 6). Plotting values obtained from M-BS cell interface with values from M-M cell interface for the same species resulted in statistically different
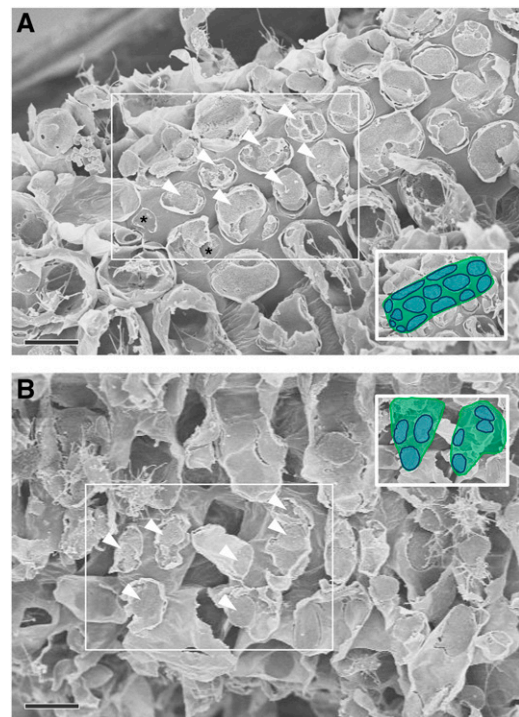
Figure 3. Field Emission Scanning Electron Micrograph of Cell Interfaces in *S. viridis* Leaf.

(A) M-BS cell interface. The torn patches (arrowheads) are mesophyll cell remnants on the surface of underlying cylindrical bundle sheath cells.
(B) M-M cell interface. The torn patches (arrowheads) are mesophyll cell remnants on the sides of highly lobed mesophyll cells.
In each case, the torn patches (arrowheads) on the cell surfaces are remnants of attachment sites with neighboring mesophyll cells. Most patches are covered in mesophyll cell debris, and only sites lacking cell debris (asterisk) were used for plasmodesmata quantification. Inset is the boxed area with underlying bundle sheath **(A)** or mesophyll **(B)** cell area in green and attachment sites in blue. Bars = 10 μm.
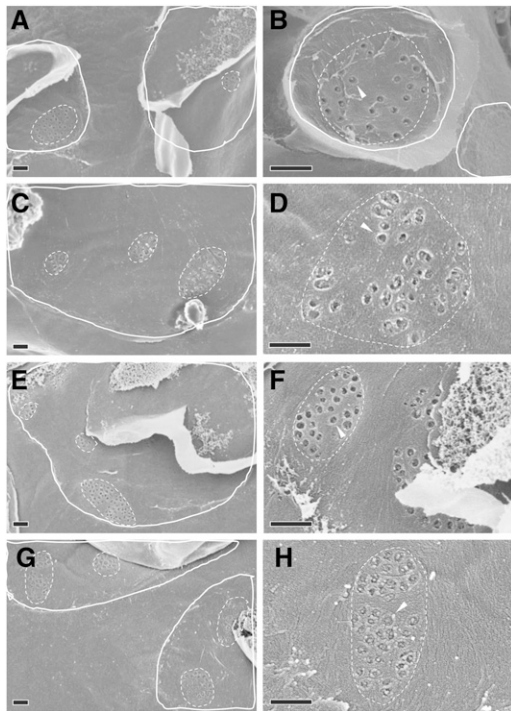
Figure 4. Field Emission Scanning Electron Micrographs of Plasmodesmata at the M-BS Cell Interface of C_3 and C_4 Species.

(A) and **(B)** Rice, C_3.
(C) and **(D)** Wheat, C_3.
(E) and **(F)** *S. viridis*, C_4.
(G) and **(H)** Maize, C_4.
(A), **(C)**, **(E)**, and **(G)** Example enlargements from M-BS attachment sites (solid white outlines) free of overlying mesophyll cell debris, containing pitfields (dotted white outlines). The underlying bundle sheath cell surface outside the attachment sites would normally face an intercellular space within the leaf. The clear areas within the attachment sites indicate M-BS cell wall connections that lack plasmodesmata.
(B), **(D)**, **(F)**, and **(H)** Individual pitfields (dotted outlines) within M-BS attachment sites, showing pitfield plasmodesmata (arrowheads). Bars = 0.5 μm.

regression lines in rice, wheat, and maize but not in *S. viridis* (Figure 6). Calculated PD per μm^2 pitfield based on the linear regressions obtained revealed that the C_4 species, *S. viridis* and maize, had almost double the PD per μm^2 pitfield in the M-BS cell interface compared with C_3 species, rice and wheat (Figure 6, Table 1). Similarly, a higher PD per μm^2 pitfield in the M-M cell interface was found in C_4 species, *S. viridis* and maize, compared with the C_3 species, rice and wheat (Figure 6, Table 1).

Using 3D Immunolocalization to Quantify Pitfield Area per Cell Interface Area

3D immunolocalization of pitfields allowed quantification of total pitfield area on cell interfaces over large surface areas in leaves (Figure 7). The area corresponding to cell/cell

interfaces was derived from the 3D image by selecting a subset of images from the complete z-stack that included all focal planes of the cell file of interest. Maximum intensity projections generated a single in-focus image that captured all the pitfield signals within that cell interface. In cases where there was an overlap of pitfield signals from different cell interfaces, it was possible to eliminate extraneous signals by filtering based on the size and shape of typical pitfields. The pitfields on the M-BS cell interface (parallel to the surface) were smaller than those on the M-M cell interface (perpendicular to the surface) mainly because of the pitfield orientation (Figure 7). The pitfields on the M-BS cell interface were also more evenly distributed than those on the M-M cell interface, which appeared to be clustered (Figure 8). Quantification using ImageJ software revealed that the two C_4 species had more pitfields per cell interface area than the two C_3 species (Figure 8, Table 1). On the M-BS cell interface, *S. viridis* and maize had 12.7% ± 0.3% and 11.4% ± 0.3% pitfield area coverage, respectively, while rice had 2.8% ± 0.1% and wheat had 5.5% ± 0.3% (Table 1). Similarly, on the M-M cell interface, the two C_4 species had higher pitfield area coverage than the two C_3 species. *S. viridis* was recorded to have 8.5% ± 0.1% pitfield area per cell interface area while maize had 14.4% ± 0.2%. Only 4.8% ± 0.1% and 3.7% ± 0.2% were found for rice and wheat, respectively (Table 1).

Calculation of Plasmodesmata Density on Cell Interface Areas

By combining the values for PD per μm^2 pitfield with pitfield area per cell interface area, we could calculate PD density per cell interface area (Table 1). Between M and BS cells, the C_4 species had up to 9 times more PD per cell interface area (*S. viridis* had 9.3 ± 0.2 PD μm^{-2}; maize had 7.5 ± 0.2 PD μm^{-2}) than the C_3 species (rice had 1.0 ± 0.1 PD μm^{-2}; wheat had 2.6 ± 0.1 PD μm^{-2}) (Table 1). Similarly, the
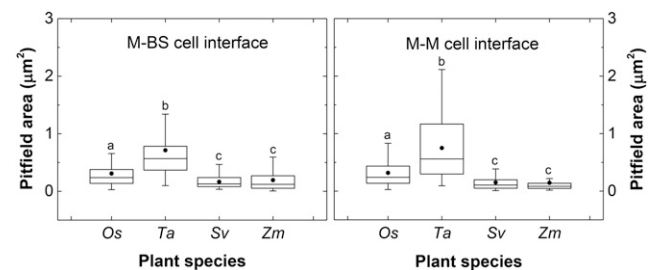
Figure 5. Pitfield Area at Cell Interfaces of Leaves of C_3 and C_4 Species Derived from Field Emission Scanning Electron Micrograph Measurements.

The box and whisker represent the 25 to 75 percentile and minimum-maximum distributions of the data, respectively. Closed circles give the overall means. Statistical differences according to MATLAB two-sample *t* test at P value < 0.05 are indicated by letters. Values indicated by the same letter are not statistically different. *Os*, *Oryza sativa*; *Ta*, *Triticum aestivum*; *Sv*, *Setaria viridis*; *Zm*, *Zea mays*.
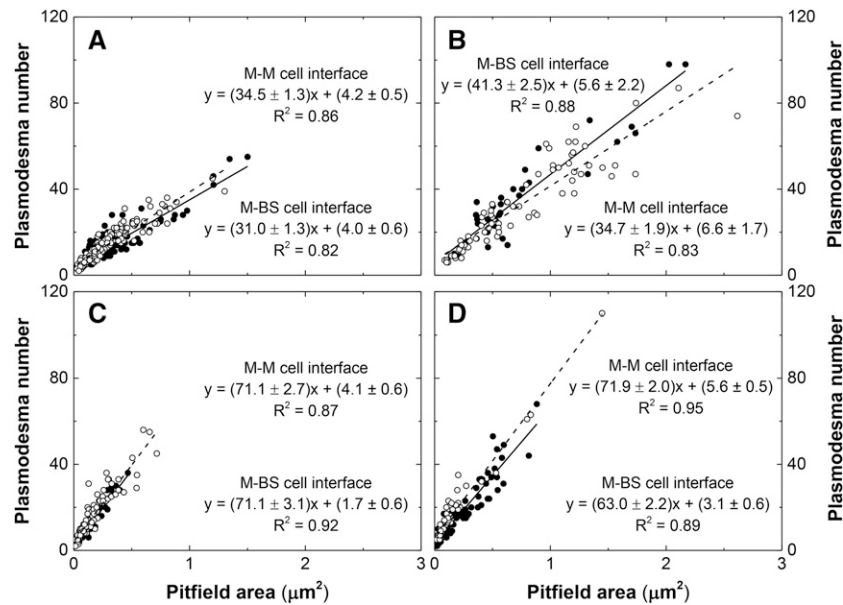
Figure 6. Plasmodesmata Frequency per Pitfield Area at Cell Interfaces in Leaves of C_3 and C_4 Species.

(A) Rice, C_3.

(B) Wheat, C_3.

(C) *S. viridis*, C_4.

(D) Maize, C_4.

Closed circles correspond to the values obtained from the M-BS cell interface. Open circles correspond to the values obtained from the M-M cell interface. Solid line and dashed line correspond to the regression lines generated using the plotted values from M-BS cell interface and M-M cell interface, respectively. Analysis using SPSS Statistics software with P value < 0.05 revealed M-BS cell interface and M-M cell interface regression lines to be statistically different in **(A)**, **(B)**, and **(D)** but not in **(C)**. The plasmodesmata frequency per pitfield area was calculated using the linear equation, y = mx + b, where y is the plasmodesmata frequency, m is the slope, x is the pitfield area, and b is the intercept. R^2 is coefficient of determination, where a value of 1 indicates that the regression line perfectly fits the data while a value of 0 indicates that the line does not fit the data at all.

PD density per cell interface area difference between M cells was larger in the C_4 species than in the C_3 species (Table 1). The C_3 species, rice and wheat, had 1.6 ± 0.1 PD μm^{-2} and 1.5 ± 0.1 PD μm^{-2}, respectively, whereas of the two C_4 species, *S. viridis* had 6.4 ± 0.1 PD μm^{-2} and maize had the highest at 11.2 ± 0.2 PD μm^{-2}.

Plasmodesmatal Flux Calculation

Measuring CO_2 assimilation rates in leaves of the C_3 and C_4 monocot species examined allowed estimates of PD flux between M cells and BS cells to be calculated. In C_4 species, the flux rate of C_4 acids into the bundle sheath has to equal or

Table 1. Density of Plasmodesmata on Cell Interfaces of C_3 and C_4 Species

Species	Mean Cell Interface Area (μm^2)	Mean Pitfield Area per Cell Interface (μm^2)	Mean Pitfield Area per Cell Interface Area (%)	PD per μm^2 Pitfield	PD per μm^2 Cell Interface	PD Area per Cell Interface Area (%)
M-BS cell interface						
Rice, C_3	609 ± 25^a	17 ± 1^a	2.8 ± 0.1^a	35.0 ± 0.4^a	1.0 ± 0.1^a	0.6 ± 0.02^a
Wheat, C_3	2704 ± 150^b	149 ± 28^b	5.5 ± 0.3^b	46.9 ± 1.0^b	2.6 ± 0.1^b	2.0 ± 0.03^b
S. viridis, C_4	486 ± 14^c	61 ± 5^c	12.7 ± 0.3^c	72.8 ± 0.9^c	9.3 ± 0.2^c	6.2 ± 0.07^c
Maize, C_4	1203 ± 32^d	137 ± 11^b	11.4 ± 0.3^d	66.1 ± 0.7^d	7.5 ± 0.2^d	5.4 ± 0.06^d
M-M cell interface						
Rice, C_3	249 ± 9^e	10 ± 2^d	4.1 ± 0.1^e	38.7 ± 0.4^e	1.6 ± 0.1^e	1.0 ± 0.02^e
Wheat, C_3	2246 ± 183^b	83 ± 16^c	3.7 ± 0.2^e	41.3 ± 0.7^f	1.5 ± 0.1^e	1.2 ± 0.02^f
S. viridis, C_4	375 ± 7^f	32 ± 2^e	8.5 ± 0.1^f	75.2 ± 0.8^c	6.4 ± 0.1^f	4.2 ± 0.05^g
Maize, C_4	810 ± 17^g	117 ± 6^b	14.4 ± 0.2^g	77.5 ± 0.6^g	11.2 ± 0.2^g	8.0 ± 0.07^h

Numbers in the "PD per μm^2 Pitfield" column are the sum of slopes and intercepts shown in Figure 6. Statistical differences according to MATLAB two-sample *t* test or SPSS Statistics software at P value < 0.05 are indicated by letters. Values indicated by the same letter within a column are not statistically different.
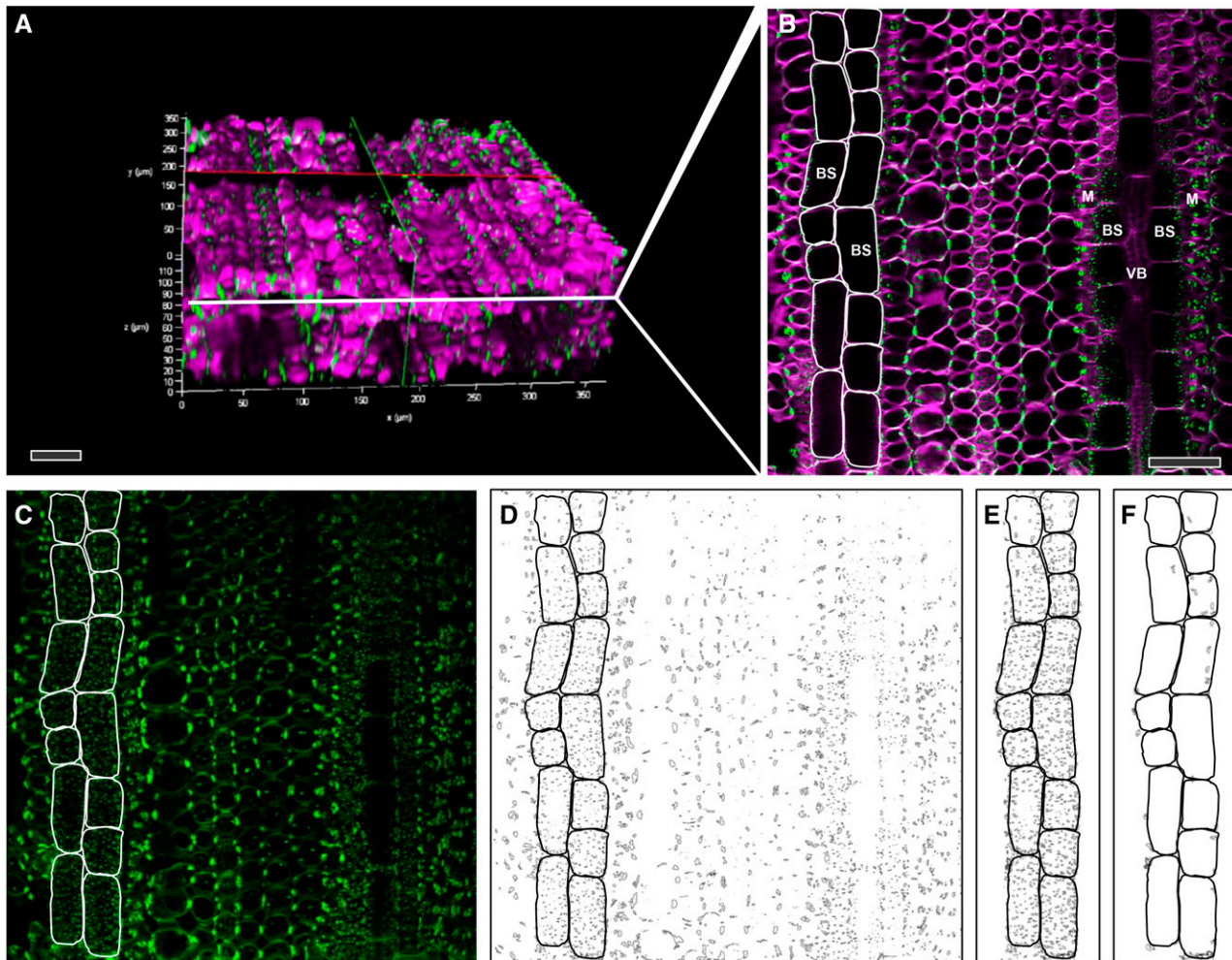
Figure 7. Determination of Total Pitfield Area per M-BS Cell Interface of Maize Leaf Using 3D Immunolocalization Confocal Micrographs.

(A) 3D reconstructed image (from 154 single focal planes) of maize leaf hybridized with primary antibody to β-1,3-glucan and secondary antibody tagged with Alexa Fluor 488 (green) and stained with calcofluor white (magenta) to show cell walls.

(B) A single optical section derived from **(A)** showing pitfields (green) between cells. The BS cells for which pitfields were quantified in this example are outlined in white.

(C) Maximum intensity projection image of 19 consecutive single focal planes (a subset of **[A]**) comprising that region of BS cell surface in contact with the neighboring M cells, outlined in white. Note the pitfield signal size difference between M-BS cell interface, with pitfields parallel to the image plane, and M-M cell interface, with pitfields perpendicular to the image plane.

(D) Corresponding binary image of **(C)** after processing (Supplemental Figure 2).

(E) Selected area of interest from **(D)** used for pitfield quantification.

(F) Area from **(E)** corresponding to M-M cell interface pitfields detected at the edges of certain focal planes. This area is subtracted from the total pitfield area obtained in **(E)** to obtain the final area of M-BS pitfields.

VB, vascular bundle. Bars = 50 μm.

slightly exceed the CO_2 assimilation rate. In C_3 species, the estimates give the fluxes per PD needed if a C_4 photosynthetic pathway were installed without changes in PD frequency (Table 2). The CO_2 assimilation rate per leaf area was found to be lowest in rice (27.1 ± 0.96 μmol CO_2 m^{-2} s^{-1}), but this value is not statistically different from that of *S. viridis* (29.5 ± 1.50 μmol CO_2 m^{-2} s^{-1}). Maize had the highest CO_2 assimilation rate per leaf area at 38.6 ± 1.14 μmol CO_2 m^{-2} s^{-1}, but this is not statistically different from wheat

at 35.0 ± 1.48 μmol CO_2 m^{-2} s^{-1} (Table 2). However, C_4 species were found to have twice as much BS surface area per unit leaf area (S_b) compared with C_3 species (Table 2). Consequently, CO_2 assimilation rate (a surrogate for C_4 and C_3 metabolite flux) per BS surface area was greater in C_3 species (rice, 24.7 ± 0.87 μmol CO_2 m^{-2} s^{-1}; wheat, 29.8 ± 1.26 μmol CO_2 m^{-2} s^{-1}) than in C_4 species (*S. viridis*, 18.1 ± 0.92 μmol CO_2 m^{-2} s^{-1}; maize, 19.5 ± 0.58 μmol CO_2 m^{-2} s^{-1}) (Table 2). If a C_4 photosynthetic pathway were to be installed in a C_3

Mesophyll-bundle sheath cell interface

Mesophyll-mesophyll cell interface
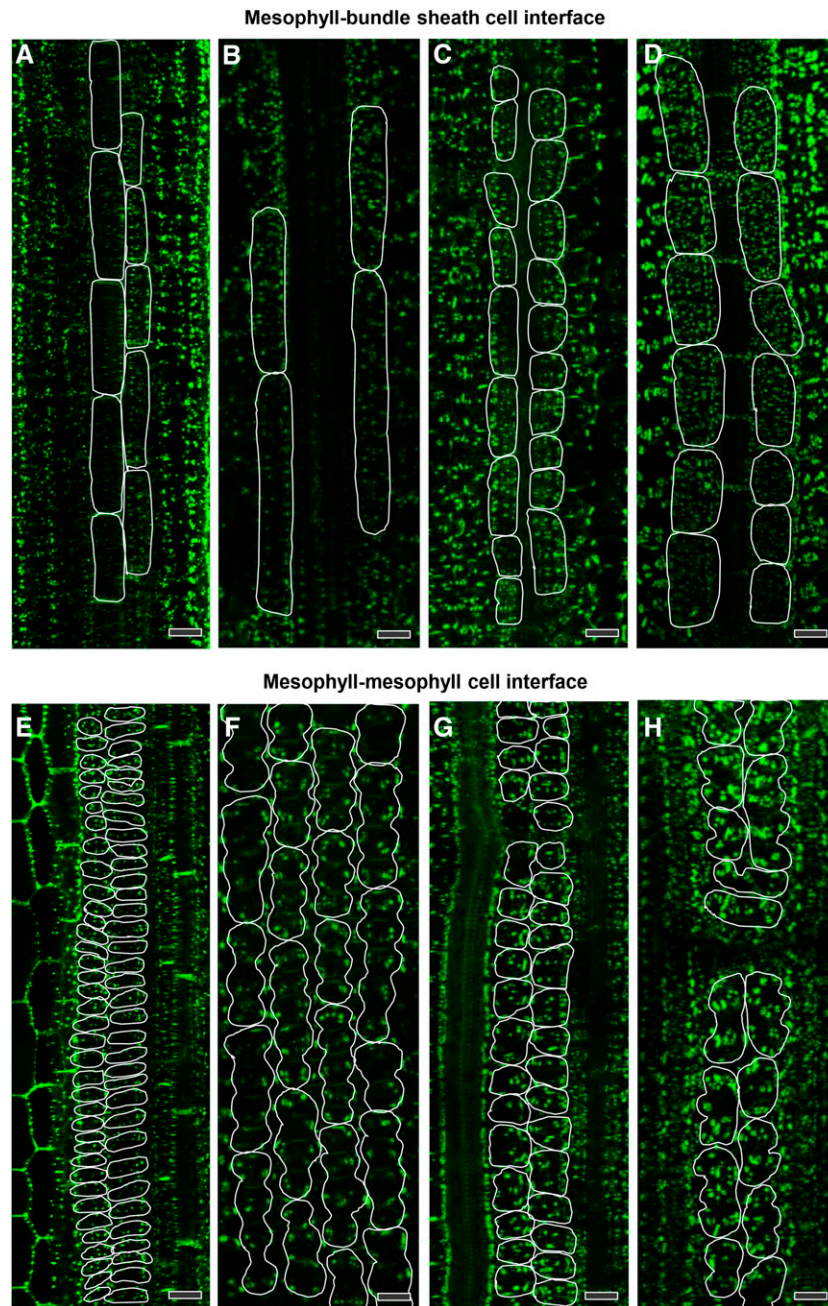
Figure 8. Pitfield Distribution at Cell Interfaces in Leaves of C_3 and C_4 Species after Immunofluorescence Detection of β-1,3-Glucan.

(A) and **(E)** Rice, C_3

(B) and **(F)** Wheat, C_3.

(C) and **(G)** *S. viridis*, C_4.

(D) and **(H)** Maize, C_4.

Pitfields are in green (Alexa Fluor 488 fluorescence). In **(A)** to **(D)**, bundle sheath cell surface areas in direct contact with mesophyll cells are outlined in white. In **(E)** to **(H)**, mesophyll cell surface areas in direct contact with other mesophyll cells are outlined in white. Bars = 20 μm.

species, which has up to 9 times lower PD density (Table 1), based on the CO_2 assimilation rate per PD (expressed as $\times 10^{-18}$ mol CO_2 s^{-1}) in the C_3 species (rice, 24.7 $\pm$ 0.87; wheat, 11.5 $\pm$ 0.49) plasmodesmatal flux per PD would need to be up to 12 times greater than in the C_4 species (*S. viridis*, 1.9 $\pm$ 0.10; maize, 2.6 $\pm$ 0.08). Assuming that sucrose passes from M to BS cells symplastically in C_3 leaves, the sucrose flux across the M-BS interface of the C_3 species per PD would be similar to that calculated for C_4 metabolite flux through PD in the C_4 species (Table 2).

Table 2. Estimates of Plasmodesmal Flux between Mesophyll and Bundle Sheath Cells in Leaves of C_3 and C_4 Species

Species	CO_2 Assimilation Rate per Leaf Area (μmol CO_2 m^{-2} s^{-1})	Mean S_b (m^2 m^{-2})	CO_2 Assimilation Rate per Bundle Sheath Surface Area (μmol CO_2 m^{-2} s^{-1})	CO_2 Assimilation Rate per PD ($\times 10^{-18}$ mol CO_2 s^{-1})	Sucrose Flux per PD ($\times 10^{-18}$ mol Sucrose s^{-1})
Rice, C_3	27.1 ± 0.96[a]	1.1 ± 0.06[a]	24.7 ± 0.87[a]	24.7 ± 0.87[a]	2.1 ± 0.07[a]
Wheat, C_3	35.0 ± 1.48[b]	1.2 ± 0.17[a]	29.8 ± 1.26[b]	11.5 ± 0.49[b]	1.0 ± 0.04[b]
S. viridis, C_4	29.5 ± 1.50[a]	1.6 ± 0.04[b]	18.1 ± 0.92[c]	1.9 ± 0.10[c]	NA
Maize, C_4	38.6 ± 1.14[b]	2.0 ± 0.08[c]	19.5 ± 0.58[c]	2.6 ± 0.08[d]	NA

For the "CO_2 Assimilation Rate per PD" column, assuming that in C_4 species the minimum flux of C_4 acids through the PD needs to be equal to or greater than the CO_2 assimilation rate. For C_3 species, the numbers indicate the fluxes required if a C_4 photosynthetic pathway were installed without anatomical changes. For the "Sucrose Flux per PD" column, assuming sucrose must pass from mesophyll to bundle sheath cells for phloem loading in C_3 monocot leaves at a rate in equilibrium with CO_2 assimilation rates. Statistical differences according to MATLAB two-sample *t* test at P value < 0.05 are indicated by letters. Values indicated by the same letter within a column are not statistically different. NA, not applicable.

DISCUSSION

We developed a new method to quantify the opportunities for cell-to-cell transport of key photosynthates between M and BS in both C_3 and C_4 species. The combination of scanning electron microscopy and 3D immunolocalization confocal microscopy allowed us to quantify both the PD distribution and pitfield distribution on these cell interfaces, and to calculate PD density.

Plasmodesmata Frequency in Pitfields and Pitfield Distribution on Cell Interfaces Both Contribute to Higher Plasmodesmata Density in C_4 Species

Scanning electron microscopy measurements revealed that PD were at higher frequency in pitfields in the C_4 species, *S. viridis* and maize, compared with the C_3 species, rice and wheat (Figure 4). Conversely, the two C_3 species had larger pitfields than C_4 species (Figure 5). Interestingly, this pattern of PD frequency was not specific to the M-BS interface but was also seen in the M-M cell interfaces, suggesting that this may be a more general phenomenon throughout the leaf (Figure 6). This may be of particular significance in regard to the evolution of the C_4 photosynthetic mechanism if the genetic basis of the high symplasmic connectivity of the M-BS is also reflected in other cells in the leaf.

3D immunolocalization provided quantitative information on how the pitfields are distributed on cell interfaces. This method served as the key technique allowing us to quantify PD density over much larger cell surface areas than reported previously (Olesen, 1975). It also provided a new and potentially improved method to measure BS and M cell size, an important consideration in quantifying pitfield distribution on a cell interface area basis and important parameters for modeling C_4 photosynthesis (von Caemmerer, 2000; von Caemmerer and Furbank, 2003; Wang et al., 2014).

Images collected showed an even distribution of pitfields on M-BS cell interfaces, while pitfields found on M-M cell interfaces appeared clustered (Figure 8). BS cells are close to cylindrical in shape and arranged in cell files, enclosing the vascular tissue. This allowed visualization of pitfields on the outer surface of BS cells, parallel to the field of view. By contrast, M cells are irregularly

shaped and in most cases arranged less regularly with air spaces in between. With one M cell having connections with other M cells in different directions, pitfields captured in the images acquired here are usually at a particular angle relative to the field of view, which would also contribute to the clustered appearance.

Measurements using 3D immunolocalization images revealed that not only did C_4 species have higher PD frequency within pitfields but they also had more abundant pitfields on cell interfaces (Figure 8, Table 1). These two factors combined resulted in C_4 species having higher PD density per cell interface area compared with C_3 species, consistent with the findings of Botha (1992). More importantly, the established PD density values for M-BS and M-M cell interfaces are species specific and therefore can be used for transport-related studies as well as in modeling.

Comparison with Traditional Methods for Quantification of Plasmodesmata Frequency

Prior to the development of the method described here, TEM was routinely used to provide semiquantitative data on PD distribution and density. Calculations using the Gunning constant (Gunning, 1978) and the plasmodesmogram method (Botha and Evert, 1988; Botha, 1992; Botha and van Bel, 1992) are common in the literature. However, it appears that this method has limited use in calculations of PD density in vascular plants, given the requirement for a random distribution of PD (Gunning, 1978). In most vascular plants, PD are clustered in pitfields, as found in our study, which makes estimates of PD density at the M-BS interface calculated using this method unreliable (Sowiński et al., 2003, 2007). Plasmodesmograms provide semiquantitative data on symplastic connectivity between cells, based on PD that can be detected using TEM and yield values in relative units (Botha and Evert, 1988; Botha, 1992; Botha and van Bel, 1992). However, these data are difficult to compare with the quantitative data derived here from combined scanning electron microscopy and 3D immunolocalization methods. Our new data will now allow quantitative modeling of metabolite transport in a range of C_3 and C_4 species to improve our understanding of C_4 evolution and efficiencies of the C_4 pathway.

Role of Plasmodesmata in Metabolite Exchange at the Mesophyll-Bundle Sheath Cell Interface

Even in early modeling and analysis of C_4 photosynthesis, it was suggested that rapid transport of C_4 acids between M and BS cells and return of C_3 products of decarboxylation was essential for the evolution of C_4 plants (Osmond, 1971; Hatch and Osmond, 1976). The cell walls of the BS abutting the M are thickened and often heavily suberized, and it has been argued that this barrier serves to minimize CO_2 leakage from the site of decarboxylation (Hatch, 1987; von Caemmerer and Furbank, 2003). This thickening and suberization has long been regarded as an insurmountable obstacle to simple diffusion or apoplastic transport of C_4 acids and the pivotal role of PDs in this pathway was proposed soon after the discovery of the C_4 pathway (Osmond, 1971).

Structures within the PD, where they penetrate the suberin lamella, are also viewed as possible regulators of PD metabolite transport in C_4 species (Robinson-Beers and Evert, 1991a), although evidence is circumstantial. The species examined here, *S. viridis* and maize, belong to the C_4 NADP-malic enzyme subtype. Examining C_4 species belonging to other subtypes, such as NAD-malic enzyme (which do not possess suberized M-BS walls) and phosphoenolpyruvate carboxykinase types, presents an opportunity to determine if suberin lamellae are involved in regulation of metabolite transport via PD in the BS cell wall and have a role in determining C_4 acid flux.

Assuming that BS cell walls are a barrier to metabolite diffusion between M and BS, the calculation of fluxes of C_4 acids and C_3 metabolites across the M-BS interface depends on accurate estimates of the cross sectional area of PD available for diffusion at this interface (Osmond, 1971; Hatch and Osmond, 1976; Stitt and Heldt, 1985; Wang et al., 2014). The absence of reliable estimates of this parameter has substantively hindered modeling studies. In early work, assumptions of the proportion of M-BS interface area populated by PD varied from 1 to 10% (Osmond, 1971); subsequently, these values and those of Hatch and Osmond (1976), based on median literature values for C_3 plant cell PD data, have been routinely used. In recent work using reaction diffusion modeling, Wang et al. (2014) used values between 0.3% and 3% for the percentage of M-BS cell wall interface area occupied by PD. The values obtained here for PD area as a proportion of M-BS cell interface area equate to between 5.4% ± 0.06 and 6.2% ± 0.07% of the cell/cell interface (Table 1) and are at the higher end of values used in models to date.

Increasing Plasmodesmata Density Might Be Necessary for a Functional C_4 Rice

This quantitative comparison of M-BS and M-M cell interface PD density between C_3 and C_4 species is of particular relevance to the creation of functional C_4 rice. In a C_3 system like rice, the M-BS interface is most likely a conduit for delivery of sucrose to the phloem for export from the leaf (Aoki et al., 2012). Fluxes of sucrose (a 12-carbon sugar) will be an order of magnitude less than the rate of photosynthesis if sucrose is continuously exported from the M tissues in the light. In C_4 plants, the CO_2-concentrating mechanism, and consequently the flux of C_4 and C_3 metabolites to and from the BS cells, must equal or exceed the

rate of net photosynthesis. We used measurements of CO_2 assimilation rates to calculate the flux of C_4 and C_3 metabolites across the M-BS interface for C_4 species, the sucrose flux across the M-BS interface in the C_3 species, as well as the hypothetical flux that would need to cross the M-BS interface in C_3 species if a C_4 photosynthetic pathway were installed without anatomical changes (Table 2). The values in Table 2 will actually underestimate the malate/aspartate and pyruvate/alanine fluxes required to support these net rates of photosynthesis by ~20%. This is an average figure for "overcycling" of the C_4 pump predicted to compensate for leakage of CO_2 from the bundle sheath compartment from gas exchange, carbon isotope discrimination, and modeling studies (von Caemmerer and Furbank, 2003). If the properties of PD are similar between C_3 and C_4 plants (physical cross sectional areas of individual C_3 and C_4 PDs measured here were similar; 0.006 to 0.008 μm^2), one would predict that the PD density at this interface would need to increase by up to 12-fold for effective exploitation of a C_4 mechanism in rice. This study revealed that the C_4 species, *S. viridis* and maize, have PD densities per M-BS cell interface area around 9-fold higher than the C_3 species, rice and wheat. The scanning electron microscopy images showed that these C_3 species commonly had regions of M-BS cell interface lacking PD entirely, suggesting that there is sufficient wall contact area available to allow the introduction of additional PD to support C_4 fluxes.

In the context of C_4 evolution and engineering, it is interesting to note that PD density is equally elevated in both M-BS and M-M interfaces of C_4 leaves compared with C_3 leaves. This suggests that in the evolution of C_4 plants, a general increase in foliar symplastic connections may have occurred, not specific to the C_4 mechanism, and a phylogenetic analysis of this hypothesis is currently underway. While the genes determining PD density are not currently known, the method reported here provides a more rapid, quantitative tool to probe the developmental biology of PD formation.

METHODS

Plant Material and Growth Conditions

Rice (*Oryza sativa* cultivar Kitaake), wheat (*Triticum aestivum* cultivar Yecora 70), *Setaria viridis* cultivar A10, and maize (*Zea mays* cultivar B73) were grown in a growth cabinet (High Resolution Plant Phenomics Centre, CSIRO Black Mountain) equipped with white fluorescent tubes (Philips TL5 HO) and maintained at 28°C day/22°C night temperatures, 60% relative humidity, and 16 h light/8 h dark with peak at 1000 μmol quanta $m^{-2} s^{-1}$ light intensity and ambient CO_2 concentration. The youngest fully expanded leaves from seedlings, 9 d after germination, were used.

Light Microscopy and Transmission Electron Microscopy

The middle portion of each leaf was cut into 1-mm^2 strips and fixed in 2.5% glutaraldehyde in 0.1 M sodium phosphate buffer, pH 7.3, overnight at 4°C. The tissue was postfixed with 1% osmium tetroxide for 2 h at room temperature. After dehydration in a graded ethanol series, the tissue was infiltrated with LR White resin and polymerized overnight at 60°C (Gunning et al., 1978). For light microscopy, semithin sections (0.5- to 1.0-μm thick) were cut with glass knives using a Reichert Jung ultramicrotome and stained with hot aqueous 0.05% Toluidine blue, pH 5.0. Imaging was done under 10× and 40× objectives using Nikon Eclipse 50i upright microscope (Nikon Instruments). For TEM, ultrathin sections (70- to 90-nm thick) were

cut with a diamond knife using a Leica EM UC7 Ultramicrotome (Leica Microsystems) and examined using a Hitachi HA7100 transmission electron microscope (Hitachi High Technologies America) at 75 to 100 kV.

Scanning Electron Microscopy

Whole leaves were cut into 10-mm strips and fixed in 4% paraformaldehyde and 0.2% glutaraldehyde in 25 mM sodium phosphate buffer, pH 7.2, overnight at 4°C. The tissue was dehydrated in a graded ethanol series and critical point dried (Balzers CPD 030). Dried tissue was ripped open parallel to the veins using forceps and mounted onto copper holders using nail polish. Scanning electron microscopy preparations were sputter coated with platinum for 4 min using an Emitech EMS550X sputter and examined using a Zeiss Ultra Plus field emission scanning electron microscope at 3 kV.

3D Immunolocalization Confocal Microscopy

The 3D immunolocalization was performed using a modification of the PEA-CLARITY protocol of Palmer et al. (2015). Leaf tissue was cut directly into hydrogel monomer solution (4% acrylamide, 0.05% bis, 0.25% VA-044 initiator, $1\times$ PBS, and 4% paraformaldehyde) and vacuum-infiltrated until the tissue sank. The gel solution was polymerized by incubating in a 37°C water bath overnight. Polymerized tissue was carefully removed from the gel using lint-free paper and transferred to clearing solution (200 mM boric acid and 4% SDS, pH 8.5). Tissue was incubated in the clearing solution with gentle shaking at room temperature for at least 6 to 8 weeks. Cleared tissue was digested in an enzyme cocktail containing 1 μL mL^{-1} β-xylanase M6 (Megazyme), 1 μL mL^{-1} α-L-arabinofuranosidase (Megazyme), 1 μL mL^{-1} pectate lyase (Megazyme), 0.5 μL mL^{-1} of 2 mg mL^{-1} cellulase (Sigma-Aldrich), 1 μL mL^{-1} α-amylase (Sigma-Aldrich), and 1 μL mL^{-1} pullulanase (Sigma-Aldrich) for at least 8 d at 37°C with gentle shaking. For rice leaf, $5\times$ enzyme cocktail was used. Incubation in clearing solution followed by enzyme digestion was repeated three to four times until rice leaf is fully clarified. Tissues were then immunolabeled by incubating the clarified and digested tissue first in 1:500 primary antibody [β(1-3)-glucan antibody (catalog no. 400-2; Biosupplies) in $1\times$ Tris-buffered saline with Tween 20 (TBST)] at 4°C for 5 to 7 days with 3×5 min vacuum infiltration each day, rinsed 5×30 min in $1\times$ TBST, pH 7.4, then incubated in 1:500 secondary antibody (Alexa Fluor 488; catalog no. ab150117, lot no. GR181100-1 [Abcam] in TBST) at 4°C for 5 to 7 d with 3×5 min vacuum infiltration each day. Labeled tissue was poststained with 0.05% aqueous calcofluor white (Sigma-Aldrich) for 30 min at room temperature, washed twice with distilled water, and mounted onto glass slides with 80% glycerol. Tissues were then examined with a Leica SP8 multiphoton confocal microscope (Leica Microsystems) using long-distance dipping lens objectives (HCX APO L U-V-I 40×/0.80 water). Excitation at 488 nm allowed visualization of pitfields (Alexa Fluor 488) with emission at 522 to 550 nm. Simultaneously, fluorescence from calcofluor white-stained cell walls was detected at 434 to 445 nm following excitation at 405 nm. Corresponding background controls were obtained by hybridizing the tissue with 1:500 secondary antibody with and without calcofluor white poststaining (Supplemental Figure 1).

Plasmodesmata Area Measurement

TEM images of transverse sections of at least 40 PD from each type of cell interface were used to quantify the PD area enclosed by the plasma membrane. Measurement was performed with ImageJ software (National Institutes of Health) and a Wacom Cintiq graphics tablet (Wacom Technology).

Plasmodesmata Frequency in Pitfields

PD were counted and pitfield area was measured in scanning electron microscopy images using ImageJ software and a Wacom Cintiq graphics tablet. Data from at least 40 pitfields located either in the M-BS cell interface or M-M cell interface were used to generate regressions of PD numbers versus pitfield area. PD frequency per μm^2 pitfield area was calculated using the linear equation, $y = mx + b$, where m is the slope, b is the intercept, and y is the PD frequency when pitfield area, $x = 1$ μm^2. This frequency value is a reflection of how the PD are distributed within the pitfield. Ultimately, a higher value means that the PD are positioned in close proximity to each other while a lower value means PD are farther apart.

Pitfield Area Quantification on Cell Interfaces

A subset of 10 to 30 consecutive single focal planes was derived from the 3D confocal image z-stack to reveal BS cell surfaces in contact with M cells and M cell surfaces in contact with adjacent M cells (Leica Application Suite X software; Supplemental Figure 2). The maximum intensity projection images generated from the cropped stack were processed in ImageJ software (Supplemental Figure 2). The cell interface area in focus was selected and the total pitfield area (pfa) was quantified. The number of cell interfaces (ci) covered by the focused area were counted and individual cell interface area (cia) was measured. Pitfield area per cell interface area was obtained using this equation: $pfa/(ci \times cia)$. Pitfields parallel to the cell interface were seen as individual pits while pitfields perpendicular to the cell interface were seen as clusters and were therefore larger. In cases where pitfield signals coming from different cell interfaces were captured, size discrimination was applied.

Plasmodesmata Density on Cell Interfaces

The PD density per cell interface area was obtained from the product of PD frequency per μm^2 pitfield area (scanning electron microscopy) and pitfield area per cell interface area (3D immunolocalization). By multiplying this value by the PD area measured using TEM images, the percentage of PD area per cell interface area was calculated.

Gas Exchange Measurement

Gas exchange was measured on the youngest fully expanded leaf of 9 d after germination seedlings using a LI-6400 equipped with a blue-red LED light source (LI-COR). Leaves were initially equilibrated for 30 min in a standard environment of 380 μmol mol^{-1} CO_2, 25°C leaf temperature, flow rate of 500 μmol s^{-1}, and an irradiance of either 1500 (for C_3 species) or 2000 (for C_4 species) μmol quanta m^{-2} s^{-1}. Photosynthetic rates measured under these conditions were used for flux calculations.

CO$_2$ Assimilation Rate and Sucrose Flux Calculations per PD

The BS surface areas per unit leaf area (S_b) for each species were calculated using the equation described by Pengelly et al. (2010). The CO_2 assimilation rate (a surrogate for C_4 acid fluxes) per BS surface area was obtained by dividing the photosynthetic rate derived from gas exchange measurements by S_b. Then, the CO_2 assimilation rate per PD was calculated by dividing CO_2 assimilation per BS surface area by the PD density per M-BS cell interface area. For the C_3 species, rice and wheat, sucrose flux per PD was obtained by dividing CO_2 assimilation rate per PD by 12.

Statistical Analysis

The statistical differences between most quantitative measurements were assessed using a MATLAB two-sample t test (The MathWorks) at 5% significance level (P value < 0.05). Statistical differences at P value < 0.05 between the M-BS cell interface and M-M cell interface regression lines in Figure 6 were evaluated using SPSS Statistics software.

Supplemental Data

Supplemental Figure 1. Confocal Micrograph Background Controls for 3D Immunolocalization.

Supplemental Figure 2. Image Processing Workflow for Pitfield Area Measurement Using 3D Immunolocalization Confocal Micrographs.

AUTHOR CONTRIBUTIONS

S.v.C. and R.T.F. conceived the project. F.R.D. conducted all the experiments, imaging, quantification, and data analysis in consultation with S.v.C., R.T.F., R.G.W, and W.P.Q. All authors contributed to writing the manuscript.

REFERENCES

Aoki, N., Hirose, T., and Furbank, R. (2012). Sucrose transport in higher plants: from source to sink. In Photosynthesis,Vol. 34, J.J. Eaton-Rye, B.C. Tripathy, T.D. Sharkey, eds (Dordrecht, The Netherlands: Springer), pp. 703–729.

Barton, D., and Overall, R. (2015). Imaging plasmodesmata with high-resolution scanning electron microscopy. In Plasmodesmata, Vol. 1217, M. Heinlein, ed (New York: Springer), pp. 55–65.

Botha, C.E.J. (1992). Plasmodesmatal distribution, structure and frequency in relation to assimilation in C_3 and C_4 grasses in southern Africa. Planta **187:** 348–358.

Botha, C.E.J., and Evert, R.F. (1988). Plasmodesmatal distribution and frequency in vascular bundles and contiguous tissues of the leaf of *Themeda triandra*. Planta **173:** 433–441.

Botha, C.E.J., and van Bel, A.J.E. (1992). Quantification of symplastic continuity as visualised by plasmodesmograms: diagnostic value for phloem-loading pathways. Planta **187:** 359–366.

Brecknock, S., Dibbayawan, T.P., Vesk, M., Vesk, P.A., Faulkner, C., Barton, D.A., and Overall, R.L. (2011). High resolution scanning electron microscopy of plasmodesmata. Planta **234:** 749–758.

Carr, D.J. (1976). Plasmodesmata in growth and development. In Intercellular Communication in Plants: Studies on Plasmodesmata, B.E.S. Gunning and A.W. Robards, eds (Berlin, Heidelberg: Springer), pp. 243–289.

Ding, B., Turgeon, R., and Parthasarathy, M.V. (1992). Substructure of freeze-substituted plasmodesmata. Protoplasma **169:** 28–41.

Evert, R.F., Eschrich, W., and Heyser, W. (1977). Distribution and structure of the plasmodesmata in mesophyll and bundle-sheath cells of *Zea mays* L. Planta **136:** 77–89.

Faulkner, C., Akman, O.E., Bell, K., Jeffree, C., and Oparka, K. (2008). Peeking into pit fields: a multiple twinning model of secondary plasmodesmata formation in tobacco. Plant Cell **20:** 1504–1518.

Gunning, B.E.S. (1978). Age-related and origin-related control of the numbers of plasmodesmata in cell walls of developing Azolla roots. Planta **143:** 181–190.

Gunning, B.E.S., Hughes, J.E., and Hardham, A.R. (1978). Formative and proliferative cell divisions, cell differentiation, and developmental changes in the meristem of Azolla roots. Planta **143:** 121–144.

Hatch, M.D. (1987). C_4 photosynthesis: a unique blend of modified biochemistry, anatomy and ultrastructure. Biochim. Biophys. Acta **895:** 81–106.

Hatch, M.D., and Osmond, C.B. (1976). Compartmentation and transport in C4 photosynthesis. In Transport in Plants, Vol. 3, C.R. Stocking and U. Heber, eds (Berlin, Heidelberg: Springer), pp. 144–184.

Olesen, P. (1975). Plasmodesmata between mesophyll and bundle sheath cells in relation to the exchange of C_4-acids. Planta **123:** 199–202.

Osmond, C.B. (1971). Metabolite transport in C_4 photosynthesis. Aust. J. Biol. Sci. **24:** 159–163.

Overall, R.L., and Blackman, L.M. (1996). A model of the macromolecular structure of plasmodesmata. Trends Plant Sci. **1:** 307–311.

Palmer, W.M., Martin, A.P., Flynn, J.R., Reed, S.L., White, R.G., Furbank, R.T., and Grof, C.P.L. (2015). PEA-CLARITY: 3D molecular imaging of whole plant organs. Sci. Rep. **5:** 13492.

Pengelly, J.J.L., Sirault, X.R.R., Tazoe, Y., Evans, J.R., Furbank, R.T., and von Caemmerer, S. (2010). Growth of the C_4 dicot *Flaveria bidentis*: photosynthetic acclimation to low light through shifts in leaf anatomy and biochemistry. J. Exp. Bot. **61:** 4109–4122.

Robards, A.W. (1976). Plasmodesmata in higher plants. In Intercellular Communication in Plants: Studies on Plasmodesmata, B.E.S. Gunning and A.W. Robards, eds (Berlin, Heidelberg: Springer), pp. 15–57.

Robinson-Beers, K., and Evert, R.F. (1991a). Fine structure of plasmodesmata in mature leaves of sugarcane. Planta **184:** 307–318.

Robinson-Beers, K., and Evert, R.F. (1991b). Ultrastructure of and plasmodesmatal frequency in mature leaves of sugarcane. Planta **184:** 291–306.

Sage, T.L., and Sage, R.F. (2009). The functional anatomy of rice leaves: implications for refixation of photorespiratory CO_2 and efforts to engineer C_4 photosynthesis into rice. Plant Cell Physiol. **50:** 756–772.

Sowiński, P., Bilska, A., Barańska, K., Fronk, J., and Kobus, P. (2007). Plasmodesmata density in vascular bundles in leaves of C_4 grasses grown at different light conditions in respect to photosynthesis and photosynthate export efficiency. Environ. Exp. Bot. **61:** 74–84.

Sowiński, P., Rudzińska-Langwald, A., and Kobus, P. (2003). Changes in plasmodesmata frequency in vascular bundles of maize seedling leaf induced by growth at sub-optimal temperatures in relation to photosynthesis and assimilate export. Environ. Exp. Bot. **50:** 183–196.

Stitt, M., and Heldt, H.W. (1985). Generation and maintenance of concentration gradients between the mesophyll and bundle sheath in maize leaves. Biochim. Biophys. Acta **808:** 400–414.

Turner, A., Wells, B., and Roberts, K. (1994). Plasmodesmata of maize root tips: structure and composition. J. Cell Sci. **107:** 3351–3361.

von Caemmerer, S. (2000). Biochemical Models of Leaf Photosynthesis. (Collingwood, Australia: CSIRO Publishing).

von Caemmerer, S., and Furbank, R.T. (2003). The C_4 pathway: an efficient CO_2 pump. Photosynth. Res. **77:** 191–207.

Wang, Y., Long, S.P., and Zhu, X.-G. (2014). Elements required for an efficient NADP-malic enzyme type C_4 photosynthesis. Plant Physiol. **164:** 2231–2246.

Check for updates

CORRECTION[OPEN]

Danila, F.R., Quick, W.P., White, R.G., Furbank, R.T., and von Caemmerer, S. (2016). The metabolite pathway between bundle sheath and mesophyll: quantification of plasmodesmata in leaves of C3 and C4 monocots. Plant Cell **28:** 1461–1471.

The original publication included three typographical errors in Table 1. Incorrect values for the "Mean Pitfield Area per Cell Interface Area (%)" were given for *Setaria viridis*, maize, and rice. The table was replaced in the pdf and xml versions of the manuscript with the correct values on February 6, 2018. The original incorrect and corrected values are shown below. The legend and all other values are unaltered. Please see the manuscript for the complete table and associated legend.

All authors are in agreement with this correction.

	Mean Pitfield Area per Cell Interface Area (%)	
	Original Published Values	Corrected Values
S. viridis, C_4	2.7 ± 0.3	12.7 ± 0.3
Maize, C_4	1.4 ± 0.3	11.4 ± 0.3
Rice, C_3	4.8 ± 0.1	4.1 ± 0.1

Editor's note: The corrected figures and accompanying text were reviewed by members of *The Plant Cell* editorial board based on the information provided by the authors. The authors are responsible for providing a complete listing and accurate explanations for all known errors associated with the original publication.

The Metabolite Pathway between Bundle Sheath and Mesophyll: Quantification of Plasmodesmata in Leaves of C$_3$ and C$_4$ Monocots

Florence R. Danila, William Paul Quick, Rosemary G. White, Robert T. Furbank and Susanne von Caemmerer

This information is current as of March 21, 2018

Supplemental Data	/content/suppl/2016/06/10/tpc.16.00155.DC1.html
References	This article cites 22 articles, 3 of which can be accessed free at: /content/28/6/1461.full.html#ref-list-1
Permissions	https://www.copyright.com/ccc/openurl.do?sid=pd_hw1532298X&issn=1532298X&WT.mc_id=pd_hw1532298X
eTOCs	Sign up for eTOCs at: http://www.plantcell.org/cgi/alerts/ctmain
CiteTrack Alerts	Sign up for CiteTrack Alerts at: http://www.plantcell.org/cgi/alerts/ctmain
Subscription Information	Subscription Information for *The Plant Cell* and *Plant Physiology* is available at: http://www.aspb.org/publications/subscriptions.cfm
Errata	An erratum has been published regarding this article. It is appended to this PDF and can also be accessed at: /content/30/2/513.full.pdf
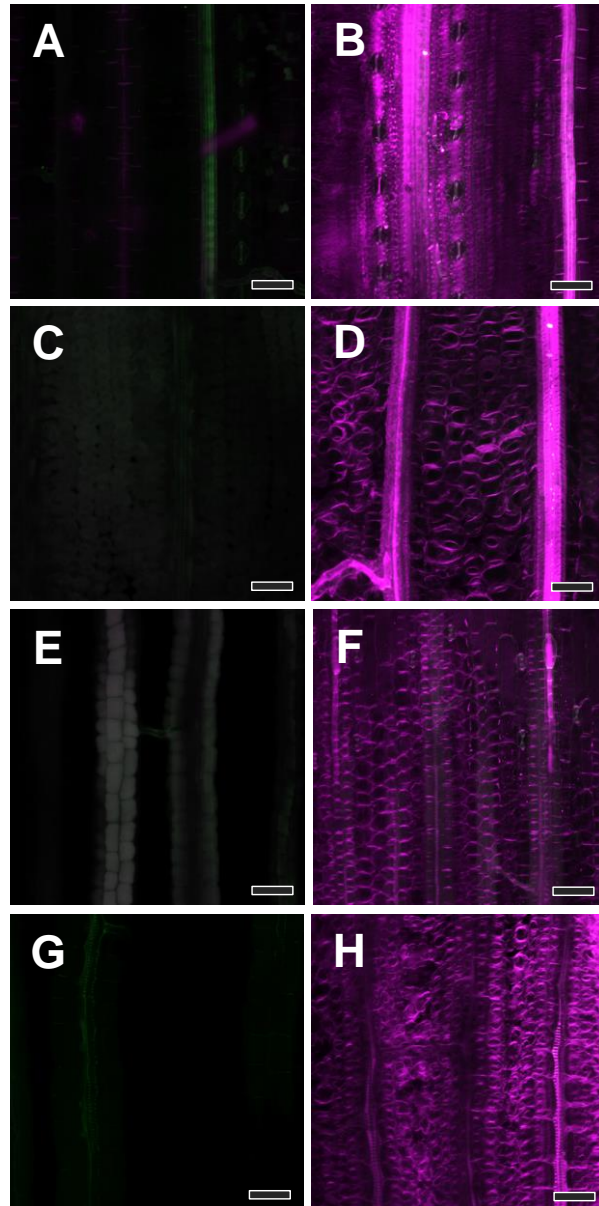
Supplemental Figure 1. Confocal Micrograph Background Controls for 3D Immunolocalisation.

(A) and (B) *O. sativa*, C_3
(C) and (D) *T. aestivum*, C_3
(E) and (F) *S. viridis*, C_4
(G) and (H) *Z. mays,* C_4
(A, C, E, G) Leaves hybridised with secondary antibody tagged with Alexa Fluor® 488.
(B, D, F, H) Leaves hybridised with secondary antibody tagged with Alexa Fluor® 488 and stained with calcofluor white. All are maximum intensity projection images obtained by combining 10-30 consecutive single focal planes simultaneously imaged with Alexa Fluor® 488 and calcofluor white channels. Bars = 50 µm.

Supplemental Figure 2. Image Processing Workflow for Pitfield Area Measurement Using 3D Immunolocalisation Confocal Micrographs.
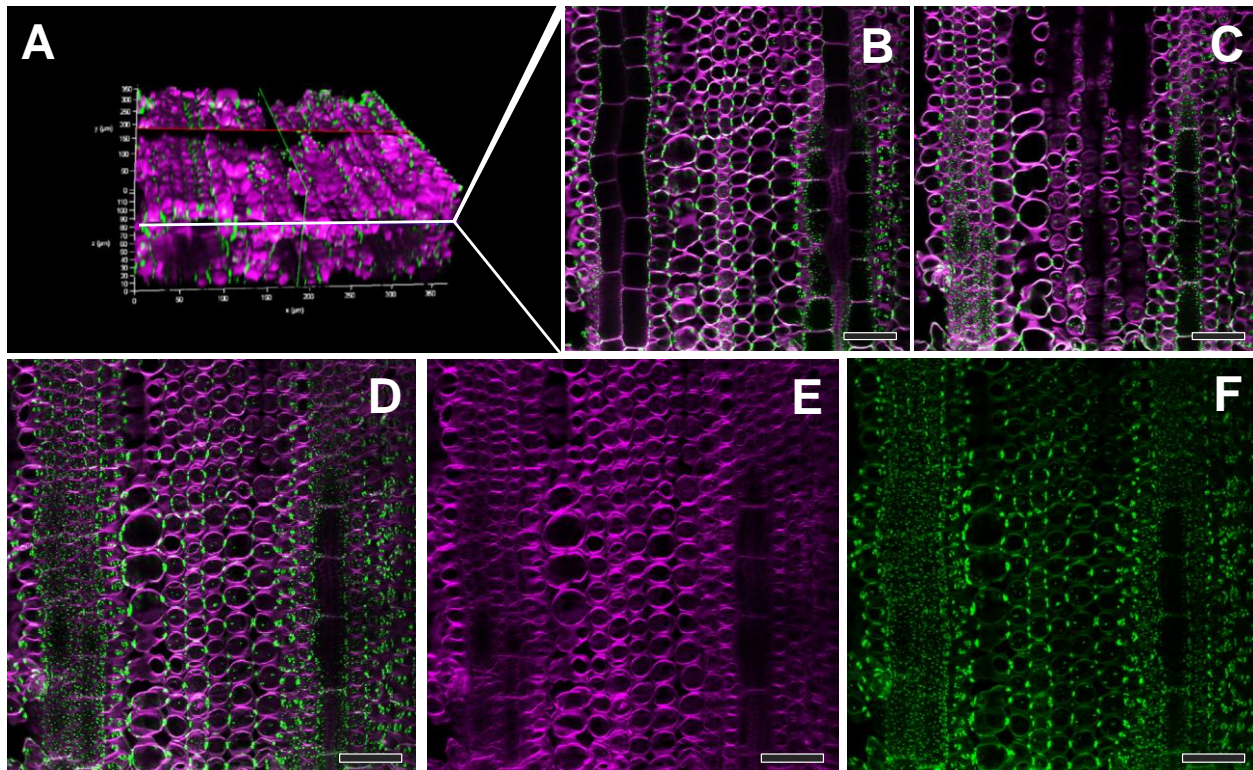
Determination of Total Pitfield Area per Mesophyll-Bundle Sheath Cell Interface of *Z. mays* Leaf Using 3D Immunolocalisation Confocal Micrographs – Workflow for Fig. 7.

(A) 3D reconstructed image (from 154 single focal planes) of *Z. mays* leaf hybridised with primary antibody to β-1,3-glucan and secondary antibody tagged with Alexa Fluor® 488 (green) and stained with calcofluor white (magenta) to show cell walls
(B) A single optical section derived from (A) showing pitfields (green) between cells. This section is focused at the plane below which no further M-BS pitfields are detected, and marks the start of the z-stack to be extracted
(C) A single optical section derived from (A), focused at the top surface of the two files of BS cells highlighted in (B), above which M-BS no additional pitfields are detected, and marks the end of the z-stack to be extracted
(D) Maximum intensity projection image of the 19 consecutive single focal planes from (B) to (C) comprising that region of BS cell surface in contact with the neighbouring M cells
(E) Calcofluor white channel from (D)
(F) Alexa Fluor® 488 channel from (D)
Bars = 50 μm.

One 3D stack (A) can contain between 150 and 300 single focal planes depending on the sample leaf thickness. Since the interfaces between cell files are not flat, extracting

several focal planes is necessary to obtain in focus images that cover the entire M-BS or M-M interface to be analysed. This workflow shows how all the pitfields contained in the M-BS cell interface of the leftmost vein were captured in a single image for subsequent analysis and quantification.

Section 1. Image processing using Leica Application Suite X Software

While this section is specific for the Leica SP8 confocal microscope software we used, similar processing software is available with most major brands of confocal microscopes.

Step 1: Projects > Open > Select file

Step 2: Process > Process Tools > Edit > Crop

> Z Stack Selection: Indicate the start (B) and end (C) position of the focal planes to be cropped and click Apply. This step will automatically create a new Crop file.

Step 3: Select Crop file > Click Max icon (located at the top right side) > Click Ch1 or Ch2 icon to turn on and off channels

The maximum intensity projection image (D) was obtained by combining 19 consecutive single focal planes derived as a subset from the whole 3D stack in (A). (E) Maximum intensity projection image showing the calcofluor white channel (cell wall). (F) Maximum intensity projection image showing the Alexa Fluor® 488 channel (pitfields).

Section 2. Image processing and pitfield area measurement using ImageJ Software.
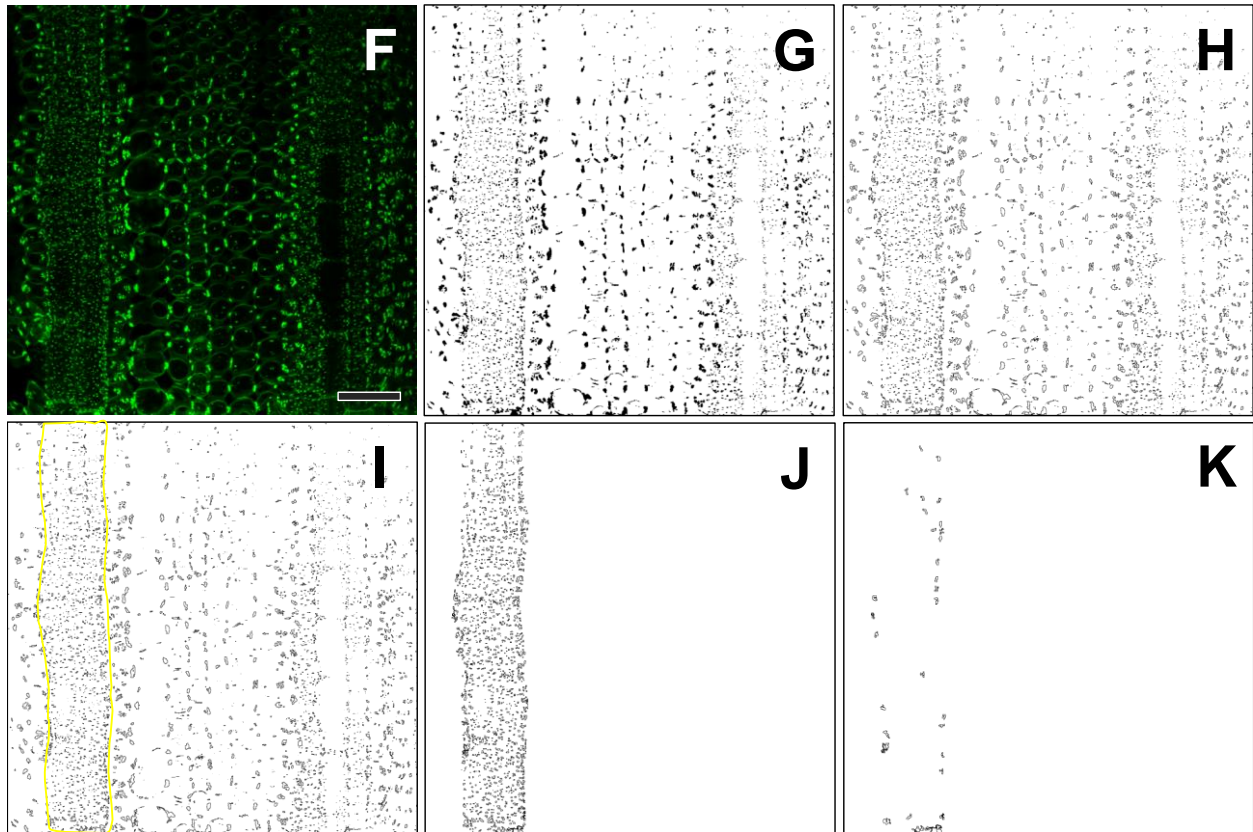
For pitfield area measurement, the maximum intensity projection image showing the AlexaFluor®488 channel (F) was used.

Step 1: File > Open… > Select image file

Step 2: Image > Adjust > Color Threshold

>   Hue: Default
>   Saturation: Default
>   Brightness: 26 (Value depends on intensity of pitfield signal)
>   Thresholding method: Triangle
>   Threshold color: B&W
>   Color space: HSB
>   Dark background ticked
>
>   This step will convert image (F) to (G).

Step 3: Image > Type > 8-bit

>   This step is necessary to allow further processing of the image.

Step 4: Process > Binary > Outline

   This step will convert image (G) to (H). Image (H) can now be used for analysis.

Step 5: Select the area of interest using Freehand selections

   The selected area (yellow outline) in (I) is derived from the BS cell outlines
   detected in (B), leftmost vein, representing the subset of BS cells in direct contact
   with the overlying M cells seen in (C).

Step 6: Analyze > Analyze Particles…

   For total pitfield area quantification (J):

         Size (inch^2): 0-Infinity
         Circularity: 0.00-1.00
         Show: Bare Outlines
         Summarize ticked

   For outlier pitfield area quantification (pitfields that are larger than the maximum
   area for this M-BS interface, as seen in FESEM images) (K):

         Size (inch^2): 0.004-Infinity (Value depends on the maximum size pitfields
         at the specific interface to be analysed)
         Circularity: 0.00-1.00
         Show: Bare Outlines
         Summarize ticked

Step 6: Subtract the outlier pitfield area value from the total pitfield area value to get the
pitfield area value reflecting only the area of interest.

4

PUBLICATION 3

Multiple mechanisms for enhanced plasmodesmata density in disparate subtypes of C$_4$ grasses

Statement of Contribution

This thesis is submitted as a Thesis by Compilation in accordance with https://policies.anu.edu.au/ppl/document/ANUP_003405

I declare that the research presented in this Thesis represents original work that I carried out during my candidature at the Australian National University, except for contributions to multi-author papers incorporated in the Thesis where my contributions are specified in this Statement of Contribution.

Title and authors: **Multiple mechanisms for enhanced plasmodesmata density in disparate subtypes of C₄ grasses. Florence R. Danila, William Paul Quick, Rosemary G. White, Steven Kelly, Susanne von Caemmerer, and Robert T. Furbank.**
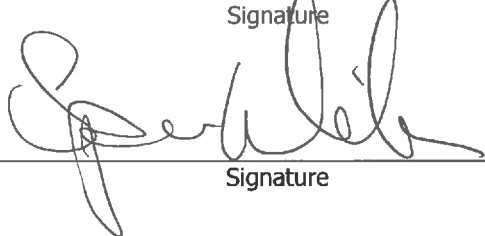
Current status of paper: **Published** (Journal of Experimental Botany, Volume 69, Issue 5, 23 February 2018, Pages 1135-1145. https://doi.org/10.1093/jxb/erx456)

Contribution to paper: **F.R.D. conducted all the experiments, imaging, quantification, data analysis, and statistics in consultation with S.v.C., R.T.F, R.G.W., S.K., and W.P.Q. S.K. constructed the phylogenetic tree. F.R.D. also prepared the first draft of the manuscript, handled all corrections based on co-authors comments and suggestions, and did all the formatting for journal submission.**

Senior author or collaborating author's endorsement:

Rosemary G. White		3. 8. 18
Senior author – Print Name	Signature	Date
Susanne von Caemmerer		1/8/18
Senior author – Print Name	Signature	Date
Robert T. Furbank		1/8/18
Senior author – Print Name	Signature	Date
Florence R. Danila		1/8/18
Candidate – Print Name	Signature	Date

Endorsed

Susanne von Caemmerer		1/8/18
Chair of Supervisory Panel – Print Name	Signature	Date
Spencer Whitney		2/8/18
Delegated Authority – Print Name	Signature	Date

RESEARCH PAPER

Multiple mechanisms for enhanced plasmodesmata density in disparate subtypes of C$_4$ grasses

Florence R. Danila[1,2,*], William Paul Quick[2,3,5], Rosemary G. White[4], Steven Kelly[6],
Susanne von Caemmerer[1,2] and Robert T. Furbank[1,2,4]

[1] Research School of Biology, Australian National University, Canberra Australian Capital Territory 2601, Australia
[2] ARC Centre of Excellence for Translational Photosynthesis, Australian National University, Canberra Australian Capital Territory 2601, Australia
[3] International Rice Research Institute, Los Baños, Laguna 4030, Philippines
[4] CSIRO Agriculture, Canberra Australian Capital Territory 2601, Australia
[5] Department of Animal and Plant Sciences, University of Sheffield, Sheffield, UK
[6] Department of Plant Sciences, University of Oxford, Oxford, OX1 3RB, UK

* Correspondence: florence.danila@anu.edu.au

Abstract

Proliferation of plasmodesmata (PD) connections between bundle sheath (BS) and mesophyll (M) cells has been proposed as a key step in the evolution of two-cell C$_4$ photosynthesis; However, a lack of quantitative data has hampered further exploration and validation of this hypothesis. In this study, we quantified leaf anatomical traits associated with metabolite transport in 18 species of BEP and PACMAD grasses encompassing four origins of C$_4$ photosynthesis and all three C$_4$ subtypes (NADP-ME, NAD-ME, and PCK). We demonstrate that C$_4$ leaves have greater PD density between M and BS cells than C$_3$ leaves. We show that this greater PD density is achieved by increasing either the pit field (cluster of PD) area or the number of PD per pit field area. NAD-ME species had greater pit field area per M–BS interface than NADP-ME or PCK species. In contrast, NADP-ME and PCK species had lower pit field area with increased number of PD per pit field area than NAD-ME species. Overall, PD density per M–BS cell interface was greatest in NAD-ME species while PD density in PCK species exhibited the largest variability. Finally, the only other anatomical characteristic that clearly distinguished C$_4$ from C$_3$ species was their greater S_b value, the BS surface area to subtending leaf area ratio. In contrast, BS cell volume was comparable between the C$_3$ and C$_4$ grass species examined.

Keywords: Bundle sheath, C$_4$ decarboxylation types, C$_4$ photosynthesis, grasses, mesophyll, pit field, plasmodesmata, symplastic transport.

Introduction

Most plants obtain sugars by fixing atmospheric CO$_2$ using the enzyme Rubisco (ribulose bis-phosphate carboxylase oxygenase). This process is inherently inefficient as O$_2$ competes with CO$_2$ at the enzyme's active site, resulting in formation of compounds that cost energy to recycle in a process known as photorespiration. The first product of photosynthetic CO$_2$ fixation by Rubisco is a three-carbon sugar, hence this process is known as C$_3$ photosynthesis. Many tropical and sub-tropical plant lineages have independently evolved a more efficient photosynthetic biochemistry, termed C$_4$ photosynthesis

(Hatch, 1987; Sage *et al.*, 2011). Here, CO_2 is first captured in mesophyll (M) cells as C_4 acids, which then diffuse into bundle sheath (BS) cells, where Rubisco is located, and decarboxylated, resulting in greatly elevated local CO_2 concentrations (Furbank and Hatch, 1987). This CO_2-concentrating mechanism reduces photorespiration and enables Rubisco to operate close to its catalytic maximum (von Caemmerer and Furbank, 2003; Sage *et al.*, 2012). It is thought that a reduction in atmospheric CO_2 concentration ~35 million years ago may have driven the evolution of this CO_2-concentrating mechanism (Sage, 2004).

Although many plants conduct C_4 photosynthesis, a range of anatomical and biochemical specialisations distinguish different C_4 lineages. For example, subcategories of C_4 plants are defined by the enzymes that catalyse the decarboxylation of the C_4 acid: NADP malic enzyme (NADP-ME) type, NAD malic enzyme (NAD-ME) type, and phosphoenolpyruvate carboxykinase (PCK) type (Hatch, 1987; Furbank, 2011). Particularly in grasses, these biochemical differences are further elaborated by anatomical specialisations that include the presence of the mestome sheath between the BS and the vasculature in NAD-ME and PCK types but not in the NADP-ME type (Hattersley and Watson, 1976); suberisation of the BS cells in NADP-ME and PCK types but not in the NAD-ME type (Hattersley and Browning, 1981); and oval chloroplasts positioned centrifugally with mitochondria in BS cells of NADP-ME and most PCK types but elongated chloroplasts positioned centripetally with mitochondria in BS cells of the NAD-ME type (Hattersley and Watson, 1976; Hattersley and Browning, 1981; Dengler *et al.*, 1994; McKown and Dengler, 2007).

Over the last 35 million years, these evolutionary changes in anatomy and biochemistry arose independently at least 66 times (Sage *et al.*, 2012). In grasses, 22–24 distinct C_4 lineages are found within the PACMAD (Panicoideae, Aristidoideae, Chloridoideae, Micrairoideae, Arundinoideae, and Danthonioideae) clade, specifically in the subfamilies Panicoideae, Aristidoideae, Chloridoideae, and Micrairoideae (GPWGII, 2012). These subfamilies comprise many highly productive crop species such as sugar cane, millets, and maize. On the other hand, the subfamilies Bambusoideae, Ehrhartoideae, and Pooideae, known as the BEP clade (GPWGII, 2012), contain no C_4 species. These subfamilies include staple food grains such as rice, wheat, and barley. Demand for food crops is predicted to increase by at least 50% in the next 35 years (Hibberd *et al.*, 2008), and yield increases through traditional breeding of these C_3 species will not meet this requirement. Recent breakthroughs in biotechnology may provide the opportunity to engineer the C_4 photosynthetic pathway into C_3 crops, which could potentially meet required improvements to feed the growing human population (Hibberd *et al.*, 2008).

The biochemistry of C_3 and C_4 photosynthesis has been well studied, with a strong focus on either down-regulation/knockout (von Caemmerer and Furbank, 2016) or overexpression (Kajala *et al.*, 2011) of one or more of the known key C_4 photosynthetic enzymes in various plant systems to understand their function. Previous work has shown how leaf anatomical traits can be used to gain insight into C_4 evolution (Hattersley and Watson, 1976; Dengler *et al.*, 1994; McKown and Dengler, 2007). These studies mainly investigated traits related to the specialised vascular anatomy of C_4 plants known as Kranz anatomy: a wreath-like arrangement of BS and M cell layers enclosing the vascular bundles. This anatomical arrangement separates the biochemical CO_2 'pump' in the M from Rubisco in the BS, and provides a barrier to CO_2 diffusion out of the BS compartment (von Caemmerer and Furbank, 2003; Sage *et al.*, 2012).

The requirement for metabolites to move at high rates between specialised C_4 cell types has long been recognised to be important for C_4 photosynthetic function (Osmond, 1971; Hatch and Osmond, 1976). Estimates of flux of photosynthetic metabolites between cell types in C_4 leaves assume that the M–BS cell wall is impermeable due to the secondary thickening of cell walls between these cells (Danila *et al.*, 2016). Hence, these metabolites must move between cell types via plasmodesmata (PD), the symplastic nanochannels that span cell walls and provide both a cytoplasmic and an endoplasmic continuum for metabolite transport (Osmond and Smith, 1976; Robards, 1976; Overall and Blackman, 1996). In leaves, PD are distributed in groups called pit fields. The available data on PD distribution between leaf cells in C_3 and C_4 species show that C_4 plants have a greater density of PD than C_3 plants (Botha, 1992; Danila *et al.*, 2016). A major barrier to quantitatively examining these symplastic connections across diverse species has been the difficulty of the microscopy required to acquire statistically robust data (e.g. Botha, 1992). Recently, a high-throughput technique has been developed to assess PD density (Danila *et al.*, 2016). This technique combines high-resolution scanning electron microscopy (SEM), which allows analysis of individual PD within pit fields, and three-dimensional (3-D) immunolocalisation confocal microscopy for relatively rapid quantification of pit field distribution in a larger surface area across many cells within a leaf. Thus, it is now possible to quantify the PD connecting leaf cells of different C_4 species and determine whether increased PD density at the M–BS interface is a conserved trait of C_4 species and whether this density varies between different C_4 subtypes. In this study, we quantify PD density between leaf cells in a selection of C_3 and C_4 grass species. These species encompass both BEP and PACMAD clades and include four origins of C_4 photosynthesis comprising all C_4 subtypes.

Materials and methods

Plant seeds and growth conditions

Seeds for *Astrebla lappacea*, *Leptochloa fusca*, *Panicum miliaceum*, *P. antidotale*, and *Urochloa panicoides* were gifted by Oula Ghannoum (Western Sydney University), *Brachypodium distachyon* seeds were obtained from CSIRO Black Mountain, and seeds from *Oryza sativa* cultivar Kitaake, *Hordeum vulgare* cultivar Yagan, *Triticum aestivum* cultivar Yecora 70, *P. bisulcatum*, *P. coloratum*, *Sorghum bicolor* cultivar Rooney, *Zea mays* cultivar B73, *Cenchrus ciliaris*, *Setaria viridis* cultivar A10, *Paspalum dilatatum*, *Chloris gayana*, and *P. maximum* (also known as *Megathyrsus maximus*) were obtained from the Research School of Biology (Australian National

University). All seeds were germinated according to Danila *et al.* (2016). Growth conditions were maintained at 28 °C day/22 °C night temperatures, 60% relative humidity, 16 h light/8 h dark with peak at 1000 mmol quanta m^{-2} s^{-1} light intensity, and ambient CO$_2$ concentration.

Phylogenetic tree construction

To construct a phylogenetic tree for this analysis the predicted protein sequences for each of the 18 species were subject to orthogroup inference using OrthoFinder (Emms and Kelly, 2015) and a set of 60 single-copy orthogroups containing sequences from at least 16 of the 18 grass species were identified (Supplementary Dataset S1 at *JXB* online). These protein sequences were aligned using MergeAlign (Collingridge and Kelly, 2012), edited to remove all gap-containing columns, concatenated, and subjected to 1000 replicates of a non-parametric bootstrapped maximum-likelihood phylogenetic inference using FastTree (Price *et al.*, 2010). The full-length concatenated alignment was also used for Bayesian phylogenetic tree inference using mrBayes v 3.2.6 (Huelsenbeck and Ronquist, 2001). The amino acid model was set to JTT and the covarion was turned on. Two runs, each of four chains, were initiated and allowed to run for 100 000 generations sampling every 100 generations. Convergence was assessed through visual inspection of log-likelihood traces and through analysis of the standard deviation of split frequencies ($\sigma^2 < 0.00001$).

Leaf anatomical sample preparation

All leaf tissue preparations for light microscopy, SEM, and 3-D immunolocalisation confocal microscopy were as described by Danila *et al.* (2016). The middle portion of the youngest fully expanded leaf from three individual 9-d-old seedlings per species were collected and pooled. From this sample pool, leaf tissues were fixed and processed accordingly. For 3-D immunolocalisation confocal microscopy, leaf tissue was cleared using PEA-CLARITY (Palmer *et al.*, 2015), hybridised with β-1,3-glucan (callose) antibody, followed by Alexa488-tagged secondary antibody, and poststained with calcofluor white to visualise cell walls (Danila *et al.*, 2016).

Microscopy

Transverse sections of all grass leaves were imaged for light microscopy under 10× and 40× objectives using a Nikon Eclipse 50i upright microscope (Nikon Instruments). SEM was performed using a Zeiss Ultra Plus field emission scanning electron microscope at 3 kV. To quantify pit field distribution, two *z*-stacks from two leaf tissues per species were obtained using a Leica SP8 multiphoton confocal microscope (Leica Microsystems). Details can be found in Danila *et al.* (2016).

Quantitative leaf anatomical measurement

Different from the conventional use of resin-embedded leaf tissue, BS cell area was measured from 25 to 50 individual cells of minor veins using virtual *z*-sections through entire confocal *z*-stacks for each species. BS cell volume was calculated by multiplying the BS cell area by BS cell length, which was measured using cell images ($n=30$ to 160) obtained from the paradermally orientated confocal micrographs of the same leaf *z*-stacks (Turrell, 1936). Vein diameter and interveinal distance (IVD) were measured using 10 to 25 individual minor veins from light micrographs of transverse leaf sections (see Supplementary Fig. S1). The bundle sheath surface area per unit leaf area, S_b, was calculated using the equation described in Pengelly *et al.* (2010). To determine cell-to-cell PD connectivity among different subtypes of C$_4$ photosynthesis, the frequency of PD within pit fields and density of pit fields per cell interface were analysed using SEM and confocal microscopy, respectively, in PCK ($n=3$ species),

NAD-ME ($n=4$), and NADP-ME ($n=6$) grasses. For reference, representative grasses from C$_3$ BEP ($n=4$) and C$_3$ PACMAD ($n=1$) were also measured. Quantitation of PD per µm^2 pit field ($n=18$ or more whole pit fields obtained from SEM), percent pit field per cell interface area ($n=5$ or more maximum intensity projection images generated from two confocal *z*-stacks), and PD per µm^2 cell interface were carried out as described in Danila *et al.* (2016). PD quantification values used for *O. sativa*, *T. aestivum*, *Z. mays*, and *S. viridis* were as reported in Danila *et al.* (2016) (see Supplementary Table S1 for specific details). The cross-sectional area of at least 40 individual PD enclosed by the wall collar (Faulkner *et al.*, 2008) (termed as PD area here) located in the M–BS cell interface was measured from SEM images. PD area per M–BS interface area and PD area per unit leaf area were calculated as follows:

$$PD \text{ area per M} - BS \text{ interface area} = \frac{PD \text{ area} \times PD \text{ per µm}^2}{M - BS \text{ cell interface}}$$

$$PD \text{ area per unit leaf area} = PD \text{ area per M} - BS \text{ interface area} \times S_b$$

All anatomical measurements were performed using ImageJ software (https://imagej.nih.gov/ij/).

Statistical analysis

Statistical analyses were carried out using one-way (photosynthetic type and species) ANOVA (OriginPro 9.1, OriginLab Corporation). Means were grouped using a *post hoc* Tukey test.

Results

C$_4$ origin and lineage representation

A phylogenetic tree of the 18 species was adapted from GPWGII (2012). It is currently thought that this set of species encompass four independent origins of C$_4$ photosynthesis (GPWGII, 2012). The independent evolutionary origins of C$_4$ are indicated in Fig. 1 where species are colour-coded according to their photosynthetic type (Table 1); this coding and species order are retained throughout the paper.

Plasmodesmata in C$_4$ grasses

Analysis of pit field size (Fig. 2, Supplementary Table S1) and patterns of pit field distribution (Fig. 3) revealed that NAD-ME species had the largest and most abundant pit fields (in terms of area coverage) on the M–BS cell interface. Both NADP-ME and PCK species had smaller and less abundant pit fields. C$_3$ species, from both the BEP (Figs 2A–D, 3A–D) and PACMAD (Figs 2K, 3K) clades, had considerably less abundant, smaller pit fields. The large pit fields in NAD-ME species had more widely spaced PD (Fig. 2, Supplementary Table S1). Indeed, NAD-ME species had fewer PD per pit field area on the M–BS cell interface compared to NADP-ME and most PCK species (Fig. 4A, Supplementary Table S1). This was offset by the greater percent pit field area per M–BS cell interface area in NAD-ME species compared to NADP-ME and PCK species (Fig. 4B, Supplementary Table S1). The resulting PD density per M–BS cell interface was greater in NAD-ME compared to NADP-ME species, with large variation observed amongst the PCK species (Fig. 4C, Supplementary Table S1). C$_4$ species also
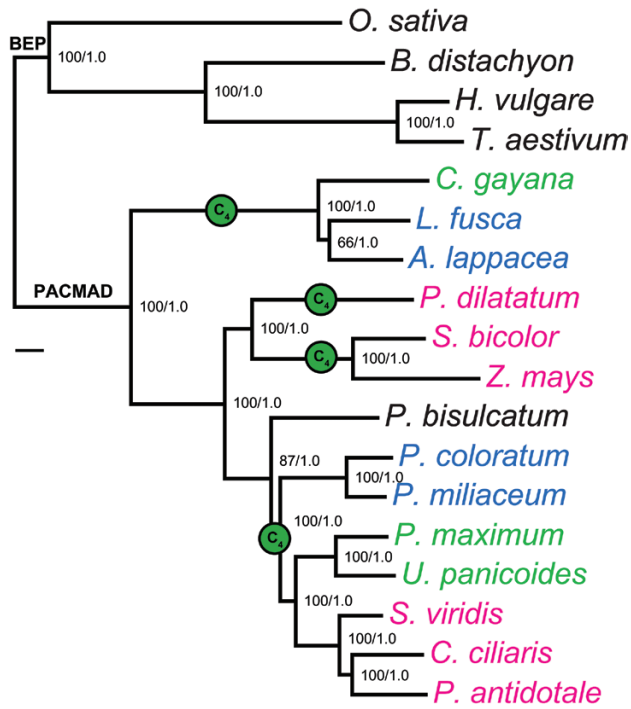
Fig. 1. Phylogenetic tree of the C_3 and C_4 grass species examined in this study, which is identical to the expected topology from GPWGII (2012). Species names are colour-coded according to photosynthetic types: black, C_3; green, C_4 PCK; blue, C_4 NAD-ME; magenta, C_4 NADP-ME. The four independent evolutionary origins of C_4 photosynthesis are indicated with green circles at the midpoint of the branches. Support values at internal nodes are ML/B, where ML is the percentage of non-parametric bootstrap replicates that support the bipartition, and B is the Bayesian posterior probability for the bipartition. The scale bar indicates 0.1 substitutions per site.

had greater PD density on the M–M cell interface relative to the C_3 species but there was no substantial variation among the C_4 subtypes (Figs. 4D–F, Supplementary Table S1). Estimates of the cross-sectional area of individual PD revealed no significant differences between the two photosynthetic pathways and among decarboxylation types (Fig. 4G, Supplementary Table S1). The proportion of the M–BS cell interface populated by PD (Fig. 4H, Supplementary Table S1) and the M–BS PD area per unit leaf area (Fig. 4I, Supplementary Table S1) were greater in C_4 species than C_3 species, and followed the pattern of PD density for the C_4 decarboxylation types.

Bundle sheath of C_4 grasses

Our 3-D approach to measure BS cell cross-sectional areas and volumes used confocal micrographs derived from *z*-stacks of the leaf (Fig. 5). Measurement of the BS cell cross-sectional areas revealed no significant difference between the C_3 and C_4 species examined (Fig. 6A, Supplementary Table S2). Although shorter BS cell length in C_4 species compared to C_3 species was observed (Fig. 6B, Supplementary Table S2), the calculated BS cell volumes were similar for the C_3 and C_4 species examined (Fig. 6C, Supplementary Table S2). Measurements from light micrographs of transverse leaf sections showed NAD-ME and NADP-ME species had the largest and smallest vein diameter, respectively, with C_3 and PCK species being intermediate (Fig. 6D, Supplementary Table S2). As expected, leaf interveinal distance (IVD) was larger in C_3 species than in C_4 species (Fig. 6E, Supplementary Table S2), but among the C_4 species the IVDs were not significantly different (Fig. 6E, Supplementary Table S2). Conversely, BS

Table 1. *Photosynthetic type, taxonomic group (subfamily and tribe), and C_4 lineage representation of the 18 grass species examined*

Grass species	Photosynthetic type	Subfamily	Tribe	C_4 lineage*
Oryza sativa cv Kitaake	C_3, BEP	Ehrhartoideae	Oryzeae	Not applicable
Brachypodium distachyon	C_3, BEP	Pooideae	Brachypoideae	Not applicable
Hordeum vulgare cv Yagan	C_3, BEP	Pooideae	Triticeae	Not applicable
Triticum aestivum cv Yecora 70	C_3, BEP	Pooideae	Triticeae	Not applicable
Chloris gayana	C_4 PCK, PACMAD	Chloridoideae	Cynodonteae	Chloridoideae
Leptochloa fusca	C_4 NAD-ME, PACMAD	Chloridoideae	Cynodonteae	Chloridoideae
Astrebla lappacea	C_4 NAD-ME, PACMAD	Chloridoideae	Cynodonteae	Chloridoideae
Paspalum dilatatum	C_4 NADP-ME, PACMAD	Panicoideae	Paspaleae	*Paspalum*
Sorghum bicolor cv Rooney	C_4 NADP-ME, PACMAD	Panicoideae	Andropogoneae	Andropogoneae
Zea mays cv B73	C_4 NADP-ME, PACMAD	Panicoideae	Andropogoneae	Andropogoneae
Panicum bisulcatum	C_3, PACMAD	Panicoideae	Paniceae	C_3 sister to MPC
Panicum coloratum	C_4 NAD-ME, PACMAD	Panicoideae	Paniceae	MPC
Panicum miliaceum	C_4 NAD-ME, PACMAD	Panicoideae	Paniceae	MPC
Panicum maximum	C_4 PCK, PACMAD	Panicoideae	Paniceae	MPC
Urochloa panicoides	C_4 PCK, PACMAD	Panicoideae	Paniceae	MPC
Setaria viridis cv A10	C_4 NADP-ME, PACMAD	Panicoideae	Paniceae	MPC
Cenchrus ciliaris	C_4 NADP-ME, PACMAD	Panicoideae	Paniceae	MPC
Panicum antidotale	C_4 NADP-ME, PACMAD	Panicoideae	Paniceae	MPC

*According to GPWGII, (2012).
MPC, Melinidinae, Panicinae, and Cenchrinae.
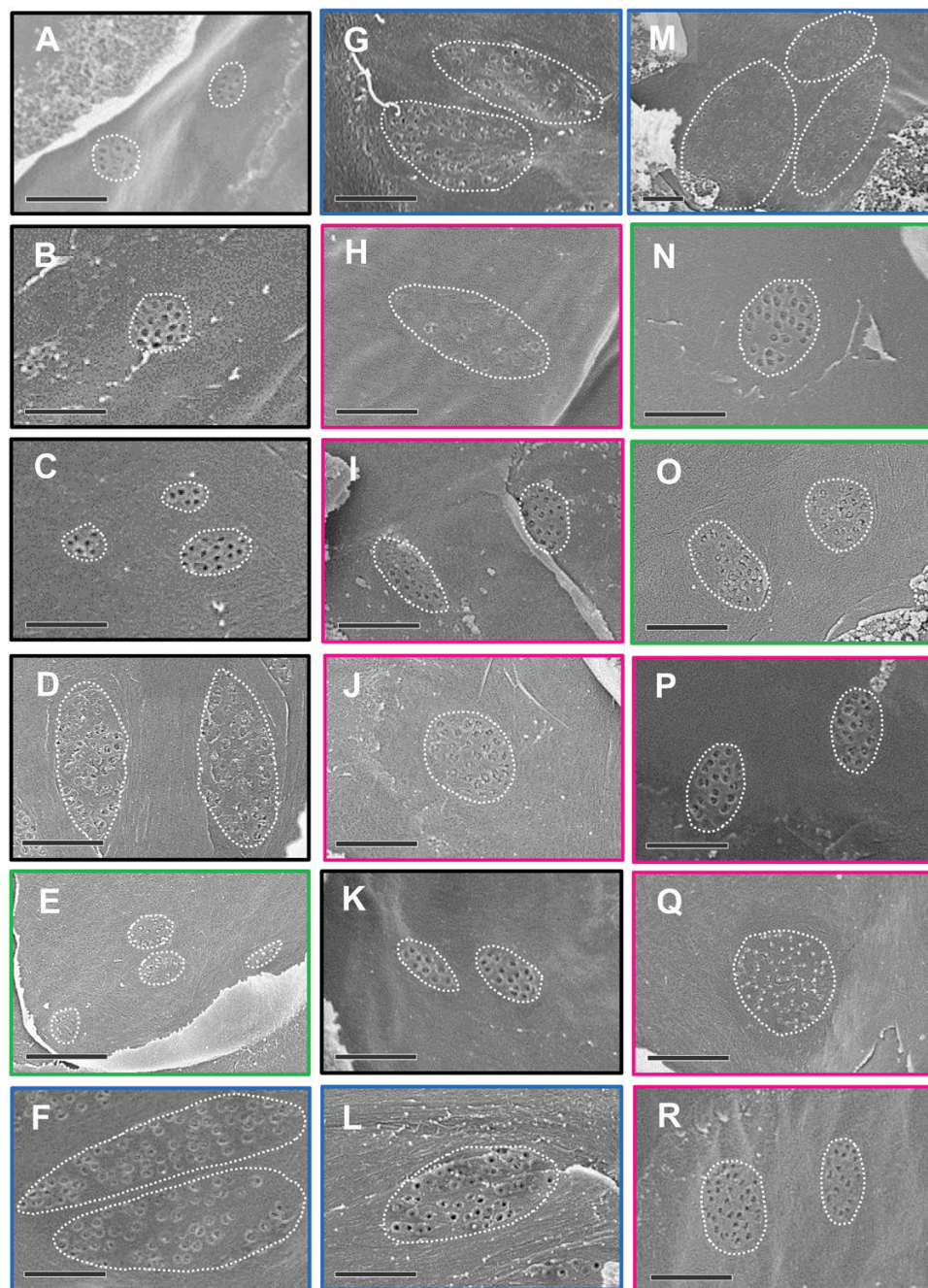
Fig. 2. Scanning electron micrographs showing pit field size on the mesophyll–bundle sheath cell interface of C$_3$ and C$_4$ grass leaves. (A–D) C$_3$ BEP species (black frames): (A) *Oryza sativa*, (B) *Brachypodium distachyon*, (C) *Hordeum vulgare*, and (D) *Triticum aestivum*. (E, N, O) C$_4$ PCK (green frames): (E) *Chloris gayana*, (N) *Panicum maximum*, and (O) *Urochloa panicoides*. (F, G, L, M) C$_4$ NAD-ME (blue frames): (F) *Leptochloa fusca*, (G) *Astrebla lappacea*, (L) *Panicum coloratum*, and (M) *Panicum miliaceum*. (H–J, P–R) C$_4$ NADP-ME (magenta frames): (H) *Paspalum dilatatum*, (I) *Sorghum bicolor*, (J) *Zea mays*, (P) *Setaria viridis*, (Q) *Cenchrus ciliaris*, and (R) *Panicum antidotale*. (K) C$_3$ PACMAD (black frame): *Panicum bisulcatum*. Each pit field is enclosed with a dotted white line. The micrograph of *P. miliaceum* (M) is zoomed out to show whole pit fields. Scale bars are 1 μm.

cell surface area per unit leaf area (S_b) of C$_4$ species was double that of C$_3$ species (Fig. 6F, Supplementary Table S2).

Discussion

Previous studies have shown that PD are more abundant at the M–BS cell interface in a C$_4$ leaf compared to a C$_3$ leaf (Botha, 1992; Danila *et al.*, 2016), presumably to accommodate the higher demand for metabolite transport between cell types in the C$_4$ leaf that is required to support the C$_4$

photosynthetic mechanism (Hatch and Osmond, 1976; Weber and von Caemmerer, 2010). However, little is known about the variation of PD density at the M–BS interface amongst C$_4$ species and the different decarboxylation types. Modelling of metabolite movement between M and BS cells has been hampered by the lack of quantitative data on PD density at this key cellular interface (Danila *et al.*, 2016). To address this, we extended our PD density quantification to a larger subset of grasses representative of C$_3$ photosynthesis, in both BEP (*n*=4) and PACMAD (*n*=1) clades, and in all
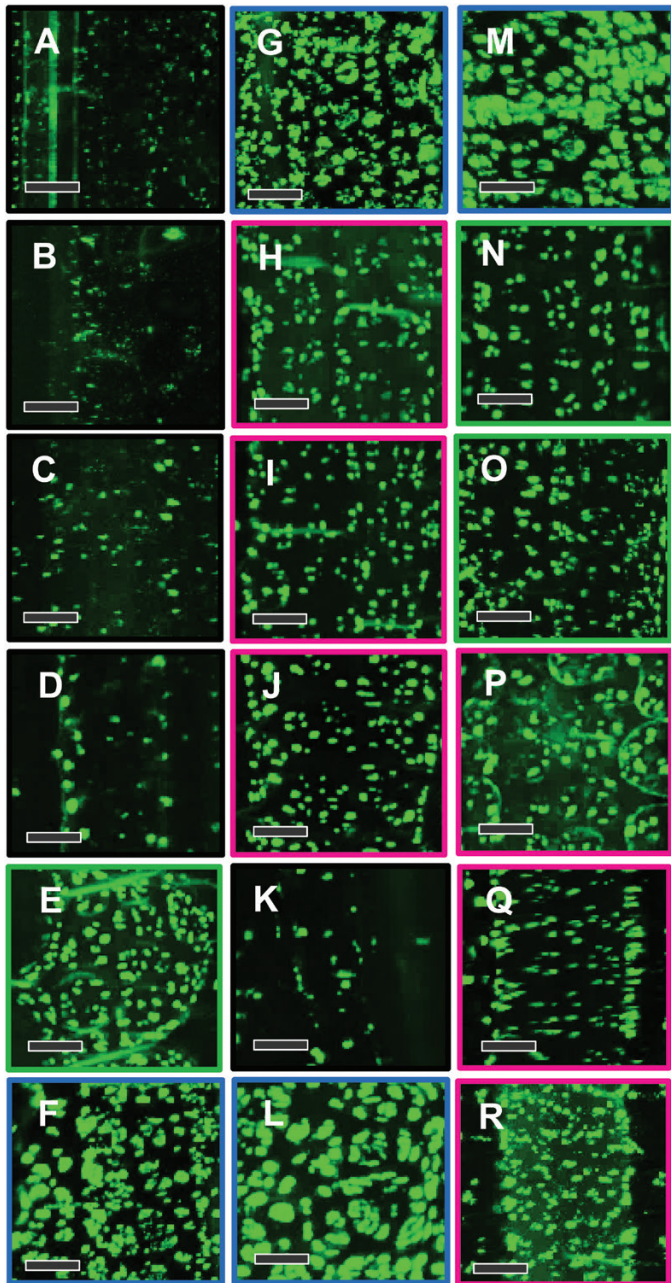
Fig. 3. Confocal micrographs showing the patterns of pit field distribution on the mesophyll–bundle sheath cell interface of C_3 and C_4 grass leaves. (A–D) C_3 BEP species (black frames): (A) *Oryza sativa*, (B) *Brachypodium distachyon*, (C) *Hordeum vulgare*, and (D) *Triticum aestivum*. (E, N, O) C_4 PCK (green frames): (E) *Chloris gayana*, (N) *Panicum maximum*, and (O) *Urochloa panicoides*. (F, G, L, M) C_4 NAD-ME (blue frames): (F) *Leptochloa fusca*, (G) *Astrebla lappacea*, (L) *Panicum coloratum*, and (M) *Panicum miliaceum*. (H–J, P–R) C_4 NADP-ME (magenta frames): (H) *Paspalum dilatatum*, (I) *Sorghum bicolor*, (J) *Zea mays*, (P) *Setaria viridis*, (Q) *Cenchrus ciliaris*, and (R) *Panicum antidotale*. (K) C_3 PACMAD (black frame): *Panicum bisulcatum*. Green fluorescence corresponds to pit fields. Scale bars are 10 µm.

the C_4 decarboxylation types: NAD-ME (*n*=4), NADP-ME (*n*=6), and PCK (*n*=3) (Table 1). We confirmed that not only did all the C_4 species examined have greater PD density than the C_3 species, but that there was also substantial variation in how the high M–BS PD density was achieved among different C_4 subtypes.

Increased PD density in C_4 grasses is a result of larger pit fields and/or more abundant PD per pit field area

Here we show that C_4 species have evolved greater PD density than C_3 species. Greater symplastic connectivity can be achieved by increasing the pit field area or by increasing the PD per pit field area. Interestingly we saw both solutions in our data, particularly in the M–BS interface. In NAD-ME species we saw an increase in pit field area without increasing PD per pit field area, while in PCK and NADP-ME species we saw an increase in both. We propose that the NAD-ME solution is due to their larger veins and thus their need for larger pit fields to facilitate transport. However, in PCK and NADP-ME types where veins are smaller it is sufficient just to increase PD per pit field area without much increase in pit field area to achieve the same effect. These results indicate that there is genetic plasticity in the way in which increased PD transport is achieved in C_4 grasses.

NAD-ME grasses have the greatest pit field area per M–BS interface among the C_4 decarboxylation types

High PD density at the M–BS interface in NAD-ME grasses was solely determined by increases in pit field area per M–BS area driven by larger pit fields (rather than more numerous small pit fields). This is interesting in light of the unique aspects of NAD-ME BS cell anatomy (Dengler *et al.*, 1994). The distinct characteristics of BS cell chloroplasts and mitochondria in NAD-ME species compared to NADP-ME and PCK types (Dengler *et al.*, 1994) are consistent with the different solution they used to achieve high M–BS PD density. This supports the suggestion that PD function and formation are strongly coordinated with the function of both chloroplasts and mitochondria (Brunkard *et al.*, 2013; Wang *et al.*, 2017). Both the centripetal arrangement of mitochondria and larger BS cell cross-sectional area provide a longer diffusion pathlength in the NAD-ME leaf (von Caemmerer *et al.*, 2007). While this anatomical attribute minimises CO_2 leakage across the M–BS interface, it may limit the rate of the C_4 cycle activity (von Caemmerer *et al.*, 2007). More PD connections between M and BS cells allows rapid metabolite shuttling for the C_4 cycle in the NAD-ME type (von Caemmerer *et al.*, 2007), therefore sustaining the high C_4 photosynthetic rate (Henderson *et al.*, 1992; Pinto *et al.*, 2014). Correspondingly, the centrifugal arrangement of chloroplasts and mitochondria in the NADP-ME type presents a greater possibility of CO_2 leakage (von Caemmerer *et al.*, 2007). However, fewer PD between M and BS cells in NADP-ME leaves, in combination with the suberin lamella surrounding the BS, minimises this possibility (von Caemmerer *et al.*, 2007). It is interesting that there was almost as much diversity in the PD density at the M–BS interface among PCK species as there was across C_4 grasses as a whole. This wide range of PD densities in the PCK species examined could result from both PCK and NAD decarboxylation located in the BS (von Caemmerer and Furbank, 2003) together with their considerable variation in BS cell cross-sectional areas, BS chloroplast morphology and positioning, and abundance of mitochondria in the BS (Hattersley and Browning, 1981).

Fig. 4. Distribution of plasmodesmata trait values among photosynthetic types. The distribution of nine variables is summarised by boxplots individually for the C3 BEP and PACMAD (black, *n*=5), C4 PCK (green, *n*=3), C4 NAD-ME (blue, *n*=4), and C4 NADP-ME (magenta, *n*=6). Box and whiskers represent the 25 to 75 percentiles, and the minimum and maximum distribution. Means are denoted by dots. Letters show the statistical ranking using a *post hoc* Tukey test among photosynthetic types (different letters indicate differences at *P*<0.05). Data for individual species are given in Supplementary Table S1. M, mesophyll; BS, bundle sheath; PD, plasmodesmata.

Large PD size between photosynthetic cells is found in leaves of all the grass species examined

Using TEM sections for PD studies presents advantages and disadvantages, highly dependent on the purpose of the study (i.e. ultrastructure versus quantification). For our purpose of analysing many samples, SEM analysis was a more rapid and rigorous way to quantify the cross-sectional area of individual PD in grasses. Random tearing of leaf tissue to reveal M–BS or M–M cell interfaces allowed us to expose the cross-sectional area of PD, almost always within the middle cavity because the tissue tended to separate along the middle lamella between tissue layers. In our previous paper (Danila *et al.*, 2016), our PD area measurements from TEM micrographs used only PD cross-sections with distinct central desmotubules. Similar measurements taken from previously published TEM micrographs of grass leaf PD (fig. 8 from Botha, 1992) generated values similar to both our TEM and SEM results. In fact, the similarity

of PD area values we obtained when we compared our TEM and SEM measurements for *O. sativa*, *Z. mays*, and *S. viridis* encouraged us to use SEM in place of TEM for PD area measurement. We find it interesting that the PD areas we obtained in all cases were very large (about 0.006 μm^2), the diameter being in the range of 90 nm, while the majority of published values for land-plant PD, many of which were obtained from root PD measurements, have a diameter of 50 nm or smaller (Overall, 1999; Ehlers and Kollmann, 2001).

Anatomical enablers of C4 photosynthesis

It has been proposed that enlargement of the BS cells in C4 leaves compared to C3 leaves and their 'functionalisation' by increases in chloroplast number was an early step in C4 evolution (Sage, 2004). Clearly, in this study we showed that there is little evidence for BS cells in C4 grasses being larger in volume than their C3 counterparts. What we saw instead was
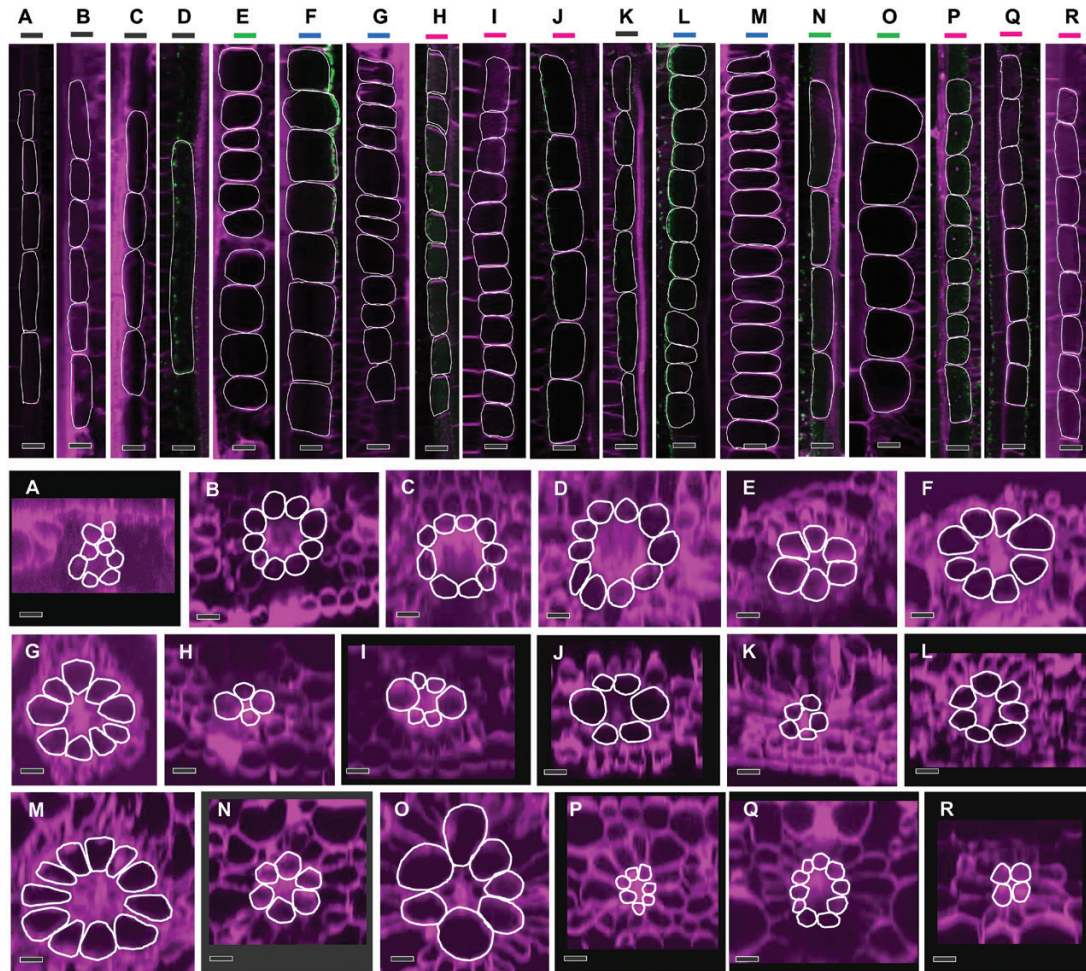
Fig. 5. Confocal micrographs obtained from 3-D stacks of C$_3$ and C$_4$ grass leaves showing bundle sheath cells in paradermal (top) and transverse (bottom) orientations. (A–D) C$_3$ BEP species (black lines): (A) *Oryza sativa*, (B) *Brachypodium distachyon*, (C) *Hordeum vulgare*, and (D) *Triticum aestivum*. (E, N, O) C$_4$ PCK (green lines): (E) *Chloris gayana*, (N) *Panicum maximum*, and (O) *Urochloa panicoides*. (F, G, L, M) C$_4$ NAD-ME (blue lines): (F) *Leptochloa fusca*, (G) *Astrebla lappacea*, (L) *Panicum coloratum*, and (M) *Panicum miliaceum*. (H–J, P–R) C$_4$ NADP-ME (magenta lines): (H) *Paspalum dilatatum*, (I) *Sorghum bicolor*, (J) *Zea mays*, (P) *Setaria viridis*, (Q) *Cenchrus ciliaris*, and (R) *Panicum antidotale*. (K) C$_3$ PACMAD (black line): *Panicum bisulcatum*. Bundle sheath cells are outlined in white. Scale bars are 20 μm.

a distinctively large BS surface area to leaf area ratio (S_b) in C$_4$ grass leaves compared to C$_3$ leaves, consistent with the report of Hattersley (1984). We therefore argue that increasing S_b, but not BS cell size, is important in C$_4$ leaf physiology (von Caemmerer *et al.*, 2007). This finding emphasises the importance of looking at the 3-D geometry of cells in addition to the 2-D view for a more global cell perspective and for improved accuracy in terms of reporting measured values (Théroux-Rancourt *et al.*, 2017). Large IVD is also not always a clear indication of C$_3$ anatomy because it can be interpreted as either an increase in interveinal M cell number (as in C$_3$ grasses) or an increase in BS cell cross-sectional area (as in most NAD-ME and PCK grasses). Our observations showed consistently greater PD density on the M–BS interface in all the C$_4$ species examined relative to the C$_3$ species. Another potentially useful diagnostic character is pit field density, as seen in the substantial difference between the NAD-ME types and other decarboxylation types. This could be used to distinguish not only C$_3$ from C$_4$ photosynthesis but also among C$_4$ biochemical types, at least in grasses.

PD density, metabolite flux, and CO$_2$ diffusion in the C$_4$ BS

PD density at the M–BS interface affects not only metabolite diffusion but also leakage of inorganic carbon and O$_2$ out of the BS compartment, an important determinant of the efficiency of C$_4$ photosynthesis (von Caemmerer and Furbank, 2003). While it is difficult to directly determine the CO$_2$ concentration in the BS of C$_4$ plants, this parameter can be modelled using certain assumptions concerning leaf cell anatomical dimensions, inorganic carbon equilibration, and diffusion properties of membranes and PD (Furbank and Hatch, 1987; Jenkins *et al.*, 1989; von Caemmerer and Furbank, 2003). Based on permeability coefficients determined for metabolites moving into isolated BS cells through PD (Weiner *et al.*, 1988) and for CO$_2$ in C$_4$ leaves and isolated BS cells (Furbank *et al.*, 1989; Jenkins *et al.*, 1989), Jenkins *et al.* (1989) calculated that approximately 40% of the CO$_2$ leakage from the BS occurs via an apoplastic route and 60% via the PD. For oxygen, which moves poorly through lipid bilayers and polymeric barriers such as
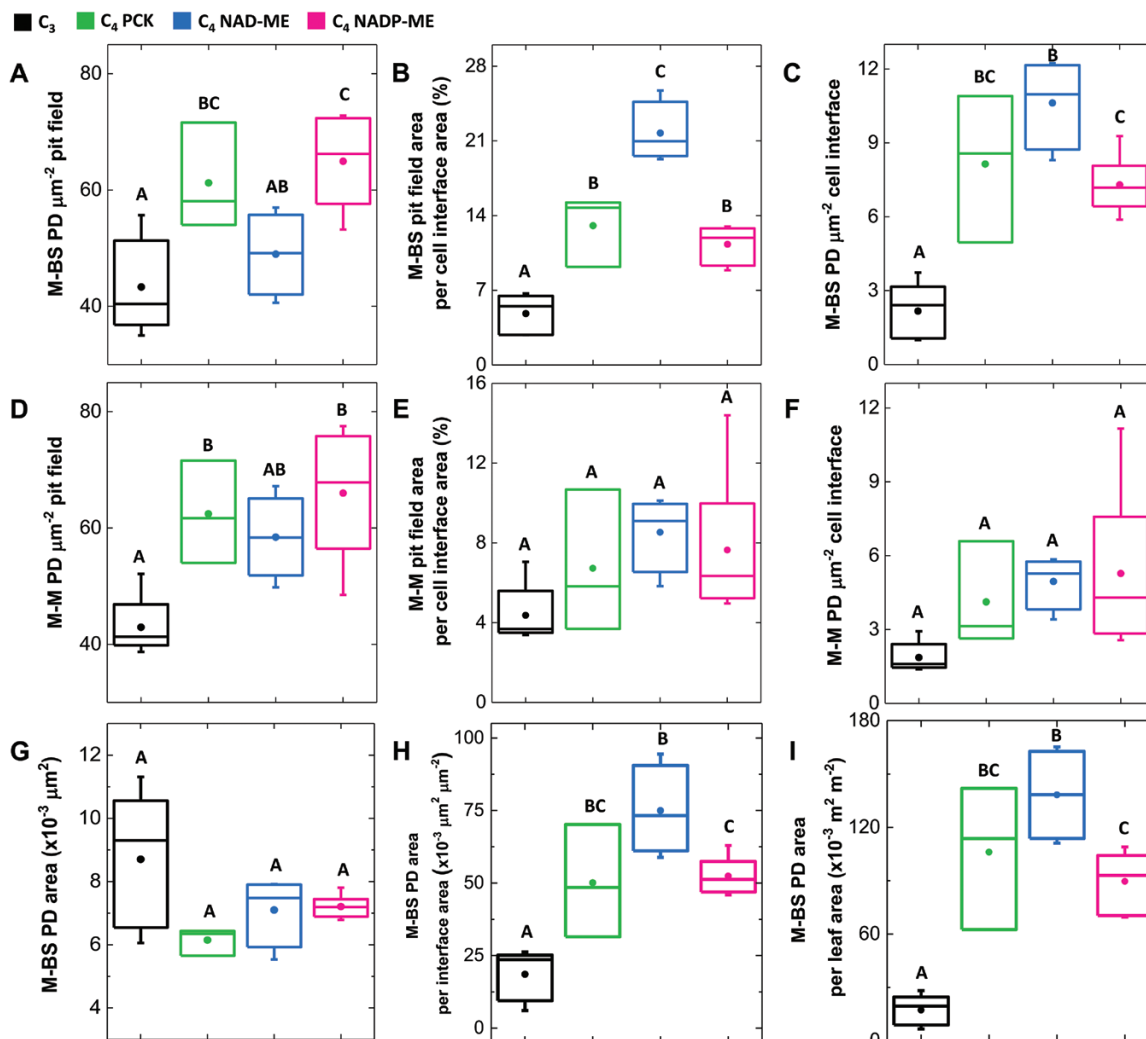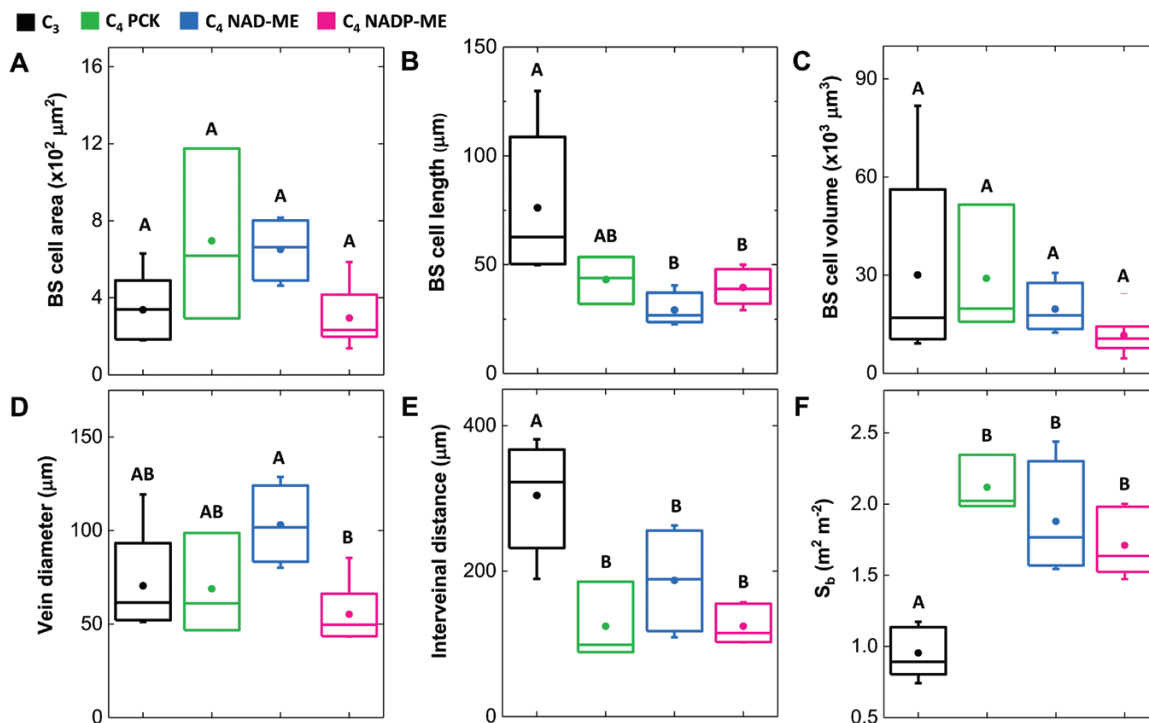
Fig. 6. Distribution of bundle sheath-related trait values among photosynthetic types. The distribution of six variables is summarised by boxplots individually for the C3 BEP and PACMAD (black, *n*=5), C4 PCK (green, *n*=3), C4 NAD-ME (blue, *n*=4), and C4 NADP-ME (magenta, *n*=6). Boxes and whisker plots are as described in Fig. 4. Data for individual species are given in Supplementary Table S2. BS, bundle sheath; S_b, bundle sheath surface area per unit leaf area.

suberin (Jenkins *et al.*, 1989), the majority of diffusion will be through the aqueous route, i.e. via PD. Likewise, bicarbonate moves poorly through lipid membranes and will diffuse out of the BS mostly via PD (Furbank *et al.*, 1989). Given these modelled values for inorganic carbon and O_2 movement at the M–BS interface, the 'optimal' PD density for a C4 leaf would be a compromise between high density for metabolite transport and dissipation of O_2 (in species with PSII in the BS chloroplast), and leakage of inorganic carbon from the BS compartment. The quantification of PD density made here is a first step towards enabling more accurate modelling of metabolite flux and leakage of inorganic carbon from the BS across a range of species and decarboxylation types (Wang *et al.*, 2014). The key parameter required for predicting metabolite gradients and leaf cell metabolite concentrations required to support the C4 pathway is the proportion of M–BS interface comprised of PD pores (Osmond, 1971; Hatch and Osmond, 1976). The current work provides these data for a range of species. The values provide an upper limit given that not all PD may be functional and the obstruction of the PD area by the desmotubule has not been taken into account. Nevertheless, these data facilitate modelling of inorganic carbon leakage rates from the BS without resorting to the use of permeability values obtained from isolated cells (Jenkins *et al.*, 1989). This will be particularly useful for interspecific comparisons given the diversity in suberisation of the M–BS interface between species and the diverse arrangements of organelles and cellular sites of C4 acid decarboxylation across the three biochemical types.

Evolution of symplastic connections to the BS in C4 leaves

It has been reported previously that the transition from C3 to C4 photosynthesis involved a series of genetic alterations, mostly gain of function, leading to numerous changes in plant anatomy and biochemistry (Sage *et al.*, 2012; Bräutigam *et al.*, 2014; Wang *et al.*, 2014; Emms *et al.*, 2016). Recently it was suggested that evolution of C4 photosynthesis has involved a change in the apoplastic transport of sugars in the BS cells of C4 leaves (Emms *et al.*, 2016). A sugar effluxer (or SWEET protein) appears to have been recruited from a relatively minor role in the M cells of C3 grasses to become one of the most highly expressed transcripts in the C4 BS cells (Emms *et al.*, 2016). While we have not as yet identified the genetic changes responsible, we show here that PD density was at least doubled in C4 species compared to C3 species, a clear indication of enhanced expression of PD developmental genes. However, to date, the genes underpinning PD development remain largely unknown (Brunkard and Zambryski, 2017). It is intriguing to consider whether the proposed evolutionary pressures to recruit a highly expressed sugar effluxer to the BS cells of C4 plants were linked to the proliferation of PD at the M–BS interface in C4 leaves. Recent data from genome-wide gene-tree/species-tree reconciliation in grasses has revealed multiple functional categories of genes, of which 10 genes were found to have plausible association with the symplastic transport function (Emms *et al.*, 2016). This leads us to be optimistic that the discovery of candidate genes controlling PD development may be not too far away.

Supplementary data

Supplementary data are available at *JXB* online.

Dataset S1. Single-copy orthologous gene sequences used for phylogenetic tree construction (supplied as a BZIP2 file).

Fig. S1. Light micrographs of transverse sections of C_3 and C_4 grass leaves.

Table S1. Quantitative plasmodesmata traits of the 18 grass species examined.

Table S2. Leaf anatomical traits quantified in the 18 grass species examined.

Acknowledgements

References

Botha CE. 1992. Plasmodesmatal distribution, structure and frequency in relation to assimilation in C_3 and C_4 grasses in southern Africa. Planta **187,** 348–358.

Bräutigam A, Schliesky S, Külahoglu C, Osborne CP, Weber AP. 2014. Towards an integrative model of C_4 photosynthetic subtypes: insights from comparative transcriptome analysis of NAD-ME, NADP-ME, and PEP-CK C_4 species. Journal of Experimental Botany **65,** 3579–3593.

Brunkard JO, Runkel AM, Zambryski PC. 2013. Plasmodesmata dynamics are coordinated by intracellular signaling pathways. Current Opinion in Plant Biology **16,** 614–620.

Brunkard JO, Zambryski PC. 2017. Plasmodesmata enable multicellularity: new insights into their evolution, biogenesis, and functions in development and immunity. Current Opinion in Plant Biology **35,** 76–83.

Collingridge PW, Kelly S. 2012. MergeAlign: improving multiple sequence alignment performance by dynamic reconstruction of consensus multiple sequence alignments. BMC Bioinformatics **13,** 117.

Danila FR, Quick WP, White RG, Furbank RT, von Caemmerer S. 2016. The metabolite pathway between bundle sheath and mesophyll: quantification of plasmodesmata in leaves of C_3 and C_4 monocots. The Plant Cell **28,** 1461–1471.

Dengler NG, Dengler RE, Donnelly PM, Hattersley PW. 1994. Quantitative leaf anatomy of C_3 and C_4 grasses (Poaceae): bundle sheath and mesophyll surface area relationships. Annals of Botany **73,** 241–255.

Ehlers K, Kollmann R. 2001. Primary and secondary plasmodesmata: structure, origin, and functioning. Protoplasma **216,** 1–30.

Emms DM, Covshoff S, Hibberd JM, Kelly S. 2016. Independent and parallel evolution of new genes by gene duplication in two origins of C_4 photosynthesis provides new insight into the mechanism of phloem loading in C_4 species. Molecular Biology and Evolution **33,** 1796–1806.

Emms DM, Kelly S. 2015. OrthoFinder: solving fundamental biases in whole genome comparisons dramatically improves orthogroup inference accuracy. Genome Biology **16,** 157.

Faulkner C, Akman OE, Bell K, Jeffree C, Oparka K. 2008. Peeking into pit fields: a multiple twinning model of secondary plasmodesmata formation in tobacco. The Plant Cell **20,** 1504–1518.

Furbank RT. 2011. Evolution of the C_4 photosynthetic mechanism: are there really three C_4 acid decarboxylation types? Journal of Experimental Botany **62,** 3103–3108.

Furbank RT, Hatch MD. 1987. Mechanism of C_4 photosynthesis: the size and composition of the inorganic carbon pool in bundle sheath cells. Plant Physiology **85,** 958–964.

Furbank RT, Jenkins CL, Hatch MD. 1989. CO_2 concentrating mechanism of C_4 photosynthesis: permeability of isolated bundle sheath cells to inorganic carbon. Plant Physiology **91,** 1364–1371.

GPWGII (Grass Phylogeny Working Group II). 2012. New grass phylogeny resolves deep evolutionary relationships and discovers C_4 origins. New Phytologist **193,** 304–312.

Hatch MD. 1987. C_4 photosynthesis: a unique blend of modified biochemistry, anatomy and ultrastructure. Biochimica et Biophysica Acta **895,** 81–106.

Hatch MD, Osmond CB. 1976. Compartmentation and transport in C_4 photosynthesis. In: **Stocking CR, Heber U**, eds. Transport in plants III. Berlin, Heidelberg: Springer, 144–184.

Hattersley PW. 1984. Characterization of C_4 type leaf anatomy in grasses (Poaceae). mesophyll: bundle sheath area ratios. Annals of Botany **53,** 163–180.

Hattersley PW, Browning AJ. 1981. Occurrence of the suberized lamella in leaves of grasses of different photosynthetic types. I. In parenchymatous bundle sheaths and PCR ("Kranz") sheaths. Protoplasma **109,** 371–401.

Hattersley PW, Watson L. 1976. C_4 Grasses: an anatomical criterion for distinguishing between NADP-malic enzyme species and PCK or NAD-malic enzyme species. Australian Journal of Botany **24,** 297–308.

Henderson S, Caemmerer S, Farquhar G. 1992. Short-term measurements of carbon isotope discrimination in several C_4 species. Functional Plant Biology **19,** 263–285.

Hibberd JM, Sheehy JE, Langdale JA. 2008. Using C_4 photosynthesis to increase the yield of rice—rationale and feasibility. Current Opinion in Plant Biology **11,** 228–231.

Huelsenbeck JP, Ronquist F. 2001. MRBAYES: Bayesian inference of phylogenetic trees. Bioinformatics **17,** 754–755.

Jenkins CL, Furbank RT, Hatch MD. 1989. Mechanism of C_4 photosynthesis: a model describing the inorganic carbon pool in bundle sheath cells. Plant Physiology **91,** 1372–1381.

Kajala K, Covshoff S, Karki S, *et al*. 2011. Strategies for engineering a two-celled C_4 photosynthetic pathway into rice. Journal of Experimental Botany **62,** 3001–3010.

McKown AD, Dengler NG. 2007. Key innovations in the evolution of Kranz anatomy and C_4 vein pattern in *Flaveria* (Asteraceae). American Journal of Botany **94,** 382–399.

Osmond CB. 1971. Metabolite transport in C4 photosynthesis. Australian Journal of Biological Sciences **24,** 159–163.

Osmond CB, Smith FA. 1976. Symplastic transport of metabolites during C_4-photosynthesis. In: **Gunning BES, Robards AW**, eds. Intercellular communication in plants: studies on plasmodesmata. Berlin, Heidelberg: Springer, 229–241.

Overall RL. 1999. Substructure of plasmodesmata. In: **van Bel AJE, Van Kesteren WP**, eds. Plasmodesmata. Berlin, Heidelberg: Springer, 129–148.

Overall RL, Blackman LM. 1996. A model of the macromolecular structure of plasmodesmata. Trends in Plant Science **1,** 307–311.

Palmer WM, Martin AP, Flynn JR, Reed SL, White RG, Furbank RT, Grof CP. 2015. PEA-CLARITY: 3D molecular imaging of whole plant organs. Scientific Reports **5,** 13492.

Pengelly JJ, Sirault XR, Tazoe Y, Evans JR, Furbank RT, von Caemmerer S. 2010. Growth of the C_4 dicot *Flaveria bidentis*: photosynthetic acclimation to low light through shifts in leaf anatomy and biochemistry. Journal of Experimental Botany **61,** 4109–4122.

Pinto H, Sharwood RE, Tissue DT, Ghannoum O. 2014. Photosynthesis of C_3, C_3-C_4, and C_4 grasses at glacial CO_2. Journal of Experimental Botany **65,** 3669–3681.

Price MN, Dehal PS, Arkin AP. 2010. FastTree 2 – approximately maximum-likelihood trees for large alignments. PLoS ONE **5,** e9490.

Robards AW. 1976. Plasmodesmata in higher plants. In: **Gunning BES, Robards AW**, eds. Intercellular communication in plants: studies on plasmodesmata. Berlin Heidelberg: Springer, 15–57.

Sage RF. 2004. The evolution of C_4 photosynthesis. New Phytologist **161,** 341–370.

Sage RF, Christin PA, Edwards EJ. 2011. The C_4 plant lineages of planet Earth. Journal of Experimental Botany **62,** 3155–3169.

Sage RF, Sage TL, Kocacinar F. 2012. Photorespiration and the evolution of C4 photosynthesis. Annual Review of Plant Biology **63,** 19–47.

Théroux-Rancourt G, Earles JM, Gilbert ME, Zwieniecki MA, Boyce CK, McElrone AJ, Brodersen CR. 2017. The bias of a two-dimensional view: comparing two-dimensional and three-dimensional mesophyll surface area estimates using noninvasive imaging. New Phytologist **215,** 1609–1622.

Turrell FM. 1936. The area of the internal exposed surface of dicotyledon leaves. American Journal of Botany **23,** 255–264.

von Caemmerer S, Evans JR, Cousins AB, Badger MR, Furbank RT. 2007. C$_4$ photosynthesis and CO$_2$ diffusion. In: **Sheehy JE, Mitchell PL, Hardy B**, eds. Charting new pathways to C$_4$ rice. Los Baños, Philippines: International Rice Research Institute, 95–115.

von Caemmerer S, Furbank RT. 2003. The C$_4$ pathway: an efficient CO$_2$ pump. Photosynthesis Research **77,** 191–207.

von Caemmerer S, Furbank RT. 2016. Strategies for improving C$_4$ photosynthesis. Current Opinion in Plant Biology **31,** 125–134.

Wang P, Khoshravesh R, Karki S, *et al*. 2017. Re-creation of a key step in the evolutionary switch from C$_3$ to C$_4$ leaf anatomy. Current Biology **27,** 3278–3287.e6.

Wang Y, Bräutigam A, Weber AP, Zhu XG. 2014. Three distinct biochemical subtypes of C$_4$ photosynthesis? A modelling analysis. Journal of Experimental Botany **65,** 3567–3578.

Weber AP, von Caemmerer S. 2010. Plastid transport and metabolism of C$_3$ and C$_4$ plants — comparative analysis and possible biotechnological exploitation. Current Opinion in Plant Biology **13,** 257–265.

Weiner H, Burnell JN, Woodrow IE, Heldt HW, Hatch MD. 1988. Metabolite diffusion into bundle sheath cells from C$_4$ plants: relation to C$_4$ photosynthesis and plasmodesmatal function. Plant Physiology **88,** 815–822.
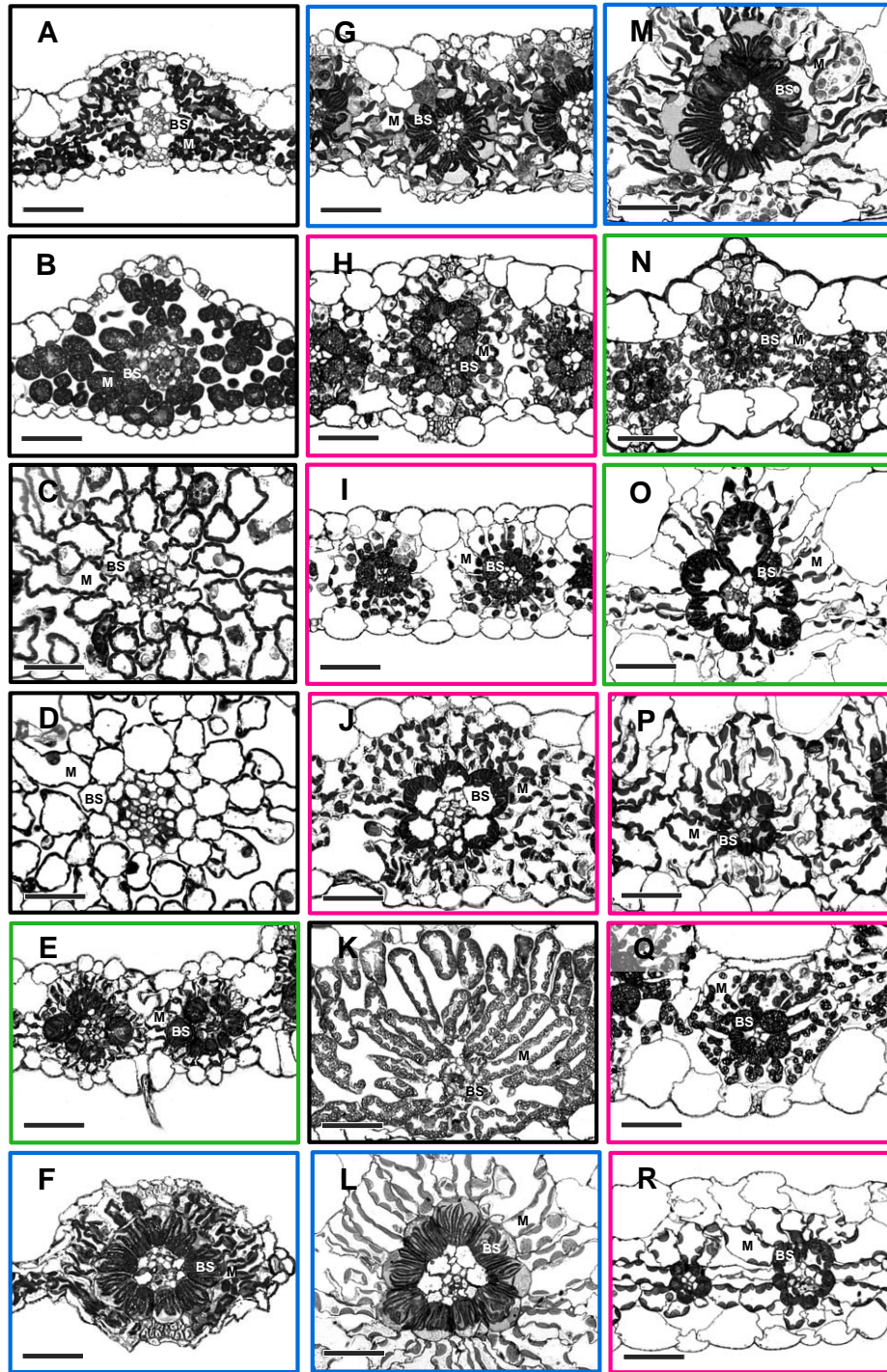
Figure S1 Light micrographs of transverse sections of C_3 and C_4 grass leaves. (A-D) C_3 BEP species, black frame: (A) *Oryza sativa*, (B) *Brachypodium distachyon*, (C) *Hordeum vulgare*, and (D) *Triticum aestivum.* (E, N-O) C_4 PCK, green frame: (E) *Chloris gayana*, (N) *Panicum maximum*, and (O) *Urochloa panicoides.* (F-G, L-M) C_4 NAD-ME, blue frame: (F) *Leptochloa fusca*, (G) *Astrebla lappacea*, (L) *Panicum coloratum*, and (M) *Panicum miliaceum.* (H-J, P-R) C_4 NADP-ME, magenta frame: (H) *Paspalum dilatatum*, (I) *Sorghum bicolor*, (J) *Zea mays*, (P) *Setaria viridis*, (Q) *Cenchrus ciliaris*, and (R) *Panicum antidotale.* (K) C_3 PACMAD, black frame: *Panicum bisulcatum.* Mesophyll (M) and bundle sheath (BS) cells are labelled. Bars = 50 μm.

Table S1. Quantitative plasmodesmata traits of the 18 grass species examined.

Grass species	Photosynthetic type	M-BS PD per μm^2 pit field	M-BS pit field area per cell interface area (%)	M-BS PD per μm^2 cell interface	M-M PD per μm^2 pit field	M-M pit field area per cell interface area (%)	M-M PD per μm^2 cell interface	Pit field area (μm^2)	PD area (x10^{-3} μm^2)	PD area per interface area (x10^{-3} μm^2 μm^{-2})	PD area per leaf area (x10^{-3} m^2 m^{-2})
O. sativa	C$_3$, BEP	35 ± 0.4*	2.8 ± 0.07*	1.0 ± 0.02*	39 ± 0.4*	4.1 ± 0.15*	1.6 ± 0.08*	0.3 ± 0.06	6.1 ± 0.20	6.0 ± 0.07	6.6 ± 0.07
B. distachyon	C$_3$, BEP	40 ± 0.6	2.8 ± 0.15	1.1 ± 0.06	41 ± 0.4	3.4 ± 0.17	1.4 ± 0.07	0.4 ± 0.03	11.3 ± 0.33	12.9 ± 0.23	11.1 ± 0.15
H. vulgare	C$_3$, BEP	39 ± 0.6	6.2 ± 0.17	2.4 ± 0.06	42 ± 0.6	7.0 ± 0.08	2.9 ± 0.04	0.4 ± 0.03	9.8 ± 0.29	23.6 ± 0.27	21.1 ± 0.29
T. aestivum	C$_3$, BEP	47 ± 1.0*	5.5 ± 0.32*	2.6 ± 0.15*	41 ± 0.7*	3.7 ± 0.22*	1.5 ± 0.09*	1.6 ± 0.17	9.3 ± 0.30	24.0 ± 0.46	28.2 ± 0.71
C. gayana	C$_4$ PCK, PACMAD	58 ± 1.2	14.8 ± 0.28	8.6 ± 0.17	62 ± 1.2	10.7 ± 0.34	6.6 ± 0.21	0.3 ± 0.04	5.7 ± 0.20	48.5 ± 0.56	113.7 ± 1.02
L. fusca	C$_4$ NAD-ME, PACMAD	41 ± 0.5	20.5 ± 0.45	8.3 ± 0.18	67 ± 0.4	8.7 ± 0.41	5.8 ± 0.28	1.5 ± 0.40	7.1 ± 0.33	58.9 ± 0.87	111.1 ± 1.58
A. lappacea	C$_4$ NAD-ME, PACMAD	57 ± 0.7	21.5 ± 0.20	12.2 ± 0.12	58 ± 0.9	9.5 ± 0.27	5.5 ± 0.16	1.4 ± 0.17	5.5 ± 0.16	67.7 ± 0.61	165.2 ± 3.18
P. dilatatum	C$_4$ NADP-ME, PACMAD	53 ± 2.9	12.4 ± 0.25	6.6 ± 0.13	49 ± 1.0	5.3 ± 0.18	2.6 ± 0.09	0.9 ± 0.14	7.2 ± 0.18	47.3 ± 0.43	94.6 ± 0.91
S. bicolor	C$_4$ NADP-ME, PACMAD	66 ± 1.0	8.9 ± 0.26	5.9 ± 0.18	64 ± 1.6	6.4 ± 0.25	4.1 ± 0.16	0.4 ± 0.05	7.8 ± 0.17	45.9 ± 0.49	70.7 ± 0.58
Z. mays	C$_4$ NADP-ME, PACMAD	66 ± 0.7*	11.4 ± 0.27*	7.5 ± 0.18*	78 ± 0.6*	14.4 ± 0.24*	11.2 ± 0.18*	0.7 ± 0.08	7.3 ± 0.12	55.2 ± 0.46	109.0 ± 0.86
P. bisulcatum	C$_3$, PACMAD	56 ± 0.6	6.7 ± 0.33	3.7 ± 0.19	52 ± 0.4	3.6 ± 0.09	1.9 ± 0.05	0.5 ± 0.04	7.0 ± 0.14	26.3 ± 0.40	19.5 ± 0.17
P. coloratum	C$_4$ NAD-ME, PACMAD	46 ± 0.4	25.7 ± 0.41	11.9 ± 0.19	50 ± 0.7	10.1 ± 0.42	5.0 ± 0.21	1.2 ± 0.10	7.9 ± 0.24	94.5 ± 0.92	155.3 ± 2.59
P. miliaceum	C$_4$ NAD-ME, PACMAD	52 ± 0.7	19.3 ± 0.29	10.0 ± 0.15	59 ± 0.4	5.8 ± 0.27	3.4 ± 0.16	2.4 ± 0.40	7.9 ± 0.38	78.8 ± 1.15	121.6 ± 1.14
P. maximum	C$_4$ PCK, PACMAD	54 ± 0.3	9.2 ± 0.27	5.0 ± 0.15	54 ± 0.3	5.8 ± 0.17	3.1 ± 0.09	0.6 ± 0.05	6.4 ± 0.22	31.5 ± 0.42	62.6 ± 0.55
U. panicoides	C$_4$ PCK, PACMAD	72 ± 0.6	15.2 ± 0.30	10.9 ± 0.21	72 ± 0.6	3.7 ± 0.06	2.6 ± 0.04	0.7 ± 0.05	6.4 ± 0.16	70.2 ± 0.64	142.0 ± 0.75
S. viridis	C$_4$ NADP-ME, PACMAD	73 ± 0.9*	12.7 ± 0.34*	9.3 ± 0.25*	75 ± 0.8*	8.5 ± 0.14*	6.4 ± 0.11*	0.6 ± 0.07	6.8 ± 0.16	63.0 ± 0.64	102.6 ± 0.70
C. ciliaris	C$_4$ NADP-ME, PACMAD	72 ± 1.0	9.5 ± 0.16	6.8 ± 0.12	72 ± 1.0	6.3 ± 0.13	4.5 ± 0.09	0.6 ± 0.06	6.9 ± 0.19	47.2 ± 0.45	69.6 ± 0.76
P. antidotale	C$_4$ NADP-ME, PACMAD	59 ± 0.5	13.0 ± 0.18	7.7 ± 0.11	59 ± 0.5	5.0 ± 0.11	2.9 ± 0.07	0.7 ± 0.06	7.2 ± 0.14	55.6 ± 0.39	91.4 ± 0.50

Asterisks indicate values previously reported in (Danila et al., 2016). M-BS = mesophyll-bundle sheath, PD = plasmodesmata, M-M = mesophyll-mesophyll, PD area = cross sectional area of individual PD measured from SEM.

Table S2. Leaf anatomical traits quantified in the 18 grass species examined.

Grass species	Photosynthetic type	BS cell area (μm^2)[a]	BS cell length (μm)[a]	BS cell volume (μm^3)[a]	Vein diameter (μm)[b]	IVD (μm)[b]	S_b (m^2 m^{-2})[b]
O. sativa	C₃, BEP	180 ± 6.2	51 ± 1.8	9113 ± 130.3	53 ± 3.6	189 ± 3.1	1.1 ± 0.06*
B. distachyon	C₃, BEP	340 ± 15.7	50 ± 2.0	16927 ± 300.0	61 ± 1.7	322 ± 7.2	0.9 ± 0.05
H. vulgare	C₃, BEP	349 ± 11.4	88 ± 2.8	30609 ± 401.6	67 ± 3.1	381 ± 12.3	0.9 ± 0.07
T. aestivum	C₃, BEP	630 ± 47.4	130 ± 9.1	81758 ± 2433.3	119 ± 2.9	353 ± 2.0	1.2 ± 0.17*
C. gayana	C₄ PCK, PACMAD	618 ± 31.5	32 ± 0.7	19767 ± 313.2	61 ± 5.8	99 ± 6.2	2.3 ± 0.09
L. fusca	C₄ NAD-ME, PACMAD	756 ± 40.7	41 ± 1.0	30648 ± 525.8	80 ± 3.0	143 ± 16.9	1.9 ± 0.14
A. lappacea	C₄ NAD-ME, PACMAD	570 ± 26.1	27 ± 0.8	16883 ± 258.3	93 ± 4.0	109 ± 0.5	2.4 ± 0.28
P. dilatatum	C₄ NADP-ME, PACMAD	241 ± 13.5	36 ± 1.2	8743 ± 165.4	50 ± 2.2	103 ± 4.4	2.0 ± 0.10
S. bicolor	C₄ NADP-ME, PACMAD	360 ± 19.7	29 ± 0.6	10474 ± 177.8	43 ± 1.2	102 ± 4.5	1.5 ± 0.05
Z. mays	C₄ NADP-ME, PACMAD	586 ± 44.6	42 ± 1.1	24318 ± 566.5	85 ± 4.6	155 ± 5.1	2.0 ± 0.08*
P. bisulcatum	C₃, PACMAD	188 ± 9.5	63 ± 2.1	11778 ± 205.3	51 ± 2.0	274 ± 5.5	0.7 ± 0.01
P. coloratum	C₄ NAD-ME, PACMAD	463 ± 20.6	27 ± 0.5	12421 ± 174.2	110 ± 2.5	234 ± 14.4	1.6 ± 0.16
P. miliaceum	C₄ NAD-ME, PACMAD	816 ± 28.0	23 ± 0.6	18484 ± 226.9	129 ± 3.7	263 ± 6.8	1.5 ± 0.05
P. maximum	C₄ PCK, PACMAD	293 ± 22.1	54 ± 1.8	15699 ± 373.3	47 ± 1.5	89 ± 2.7	2.0 ± 0.06
U. panicoides	C₄ PCK, PACMAD	1175 ± 87.2	44 ± 1.1	51545 ± 1167.1	99 ± 3.9	185 ± 6.7	2.0 ± 0.02
S. viridis	C₄ NADP-ME, PACMAD	137 ± 6.4	33 ± 1.0	4528 ± 73.0	49 ± 1.7	126 ± 2.6	1.6 ± 0.04*
C. ciliaris	C₄ NADP-ME, PACMAD	218 ± 9.5	50 ± 1.3	10913 ± 159.3	60 ± 3.7	157 ± 21.2	1.5 ± 0.09
P. antidotale	C₄ NADP-ME, PACMAD	225 ± 6.3	47 ± 1.2	10634 ± 116.9	44 ± 2.4	102 ± 6.6	1.6 ± 0.04

[a]Measured from confocal micrographs derived from whole leaf z-stacks.

[b]Measured from light micrographs of transverse leaf sections.

Asterisks indicate values previously reported in (Danila et al., 2016). BS = bundle sheath, VB = vascular bundle, IVD = interveinal distance, S_b = bundle sheath surface area per unit leaf area.

5

Response of plasmodesmata formation in leaves of C_4 grasses to growth irradiance

Statement of Contribution

This thesis is submitted as a Thesis by Compilation in accordance with https://policies.anu.edu.au/ppl/document/ANUP_003405
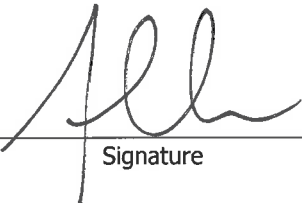
I declare that the research presented in this Thesis represents original work that I carried out during my candidature at the Australian National University, except for contributions to multi-author papers incorporated in the Thesis where my contributions are specified in this Statement of Contribution.

Title and authors: **Response of plasmodesmata formation in leaves of C$_4$ grasses to growth irradiance. Florence R. Danila, William Paul Quick, Rosemary G. White, Susanne von Caemmerer, and Robert T. Furbank.**
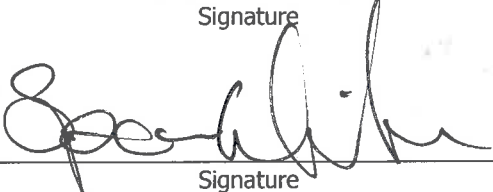
Current status of paper: **Submitted** (Plant, Cell and Environment)

Update prior to submission of thesis corrections: **Published** (Plant, Cell and Environment. April 2019. https://doi.org/10.1111/pce.13558)

Contribution to paper: **F.R.D. conducted all the experiments, imaging, quantification, data analysis, and statistics in consultation with S.v.C., R.T.F, R.G.W., and W.P.Q. F.R.D. also prepared the first draft of the manuscript, handled all corrections based on co-authors comments and suggestions, and did all the formatting for journal submission.**

Senior author or collaborating author's endorsement:

Susanne von Caemmerer	_signature_	5/12/2018
Senior author – Print Name	Signature	Date
Robert T. Furbank	_signature_	5/12/2018
Senior author – Print Name	Signature	Date
Florence R. Danila	_signature_	5/12/2018
Candidate – Print Name	Signature	Date

Endorsed

Susanne von Caemmerer	_signature_	5/12/2018
Chair of Supervisory Panel – Print Name	Signature	Date
Spencer Whitney	_signature_	5.12.18.
Delegated Authority – Print Name	Signature	Date

Title

Response of plasmodesmata formation in leaves of C_4 grasses to growth irradiance

Authors

Florence R. Danila[1,2*], William Paul Quick[2,3,5], Rosemary G. White[4], Susanne von Caemmerer[1,2], Robert T. Furbank[1,2,4]

Contact information

[1]Research School of Biology, Australian National University, Canberra Australian Capital Territory 2601, Australia.
[2]ARC Centre of Excellence for Translational Photosynthesis, Australian National University, Canberra Australian Capital Territory 2601, Australia.
[3]International Rice Research Institute, Los Baños, Laguna 4030, Philippines.
[4]CSIRO Agriculture and Food, Canberra Australian Capital Territory 2601, Australia.
[5]University of Sheffield, Sheffield, United Kingdom.

*To whom correspondence should be addressed. E-mail:
florence.danila@anu.edu.au

Funding

Abstract

Rapid metabolite diffusion across the mesophyll (M) and bundle sheath (BS) cell interface in C_4 leaves is a key requirement for C_4 photosynthesis and occurs via plasmodesmata (PD). Here, we investigated how growth irradiance affects PD density between M and BS cells and between M cells in two C_4 species using our PD

quantification method, which combines three-dimensional laser confocal fluorescence microscopy and scanning electron microscopy. The response of leaf anatomy and physiology of NADP-ME species, *Setaria viridis* and *Zea mays* to growth under different irradiances, low light (100 µmol m^{-2} s^{-1}) and high light (1000 µmol m^{-2} s^{-1}), was observed both at seedling and established growth stages. We found that the effect of growth irradiance on C$_4$ leaf PD density depended on plant age and species. The high light treatment resulted in two to four-fold greater PD density per unit leaf area than at low light, due to greater area of PD clusters and greater PD size in high light plants. These results along with our finding that the effect of light on M-BS PD density was not tightly linked to photosynthetic capacity suggest a complex mechanism underlying the dynamic response of C$_4$ leaf PD formation to growth irradiance.

Short Abstract

Using our recently developed method of visualizing plasmodesmata (PD), we found that the response of PD formation in leaves of C$_4$ grasses to growth irradiance is both plant age and species-dependent and is not tightly linked to photosynthetic capacity.

Keywords

growth irradiance; photosynthetic capacity; plant age; plasmodesmata density; *Setaria viridis*; *Zea mays*

Abbreviations

NADP-ME   nicotinamide adenine dinucleotide phosphate-malic enzyme
PCK   phosphoenolpyruvate carboxykinase

Introduction

High photosynthetic efficiency in C$_4$ plants is attributed to the ability to concentrate carbon dioxide at the site of rubisco (ribulose-1,5-biphosphate

carboxylase/oxygenase), consequently diminishing photorespiration (Hatch, 1987). In a C_4 leaf, fixation of atmospheric CO_2 and photosynthetic carbon reduction are spatially separated into two anatomically and biochemically distinct cells (Kranz anatomy); these are the mesophyll (M) and bundle sheath (BS) cells, respectively (Hatch and Osmond, 1976). The CO_2-tight anatomy of BS cells and high affinity of carbonic anhydrase and phosphoenolpyruvate carboxylase to CO_2 and bicarbonate respectively, contribute to the elevation of CO_2 around the active site of rubisco to levels up to 10-fold ambient CO_2 concentrations in the M (Furbank et al., 1990; Hatch, 1987; von Caemmerer and Furbank, 2003). Although the efficiency of the CO_2 concentrating mechanism is reliant on minimising diffusion of CO_2 out of the BS cells, rapid metabolite exchange between M and BS during C_4 photosynthesis is required to support photosynthetic flux of C_4 acids to the BS cells and for C_3 products to return to the M to regenerate PEP. Given that the M-BS cell interface is characterised by cell walls, which are heavily thickened and often suberised, metabolites must pass symplastically across this barrier, via diffusion through plasmodesmata (PD) (Hatch and Osmond, 1976).

PD are cytoplasmic conduits that traverse plant cell walls to enable intercellular continuity. Evidence for the existence of PD in plants was published more than a hundred years ago (Tangl, 1879), but a comprehensive understanding of their role in developmental, intercellular transport, and signalling processes as well as their molecular anatomy and genetic networks controlling their function still remains to be realized (Lu et al., 2018). The main challenge underlying PD research has been their minute size and difficulty in viable isolation. For a long time, transmission electron microscopy (TEM)-based methods have been used to quantify the intercellular PD connections between plant cells using arduous serial sectioning and visual counting of PD (Botha, 1992; Gunning, 1978; Seagull, 1983). This has limited both data accuracy due to the 3-D nature of cell interfaces and patchy, nonrandom distribution of PD at those interfaces, and statistical robustness due to insufficient sampling coverage. The application of 3-D imaging of intact plant tissue to this problem (Danila et al., 2016) has avoided many of these limitations and provided not only more accurate PD density measurements in leaves but also the first comprehensive PD density survey in monocot species (Danila et al., 2018). In the latter study, C_4

grasses were found to have up to 12 times more PD connecting photosynthetic cells compared with the C_3 species (Danila et al., 2018).

The CO_2 concentrating mechanism of C_4 photosynthesis requires at least two additional ATP per CO_2 fixed compared to C_3 photosynthesis (Furbank et al., 1990) thus, C_4 plants suffer an energetic penalty under some environmental conditions. Indeed, in natural ecosystems, C_4 plants are typically found in high light environments under higher ambient temperatures where the benefits of the CO_2 concentrating mechanism outweigh the costs (Sage and Pearcy, 2000). Nevertheless, in most field situations where C_4 crops and grasses form thick canopies, a substantial proportion of the vegetative part of the plant may experience shade or natural low light. Under such unfavourable conditions, C_4 leaves can undergo both biochemical and anatomical changes as part of their acclimatory response (Pengelly et al., 2010; Sonawane et al., 2018; Tazoe et al., 2008; Tazoe et al., 2006). Responses of C_4 plants, however, appear to differ depending on the decarboxylation subtype (NADP-ME, NAD-ME, or PCK) (Sonawane et al., 2018), whether the plants are monocots or dicots (Pengelly et al., 2010; Sonawane et al., 2018; Tazoe et al., 2008; Tazoe et al., 2006), or even between species (Ward and Woolhouse, 1986). Photosynthetic efficiency may also be compromised in low light-grown C_4 plants, which have been reported to show lower CO_2 assimilation rates compared to high light-grown plants (Sharwood et al., 2014; Sonawane et al., 2018).

Despite the importance of PD in facilitating transport between M and BS in C_4 plants, there is only one report of the effects of different growth irradiance on PD density in C_4 grass leaves (Sowiński et al., 2007). This study concluded that there was a proportional increase in M-BS PD density with increasing light intensity across all subtypes. However, the TEM technique described above was used, giving a restricted view of PD distribution over this 3D cell-cell interface, hence, it is not clear how these changes were achieved. In most tissues, including leaves, PD occur in clusters, one unit of which is termed a pit field. Therefore, the use of the Gunning constant (Gunning, 1978) to calculate PD density (which requires random distribution of PD on the cell interface, not clustering in pit fields) may not be appropriate for leaves, where PD are so highly clustered in pit fields (Botha and Evert, 1988; Danila et al., 2016; Danila et al., 2018).

In this study, two NADP-ME C_4 grasses, *Setaria viridis* and *Zea mays,* were grown under different light intensities: low light (100 µmol m^{-2} s^{-1}) and high light (1000 µmol m^{-2} s^{-1}). The use of *Z. mays* allows comparison with previous studies while the information generated for *S. viridis* adds to the existing knowledge about this new C_4 model species with a relatively small sequenced and publicly available genome (Brutnell et al., 2010; Li and Brutnell, 2011). The response of PD frequency between leaf cells to growth under the two different light environments was evaluated by quantifying the PD density between M and BS on the youngest fully expanded leaf at two time points in plant development: 2 and 7 weeks after germination. Implementation of our PD quantification method (Danila et al., 2016) provided detail on how PD density changed expressed both in terms of PD frequency and pit field area. Concurrent with anatomical measurements, the response of photosynthetic assimilation to light intensity was measured and a range of other leaf physiological and anatomical parameters were characterised.

Materials and methods

Plant material and growth conditions

Seeds of *Setaria viridis* cultivar A10 and *Zea mays* cultivar B73 were germinated in a growth cabinet (High Resolution Plant Phenomics Centre, CSIRO Black Mountain, Canberra, Australia) under two light conditions, 100 µmol m^{-2} s^{-1} (low light) and 1,000 µmol m^{-2} s^{-1} (high light). Cabinets were maintained at 28°C day/22°C night temperatures, 60% relative humidity, 16-hr light/8-hr dark, and ambient CO_2 concentration. Plants were supplied with Osmocote (Scotts Australia) and watered regularly. Physiological and anatomical parameters were measured on the youngest fully expanded leaf at two developmental stages: 2 and 7 weeks after germination.

Physiological measurements

Gas exchange was measured using a LI-6400 equipped with a blue-red light-emitting diode light source (LI-COR, Inc., Australia) applied to the middle portion of the youngest fully expanded leaf from three independent plants per species. Leaves

were initially equilibrated for 30 min in a standard environment of 380 µmol mol^{-1} CO_2 set in sample cell, 25°C leaf temperature, flow rate of 500 µmol s^{-1}, and an irradiance of 2,000 µmol m^{-2} s^{-1}. Light response curves were generated by imposing a stepwise decrease in irradiance (2,000, 1,500, 1,000, 800, 600, 400, 200, 100, 0 µmol m^{-2} s^{-1}), each step lasting for 5 min while maintaining temperature and CO_2 conditions. Immediately following gas exchange measurements, two sets of 0.6-cm^2 leaf discs were collected from the same leaf, one set was snap-frozen in liquid nitrogen and the other set was oven-dried at 60°C for 48 hr. Chlorophyll was extracted from the frozen leaf discs using 80% acetone in mortar and pestle. Chlorophyll *a* and *b* proportions of the extract were calculated according to (Porra et al., 1989) using values obtained from Cary® 50 Bio UV-visible spectrophotometer (Varian, Inc.) at 663.6, 646.6, and 750 nm wavelengths. Using dried leaf discs, leaf mass per area was obtained by dividing dry weight by leaf area, whereas total leaf nitrogen content was determined on the ground leaf tissue using a carbon nitrogen analyser (LECO TruSpec; LECO Corp., MI, USA).

Anatomical measurements

All leaf tissue preparations for light microscopy, TEM, scanning electron microscopy (SEM), and 3-D immunolocalisation confocal microscopy were as described by (Danila et al., 2016). Tissues were collected in the morning, between 9:00 a.m. and 11:00 a.m., from the middle portion of the same leaf used for physiological measurement. Leaf tissues were fixed and processed accordingly. For 3-D immunolocalisation confocal microscopy, leaf tissue was fixed and cleared according to Danila et al. (2016), hybridised with β-1,3-glucan (callose) antibody, followed by Alexa488-tagged secondary antibody, and poststained with calcofluor white to visualize cell walls (Danila et al., 2016). Transverse sections of resin embedded leaves were imaged for light microscopy under 10X and 40X objectives using a Nikon Eclipse 50i upright microscope (Nikon Instruments). For TEM, ultrathin sections were examined using a Hitachi HA7100 TEM (Hitachi High Technologies America) at 75 kV. SEM was performed using a Zeiss Ultra Plus field emission SEM at 3 kV.

To quantify pit field distribution, z-stacks from two leaf tissues per plant were obtained using a Leica SP8 multiphoton confocal microscope (Leica Microsystems). PD density was quantified using the method described by Danila et al. (2016). PD area and pit field area were measured using SEM images. M-BS PD area per leaf area was calculated according to (Danila et al., 2018). Vein circumference, interveinal distance, and leaf thickness of 10 to 20 individual minor veins were measured from light micrographs of transverse leaf sections. Values for M and BS cell wall thickness, M and BS chloroplast size, M and BS starch granule per chloroplast, M and BS starch granule size, M grana width, and BS chloroplast content were obtained from TEM measurements of transverse leaf sections. Average number of corresponding structures measured was specified in Tables 2 and 3. Because chloroplasts and starch granules were not circular, the measurements performed here were used only for approximate comparison given that all samples were treated the same way. BS chloroplast content was calculated as the proportion of BS cell area taken up by the chloroplasts. BS surface area per unit leaf area (S_b; $n=7$ or more) was calculated using the equation described previously (Pengelly et al., 2010). A Wacom Cintiq graphics tablet (Wacom Technology Corporation, Vancouver, WA, USA) together with ImageJ software (National Institutes of Health, Bethesda, MD, USA) were used for all anatomical measurements.

Statistical analysis

Group sizes were equal overall for all response variables. The relationship between various response variables and the main effect (growth irradiance and plant age) and their interactions were obtained using two-way ANOVA (OriginPro 9.1, OriginLab Corporation). Means comparisons were performed using post-hoc Tukey test at 0.05 significance level.

Results

CO_2 assimilation rate and leaf chemistry

In *S. viridis*, light response curves of CO_2 assimilation showed that plants grown under low light conditions had reduced photosynthetic performance when compared

to their high light-grown counterparts regardless of plant age (Figure 1A; Table 1). Similarly, low light-grown *Z. mays* had lower CO_2 assimilation rates than high light-grown plants, but there was a significant plant age and growth irradiance x plant age effect on CO_2 assimilation rate (Figure 1B; Table 1). Low CO_2 assimilation rate in low light-grown plants was particularly evident when plants were measured at high irradiance (Figure 1C, D). In both *S. viridis* and *Z. mays*, plants grown at low irradiance had 30-50% less leaf mass per area compared to high light-grown plants and across development, high light-grown plants showed a greater leaf mass per area increase over time (Figures 2A and 3A; Table 1). Significant effect of growth irradiance was also reflected in both total leaf N content (Figures 2B and 3B; Table 1) and chlorophyll content per leaf area (Figures 2C and 3C; Table 1) of *S. viridis* and *Z. mays*, where low light-grown plants had lower values.
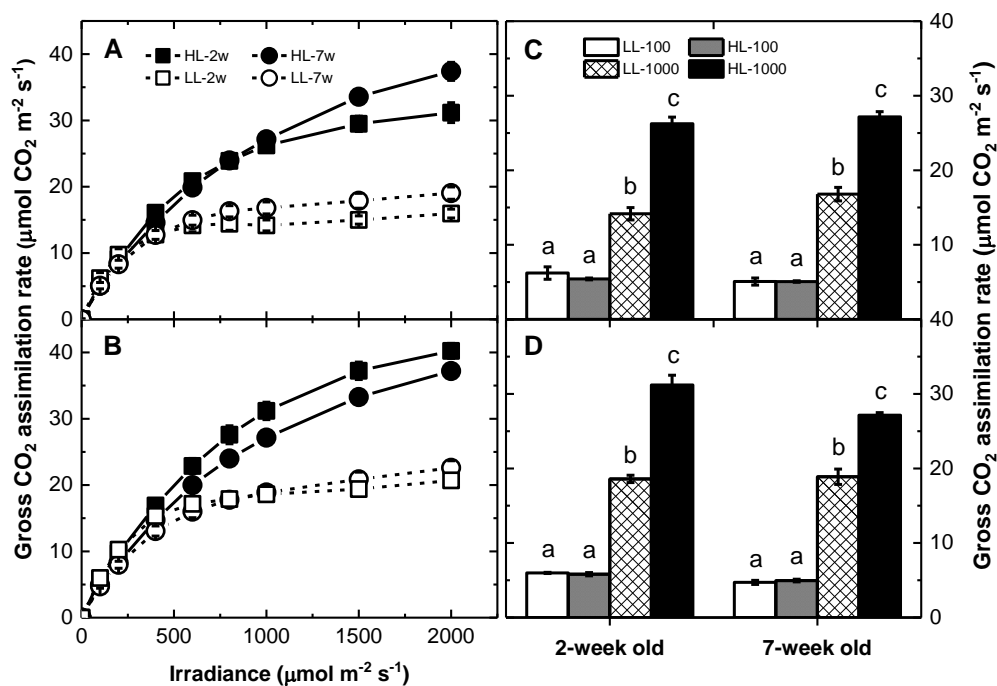
Figure 1. Light response curves of gross CO_2 assimilation of (A) *Setaria viridis* and (B) *Zea mays* grown under different irradiances. High light (HL) at 1,000 µmol m^{-2} s^{-1} and low light (LL) at 100 µmol m^{-2} s^{-1}. Photosynthetic measurement was done on the middle portion of the youngest fully expanded leaf of plants at 2 weeks (2w) and 7 weeks after germination (7w) plants. Gross CO_2 assimilation rates of *S. viridis* and *Z. mays* measured at growth irradiances are plotted in (C) and (D), respectively. Each symbol or bar represents the mean ± SE, *n*=3. Letters indicate the ranking (lowest=a) using multiple-comparison Tukey's post-hoc test. Bars with same letter are not statistically different at *p* < .05. Mean dark respiration rates and corresponding statistical analysis were provided in Figure S3 and Table 1, respectively.

Table 1. Summary of statistical analysis using two-way ANOVA to test for the effects of growth irradiance and plant age to various response parameters.

Parameter	*S. viridis*			*Z. mays*		
	Irradiance	Age	Irradiance x Age	Irradiance	Age	Irradiance x Age
A_{gross} (µmol CO_2 m^{-2} s^{-1})	***	ns	ns	***	**	*
R_d (µmol CO_2 m^{-2} s^{-1})	**	*	ns	***	**	ns
LMA (g m^{-2})	***	**	ns	***	***	***
Total leaf N (mmol m^{-2})	***	ns	ns	***	***	**
Chl a+b (µmol m^{-2})	**	**	ns	*	*	ns
Chl a/b	***	*	ns	***	ns	***
BS chloroplast content (%)	ns	***	*	*	ns	ns
BS chloroplast size (µm^2)	ns	ns	***	***	**	***
M chloroplast size (µm^2)	ns	***	ns	***	ns	ns
BS grana width (µm)	ns	ns	**	ns	*	ns
M grana width (µm)	**	***	***	*	***	ns
BS starch granule per chloroplast	***	***	***	***	ns	ns
M starch granule per chloroplast	***	***	***	*	*	*
BS starch granule size (µm^2)	***	***	***	***	ns	***
M starch granule size (µm^2)	***	***	***	***	***	***
Vein circumference (µm)	***	ns	***	***	ns	***
Interveinal distance (µm)	***	ns	***	***	***	*
Leaf thickness (µm)	***	*	***	***	ns	***
BS cell wall thickness (µm)	***	ns	ns	***	***	***
M cell wall thickness (µm)	***	**	ns	***	**	ns
S_b (m^2 m^{-2})	***	***	**	ns	**	ns
M-BS PD area per unit leaf area (m^2 m^{-2})	***	***	***	***	***	***
M-BS pit field area (µm^2)	**	ns	**	**	**	ns
M-M pit field area (µm^2)	ns	ns	ns	*	ns	***
M-BS PD area (µm^2)	ns	***	***	**	***	***
M-M PD area (µm^2)	ns	***	*	***	*	***
M-BS PD per unit pit field area (PD µm^{-2})	***	***	***	***	ns	***
M-M PD per unit pit field area (PD µm^{-2})	***	***	***	***	***	***
M-BS pit field area per cell interface area (%)	***	***	***	***	**	***
M-M pit field area per cell interface area (%)	***	***	***	ns	***	***
M-BS PD per unit cell interface area (PD µm^{-2})	***	***	***	***	ns	***
M-M PD per unit cell interface area (PD µm^{-2})	***	***	***	***	***	***

Abbreviations: A_{gross}, gross CO_2 assimilation rate; BS, bundle sheath; Chl, chlorophyll; LMA, leaf mass per area; M, mesophyll; ns, not significant ($p > .05$); PD, plasmodesmata; R_d, dark respiration rate; S_b, bundle sheath surface area per unit leaf area.
*$p < .05$.
**$p < .01$.
***$p < .001$.
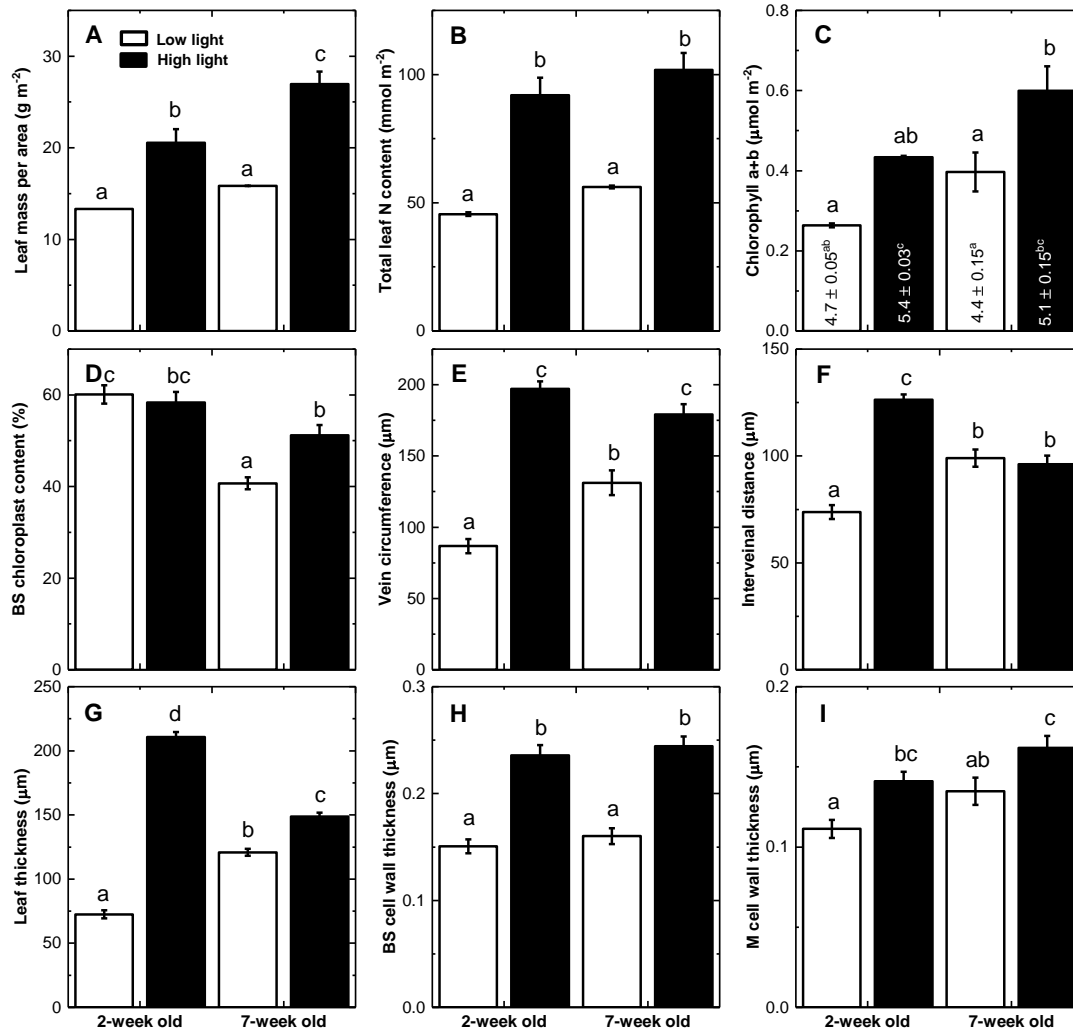
Figure 2. Leaf properties of *Setaria viridis* grown under different irradiances. Low light at 100 µmol m^{-2} s^{-1} and high light at 1,000 µmol m^{-2} s^{-1}. Embedded values on (C) correspond to chlorophyll a/b ratio. All measurements were done using the middle portion of the youngest fully expanded leaf harvested immediately after gas exchange measurement. Letters indicate the ranking (lowest=a) using multiple-comparison Tukey's post-hoc test. Bars with same letter are not statistically different at $p < .05$. N, nitrogen; BS, bundle sheath; M, mesophyll.
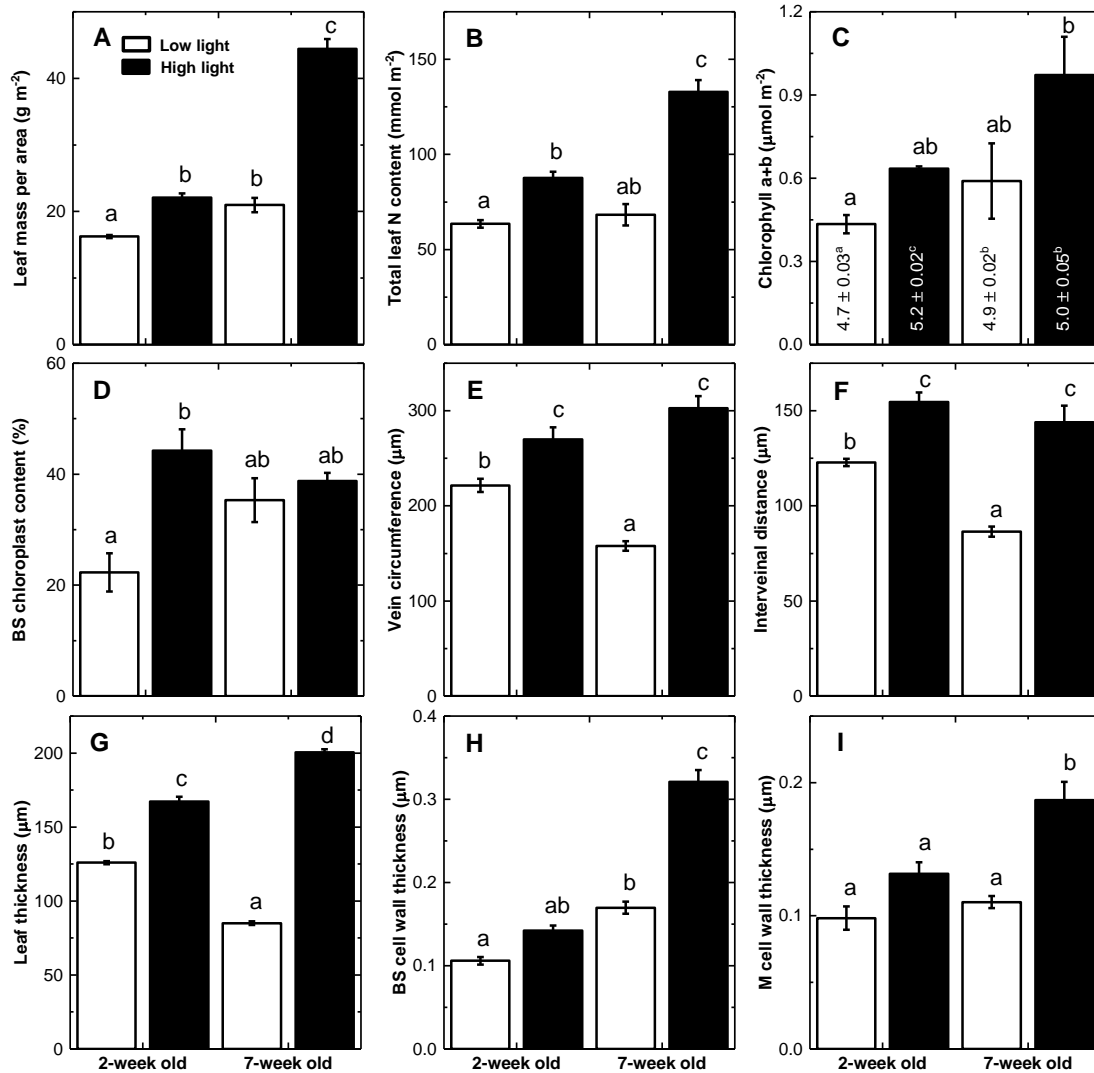
Figure 3. Leaf properties of *Zea mays* grown under different irradiances. Details and statistics are as described in Figure 2.

Leaf anatomy

There was a significant plant age and growth irradiance x plant age effect on BS chloroplast content and chloroplast size in *S. viridis* (Figure 2D; Tables 1, 2). Specifically, 7-week-old *S. viridis* grown under low light had lower BS chloroplast content (Figure 2D) but bigger chloroplasts (Table 2) compared with the high light-grown plants. In *Z. mays*, growth irradiance had a significant effect on both BS chloroplast content and chloroplast size (Table 1) where low light-grown plants have lower BS chloroplast content (Figure 3D; Table 1) and smaller chloroplasts (Tables 1 and 3) than the high light-grown plants. For both species, smaller leaf veins (Figures

2E and 3E; Table 1), shorter interveinal distance (Figures 2F and 3F; Table 1), and thinner leaves (Figures 2G, 4A-D, 3G, 5A-D; Table 1) were observed in plants grown under low light indicative of reduced investment in photosynthetic machinery per unit leaf area, which is also seen in the strong correlation between photosynthetic rate and leaf N content (Figure S1). Transmission electron micrographs also revealed thinner cell walls in both BS (Figures 2H and 3H; Table 1) and M (Figures 2I and 3I; Table 1) cells in low light plants. There were also more and larger starch granules in both the M and BS chloroplasts in leaves of low light plants compared with the high light plants (Figures 4E-L and 5E-L; Tables 1, 2, and 3). Grana width was significantly wider in BS chloroplasts of 2-week-old high light *S. viridis* and M chloroplast of 7-week-old low light *S. viridis*, whereas there was no significant difference observed in grana development between low light and high light-grown *Z. mays* (Figures 4I-L and 5I-L; Tables 1, 2, and 3).

Table 2. Chloroplast properties of *Setaria viridis* grown under low (100 μmol m^{-2} s^{-1}) and high (1,000 μmol m^{-2} s^{-1}) irradiances.

| Parameter | *Setaria viridis* | | | |
| | 2-week old | | 7-week old | |
	Low	High	Low	High
BS chloroplast size (μm^2), *n*=39	19.6 ± 1.07^{ab}	25.6 ± 1.76^c	22.8 ± 1.52^{bc}	16.5 ± 1.73^a
M chloroplast size (μm^2), *n*=12	21.2 ± 1.93^{ab}	25.2 ± 2.46^b	16.6 ± 1.71^a	15.9 ± 1.33^a
BS grana width (μm), *n*=47	0.09 ± 0.007^a	0.12 ± 0.004^b	0.11 ± 0.009^{ab}	0.10 ± 0.004^b
M grana width (μm), *n*=120	0.32 ± 0.012^a	0.33 ± 0.014^a	0.45 ± 0.024^b	0.35 ± 0.015^a
BS starch granule per chloroplast, *n*=39	15 ± 1.1^b	6 ± 0.4^a	5 ± 0.5^a	4 ± 0.4^a
M starch granule per chloroplast, *n*=12	8 ± 0.9^b	1 ± 0.4^a	2 ± 0.5^a	0 ± 0.0^a
BS starch granule size (μm^2), *n*=125	0.27 ± 0.007^c	0.08 ± 0.003^a	0.15 ± 0.006^b	0.06 ± 0.003^a
M starch granule size (μm^2), *n*=25	0.33 ± 0.021^b	0.07 ± 0.005^a	0.05 ± 0.007^a	na

Note. Values are shown as mean ± SE. The number of corresponding structures measured is indicated by n. Letters indicate the ranking (lowest=a) of plants within each single row using multiple-comparison Tukey's post-hoc test. Values followed by the same superscript letter are not significantly different at the 5% level.
Abbreviations: BS, bundle sheath; M, mesophyll; na, not applicable.

Table 3. Chloroplast properties of *Zea mays* grown under low (100 µmol m^{-2} s^{-1}) and high (1,000 µmol m^{-2} s^{-1}) irradiances.

Parameter	*Zea mays*			
	2-week old		7-week old	
	Low	High	Low	High
BS chloroplast size (µm^2), *n*=56	8.9 ± 0.44[a]	12.5 ± 0.78[b]	8.3 ± 0.39[a]	17.4 ± 0.91[c]
M chloroplast size (µm^2), *n*=30	10.8 ± 1.13[a]	16.3 ± 1.13[b]	11.4 ± 0.82[ac]	15.2 ± 0.99[bc]
BS grana width (µm), *n*=28	0.07 ± 0.003[a]	0.07 ± 0.003[a]	0.08 ± 0.006[a]	0.08 ± 0.005[a]
M grana width (µm), *n*=130	0.43 ± 0.014[a]	0.49 ± 0.019[ab]	0.54 ± 0.035[bc]	0.58 ± 0.026[c]
BS starch granule per chloroplast, *n*=56	4 ± 0.5[a]	1 ± 0.3[b]	4 ± 0.4[a]	0 ± 0.0[b]
M starch granule per chloroplast, *n*=30	0 ± 0.0[a]	0 ± 0.0[a]	1 ± 0.4[b]	0 ± 0.0[a]
BS starch granule size (µm^2), *n*=107	0.12 ± 0.005[a]	0.07 ± 0.012[a]	0.15 ± 0.005[b]	na
M starch granule size (µm^2), *n*=34	na	na	0.09 ± 0.008[b]	na

Note. Values are shown as mean ± SE. The number of corresponding structures measured is indicated by n. Letters indicate the ranking (lowest=a) of plants within each single row using multiple-comparison Tukey's post-hoc test. Values followed by the same superscript letter are not significantly different at the 5% level.
Abbreviations: BS, bundle sheath; M, mesophyll; na, not applicable.

Plasmodesmata connections between mesophyll and bundle sheath

Overall, there was significant growth irradiance, plant age, and interaction effect on M-BS PD parameters in both *S. viridis* and *Z. mays* (Table 1). M-BS PD area per unit leaf area in *S. viridis* leaves was four-fold greater in high light plants compared to low light plants in 7-week-old plants, whereas in younger plants, low light plants had greater M-BS PD area per unit leaf area (Figure 6A; Table 1). In addition to lower BS surface area per unit leaf area (S$_b$; Figure 6B), the reduction in M-BS PD area per unit leaf area in 7-week-old low light-grown *S. viridis* resulted from smaller pit fields (Figures 4M-P and 6C) populated by smaller PD (Figure 6E), lower pit field area per unit cell interface area (Figures 4Q-T and 6I) and lower number of PD per unit cell interface area (Figure 6K). Meanwhile, bigger PD (Figure 6E), greater pit field area per unit cell interface area (Figure 6I) and more PD per unit cell interface area (Figure 6K) resulted in a greater M-BS PD area per unit leaf area in 2-week-old low light *S. viridis* compared with the high light-grown counterpart.
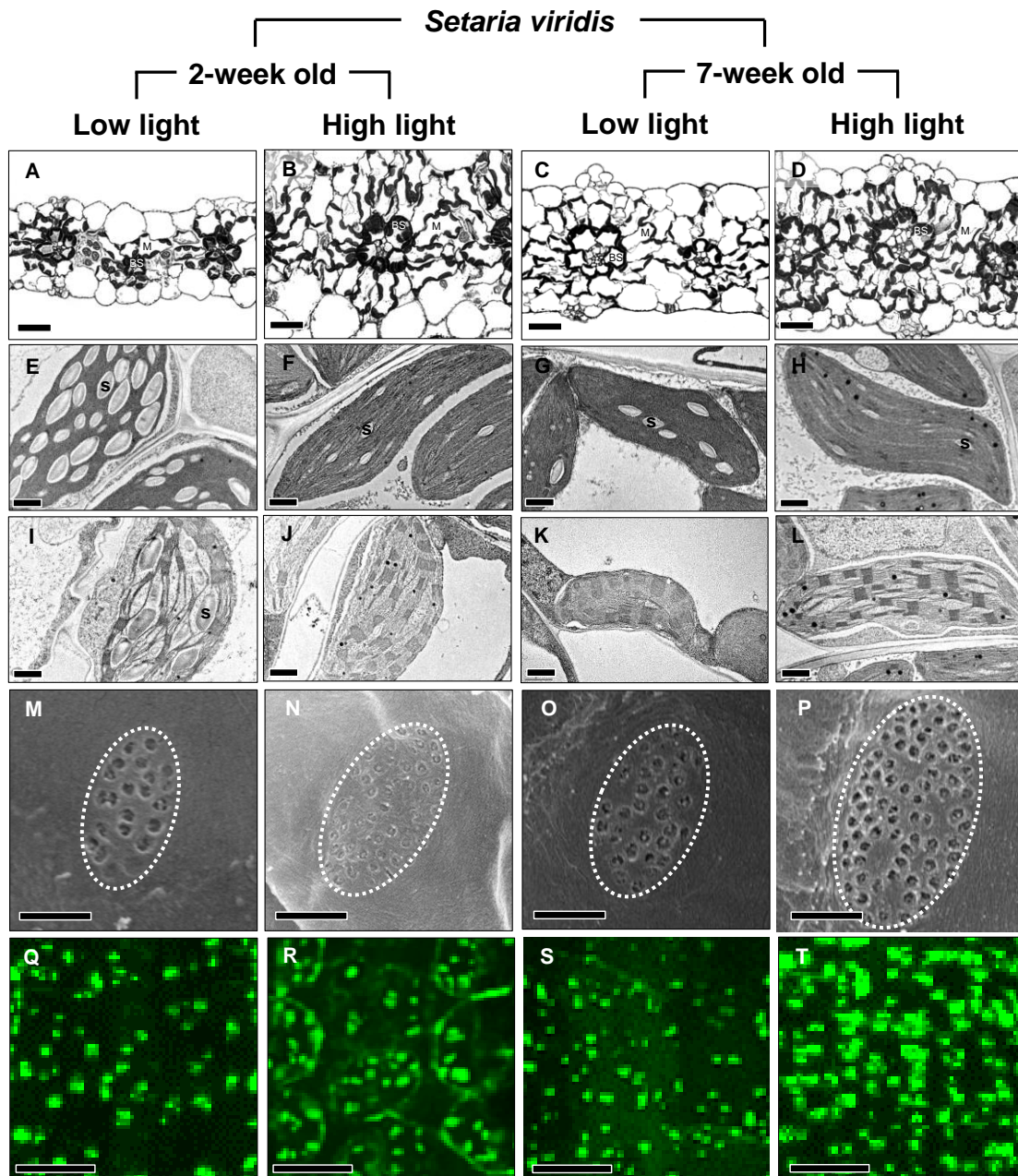
Figure 4. Leaf micrographs of *Setaria viridis* grown under different irradiances. Low light at 100 µmol m^{-2} s^{-1} and high light at 1,000 µmol m^{-2} s^{-1}. Light micrographs (A-D) were generated using the middle portion of the youngest fully expanded leaf harvested immediately after gas exchange measurement. Corresponding transmission electron micrographs of bundle sheath (BS) chloroplasts (E-H) and mesophyll (M) chloroplasts (I-L) were obtained. Pit field size (white outline in scanning electron micrographs; M-P) and pit field (green fluorescence in confocal micrographs) distribution (Q-T) between M and BS were also shown. s, starch grain. Light micrograph bars = 25 µm. Transmission electron micrographs bars = 1 µm, confocal micrograph bars = 10 µm, scanning electron micrographs bars = 0.5 µm.
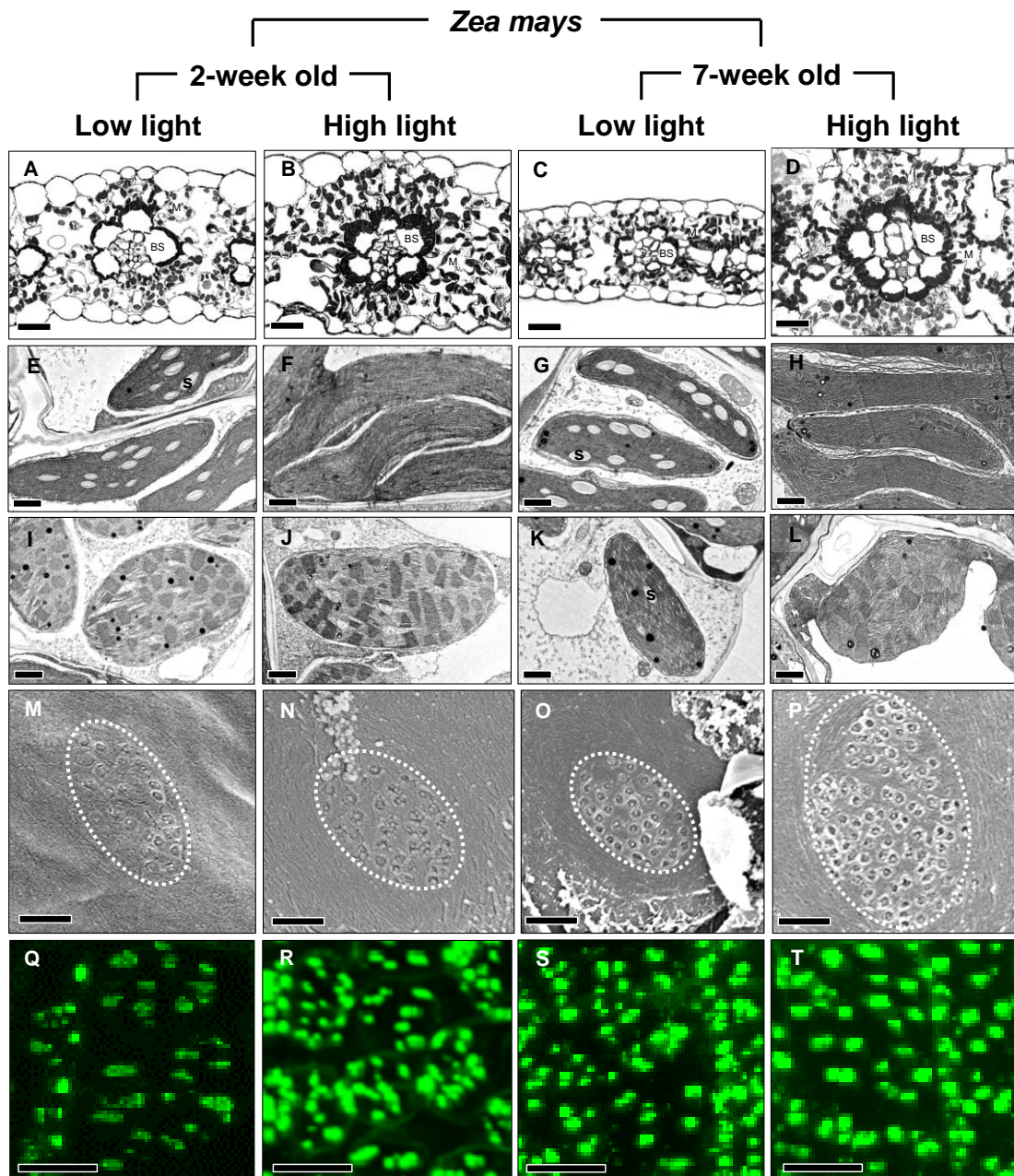
Figure 5. Leaf micrographs of *Zea mays* grown under different irradiances. Details are as described in Figure 4.
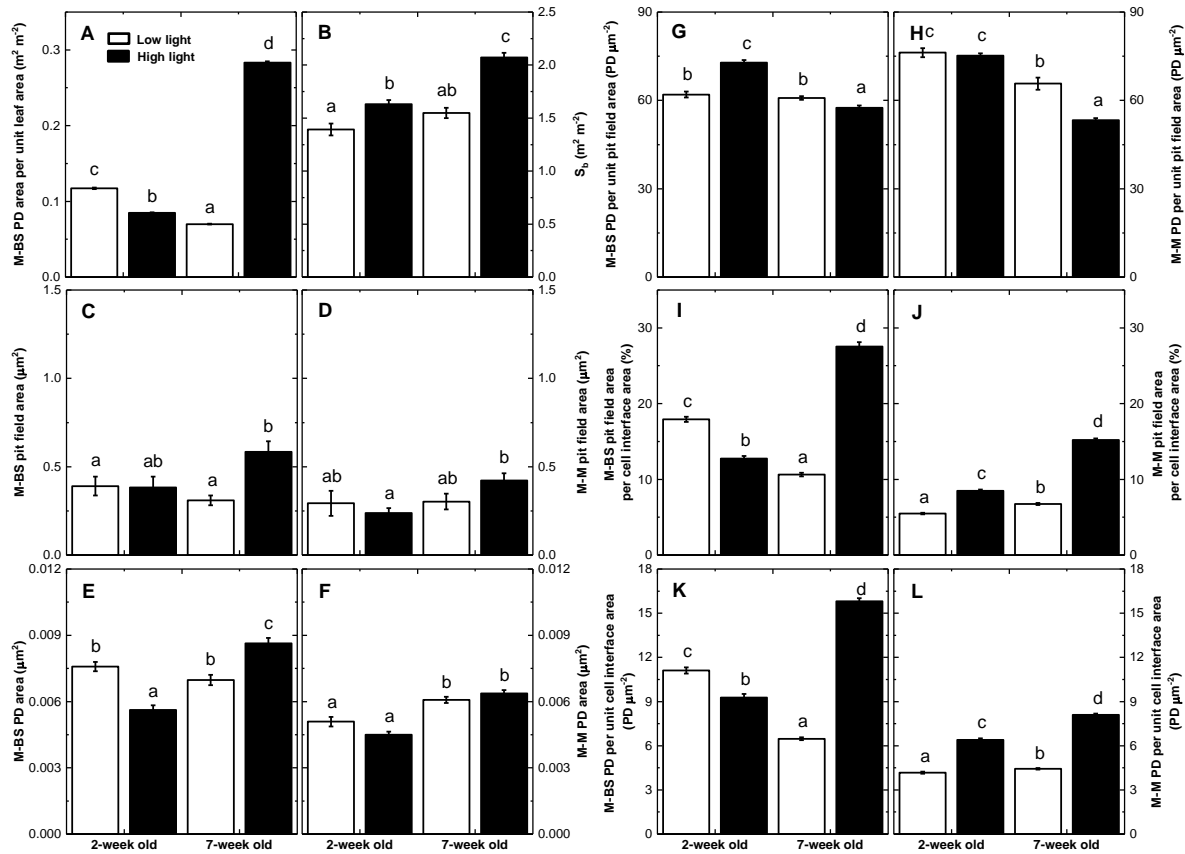
Figure 6. Leaf plasmodesmata properties of *Setaria viridis* grown under different irradiances. Low light at 100 μmol m^{-2} s^{-1} and high light at 1,000 μmol m^{-2} s^{-1}. All measurements were done using the middle portion of the youngest fully expanded leaf harvested immediately after gas exchange measurement. Letters indicate the ranking (lowest=a) using multiple-comparison Tukey's post-hoc test. Bars with same letter are not statistically different at $p < .05$. M, mesophyll; BS, bundle sheath; S_b, bundle sheath surface area per leaf unit area.

In 2-week-old *Z. mays*, high light plants had two-fold greater M-BS PD area per unit leaf area compared to the low light plants, whereas in older plants, this gap was greatly reduced (Figure 7A; Table 1). The smaller M-BS PD area per unit leaf area discrepancy between low light and high light plants in older *Z. mays* was a result of significantly smaller pit field size (Figure 7C) and PD area (Figure 7E) but greater pit field area per unit cell interface area (Figure 7I) and PD per unit cell interface area (Figure 7K) in low light plants. Meanwhile, lower PD connections between M and BS in leaves of 2-week-old low light-grown *Z. mays* was a result of having fewer PD per unit pit field area (Figures 5M-P and 7G) and fewer pit fields (Figures 5Q-T and 7I).
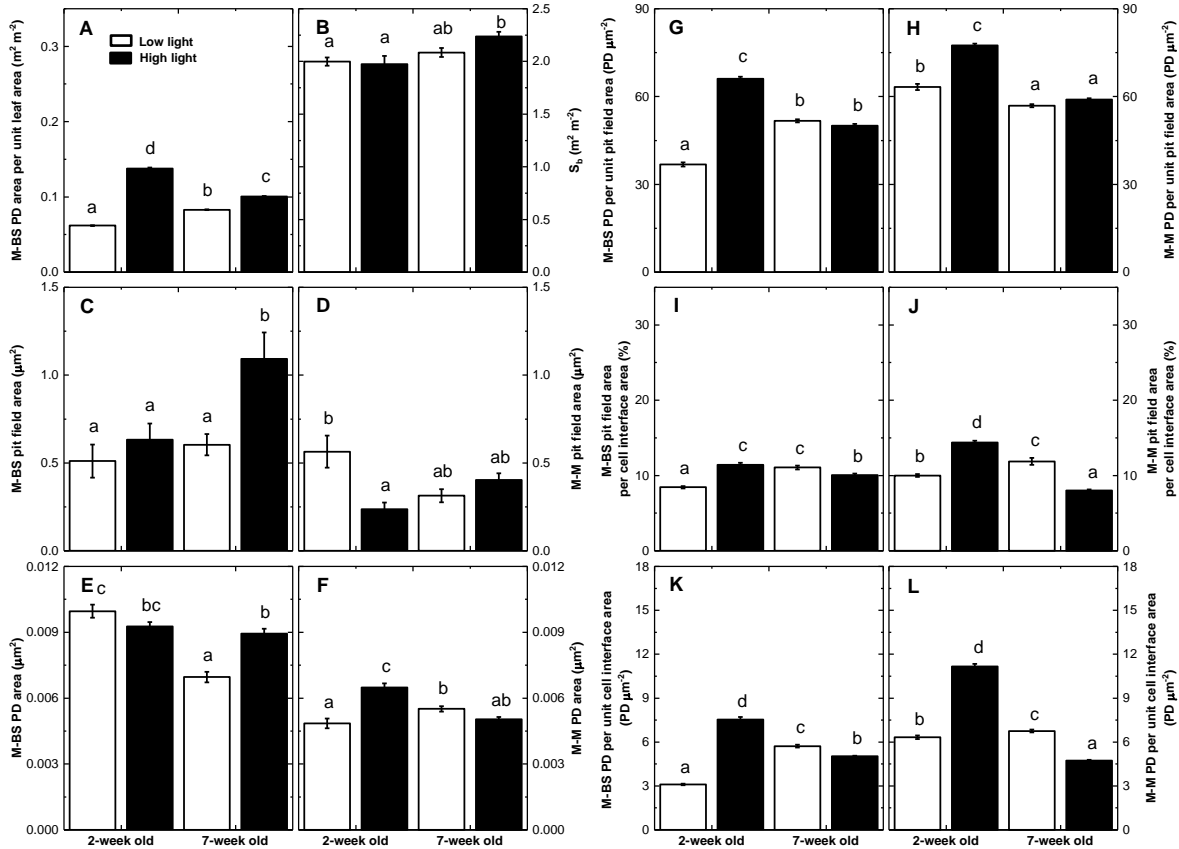
Figure 7. Leaf plasmodesmata properties of *Zea mays* grown under different irradiances. Details and statistics are as described in Figure 6.

Plasmodesmata connections between mesophyll

Except for *S. viridis* M-M pit field area, there was significant growth irradiance, plant age, and interaction effect in all M-M PD parameters in both *S. viridis* and *Z. mays* (Table 1). In *S. viridis*, greater pit field area per unit cell interface area (Figure 6J; Table 1) resulted to two-fold greater PD per unit cell interface area in high light plants compared to low light plants (Figure 6L; Table 1). Meanwhile, in 2-week-old *Z. mays*, two-fold greater PD per unit cell interface area (Figure 7L; Table 1) resulted from having bigger PD (Figure 7F), more PD per unit pit field area (Figure 7H), and greater pit field area per unit cell interface area (Figure 7J) in high light plants compared to low light plants. In older *Z. mays*, greater pit field area per unit cell interface area (Figure 7J) resulted to greater PD per unit cell interface area in low light plants compared to high light plants (Figure 7L; Table 1).

Discussion

The effect of growth irradiance on C$_4$ leaf PD density depends on plant age and species

Despite the suggestion that C$_4$ plants are less plastic than C$_3$ plants due to their complex biochemical and anatomical attributes (Kromdijk et al., 2008; Pignon et al., 2017; Sage and McKown, 2006), there have been numerous reports on C$_4$ species being capable of acclimatory response and/or plasticity to growth irradiance (Pengelly et al., 2010; Sonawane et al., 2018; Tazoe et al., 2008). Similarly, our results showed that when NADP-ME species, *S. viridis* and *Z. mays* were grown under different irradiances, there was a species-specific difference and an overall significant plant age effect in leaf PD density.

For a given plant developmental stage where the difference in M-BS PD area per unit leaf area between low light-grown and high light-grown plants is at least two-fold (as in 7-week-old *S. viridis* and in 2-week-old *Z. mays*), there is also an observed significant difference in BS chloroplasts content. This finding supports a previous report (Wang et al., 2017) which suggested that chloroplast development and function are strongly coordinated with PD function and formation in bundle sheath cells (Brunkard et al., 2013). We also found that the overall lower M-BS PD area per unit leaf area in low light-grown plants was largely attributed to impaired pit field formation manifested by lower pit field coverage, smaller pit fields, and smaller PD. It is believed that the primary PD formed during cytokinesis are pit field initials (Giannoutsou et al., 2013) and that pit fields are formed as a result of primary PD modification and/or secondary PD formation that happens later in development (Ehlers and Kollmann, 2001; Faulkner et al., 2008). Addition of PD during primary PD modification and/or secondary PD formation would entail resource and energy costs, which plants with more source leaves grown under nonlimiting light could energetically accommodate (Figure S2). On that same note, having thin cell walls might also be an advantage for PD development. However, in this study this is not supported as low light-grown plants, which had thinner M and BS cell walls also had fewer PD.

88

Although it is not possible to make firm conclusions from only two species, it is tempting to speculate that the species-specific and plant age-dependent response of PD formation of these two C_4 species to low light is associated with their C_4 lineage. *S. viridis* is a member of the subtribe Cenchrinae of the MPC C_4 lineage. whereas *Z. mays* is from the subtribe and C_4 lineage, Andropogoneae (GPWGII, 2012). This hypothesis agrees with the subtype-dependent and species-specific responses observed in other growth irradiance studies performed in C_4 plants. For instance, a previous comparison between *Z. mays* and another NADP-ME C_4 grass, *Paspalum conjugatum* showed two different responses to growth irradiance in terms of chlorophyll and rubisco content, mainly attributed to their different habitats (Ward and Woolhouse, 1986) but this could also be due to C_4 lineage differences (GPWGII, 2012). Similarly, C_4 dicots belonging to different subtypes, *Amaranthus cruentus* (NAD-ME; Tazoe et al., 2006) and *Flaveria bidentis* (NADP-ME; Pengelly et al., 2010), showed contrasting responses to growth irradiance in terms of chlorophyll content. It would be very interesting to see if members of the same subtribe and/or C_4 lineage have similar patterns of leaf phenotypic response to growth irradiance.

There is not a tight link between PD density and photosynthetic capacity

In this study, plant age had no effect on photosynthetic rates of the youngest fully expanded leaves but there was an obvious difference in PD density between these developmental stages. This observation, and the lack of correspondence between PD density and photosynthetic flux under different growth irradiances, is summarised in Figure 8. Here, the response of photosynthetic flux to incident light intensity is calculated per M-BS interface PD at the two developmental stages and at the two growth irradiances. If PD frequency was "adjusting" to photosynthetic flux, or indeed limiting it, one might expect these light response curves to all be similar on a flux per PD basis regardless of age or treatment. This is clearly not the case. One must assume that these leaves are capable of maintaining M-BS fluxes of C_4 acids and C_3 products by tolerating considerable variation in diffusion gradients across this interface and hence tolerate widely different levels of metabolites in the two compartments (Hatch and Osmond, 1976). Although it is difficult to directly measure metabolite gradients in C_4 leaves, whole leaf metabolite measurements and recent work using nonaqueous fractionation and stable isotope labelling (Arrivault et al.,

2017; Leegood and von Caemmerer, 1988) support this hypothesis. This is also true when comparing C_4 species where PD densities between M and BS cells vary between 5 and 12 PD μm^{-2} cell interface (Danila et al., 2018) despite these species all having similar photosynthetic rates (Pinto et al., 2014).
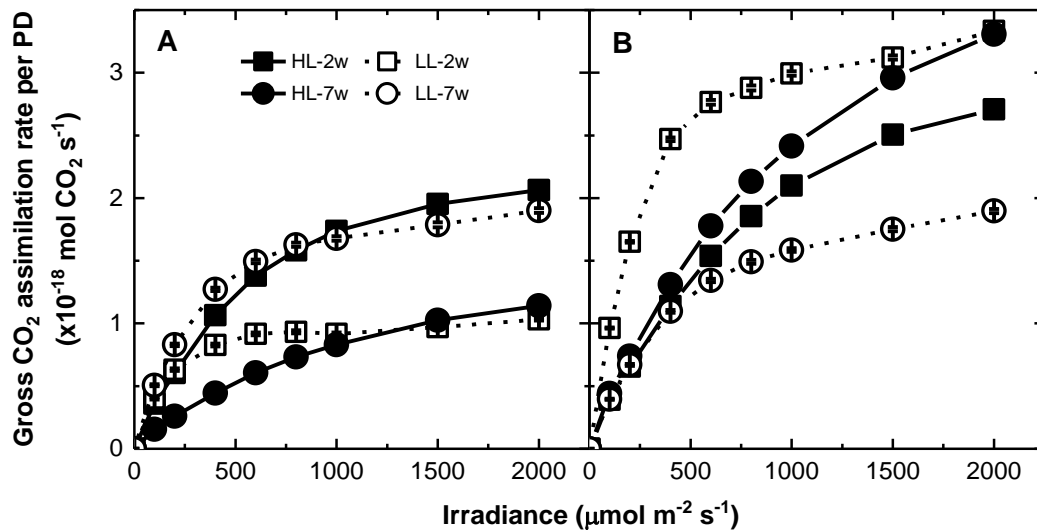
Figure 8. Light response curves of plasmodesmata (PD) flux between mesophyll and bundle sheath cells of *Setaria viridis* (A) and *Zea mays* (B) grown under different irradiances. Calculations as previously described in Danila et al. (2016). Gross CO_2 assimilation rate per PD assumes that in C_4 species the minimum flux of C_4 acids through the PD needs to be equal to or greater than the gross CO_2 assimilation rate (Henderson et al., 1992). See Figure 1 for details.

Light affects starch formation but not grana development in C_4 BS chloroplasts

In C_3 species, increased grana development is often observed in plants grown under low light to maximise light capture under limiting environment (Björkman, 1981). However, in this study, there was no overall enhancement in grana formation observed in M or BS chloroplasts of low light plants. This could be because of the complexity of the energy requirements of metabolism across the two cell types. It has been proposed that plasticity in decarboxylation mechanism, the form of the C_4 acid transported to the BS and the shuttling of 3-PGA from the BS to the M chloroplasts for reduction might all be ways in which energy balance could be maintained under low irradiance in C_4 leaves (Furbank, 2011; Sharwood et al., 2014;

90

von Caemmerer and Furbank, 2016). Previous studies had also shown that when NADP-ME type C_4 plants were grown under low light, the activity and protein expression of both the decarboxylating enzyme NADP-ME (Sharwood et al., 2014; Sonawane et al., 2018) and rubisco (Sharwood et al., 2014) were proportionally reduced.

Meanwhile, accumulation of more and larger starch grains in the chloroplasts of low light *S. viridis* and *Z. mays* leaves were somewhat surprising as growth at low irradiance in most plants results in a reduction in starch levels (Zeeman et al., 2004). Our study, however, was not the first to show this as similar observations were also reported in low light-grown *Z. mays* and *Digitaria sanguinalis* from an independent study (Sowiński et al., 2007). Interestingly, these results were only observed in NADP-ME species but not in species belonging to NAD-ME or PCK subtypes (Sowiński et al., 2007). It is possible that the specialised metabolism of the NADP-ME type C_4 grasses plays a role in the availability of energy to fuel carbohydrate export from the BS or perhaps there are other unique biochemical features in the starch synthesis and degradation pathways in plants of this decarboxylation type (Ma et al., 2009; Russin et al., 1996; Slewinski et al., 2009).

Concluding Comments

The observation that PD density at the M-BS cell interface is greatly enhanced in C_4 leaves compared to C_3 leaves (Danila et al., 2016; Danila et al., 2018) to support C_4 photosynthetic metabolite flux would imply some functional relationship between PD density and photosynthetic capacity. Although the data presented here indicate that there was some plasticity in PD density of C_4 leaves in response to growth irradiance, there was no clear correlation found between either photosynthetic capacity or photosynthetic flux and PD density at the M-BS cell interface. These results suggest a complex mechanism underlying the dynamic response of C_4 leaf PD formation to growth irradiance.

Acknowledgements

References

Arrivault, S., Obata, T., Szecówka, M., Mengin, V., Guenther, M., Hoehne, M., Fernie, A.R., Stitt, M., 2017. Metabolite pools and carbon flow during C_4 photosynthesis in maize: $^{13}CO_2$ labeling kinetics and cell type fractionation. *Journal of Experimental Botany* 68, 283-298.

Björkman, O., 1981. Responses to different quantum flux densities, in: Lange, O.L., Nobel, P.S., Osmond, C.B., Ziegler, H. (Eds.), *Physiological Plant Ecology I: Responses to the Physical Environment.* Springer Berlin Heidelberg, Berlin, Heidelberg, pp. 57-107.

Botha, C.E.J., 1992. Plasmodesmatal distribution, structure and frequency in relation to assimilation in C_3 and C_4 grasses in Southern Africa. *Planta* 187, 348-358.

Botha, C.E.J., Evert, R.F., 1988. Plasmodesmatal distribution and frequency in vascular bundles and contiguous tissues of the leaf of *Themeda triandra*. Planta 173, 433-441.

Brunkard, J.O., Runkel, A.M., Zambryski, P.C., 2013. Plasmodesmata dynamics are coordinated by intracellular signaling pathways. *Current Opinion in Plant Biology* 16, 10.1016/j.pbi.2013.1007.1007.

Brutnell, T.P., Wang, L., Swartwood, K., Goldschmidt, A., Jackson, D., Zhu, X.-G., Kellogg, E., Van Eck, J., 2010. *Setaria viridis*: a model for C_4 photosynthesis. *The Plant Cell* 22, 2537-2544.

Danila, F.R., Quick, W.P., White, R.G., Furbank, R.T., von Caemmerer, S., 2016. The metabolite pathway between bundle sheath and mesophyll: quantification of plasmodesmata in leaves of C_3 and C_4 monocots. *The Plant Cell* 28, 1461-1471.

Danila, F.R., Quick, W.P., White, R.G., Kelly, S., von Caemmerer, S., Furbank, R.T., 2018. Multiple mechanisms for enhanced plasmodesmata density in disparate subtypes of C_4 grasses. *Journal of Experimental Botany* 69, 1135-1145.

Ehlers, K., Kollmann, R., 2001. Primary and secondary plasmodesmata: structure, origin, and functioning. *Protoplasma* 216, 1-30.

Faulkner, C., Akman, O.E., Bell, K., Jeffree, C., Oparka, K., 2008. Peeking into pit fields: a multiple twinning model of secondary plasmodesmata formation in tobacco. *The Plant Cell* 20, 1504-1518.

Furbank, R., Jenkins, C., Hatch, M., 1990. C_4 photosynthesis: quantum requirement, C_4 acid overcycling and *Q*-cycle involvement. *Functional Plant Biology* 17, 1-7.

Furbank, R.T., 2011. Evolution of the C_4 photosynthetic mechanism: are there really three C_4 acid decarboxylation types? *Journal of Experimental Botany* 62, 3103-3108.

Giannoutsou, E., Sotiriou, P., Apostolakos, P., Galatis, B., 2013. Early local differentiation of the cell wall matrix defines the contact sites in lobed mesophyll cells of *Zea mays*. *Annals of Botany* 112, 1067-1081.

GPWGII, 2012. New grass phylogeny resolves deep evolutionary relationships and discovers C_4 origins. *New Phytologist* 193, 304-312.

Gunning, B.E.S., 1978. Age-related and origin-related control of the numbers of plasmodesmata in cell walls of developing *Azolla* roots. *Planta* 143, 181-190.

Hatch, M.D., 1987. C_4 photosynthesis: a unique blend of modified biochemistry, anatomy and ultrastructure. *Biochimica et Biophysica Acta (BBA) - Reviews on Bioenergetics* 895, 81-106.

Hatch, M.D., Osmond, C.B., 1976. Compartmentation and transport in C_4 photosynthesis, in: Stocking, C.R., Heber, U. (Eds.), *Transport in Plants III*. Springer Berlin Heidelberg, pp. 144-184.

Henderson, S., Caemmerer, S., Farquhar, G., 1992. Short-term measurements of carbon isotope discrimination in several C_4 species. *Functional Plant Biology* 19, 263-285.

Kromdijk, J., Schepers, H.E., Albanito, F., Fitton, N., Carroll, F., Jones, M.B., Finnan, J., Lanigan, G.J., Griffiths, H., 2008. Bundle sheath leakiness and light limitation during C_4 leaf and canopy CO_2 uptake. *Plant Physiology* 148, 2144-2155.

Leegood, R.C., von Caemmerer, S., 1988. The relationship between contents of photosynthetic metabolites and the rate of photosynthetic carbon assimilation in leaves of *Amaranthus edulis* L. *Planta* 174, 253-262.

Li, P., Brutnell, T.P., 2011. *Setaria viridis* and *Setaria italica*, model genetic systems for the Panicoid grasses. *Journal of Experimental Botany* 62, 3031-3037.

Lu, K.J., Danila, F.R., Cho, Y., Faulkner, C., 2018. Peeking at a plant through the holes in the wall – exploring the roles of plasmodesmata. *New Phytologist* 218, 1310-1314.

Ma, Y., Slewinski, T.L., Baker, R.F., Braun, D.M., 2009. Tie-dyed 1 encodes a novel, phloem-expressed transmembrane protein that functions in carbohydrate partitioning. *Plant Physiology* 149, 181-194.

Pengelly, J.J.L., Sirault, X.R.R., Tazoe, Y., Evans, J.R., Furbank, R.T., von Caemmerer, S., 2010. Growth of the C_4 dicot *Flaveria bidentis*: photosynthetic acclimation to low light through shifts in leaf anatomy and biochemistry. *Journal of Experimental Botany* 61, 4109-4122.

Pignon, C.P., Jaiswal, D., McGrath, J.M., Long, S.P., 2017. Loss of photosynthetic efficiency in the shade. An Achilles heel for the dense modern stands of our most productive C_4 crops? *Journal of Experimental Botany* 68, 335-345.

Pinto, H., Sharwood, R.E., Tissue, D.T., Ghannoum, O., 2014. Photosynthesis of C_3, C_3–C_4, and C_4 grasses at glacial CO_2. J*ournal of Experimental Botany* 65, 3669-3681.

Porra, R.J., Thompson, W.A., Kriedemann, P.E., 1989. Determination of accurate extinction coefficients and simultaneous equations for assaying chlorophylls a and b extracted with four different solvents: verification of the concentration of chlorophyll standards by atomic absorption spectroscopy. *Biochimica et Biophysica Acta (BBA) - Bioenergetics* 975, 384-394.

Russin, W.A., Evert, R.F., Vanderveer, P.J., Sharkey, T.D., Briggs, S.P., 1996. Modification of a specific class of plasmodesmata and loss of sucrose export ability in the sucrose export defective 1 maize mutant. *The Plant Cell* 8, 645-658.

Sage, R.F., McKown, A.D., 2006. Is C_4 photosynthesis less phenotypically plastic than C_3 photosynthesis?*. *Journal of Experimental Botany* 57, 303-317.

Sage, R.F., Pearcy, R.W., 2000. The physiological ecology of C_4 photosynthesis, in: Leegood, R.C., Sharkey, T.D., von Caemmerer, S. (Eds.), *Photosynthesis: Physiology and Metabolism*. Springer Netherlands, Dordrecht, pp. 497-532.

Seagull, R.W., 1983. Differences in the frequency and disposition of plasmodesmata resulting from root cell elongation. *Planta* 159, 497-504.

Sharwood, R.E., Sonawane, B.V., Ghannoum, O., 2014. Photosynthetic flexibility in maize exposed to salinity and shade. *Journal of Experimental Botany* 65, 3715-3724.

Slewinski, T.L., Meeley, R., Braun, D.M., 2009. Sucrose transporter 1 functions in phloem loading in maize leaves. *Journal of Experimental Botany* 60, 881-892.

Sonawane, B.V., Sharwood, R.E., Whitney, S., Ghannoum, O., 2018. Shade compromises the photosynthetic efficiency of NADP-ME less than that of PEP-CK and NAD-ME C_4 grasses. *Journal of Experimental Botany* 69, 3053-3068.

Sowiński, P., Bilska, A., Barańska, K., Fronk, J., Kobus, P., 2007. Plasmodesmata density in vascular bundles in leaves of C_4 grasses grown at different light conditions in respect to photosynthesis and photosynthate export efficiency. *Environmental and Experimental Botany* 61, 74-84.

Tangl, E., 1879. ober offene Kommunikation zwischen den Zellen des Endosperms einiger Samen. *Jb Wiss Bot* 12, 170-190.

Tazoe, Y., Hanba, Y.T., Furumoto, T., Noguchi, K., Terashima, I., 2008. Relationships between quantum yield for CO_2 assimilation, activity of key

94

enzymes and CO_2 leakiness in *Amaranthus cruentus*, a C_4 dicot, grown in high or low light. *Plant and Cell Physiology* 49, 19-29.

Tazoe, Y., Noguchi, K., Terashima, I., 2006. Effects of growth light and nitrogen nutrition on the organization of the photosynthetic apparatus in leaves of a C_4 plant, *Amaranthus cruentus*. *Plant, Cell & Environment* 29, 691-700.

von Caemmerer, S., Furbank, R., 2003. The C_4 pathway: an efficient CO_2 pump. *Photosynthesis Research* 77, 191-207.

von Caemmerer, S., Furbank, R.T., 2016. Strategies for improving C_4 photosynthesis. *Current Opinion in Plant Biology* 31, 125-134.

Wang, P., Khoshravesh, R., Karki, S., Tapia, R., Balahadia, C.P., Bandyopadhyay, A., Quick, W.P., Furbank, R.T., Sage, T.L., Langdale, J.A., 2017. Re-creation of a key step in the evolutionary switch from C_3 to C_4 leaf anatomy. *Current Biology* 27, 3278-3287.

Ward, D.A., Woolhouse, H.W., 1986. Comparative effects of light during growth on the photosynthetic properties of NADP-ME type C_4 grasses from open and shaded habitats. I. Gas exchange, leaf anatomy and ultrastructure*. *Plant, Cell & Environment* 9, 261-270.

Zeeman, S.C., Smith, S.M., Smith, A.M., 2004. The breakdown of starch in leaves. *New Phytologist* 163, 247-261.
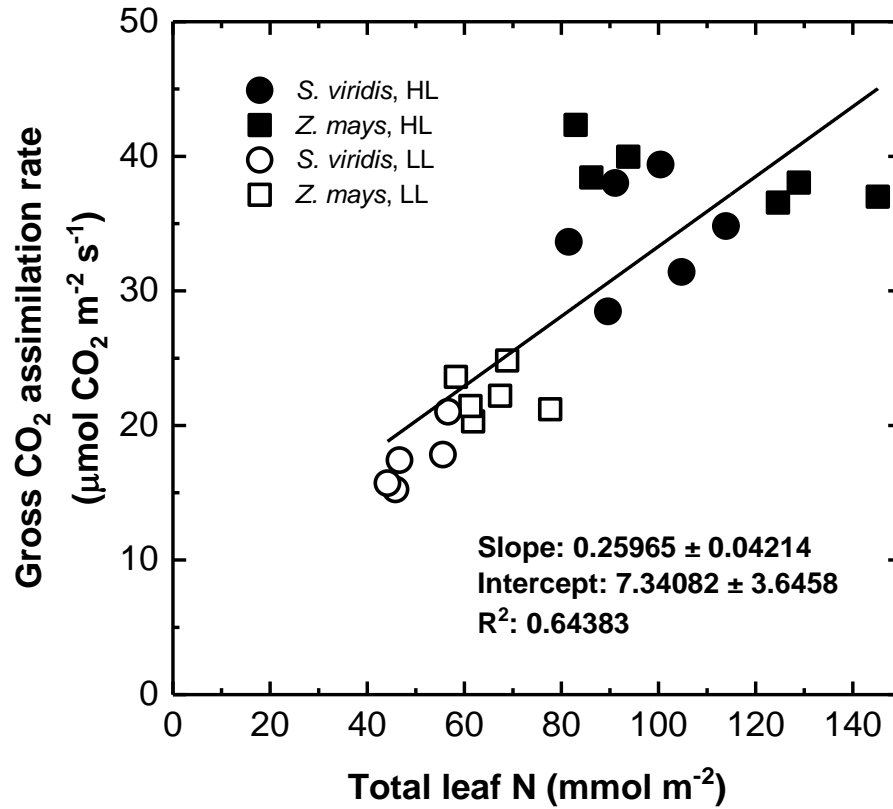
Supplementary Figure 1. Relationship between gross CO_2 assimilation rate and total leaf N content of *Setaria viridis* and *Zea mays* grown under different irradiances. Low light (LL) at 100 µmol m^{-2} s^{-1} and high light (HL) at 1000 µmol m^{-2} s^{-1}.
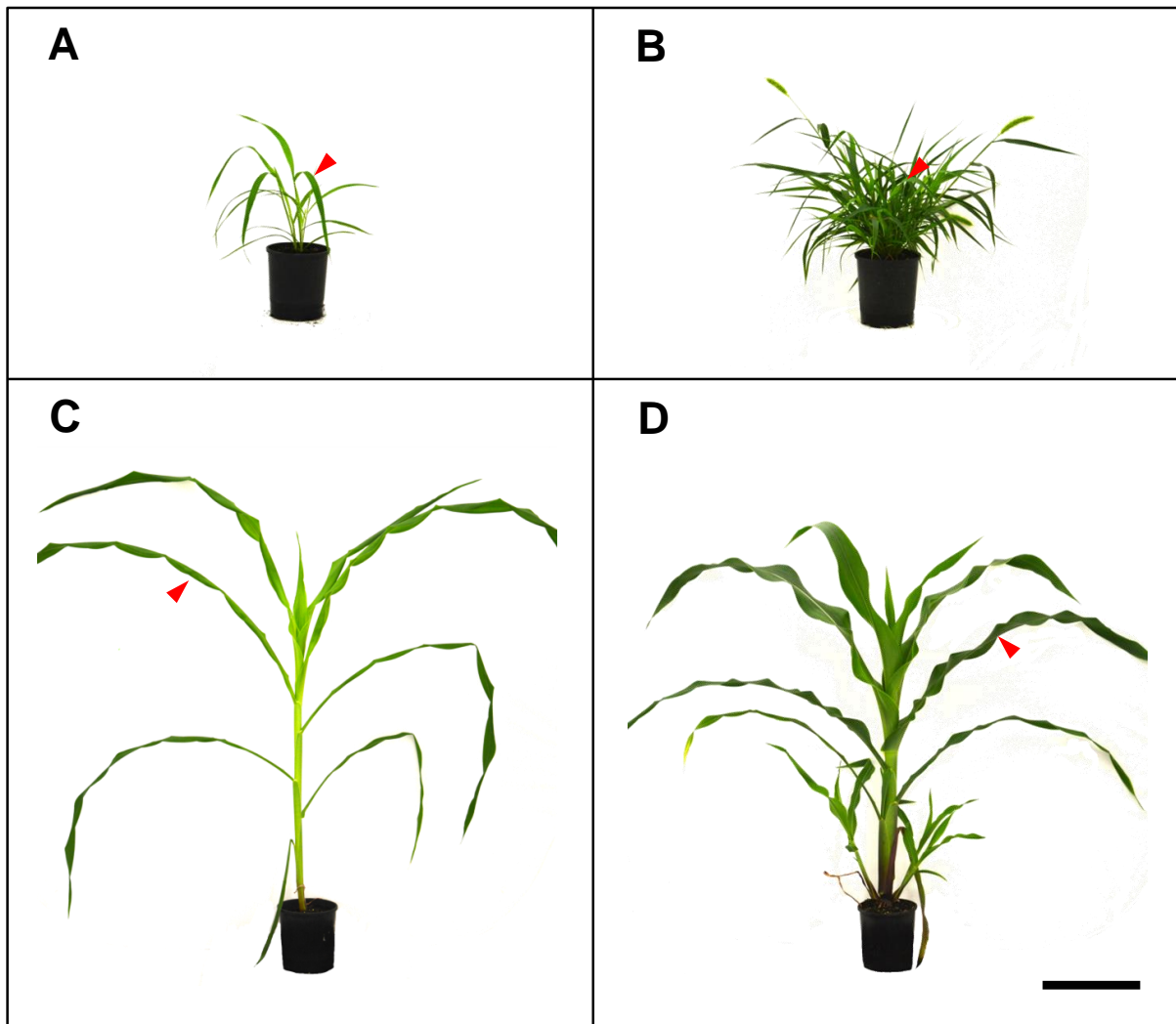
Supplementary Figure 2. Seven week-old *Setaria viridis* and *Zea mays* grown under different irradiances. Low light at 100 µmol m^{-2} s^{-1} and high light at 1000 µmol m^{-2} s^{-1}. (A) Low light-grown *Setaria viridis*, (B) high light-grown *Setaria viridis,* (C) low light-grown *Zea mays*, and (D) high light-grown *Zea mays*. Red arrowhead points to the leaf used for measurements and quantification. Bar = 20 cm.
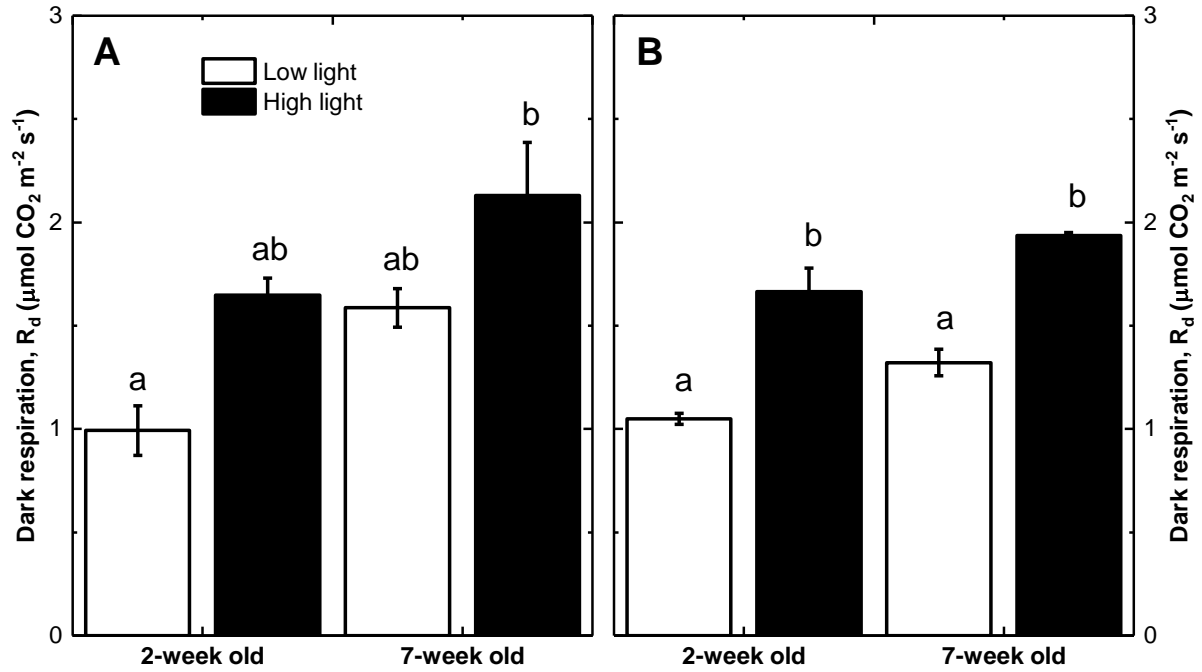
Supplementary Figure 3. Dark respiration rates of *Setaria viridis* (A) and *Zea mays* (B) grown under different irradiances. Each bar represents the mean ± SE, n=3. Letters indicate the ranking (lowest=a) using multiple-comparison Tukey's post-hoc test. Bars with same letter are not statistically different at $p < .05$.

6
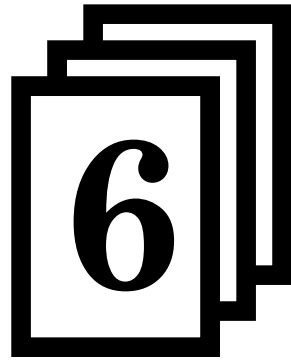
PUBLICATION 5

Diffusion of CO_2 across the mesophyll-bundle sheath cell interface in a C_4 plant with genetically reduced PEP carboxylase activity

Statement of Contribution

This thesis is submitted as a Thesis by Compilation in accordance with https://policies.anu.edu.au/ppl/document/ANUP_003405

I declare that the research presented in this Thesis represents original work that I carried out during my candidature at the Australian National University, except for contributions to multi-author papers incorporated in the Thesis where my contributions are specified in this Statement of Contribution.

Title and authors: **Diffusion of CO₂ across the mesophyll-bundle sheath cell interface in a C₄ plant with genetically reduced PEP carboxylase activity.**
Hugo Alonso-Cantabrana, Asaph B. Cousins, Florence R. Danila, Timothy Ryan, Robert Sharwood, Susanne von Caemmerer, and Robert T. Furbank.

Current status of paper: **Published** (Plant Physiology. July 2018. https://doi.org/10.1104/pp.18.00618)

Contribution to paper: **F.R.D. conducted all microscopy imaging, anatomical measurements, plasmodesmata density quantification, and corresponding data analyses and statistics. F.R.D. also prepared the anatomy-related figures and table, and contributed in writing the first draft.**
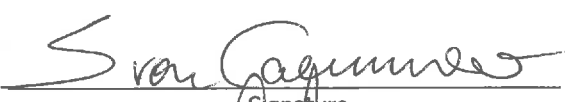
Senior author or collaborating author's endorsement:

Susanne von Caemmerer		1/8/18
Senior author – Print Name	Signature	Date
Robert T. Furbank		1/8/18
Senior author – Print Name	Signature	Date
Florence R. Danila		1/8/18
Candidate – Print Name	Signature	Date

Endorsed

Susanne von Caemmerer		1/8/18
Chair of Supervisory Panel – Print Name	Signature	Date
Spencer Whitney		2/8/18
Delegated Authority – Print Name	Signature	Date

Diffusion of CO_2 across the Mesophyll-Bundle Sheath Cell Interface in a C_4 Plant with Genetically Reduced PEP Carboxylase Activity[1][OPEN]

Hugo Alonso-Cantabrana,[a] Asaph B. Cousins,[b] Florence Danila,[a] Timothy Ryan,[a] Robert E. Sharwood,[a] Susanne von Caemmerer,[a,2] and Robert T. Furbank[a,3]

[a]Australian Research Council Centre of Excellence for Translational Photosynthesis, Division of Plant Sciences, Research School of Biology, Australian National University, Acton, Australian Capital Territory 2601, Australia

[b]School of Biological Sciences, Molecular Plant Sciences, Washington State University, Pullman, Washington 99164-4236

ORCID IDs: 0000-0002-5462-5861 (H.A.-C.); 0000-0002-7352-3852 (F.D.); 0000-0002-8366-2071 (S.v.C.)

Phospho*enol*pyruvate carboxylase (PEPC), localized to the cytosol of the mesophyll cell, catalyzes the first carboxylation step of the C_4 photosynthetic pathway. Here, we used RNA interference to target the cytosolic photosynthetic PEPC isoform in *Setaria viridis* and isolated independent transformants with very low PEPC activities. These plants required high ambient CO_2 concentrations for growth, consistent with the essential role of PEPC in C_4 photosynthesis. The combination of estimating direct CO_2 fixation by the bundle sheath using gas-exchange measurements and modeling C_4 photosynthesis with low PEPC activity allowed the calculation of bundle sheath conductance to CO_2 diffusion (g_{bs}) in the progeny of these plants. Measurements made at a range of temperatures suggested no or negligible effect of temperature on g_{bs} depending on the technique used to calculate g_{bs}. Anatomical measurements revealed that plants with reduced PEPC activity had reduced cell wall thickness and increased plasmodesmata (PD) density at the mesophyll-bundle sheath (M-BS) cell interface, whereas we observed little difference in these parameters at the mesophyll-mesophyll cell interface. The increased PD density at the M-BS interface was largely driven by an increase in the number of PD pit fields (cluster of PDs) rather than an increase in PD per pit field or the size of pit fields. The correlation of g_{bs} with bundle sheath surface area per leaf area and PD area per M-BS area showed that these parameters and cell wall thickness are important determinants of g_{bs}. It is intriguing to speculate that PD development is responsive to changes in C_4 photosynthetic flux.

C_4 plants have evolved a CO_2-concentrating mechanism that enables the elevation of CO_2 around the active sites of Rubisco by a combination of anatomical and biochemical specialization (Hatch, 1987). C_4 photosynthesis has evolved independently more than 60 times and provides one of the most widespread and effective solutions for overcoming the catalytic inefficiency of Rubisco (Sage et al., 2012; Christin and Osborne, 2013). The two key carboxylases of the C_4 photosynthetic pathway are localized to different cellular compartments. Phospho*enol*pyruvate carboxylase (PEPC) is localized to the cytosol of mesophyll cells, and Rubisco is localized to the chloroplasts of bundle sheath cells. C_4 acids produced by PEPC diffuse through plasmodesmata (PD) into the bundle sheath cells, where they are decarboxylated, thus supplying CO_2 for Rubisco. In order for the CO_2-concentrating mechanism to operate effectively, PEPC and C_4 cycle activity must exceed Rubisco and C_3 cycle activity to balance the leakage of CO_2 out of the bundle sheath compartment. This ensures above-ambient bundle sheath CO_2 partial pressure (pCO_2) but minimizes energetically wasteful overcycling of the mesophyll CO_2 pump (Furbank and Hatch, 1987; von Caemmerer and Furbank, 2003).

It has been hypothesized that a low rate of CO_2 diffusion across the bundle sheath and mesophyll interface is an essential feature of the C_4 photosynthetic CO_2-concentrating mechanism (Berry and Farquhar, 1978; Jenkins et al., 1989a; Jenkins et al., 1989b). However, what anatomical characteristics are essential for low bundle sheath conductance (g_{bs}) is poorly understood (von Caemmerer and Furbank, 2003). Jenkins (1989) demonstrated that, in C_4 species, inhibition of PEPC with the PEPC-specific inhibitor 3,3-dichloro-2-(dihydroxyphosphinoylmethyl) propenoate (DCDP) eliminated CO_2 assimilation in ambient

air. This inhibitor has been used previously to estimate g_{bs}, and values are in the range of 0.6 to 10 mmol m^{-2} s^{-1} bar^{-1} (Jenkins, 1989; Brown and Byrd, 1993; Kiirats et al., 2002).

The temperature dependence of g_{bs} is an important input into models of C$_4$ photosynthesis; however, little is known about this process (von Caemmerer, 2000; Yin et al., 2016). In C$_3$ species, strong temperature dependencies of mesophyll conductance, meaning the allowance of CO$_2$ diffusion from intercellular air space to chloroplasts, have been observed in some species but not in others (von Caemmerer and Evans, 2015). This raises questions about the temperature dependence of g_{bs} and whether similar diversity exists in the temperature dependence of g_{bs} among C$_4$ species. The only estimates of the temperature dependence of g_{bs} so far were made in the PEPC mutant of the C$_4$ dicot *Amaranthus edulis*, which lacks the C$_4$ isoform of PEPC (Kiirats et al., 2002). It often has been speculated that interspecific diversity in g_{bs} may be due to variation in the presence of secondary thickening and suberization of the bundle sheath cell walls; however, it also has been suggested that diffusion path length and positioning of organelles may be equally important (von Caemmerer and Furbank, 2003). *A. edulis* is of the NAD-malic enzyme (ME) biochemical type that lacks a suberized lamella at the mesophyll-bundle sheath (M-BS) cell interface and has been reported to have a high g_{bs} (Kiirats et al., 2002). However, other reports do not find significant differences in g_{bs} between C$_4$ species having suberized bundle sheath cell walls and those without (Jenkins et al., 1989; Brown and Byrd, 1993).

The model C$_4$ monocot species *Setaria viridis* (green foxtail millet), used in this study, is of the NADP-ME type, and its bundle sheath wall contains a suberized lamella (Danila et al., 2016). *S. viridis* is closely related to agronomically important C$_4$ crops including *Setaria italica* (foxtail millet), *Zea mays* (maize), *Sorghum bicolor* (sorghum), and *Saccharum officinarum* (sugarcane; Brutnell et al., 2010). It has become a popular model species due to its rapid generation time, small stature, high seed production, diploid status, and small sequenced and publicly available genome (Doust, 2007; Brutnell et al., 2010; Li and Brutnell, 2011). Here, we used a stable genetic transformation system to produce *S. viridis* harboring an RNA interference (RNAi) construct targeting the cytosolic C$_4$ PEPC isoform and isolated a number of independent transformants with very low PEPC activities. The biochemical properties of *S. viridis* PEPC and Rubisco are well characterized (Boyd et al., 2015), and this allowed us to estimate g_{bs} in the progeny of these plants in combination with anatomical investigations of the M-BS interface.

RESULTS

Characterization of αPEPC Transformants

Using an RNAi construct targeting the C$_4$ PEPC isoform of *S. viridis* (Supplemental Figs. S1 and S2), we
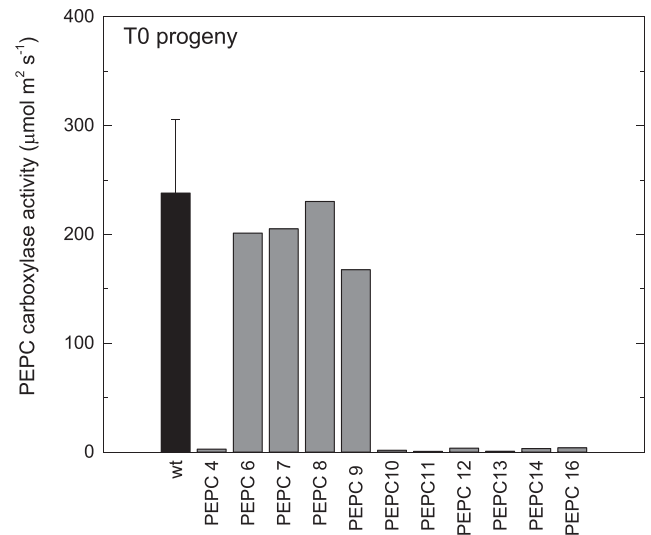
Figure 1. In vitro maximal PEPC activity of individual T0 plants compared with the average activity level of wild-type (wt) plants grown under the same growth conditions ($n = 4$). Error bars denote SE.

generated a number of T0 plants that showed either wild-type or very low PEPC activity levels (Fig. 1). The difference in PEPC activity was reflected in differences in CO$_2$ assimilation rates. T0 plants with low PEPC activity had very low CO$_2$ assimilation rates that did not saturate at intercellular pCO$_2$ above 1,200 µbar, in contrast to the wild-type-like T0 plants (Fig. 2). For the T1 progeny of selected T0 plants, in vitro measurements of PEPC and Rubisco activities and CO$_2$ response curves representing CO$_2$ assimilation rates showed that the properties of the T1 progeny mirrored those of the parent plants (Figs. 3 and 4). In plants with a severe reduction in PEPC activity, some reduction in Rubisco activity also was observed; however, the reduction in Rubisco activity was not proportional to the reduction in PEPC activity. A more detailed analysis of αPEPC 4 T1 progeny showed that soluble protein, chlorophyll, carbonic anhydrase, and ME activities, as well as the protein content, also were reduced (Table 1). These are presumably pleiotropic effects associated with the slow growth of the αPEPC 4 progeny even at ambient CO$_2$ of 2% (v/v).

Estimation of g_{bs} to CO$_2$ Diffusion

g_{bs} was estimated by two methods. In the first approach, we assumed that there was a negligible amount of C$_4$ cycle activity (Table 1) and that the leaves fixed CO$_2$ directly via Rubisco in the bundle sheath. This allowed us to estimate a total conductance for CO$_2$ diffusion from intercellular air space to the bundle sheath from the initial slope of the CO$_2$ response curves, as shown in Figure 5. In the second approach, we used the model for C$_4$ photosynthesis (von Caemmerer and Furbank, 1999; von Caemmerer, 2000) and fitted the CO$_2$ response to the enzyme-limited model as
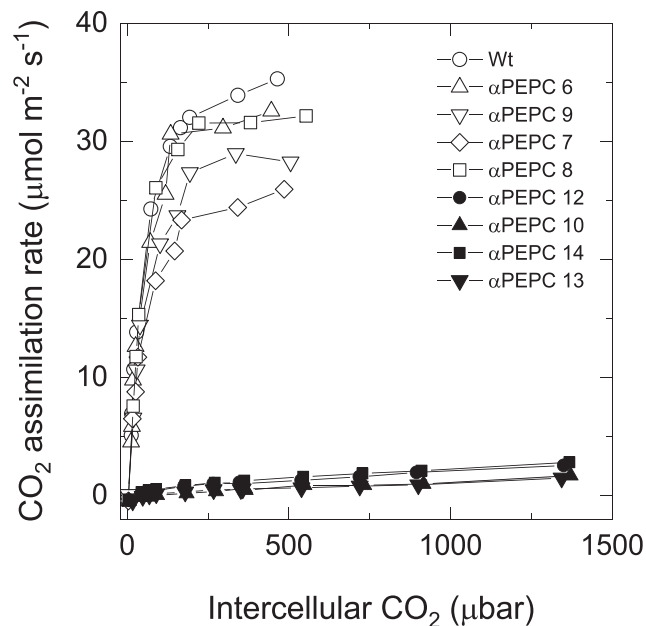
Figure 2. CO_2 response curves of leaves of wild-type (Wt) and individual T0 plants measured at 1,500 µmol quanta m^{-2} s^{-1}, leaf temperature of 25°C, and 21% oxygen.

described in "Materials and Methods." For this method, the V_{cmax} at 25°C was calculated from the measured Rubisco site content of αPEPC 4 T1 progeny of 3 ± 0.1 µmol m^{-2} and the catalytic turnover rate of 5.44 s^{-1} as 16.3 µmol m^{-2} s^{-1}. For the wild type, Rubisco site content was 6.4 ± 0.23 µmol m^{-2} (V_{cmax} = 34.7 µmol m^{-2} s^{-1}). Additionally, V_{pmax} for each individual plant was determined from the in vitro activity of PEPC at 25°C. We used the temperature dependence of enzyme kinetic parameters for PEPC and Rubisco determined by Boyd et al. (2015) for *S. viridis* and the temperature dependence of mesophyll conductance determined by Ubierna et al. (2017). The parameters used are given in Supplemental Table S1. Both techniques gave low values of g_{bs} of 2.9 ± 0.14 and 3.8 ± 0.32 mmol m^{-2} s^{-1} bar^{-1} for the two methods at 25°C, respectively, in the αPEPC 4 mutant. The slope method predicted a monotonic increase of g_{bs} from 2.7 ± 0.28 to 4.9 ± 0.14 mmol m^{-2} s^{-1} bar^{-1} at 20°C to 40°C (Fig. 6). However, there was no significant temperature dependence predicted using the C_4 model-fitting routine. Estimates of the two techniques differed significantly at 20°C, 25°C, and 40°C. g_{bs} also was estimated in wild-type leaves after feeding with the PEPC inhibitor DCDP (Supplemental Fig. S3) using the slope method. This resulted in an average g_{bs} of 2.2 ± 0.05 mmol m^{-2} s^{-1} bar^{-1} at 25°C, which was significantly less (P < 0.001) than the g_{bs} estimated for the αPEPC 4 mutant.

Anatomical Measurements and PD Density

The comparison of leaf anatomical characteristics of wild-type *S. viridis* with the T1 progeny of αPEPC 12,

αPEPC 13, and αPEPC 4 mutants shows that reduction in PEPC activity affected leaf anatomy (Fig. 7). There was a visible decrease in chloroplast content in the bundle sheath cells of all mutant lines. Starch production within chloroplasts of all mutant lines was less than that of the wild type, as shown by the decreased size of starch granules particularly in αPEPC 4. Chloroplasts in αPEPC 4 leaves were smaller in both mesophyll and bundle sheath cells compared with those in the wild type. It is interesting, however, that starch was visible in both mesophyll and bundle sheath chloroplasts in these plants. g_{bs} on a leaf area basis is the product of the conductance across the M-BS interface and the bundle sheath surface area-to-leaf area ratio (S_b). All PEPC mutants had thinner bundle sheath and mesophyll cell walls. There was, however, little difference in S_b, and only αPEPC 4 had slightly lower S_b values of 2.06 ± 0.037 compared with 2.38 ± 0.035 of the wild type (Table 2). C_4 acids and inevitably CO_2 diffuse through PD, which are distributed in clusters called pit fields in leaves (Danila et al., 2016). There was little difference between the wild type and mutants in terms of PD per pit field area at either the M-BS or the M-M interface. However, the pit field area per M-BS interface area was greater in all mutants compared with that in the wild type, with αPEPC 4 showing almost twice the coverage. This increase in pit field area was not observed at the M-M interface, where there was a decrease in pit field area (Fig. 8; Table 2; Supplemental Fig. S4). An increased number of pit fields drove the increase in pit
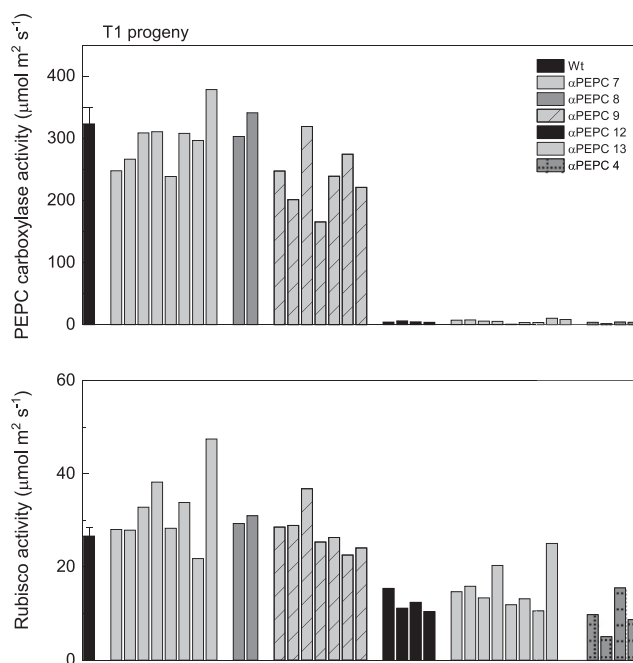
Figure 3. In vitro maximal PEPC and Rubisco activity of wild-type (Wt) plants (average value, n = 4) and plants of the T1 progeny of selected T0 plants (individual values). Error bars denote SE.

Figure 4. Leaf CO_2 response curves of wild-type plants (average value, $n = 4$) and individual T1 progeny selected from T0 plants measured at 1,500 µmol quanta m^{-2} s^{-1}, leaf temperature of 25°C, and 21% oxygen. Error bars denote SE.
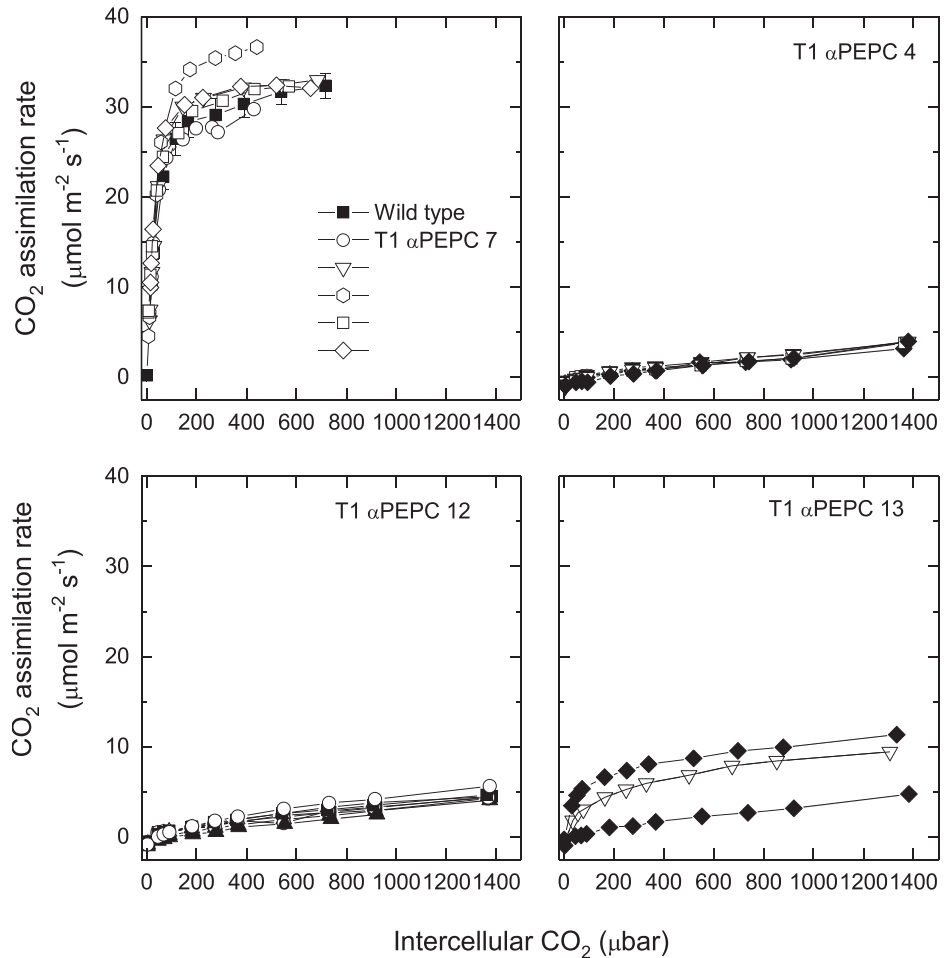
DISCUSSION

PEPC Is Required for High Rates of C_4 Photosynthesis

Using a PEPC RNAi construct targeting the C_4 PEPC isoform of *S. italica*, we isolated several independent transgenic lines with very low PEPC activity in leaves that resulted in low net CO_2 assimilation rates at ambient pCO_2 (Figs. 2 and 4). Our results confirm that lack of this isoform of PEPC greatly impairs C_4 photosynthesis, as has been shown previously in a PEPC knockout mutant of *A. edulis* (Dever, 1997). The nonsaturating nature of the CO_2 response curves of the mutants with very low PEPC activity suggests that CO_2 fixation occurred via the direct fixation of CO_2 by Rubisco. Despite a CO_2 environment of 2% in the growth facility, the PEPC mutants grew more slowly and showed reductions in other photosynthetic enzymes such as

Table 1. Average in vitro activities of key photosynthetic enzymes and chlorophyll content for wild-type and *α*PEPC 4 T1 progeny ($n > 4 \pm$ SE)

In vitro activities were measured as described in "Materials and Methods" at 25°C. Different lowercase letters following the values indicate statistically significant differences ($P < 0.05$, Tukey-Kramer honestly significant difference).

Parameter	Wild Type	*α*PEPC 4
Chlorophyll content (mmol m^{-2})	0.48 ± 0.10 a,b	0.34 ± 0.02 b
Chlorophyll *a:b* ratio	5.28 ± 0.21 a	3.40 ± 0.18 b
Rubisco (µmol CO_2 m^{-2} s^{-1})	25.4 ± 1.90 a	9.2 ± 1.7 b
PEPC (µmol CO_2 m^{-2} s^{-1})	311.6 ± 25.3 a	1.67 ± 0.53 b
NADP-ME (µmol CO_2 m^{-2} s^{-1})	36.9 ± 2.4 a,b	27.0 ± 3.5 b
Carbonic anhydrase (µmol CO_2 m^{-2} s^{-1})	1,703 ± 186 a	928 ± 152 b
Soluble protein (g m^{-2})	13.7 ± 1.2 a	9.6 ± 1.4 b
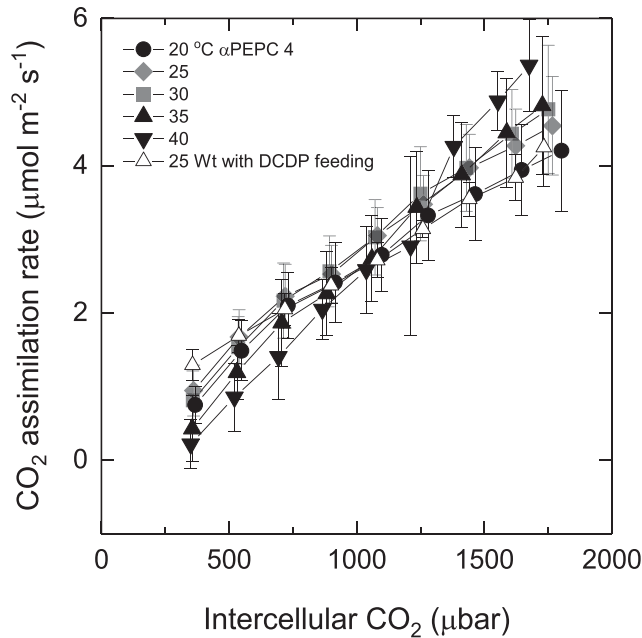
Figure 5. CO_2 response curves of leaves of *α*PEPC 4 T1 progeny measured at different leaf temperatures of 20°C, 25°C, 30°C, and 35°C (*n* = 4) or 25°C, 30°C, 35°C, and 40°C (*n* = 4). Measurements were made at 1,800 µmol quanta m^{-2} s^{-1} and 2% oxygen. Error bars denote SE. Wt, Wild type.

Rubisco, NADP-ME, and carbonic anhydrase activity (Table 1). This was not observed in *A. edulis* PEPC mutants, where Rubisco and carbonic anhydrase activity were not affected (Cousins et al., 2007). *A. edulis* is an NAD-ME-type C_4 species that lacks a suberin lamella at the M-BS interface. It could be that the greater g_{bs} (~10 mmol m^{-2} s^{-1} bar^{-1}) estimated for this species allows for the direct fixation of CO_2 by Rubisco and growth at high CO_2 concentrations (Kiirats et al., 2002). Furthermore, *S. viridis* is an NADP-ME species, where the C_3 cycle in the bundle sheath relies on NADPH resulting from malate decarboxylation and CO_2 assimilation may be more dependent on some C_4 cycle activity for C_3 cycle operation (Hatch, 1987; Furbank, 2011).

Interaction between Leaf Anatomy, PD Density, and C_4 Photosynthetic Biochemistry

It has been suggested from modeling that CO_2 diffusion across the M-BS interface can occur both through the PD (57%) and directly through the cell wall (43%; Jenkins et al., 1989b). The availability of 3D imaging technology allows for the visualization of pit fields by confocal microscopy with the use of a callose antibody and the visualization of PD in pit fields by scanning electron microscopy (Danila et al., 2016; Supplemental Fig. S4), providing us with a method to quantify the M-BS PD density in both wild-type and low-PEPC *S. viridis*. Our data highlight that 57% of the CO_2 leakage out of the bundle sheath occurs across

7% to 12% of the M-BS interface area. Furthermore, our examination of three independent lines with low PEPC presents a surprising result. PD density at the M-BS interface is increased substantially, and this is not observed at the M-M interface (Fig. 8). This increase in PD density is driven largely by an increase in the number of pit fields rather than an increase in PD per pit field or the size of pit fields. We have shown previously that PD density was at least doubled in C_4 species compared with C_3 species, which gave a clear indication of the enhanced expression of PD developmental genes in C_4 species (Danila et al., 2016). The reduction of available CO_2 in the bundle sheath cells of plants with low PEPC may trigger a compensation mechanism to allow for a higher CO_2 flux. However, until now, the genes underpinning PD development remain largely unknown (Brunkard and Zambryski, 2017). In a recent study where chloroplast and mitochondrial development was induced in rice (*Oryza sativa*) bundle sheath through the constitutive expression of maize *GOLDEN2-LIKE* genes, increased organelle volume was accompanied by the accumulation of photosynthetic enzymes and by increased intercellular connections (Wang et al., 2017). Genetic studies have revealed that PD development is regulated by intercellular signaling pathways, which may involve stromules from chloroplasts (Stonebloom et al., 2012). In NADP-ME C_4 decarboxylation types such as *S. viridis*, chloroplasts appress the M-BS interface that would facilitate such interactions. It is tempting
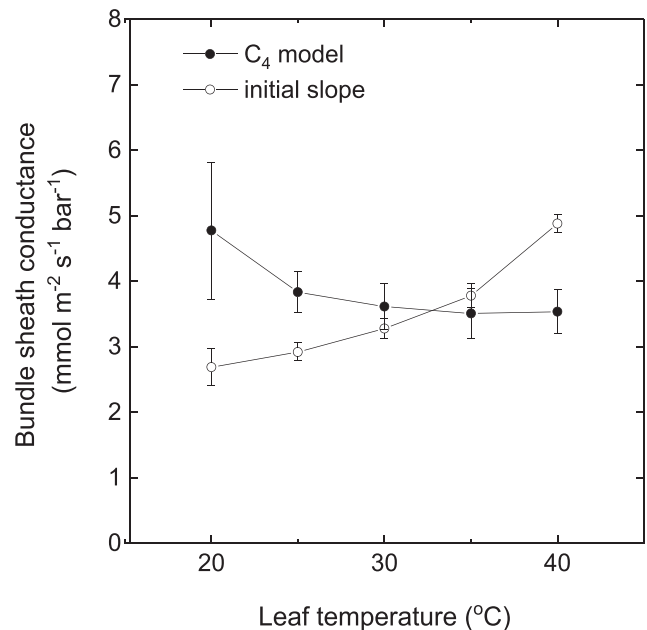
Figure 6. Estimation of the g_{bs} at different leaf temperatures. Estimations were made either from the initial slope of the CO_2 response curves shown in Figure 4 or by fitting the C_4 photosynthesis model (von Caemmerer and Furbank, 1999; von Caemmerer, 2000) as described in "Materials and Methods."
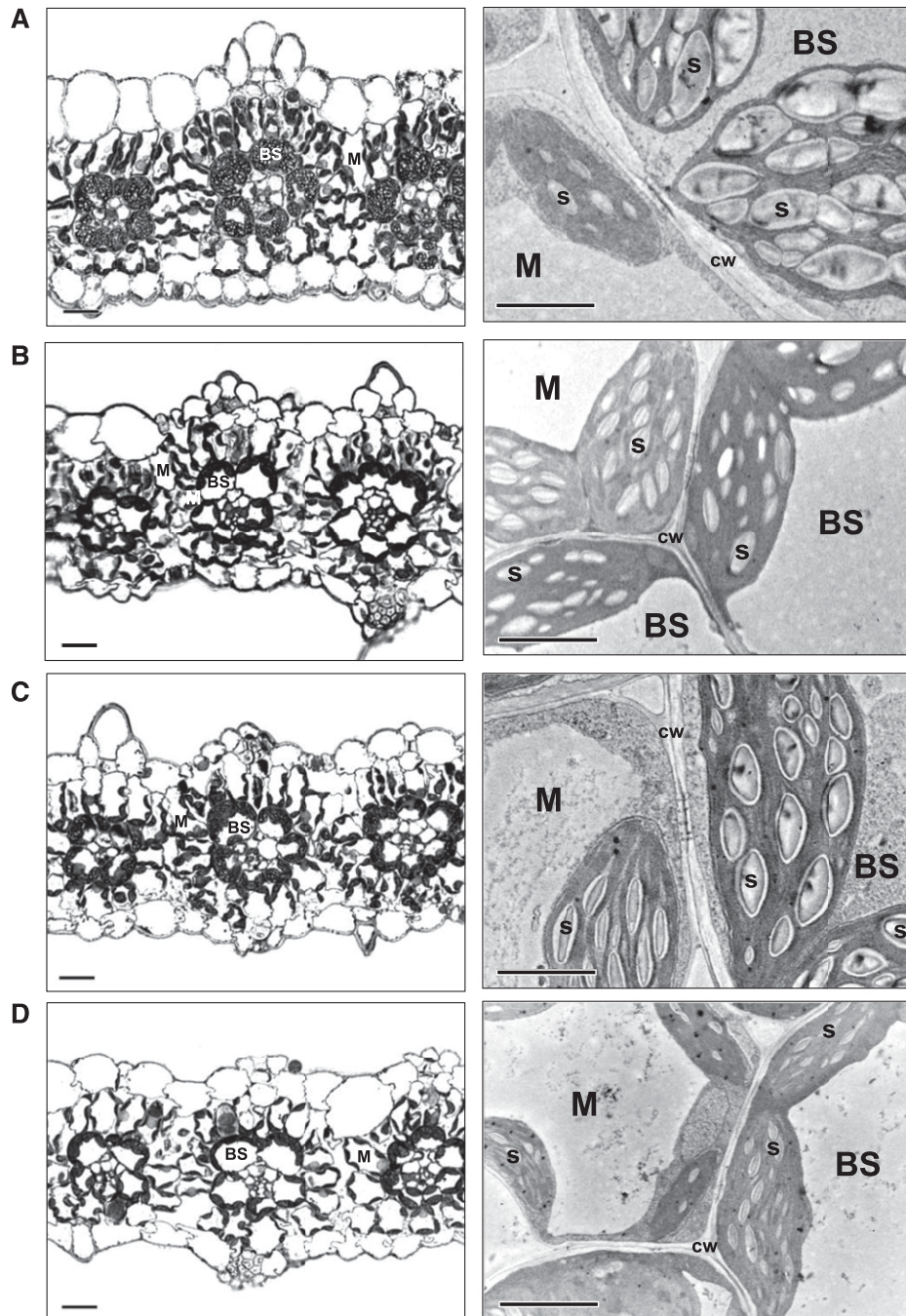
Figure 7. Light (left) and transmission electron (right) micrographs of transverse leaf sections of wild-type and PEPC RNAi T1 progeny of *S. viridis*. A, Wild type. B, *α*PEPC 12. C, *α*PEPC 13. D, *α*PEPC 4. BS, Bundle sheath cell; cw, cell wall; M, mesophyll cell; s, starch granule. Light micrograph bars = 20 μm and transmission electron micrograph bars = 5 μm.

to speculate that a shift in photosynthetic metabolism and direct CO_2 fixation by the bundle sheath chloroplast affects intercellular signaling pathways and PD development.

g_{bs}

g_{bs} is an essential parameter of all models of C_4 photosynthesis, but it remains difficult to estimate (Berry and Farquhar, 1978; von Caemmerer and Furbank, 1999; von Caemmerer, 2000; Wang et al., 2014; Bellasio et al., 2016). Our measured values of g_{bs} to CO_2 are in the range of values reported in the literature for the NADP-ME species sorghum and maize; however, the previously reported g_{bs} values vary widely, in the range of 1.13 to 60 mmol m^{-2} s^{-1} (Brown and Byrd, 1993; He and Edwards, 1996), but less than the values reported

Table 2. Leaf anatomical measurements in the wild type and αPEPC mutants of *S. viridis*

Statistically significant differences according to posthoc Tukey's test at $P < 0.05$ are indicated by different lowercase letters. Values followed by the same letter within a row are not significantly different. BS, Bundle sheath; M, mesophyll; M-M, mesophyll-mesophyll cell interface.

Parameter	Wild Type	αPEPC 12	αPEPC 13	αPEPC 4
BS cell wall thickness (µm)	0.68 ± 0.029 a	0.29 ± 0.019 b	0.52 ± 0.026 c	0.23 ± 0.009 b
M cell wall thickness (µm)	0.27 ± 0.009 a	0.11 ± 0.004 b	0.22 ± 0.011 c	0.12 ± 0.005 b
S_b (m² m⁻²)	2.38 ± 0.035 a	2.33 ± 0.042 a	2.32 ± 0.046 a	2.06 ± 0.037 b
M-BS PD per pit field area (PD µm⁻²)	50.8 ± 0.49 a	61.6 ± 1.19 b	55.7 ± 0.55 c	51.0 ± 0.57 a
M-BS pit field area per interface area (%)	12.9 ± 0.27 a	16.4 ± 0.27 b	18.9 ± 0.54 c	22.9 ± 0.42 d
M-BS PD per interface area (PD µm⁻²)	6.6 ± 0.12 a	10.1 ± 0.13 b	10.5 ± 0.10 b	11.7 ± 0.17 c
M-BS average pit field area (µm²)	0.6 ± 0.05 a	0.5 ± 0.04 a	0.7 ± 0.06 a	0.6 ± 0.07 a
M-BS PD area (µm²)	0.008 ± 0.0002 a	0.008 ± 0.0002 a,b	0.007 ± 0.0002 b	0.005 ± 0.0002 c
M-BS PD area per interface area (µm² µm⁻²)	0.054 ± 0.0005 a	0.079 ± 0.0007 b	0.077 ± 0.0006 c	0.061 ± 0.0007 d
M-BS PD area per unit of leaf area (m² m⁻²)	0.128 ± 0.0007 a	0.184 ± 0.0010 b	0.178 ± 0.0010 c	0.125 ± 0.0009 a
M-M PD per pit field area (PD µm⁻¹)	55.0 ± 1.26 a	62.9 ± 1.14 b	55.0 ± 0.74 a	71.1 ± 0.76 c
M-M pit field area per interface area (%)	6.3 ± 0.15 a	3.4 ± 0.10 b	4.8 ± 0.12 c	6.8 ± 0.16 a
M-M PD per interface area (PD µm⁻²)	3.5 ± 0.04 a	2.1 ± 0.02 b	2.6 ± 0.04 c	4.9 ± 0.08 d
M-M average pit field area (µm²)	0.6 ± 0.10 a	0.3 ± 0.03 b	0.4 ± 0.04 a,b	0.3 ± 0.04 b
M-M PD area (µm²)	0.010 ± 0.0004 a	0.006 ± 0.0002 b	0.006 ± 0.0001 b	0.004 ± 0.0001 c

for *A. edulis*. *S. viridis* has become a popular model C_4 grass species, and the availability of species-specific enzyme kinetic constants no doubt improved our ability to estimate g_{bs}. However, the interpretation of the temperature dependencies of g_{bs} obtained here remains challenging. When using the initial slope method, the same approach used by Kiirats et al. (2002), we calculated a temperature dependence not unlike that observed previously with a low Q(10) of ~1.3. However, when we incorporated a small amount of residual PEPC activity and used the C_4 model to estimate g_{bs}, we calculated no temperature dependence. Unfortunately, we cannot resolve this discrepancy. Evans and von Caemmerer (2013) calculated that CO_2 diffusion through a liquid phase alone should result in a small decline in conductance with increasing temperature. They hypothesized that it is the membrane diffusion component that is responsible for the observed increase in mesophyll conductance with temperature in many C_3 species, depending on the balance between the liquid and membrane diffusion path (von Caemmerer and Evans, 2015). It is difficult to predict this response for an NADP-ME-type C_4 species, where CO_2 is produced in the bundle sheath chloroplasts and diffuses out across the chloroplast envelope, through the liquid phase of the cytosol and through a membrane/liquid phase in PD, in addition to the complex pathway across a suberized cell wall.

Based on permeability coefficients determined for CO_2 in C_4 leaves and isolated bundle sheath cells (Furbank et al., 1989; Jenkins et al., 1989a), Jenkins et al. (1989b) suggested that approximately 43% of the CO_2 leakage from the bundle sheath occurs via an apoplastic route and 57% via PD. In the αPEPC 4 transgenic line, the PD number at the M-BS interface was almost doubled but PD size was reduced, and this led to a 13% increase in PD area per M-BS interface (Fig. 8; Table 2). When comparing g_{bs} calculated from DCDP-fed

wild-type plants with that obtained for this transgenic line, values are around 50% higher on a bundle sheath surface area basis (1.4 mmol m⁻² s⁻¹ bar⁻¹ for αPEPC 4 compared with 0.92 mmol m⁻² s⁻¹ bar⁻¹ for the wild type). The diffusion paths via PD and the apoplast are in parallel, and the 13% increase in PD area is insufficient to account for the 50% difference. This suggests that reduced cell wall thickness in αPEPC 4 transgenic plants results in a significant increase in conductance via the apoplastic route.

The leakage of CO_2 outward from the bundle sheath has long been recognized as a crucial determinant of the efficiency of the C_4 pathway (Furbank and Hatch, 1987; Furbank et al., 1990; von Caemmerer and Furbank, 2003). However, the relative importance of the symplastic and apoplastic barriers to diffusion remains somewhat elusive. During the evolution of C_4 plants, increases in symplastic connectivity between mesophyll and bundle sheath cells were required to support C_4 metabolite flux (Danila et al., 2016), but inevitably, this increase in metabolite conductance would lead to an increase in g_{bs} for CO_2. We show here that the symplastic diffusion pathway between mesophyll and bundle sheath cells is not entirely genetically predetermined and that the manipulation of metabolism can affect PD development and cell-to-cell connectivity in C_4 leaves.

MATERIALS AND METHODS

Selection of the PEPC Gene

The genome sequence of *Setaria italica*, obtained from the Phytozome database (https://phytozome.jgi.doe.gov), was used as a reference because no genome sequence was available for *Setaria viridis* at the time of the experiment (Bennetzen et al., 2012). There are six genes encoding PEPC enzymes in *S. italica* and seven in *S. viridis* (Xu et al., 2013). The cytosolic PEPC isoform involved in C_4 photosynthesis in *S. italica*, Si005789m, was identified due to the presence of a conserved substitution of an Ala to a Ser in the C-terminal region of the protein (Supplemental Fig. S1) that has been shown to be common to many
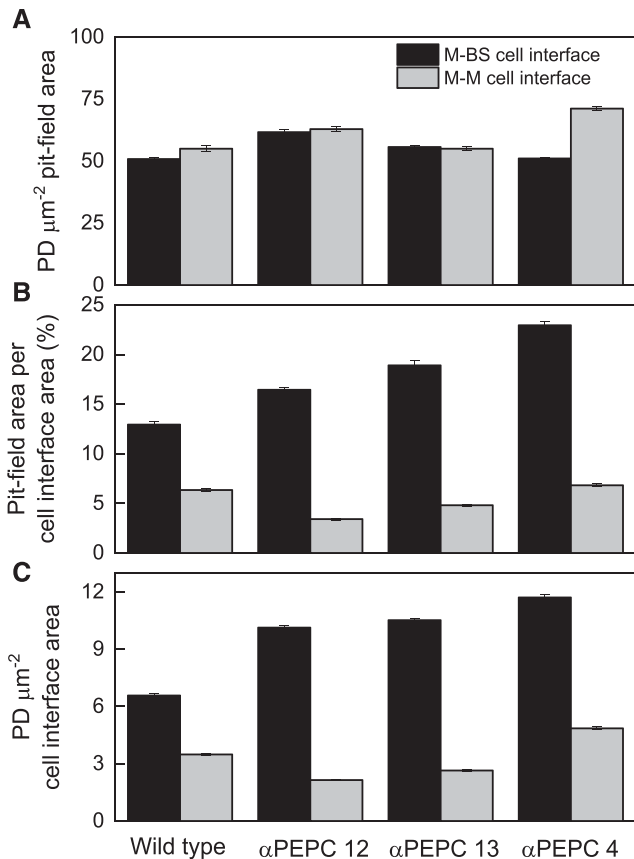
Figure 8. Quantification of PD in wild-type and select *α*PEPC T1 progeny of *S. viridis*. A, Number of PD per pit field was estimated from scanning electron microscopy images. B, Percentage pit field area per interface area. C, Number of PD per interface area. Scanning electron microscopy images were used to quantify PD per PD pit field area, and 3D confocal images were used to quantify percentage PD pit field area per interface area as described in "Materials and Methods" and by Danila et al. (2016). Sample images are shown in Supplemental Figure S5.

C_4 isoforms of PEPC in both monocots and dicots (Bläsing et al., 2000). The homolog in *S. viridis* is Sevir.4G143500.

Plasmid Construction

Total RNA was isolated and purified from wild-type *S. viridis* A10 leaves using the TRIzol reagent (Invitrogen). cDNA was synthesized using the SuperScript III First-Strand Synthesis kit (Invitrogen) from 1 µg of total RNA. Primers (SiPEPC1F, 5′-CACCCCCGGAGACGGAGTACGGCA-3′; and SiPEPC1R, 5′-GCGGCGATGCCCTTCATGGT-3′) were designed targeting the cytosolic C_4 isoform of the PEPC open reading frame from *S. italica* (GenBank accession no. NP_001267758.1). These were used to amplify via PCR a 658-bp DNA fragment from the *S. viridis* cDNA library, from positions 2,223 to 2,881 in the Sevir.4G143500 coding sequence. The fragment was ligated subsequently into the pENTR-dTOPO vector (Invitrogen) and sequenced to confirm its identity. The fragment was then inserted via a double Gateway system LR reaction (Invitrogen) into the hairpin RNAi binary vector pSTARGATE (Wesley et al., 2001) to form a stem-loop PEPC region under the control of the ubiquitin promoter/intron and octopine synthase terminator (Supplemental Fig. S1). The resulting pSTARGATE-*α*PEPC RNAi construct was validated by sequencing and introduced into *Agrobacterium tumefaciens* strain AGL1.

Callus Induction and Plant Transformation

Stable transformation of *S. viridis* (accession A10.1) was carried out as described by Brutnell et al. (2010). Seed coats were removed mechanically from mature *S. viridis* seeds to improve germination. Seeds were sterilized before plating on callus induction medium (CIM; 4.3 g L^{-1} Murashige and Skoog [MS] salts, pH 5.8, 10 mL L^{-1} 100× MS vitamin stock, 40 g L^{-1} maltose, 35 mg L^{-1} ZnSO$_4$·7H$_2$O, 0.6 mg L^{-1} CuSO$_4$·5H$_2$O, 4 g L^{-1} Gelzan, 0.5 mg L^{-1} kinetin, and 2 mg L^{-1} 2,4-D). After 4 weeks in the dark at 24°C, any seedling structures or gelatinous calli were removed and remaining calli were transferred to fresh CIM. After a further 2 weeks, good-quality calli or portions of calli were selected based on their white color and dry texture, separated from brown or gelatinous tissue, divided in 2-mm pieces, and replated onto fresh CIM. One week later, transformations were performed.

A. tumefaciens AGL1 containing the construct of interest were grown in the presence of 50 µg L^{-1} kanamycin and 50 µg L^{-1} rifampicin at 28°C to OD$_{600}$ = 0.5 and then resuspended in CIM without Gelzan and hormones. Acetosyringone (200 mM) and synperonic (0.01%, w/v) were added to the *A. tumefaciens* solution before incubating the calli in the medium for 5 min at room temperature. The calli were blotted dry on sterile filter paper and incubated at 22°C for 3 d in the dark. The calli were then transferred to selective CIM (CIM containing 40 mg L^{-1} hygromycin and 150 mg L^{-1} timentin) and incubated in the dark at 24°C for 16 d. Calli were then transferred to selective plant regeneration medium containing 4.3 g L^{-1} MS salts, pH 5.8, 10 mL L^{-1} 100× MS vitamins, 20 g L^{-1} Suc, 7 g L^{-1} Phytoblend, 2 mg L^{-1} kinetin, 150 mg L^{-1} timentin, and 15 mg L^{-1} hygromycin. Calli were maintained at 24°C under a 16-h-light/8-h-dark photoperiod and a light intensity of 60 µmol photons m^{-2} s^{-1}. Developing shoots were transferred to selective rooting medium containing 2.15 g L^{-1} MS salts, pH 5.7, 10 mL L^{-1} 100× MS vitamins, 30 g L^{-1} Suc, 7 g L^{-1} Phytoblend, 150 mg L^{-1} timentin, and 20 mg L^{-1} hygromycin. Shoots that survived and developed roots were genotyped by PCR to amplify the pSTARGATE-PEPC vector using primers (PSIntF1, 5′-TAATGCTAATATAACAAAGCGCAAGATCTA-3′; and PSIntR1, 5′-AAGATCAATGATAACACAATGACATGATCT-3′) or primers directed against the hygromycin phosphotransferase gene (F, 5′-TGGCGTGATTTCATATGCGC-3′; and R, 5′-CGTCAACCAAGCTCTGATAG-3′). Positive transformants were transplanted to soil.

Plant Growth Conditions

Wild-type, T0, and T1 plants were grown in controlled environmental chambers with the following conditions: irradiance of 500 µmol quanta m^{-2} s^{-1}, 16-h photoperiod, 28°C day temperature, 24°C night temperature, and 2% CO$_2$. Each plant was grown in 2-L pots filled with garden soil mix and fertilized with Osmocote (Scotts). Pots were watered daily.

To promote germination, T1 seeds were first incubated in 5% liquid smoke (Wrights) for 24 h. Treated T1 seeds were then allowed to germinate in garden soil mix fertilized with Osmocote (Scotts) in small containers before being transferred to individual 2-L pots.

Gas-Exchange Measurements

Net CO$_2$ assimilation rate (*A*) was measured over a range of intercellular pCO$_2$ (C_i) values on the uppermost, fully expanded leaf of 5-week-old *S. viridis* plants using a portable gas-exchange system (LI-COR 6400XT; LI-COR Biosciences). Measurements were made after leaves had equilibrated at 380 µbar, flow rate of 500 µmol s^{-1}, leaf temperature of 25°C, and irradiance of 1,500 µmol quanta m^{-2} s^{-1}. CO$_2$ response curves were measured in a stepwise increase (3-min intervals) at pCO$_2$ ranging from 0 to 2,000 µbar while maintaining leaf temperature and irradiance conditions. For estimates of g_{bs} done for T1 progeny of *α*PEPC 4, measurements were made at 1,800 µmol quanta m^{-2} s^{-1} and 2% oxygen at pCO$_2$ ranging from 400 to 2,000 µbar.

Gas-Exchange Measurements after DCDP Feeding of Wild-Type Leaves

The PEPC inhibitor DCDP has been shown to reduce PEPC activity in vivo (Jenkins, 1989; Brown and Byrd, 1993; Kiirats et al., 2002). Detached wild-type leaves whose cut edge was immersed in water were stabilized in the gas-exchange system at 1,800 µmol quanta m^{-2} s^{-1} and 2% oxygen, leaf temperature of 25°C, and 400 µbar pCO$_2$. Then, DCDP was added to achieve a final concentration of 2 to 4 mM. After CO$_2$ assimilation rates decreased to a steady very low rate of 0.5 ± 0.15 µmol m^{-2} s^{-1}, CO$_2$ response curves were measured as described above for the estimation of g_{bs}.

Determination of Enzyme Activities

For carbonic anhydrase activity, leaf discs (0.78 cm²) were collected from the uppermost fully expanded leaf of 5-week-old *S. viridis* plants and frozen in liquid nitrogen. Soluble protein was extracted by grinding one frozen leaf disc (0.5 cm²) in ice-cold glass homogenizers (Tenbroek) in 500 µL of extraction buffer (50 mM HEPES, pH 7.8, 1% [w/v] polyvinylpyrrolidone, 1 mM EDTA, 10 mM DTT, 0.1% [v/v] Triton X-100, and 2% [v/v] protease inhibitor cocktail [Sigma]). Crude extracts were centrifuged at 4°C for 1 min at 13,000*g*, and the supernatant was collected for the soluble carbonic anhydrase assay. Activity was measured on a membrane inlet mass spectrometer to measure the rates of ^{18}O exchange from labeled $^{13}C^{18}O_2$ to $H_2^{16}O$ at 25°C (Badger and Price, 1989; von Caemmerer et al., 2004). The hydration rates were calculated as described by Jenkins et al. (1989b).

For Rubisco, PEPC, and NADP-ME activities, soluble protein was extracted from fresh leaf discs collected from leaves used for gas-exchange analysis. Spectrophotometric assays were then performed as described previously (Pengelly et al., 2010, 2012; Sharwood et al., 2016).

For the experiment where g_{bs} was estimated for wild-type and αPEPC 4 plants, the Rubisco catalytic site content was measured by stoichiometric binding of [¹⁴C]carboxy-arabinitol-P₂ as described by Ruuska et al. (1998) and Sharwood et al. (2008). Leaf discs (0.5 cm²) were extracted in extraction buffer as described above. $MgCl_2$ and $NaHCO_3$ were added to final concentrations of 20 and 15 mM, respectively, together with 29 µM [¹⁴C]carboxy-arabinitol-P₂ (specific radioactivity about 10,6651 cpm nmol⁻¹) to 100-µL aliquots of extracts, which were incubated for 45 min before gel filtration.

Anatomical Measurements

Tissue from the midportion of the third fully expanded leaf was collected from wild-type and transgenic plants. This tissue was used for light microscopy, electron microscopy, and 3D immunolocalization preparations (Danila et al., 2016). The S_b was measured using at least 10 individual small veins from light micrographs of transverse leaf sections (Pengelly et al., 2010). Bundle sheath and mesophyll cell wall thickness were measured using transmission electron micrographs of transverse leaf sections. The quantitation of PD per µm² of pit field, percentage pit field per interface area, and PD per µm² of interface was carried out as described (Danila et al., 2016). All measurements were performed using ImageJ software (National Institutes of Health).

Estimation of g_{bs}

g_{bs} was estimated by two methods. In the first approach, it was assumed that there was a negligible amount of C_4 cycle activity and that the leaves fixed CO_2 via Rubisco in the bundle sheath. Under these conditions a total conductance from intercellular air space to the bundle sheath can be estimated from the initial slope of the CO_2 response by using Equation 2.45 from von Caemmerer (2000):

$$g_t = \frac{\frac{dA}{dC_i}(V_{cmax} - R_d)}{(V_{cmax} - \frac{dA}{dC_i}(\Gamma_* + K_c(1 + O/K_o)))} \quad (1)$$

Where g_t is the total conductance to CO_2 diffusion from the intercellular air space to the site of Rubisco carboxylation in the bundle sheath. dA/dC_i is the initial slope of the CO_2 response curve of CO_2 assimilation rate versus intercellular pCO_2 (C_i). V_{cmax} is the maximal Rubisco activity and R_d is leaf mitochondrial respiration in the light; K_c and K_o are the Michaelis-Menten constants of Rubisco for CO_2 and oxygen, respectively, and O is the oxygen partial pressure. Γ_* is the chloroplast pCO_2, where, in the absence of respiration, Rubisco carboxylation equals the photorespiratory CO_2 release (Laisk, 1977; von Caemmerer, 2000, Eq. 2.17), defined as:

$$\Gamma_* = 0.5 O / S_{c/o} \quad (2)$$

Rubisco kinetic constants for *S. viridis* were taken from Boyd et al. (2015) and are given in Supplemental Table S1.

Total conductance (g_t) is a good approximation for g_{bs}, since the conductances are in series and g_{bs} is 2 orders of magnitude less than g_m and g_{bs}/g_m is small:

$$g_t = \frac{g_{bs}}{1 + g_{bs}/g_m} \quad (3)$$

In the second approach, we used the model for C_4 photosynthesis (von Caemmerer and Furbank, 1999; von Caemmerer, 2000) and fitted the CO_2 response to the enzyme-limited model (von Caemmerer, 2000, Eq. 4.21) using the parameters given in Supplemental Table S1 for the fitting routine where only g_{bs} was fitted. Mesophyll pCO_2 (C_m) was calculated from the mesophyll conductance values (g_m) given in Supplemental Table S1 and measured CO_2 assimilation rates (A) as:

$$C_m = C_i - A/g_m \quad (4)$$

We assumed that no oxygen evolution occurs in the bundle sheath cells, as *S. viridis* is an NADP-ME subtype and does not have functional PSII in the bundle sheath. Therefore, the parameter α, which defines the fraction of oxygen evolution occurring in the bundle sheath, is set to zero.

Statistical Analysis

Statistical analysis of images was carried out using Origin software, and statistical differences according to posthoc Tukey's test at $P < 0.05$ were used. One-way ANOVAs with posthoc Tukey's test analyses were performed for all measurements of g_{bs} with $P = 0.05$ using the IBM SPSS Statistics 22 package.

Accession Numbers

Sequence data from this article can be found in the GenBank/EMBL data libraries under accession number MF967570.

Supplemental Data

The following supplemental materials are available.

Supplemental Figure S1. Alignment of the PEPC amino acid sequences involved in C_4 photosynthesis in maize, sorghum, *S. viridis*, and *S. italica*.

Supplemental Figure S2. Hairpin RNAi vector pSTARGATE-PEPC used for plant transformation.

Supplemental Figure S3. Effect of the PEPC inhibitor DCDP feeding on CO_2 assimilation rate in *S. viridis* wild-type leaves.

Supplemental Figure S4. Pit field distribution and pit field size at cell-cell interfaces in leaves of wild-type and αPEPC T1 progeny of *S. viridis*.

Supplemental Table S1. Temperature dependencies of PEPC and Rubisco kinetic constants and mitochondrial respiration used in the calculations of g_{bs}.

LITERATURE CITED

Badger MR, Price GD (1989) Carbonic anhydrase activity associated with the cyanobacterium *Synechococcus* PCC7942. Plant Physiol **89**: 51–60

Bellasio C, Beerling DJ, Griffiths H (2016) Deriving C_4 photosynthetic parameters from combined gas exchange and chlorophyll fluorescence using an Excel tool: theory and practice. Plant Cell Environ **39**: 1164–1179

Bennetzen JL, Schmutz J, Wang H, Percifield R, Hawkins J, Pontaroli AC, Estep M, Feng L, Vaughn JN, Grimwood J, (2012) Reference genome sequence of the model plant Setaria. Nat Biotechnol **30**: 555–561

Berry JA, Farquhar GD (1978) The CO2 concentrating function of C4 photosynthesis: a biochemical model. *In* **D Hall, J Coombs, T Goodwin**, eds, The Proceedings of the Fourth International Congress on Photosynthesis. Biochemical Society of London, London, pp 119–131

Bläsing OE, Westhoff P, Svensson P (2000) Evolution of C_4 phosphoenolpyruvate carboxylase in *Flaveria*, a conserved serine residue in the carboxyl-terminal

part of the enzyme is a major determinant for C_4-specific characteristics. J Biol Chem **275**: 27917–27923

Boyd RA, Gandin A, Cousins AB (2015) Temperature responses of C_4 photosynthesis: biochemical analysis of Rubisco, phosphoenolpyruvate carboxylase, and carbonic anhydrase in *Setaria viridis*. Plant Physiol **169**: 1850–1861

Brown RH, Byrd GT (1993) Estimation of bundle sheath cell conductance in C_4 species and O_2 insensitivity of photosynthesis. Plant Physiol **103**: 1183–1188

Brunkard JO, Zambryski PC (2017) Plasmodesmata enable multicellularity: new insights into their evolution, biogenesis, and functions in development and immunity. Curr Opin Plant Biol **35**: 76–83

Brutnell TP, Wang L, Swartwood K, Goldschmidt A, Jackson D, Zhu XG, Kellogg E, Van Eck J (2010) *Setaria viridis*: a model for C_4 photosynthesis. Plant Cell **22**: 2537–2544

Christin PA, Osborne CP (2013) The recurrent assembly of C_4 photosynthesis, an evolutionary tale. Photosynth Res **117**: 163–175

Cousins AB, Baroli I, Badger MR, Ivakov A, Lea PJ, Leegood RC, von Caemmerer S (2007) The role of phosphoenolpyruvate carboxylase during C_4 photosynthetic isotope exchange and stomatal conductance. Plant Physiol **145**: 1006–1017

Danila FR, Quick WP, White RG, Furbank RT, von Caemmerer S (2016) The metabolite pathway between bundle sheath and mesophyll: quantification of plasmodesmata in leaves of C_3 and C_4 monocots. Plant Cell **28**: 1461–1471

Dever LV (1997) Control of photosynthesis in *Amaranthus edulis* mutants with reduced amounts of PEP carboxylase. Aust J Plant Physiol **24**: 469–476

Doust A (2007) Architectural evolution and its implications for domestication in grasses. Ann Bot **100**: 941–950

Evans JR, von Caemmerer S (2013) Temperature response of carbon isotope discrimination and mesophyll conductance in tobacco. Plant Cell Environ **36**: 745–756

Furbank RT (2011) Evolution of the C_4 photosynthetic mechanism: are there really three C_4 acid decarboxylation types? J Exp Bot **62**: 3103–3108

Furbank RT, Hatch MD (1987) Mechanism of C_4 photosynthesis: the size and composition of the inorganic carbon pool in bundle sheath cells. Plant Physiol **85**: 958–964

Furbank RT, Jenkins CLD, Hatch MD (1989) CO_2 concentrating mechanism of C_4 photosynthesis: permeability of isolated bundle sheath cells to inorganic carbon. Plant Physiol **91**: 1364–1371

Furbank RT, Jenkins CLD, Hatch MD (1990) C4 photosynthesis: quantum requirement, C4 acid overcycling and Q-cycle involvement. Aust J Plant Physiol **17**: 1–7 10.1071/PP9900001

Hatch MD (1987) C_4 photosynthesis: a unique blend of modified biochemistry, anatomy and ultrastructure. Biochim Biophys Acta **895**: 81–106

He D, Edwards GE (1996) Estimation of diffusive resistance of bundle sheath cells to CO_2 from modeling of C_4 photosynthesis. Photosynth Res **49**: 195–208

Jenkins CLD (1989) Effects of the phosphoenolpyruvate carboxylase inhibitor 3,3-dichloro-2-(dihydroxyphosphinoylmethyl) propenoate on photosynthesis: C_4 selectivity and studies on C_4 photosynthesis. Plant Physiol **89**: 1231–1237

Jenkins CLD, Furbank RT, Hatch MD (1989a) Inorganic carbon diffusion between C_4 mesophyll and bundle sheath cells: direct bundle sheath CO_2 assimilation in intact leaves in the presence of an inhibitor of the C_4 pathway. Plant Physiol **91**: 1356–1363

Jenkins CLD, Furbank RT, Hatch MD (1989b) Mechanism of C4 photosynthesis: a model describing the inorganic carbon pool in bundle sheath cells. Plant Physiol **91**: 1372–1381

Kiirats O, Lea PJ, Franceschi VR, Edwards GE (2002) Bundle sheath diffusive resistance to CO_2 and effectiveness of C_4 photosynthesis and refixation of photorespired CO_2 in a C_4 cycle mutant and wild-type *Amaranthus edulis*. Plant Physiol **130**: 964–976

Laisk A (1977) Kinetics of Photosynthesis and Photorespiration in C_3 Plants. Nauka, Moscow

Li P, Brutnell TP (2011) Setaria viridis and Setaria italica, model genetic systems for the panicoid grasses. J Exp Bot **62**: 3031–3037

Pengelly JJL, Sirault XRR, Tazoe Y, Evans JR, Furbank RT, von Caemmerer S (2010) Growth of the C_4 dicot Flaveria bidentis: photosynthetic acclimation to low light through shifts in leaf anatomy and biochemistry. J Exp Bot **61**: 4109–4122

Pengelly JJL, Tan J, Furbank RT, von Caemmerer S (2012) Antisense reduction of NADP-malic enzyme in *Flaveria bidentis* reduces flow of CO_2 through the C_4 cycle. Plant Physiol **160**: 1070–1080

Ruuska SA, Andrews TJ, Badger MR, Hudson GS, Laisk A, Price GD, von Caemmerer S (1998) The interplay between limiting processes in C_3 photosynthesis studied by rapid-response gas exchange using transgenic tobacco impaired in photosynthesis. Aust J Plant Physiol **25**: 859–870

Sage RF, Sage TL, Kocacinar F (2012) Photorespiration and the evolution of C_4 photosynthesis. Annu Rev Plant Biol **63**: 19–47

Sharwood RE, von Caemmerer S, Maliga P, Whitney SM (2008) The catalytic properties of hybrid Rubisco comprising tobacco small and sunflower large subunits mirror the kinetically equivalent source Rubiscos and can support tobacco growth. Plant Physiol **146**: 83–96

Sharwood RE, Sonawane BV, Ghannoum O, Whitney SM (2016) Improved analysis of C_4 and C_3 photosynthesis via refined in vitro assays of their carbon fixation biochemistry. J Exp Bot **67**: 3137–3148

Stonebloom S, Brunkard JO, Cheung AC, Jiang K, Feldman L, Zambryski P (2012) Redox states of plastids and mitochondria differentially regulate intercellular transport via plasmodesmata. Plant Physiol **158**: 190–199

Ubierna N, Gandin A, Boyd RA, Cousins AB (2017) Temperature response of mesophyll conductance in three C_4 species calculated with two methods: 18O discrimination and in vitro V_{pmax}. New Phytol **214**: 66–80

von Caemmerer S (2000) Biochemical Models of Leaf Photosynthesis, Vol 2. CSIRO Publishing, Collingwood, Australia

von Caemmerer S, Evans JR (2015) Temperature responses of mesophyll conductance differ greatly between species. Plant Cell Environ **38**: 629–637

von Caemmerer S, Furbank RT (1999) Modeling of C_4 photosynthesis. *In* RF Sage, R Monson, eds, C_4 Plant Biology. Academic Press, San Diego, pp 169–207

von Caemmerer S, Furbank RT (2003) The C_4 pathway: an efficient CO_2 pump. Photosynth Res **77**: 191–207

von Caemmerer S, Quinn V, Hancock NC, Price GD, Furbank RT, Ludwig M (2004) Carbonic anhydrase and C_4 photosynthesis: a transgenic analysis. Plant Cell Environ **27**: 697–703

Wang P, Khoshravesh R, Karki S, Tapia R, Balahadia CP, Bandyopadhyay A, Quick WP, Furbank R, Sage TL, Langdale JA (2017) Re-creation of a key step in the evolutionary switch from C_3 to C_4 leaf anatomy. Curr Biol **27**: 3278–3287.e6

Wang Y, Long SP, Zhu XG (2014) Elements required for an efficient NADP-malic enzyme type C_4 photosynthesis. Plant Physiol **164**: 2231–2246

Wesley SV, Helliwell CA, Smith NA, Wang MB, Rouse DT, Liu Q, Gooding PS, Singh SP, Abbott D, Stoutjesdijk PA, (2001) Construct design for efficient, effective and high-throughput gene silencing in plants. Plant J **27**: 581–590

Xu J, Li Y, Ma X, Ding J, Wang K, Wang S, Tian Y, Zhang H, Zhu XG (2013) Whole transcriptome analysis using next-generation sequencing of model species Setaria viridis to support C4 photosynthesis research. Plant Mol Biol **83**: 77–87

Yin X, van der Putten PEL, Driever SM, Struik PC (2016) Temperature response of bundle-sheath conductance in maize leaves. J Exp Bot **67**: 2699–2714

Supplementary Table and Figures:

Supplemental Table S1.
Temperature dependencies of PEPC and Rubisco kinetic constants and mitochondrial respiration used in the calculations of bundle sheath conductance.
K_p and V_{pmax} are the Michaelis Menten constant for CO_2 and maximum PEPC rates, V_{cmax} is the maximum Rubisco carboxylation rate, K_c the Michaelis Menten constant for CO_2, K_o the Michaelis Menten constant for O_2. $S_{c/o}$ is the Rubisco CO_2 to O_2 specificity and R_d and R_m are the mitochondrial respiration rates of the whole leaf and of the mesophyll alone. Data are taken from (Boyd *et al.*, 2015). Mesophyll conductance to CO_2 diffusion (g_m) was measured for *S. viridis* by Ubierna *et al.*, (2016).
The V_{cmax} at 25°C was calculated from the measured Rubisco site content of αPEPC 4 T1 progeny of 3.0±0.1 and catalytic turnover rate of 5.44 s^{-1} as 16.3 µmol m^{-2} s^{-1} For wild type Rubisco site content was 6.4±0.23 (V_{cmax} =34.7 µmol m^{-2} s^{-1}).

Temperature (°C)	$K_{p\ (CO2)}$ (µbar)	V_{pmax} (µmol m^{-2} s^{-1})	V_{cmax} (µmol m^{-2} s^{-1})	K_c (µbar)	K_o (µbar)	$S_{c/o}$ (bar bar^{-1})	R_d (µmol m^{-2} s^{-1})	R_m (µmol m^{-2} s^{-1})	g_m (mol m^{-2} s^{-1} bar^{-1})
20	119	0.69	9.5	778	271648	1623	0.71	0.36	0.56
25	154	1.00	16.3	1210	292000	1310	1.00	0.50	0.9
30	198	1.35	27.4	1855	313130	1065	1.34	0.67	1.37
35	252	1.73	45.3	2804	335029	872	1.75	0.87	1.64
40	318	2.12	73.6	4184	357686	718	2.20	1.10	1.02
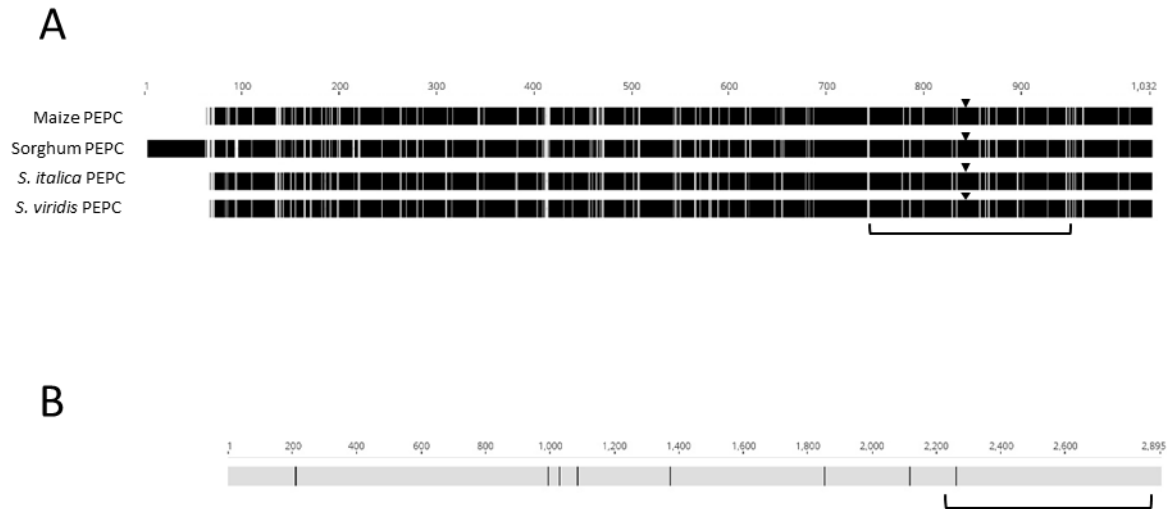
Supplemental Figure S1.

A, Alignment of the PEPC amino acid sequences involved in C_4 photosynthesis in maize, sorghum, *S. viridis* and *S. italica*. Black areas indicate regions conserved in all four species. Arrowheads indicate the position of the Ser residue typical in C_4 PEPC isoforms. Bracket indicates the region targeted for RNAi in *S. viridis*. The amino acid sequences of *S. viridis* and *S. italica* PEPC diverge only in positions 344, 362 and 617.

B, *S. viridis* Sevir.4G143500 CDS. Black marks indicate single nucleotide differences with the *S. italica* homologous gene (Si005789m). The bracket indicates the 658 bp section targeted for silencing with construct pStargate-αPEPC .
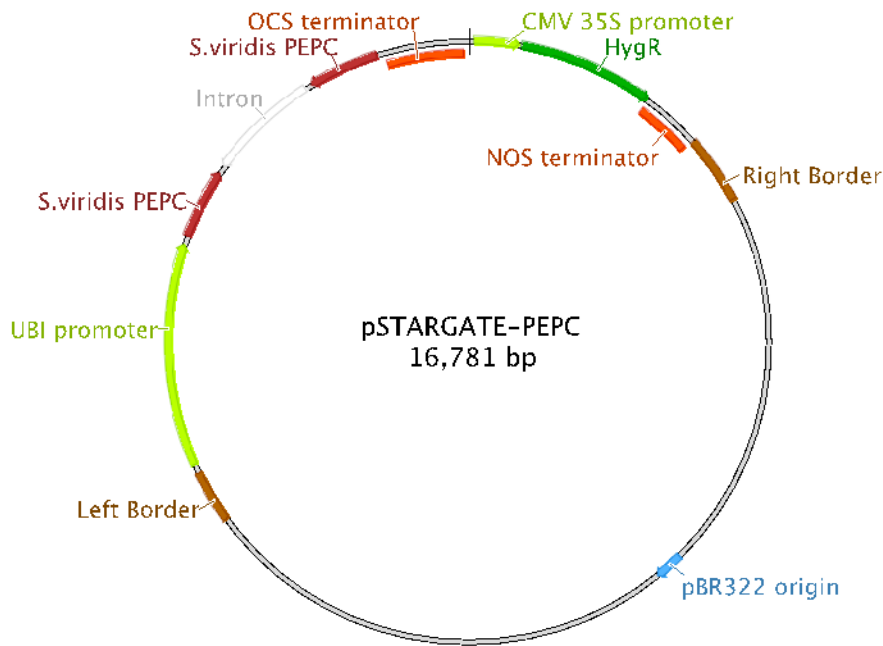
Supplemental Figure S2.
Hairpin RNAi vector pSTARGATE-PEPC used for plant transformation.
Features of the vector include an ubiquitin promoter driving transcription of a forward and reverse facing PEPC section from *Seteria viridis* separated by an intron and halted by the octopine synthase terminator to form a hairpin mRNA structure
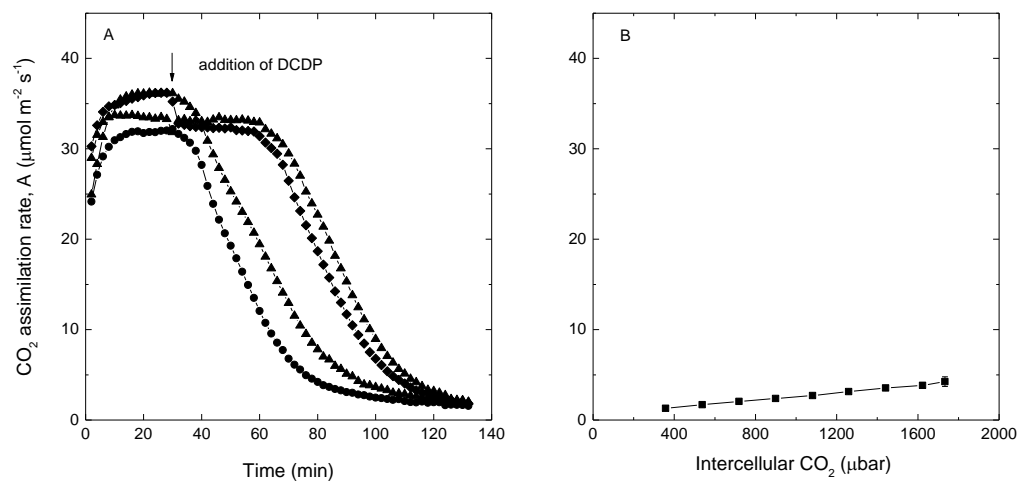
Supplemental Figure S3.

Effect of the PEPC inhibitor 3,3-dichloro-2-(dihydroxyphosphinoylmethyl) propenoate (DCDP) feeding on CO_2 assimilation rate in *S. viridis* wild-type leaves. A, Time course of CO_2 assimilation rate of detached leaves after feeding 2-4 mM DCDP. B, Subsequent measurements of CO_2 response curves of DCDP fed leaves (These are also shown in Figure 5). Gas exchange measurements were made at 1800 μmol quanta m^{-2} s^1, leaf temperature of 25 °C, and 2% O_2 and 400 μbar CO_2 (A) or a range of pCO_2 (B)

Mesophyll-bundle sheath interface

| Wild type | αPEPC 12 | αPEPC 13 | αPEPC 4 |

Mesophyll-mesophyll interface

| Wild type | αPEPC 12 | αPEPC 13 | αPEPC 4 |
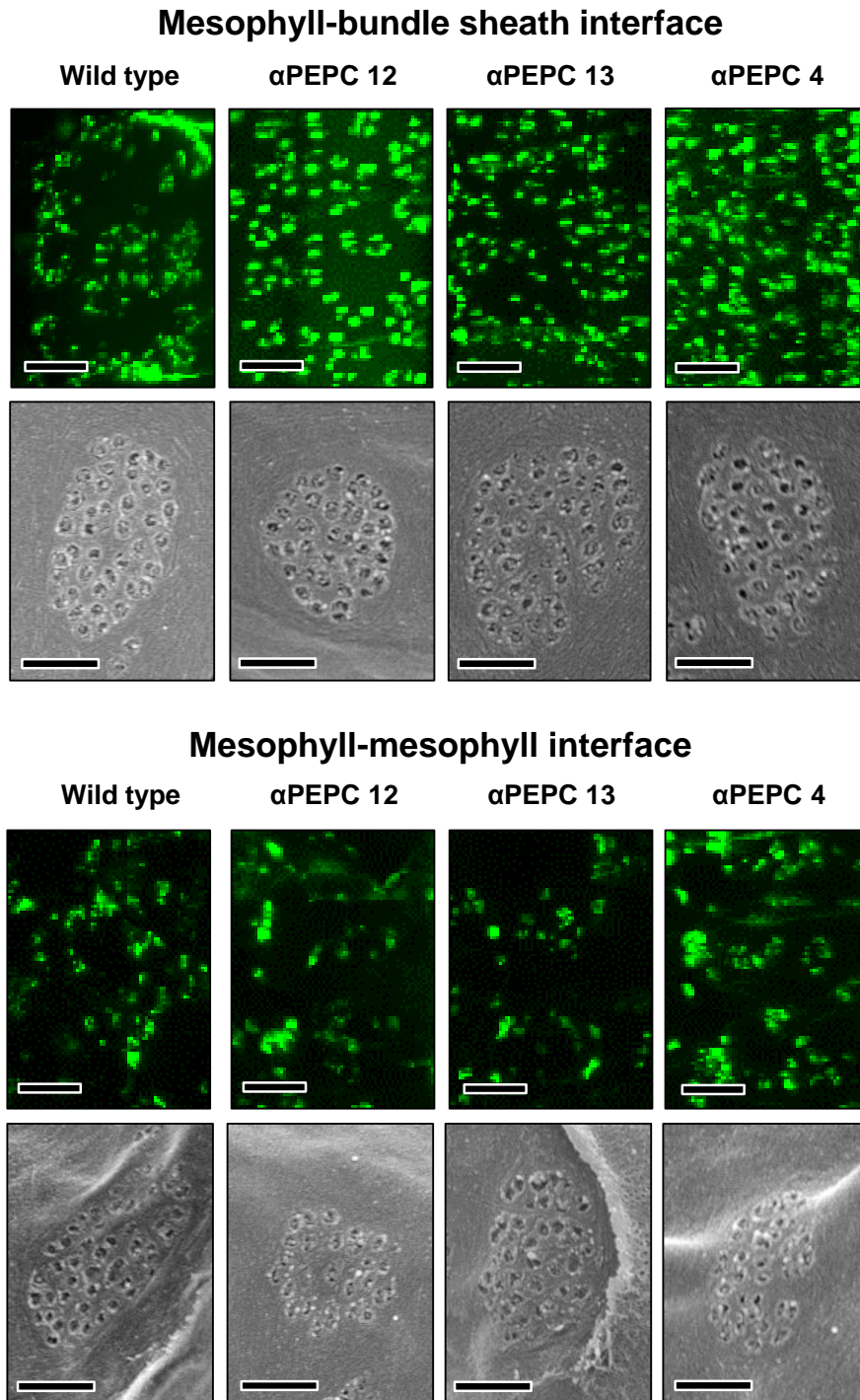
Supplemental Figure S4.
Pit field distribution (green fluorescence in upper confocal images) and pit field size (in lower SEM images) at cell-cell interfaces in leaves of wild type and αPEPC T1 progeny of *S. viridis*. Confocal micrograph bars = 10 μm. SEM bars = 0.5 μm.

7
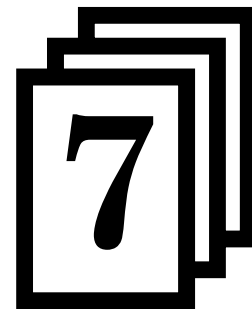
GENERAL DISCUSSION AND CONCLUSIONS

7.1   Introduction

As proposed in Chapter 1, two major research questions were tackled in this work. First, *is increased plasmodesmata density between mesophyll and bundle sheath cells in leaves an anatomical enabler of C_4 photosynthesis?,* and second, *does plasmodesmata density between mesophyll and bundle sheath cells respond to changes in photosynthetic capacity in C_4 species?* The key to answering these questions is the development of a new plasmodesmata density quantification method, which allowed accurate measurements in leaves of many grass species in a more robust and time-efficient manner.

7.2   Is increased plasmodesmata density between mesophyll and bundle sheath cells in leaves an anatomical enabler of C_4 photosynthesis?

Previous plasmodesmata density quantification performed in grasses consistently reported greater plasmodesmata densities in C_4 species compared to their C_3 counterparts (Botha, 1992; Botha and van Bel, 1992). However, limited by the number of species examined using the conventional transmission electron microscopy method prevented these studies from answering a very important research question: *Is increased plasmodesmata density between mesophyll and bundle sheath cells in leaves an anatomical enabler of C_4 photosynthesis?* The difficulty in answering this question lies on having enough species replication not only in terms of photosynthetic types, which must include the different biochemical subtypes of C_4 photosynthesis, but also in terms of taxonomic group and C_4 lineage representation (Christin et al., 2013). Development of a new plasmodesmata density quantification method (Chapter 3) has made this possible. As described in Chapter 4, the new plasmodesmata density method provided the opportunity to look at 18 grass species, which made up a list of species that satisfied replication according to photosynthetic types. However, the species list fell short in terms of taxonomic group and C_4 lineage representation. Therefore, to fully address the question, the number of grass species examined in this study was further increased from 18 to 25 by looking at seven more new grass species.

7.2.1 Extended species list and reconstructed phylogenetic tree

Grasses can be categorized into two clades, the subfamilies Bambusoideae, Ehrhartoideae, and Pooideae or BEP clade, which contains no C_4 species and the PACMAD (Panicoideae, Aristidoideae, Chloridoideae, Micrairoideae, Arundinoideae, and Danthonioideae) clade, which contains C_3 species, C_3-C_4 intermediates, and C_4 species. Within the PACMAD clade, many grasses have evolved C_4 photosynthesis. In the subfamilies Panicoideae, Aristidoideae, Chloridoideae, and Micrairoideae, there are 22-24 independent lineages of C_4 pathway found (GPWGII, 2012). Overcoming the limitations of using conventional transmission electron microscopy, the new plasmodesmata quantification method developed in this work (Chapter 3) gave the opportunity to study more closely the difference between C_3 and C_4 species in terms of plasmodesmata connectivity between leaf mesophyll cell and bundle sheath cell on a larger sample set. From comparative plasmodesmata quantification of two representative species each from the C_3 grasses and C_4 grasses (Chapter 3), this method has allowed a comprehensive plasmodesmata density survey across 18 grass species from the non-C_4 BEP clade and PACMAD clade including representative species from all the C_4 decarboxylation subtypes, NADP-ME, NAD-ME, and PCK (Chapter 4). Although greater plasmodesmata density between mesophyll cell and bundle sheath cell was consistently observed in all the C_4 species examined compared to C_3 species (Chapter 4), the extent of C_4 lineage represented by the 18 grass species was not enough to draw a strong evolutionary conclusion. Therefore, to obtain sufficient replication of taxonomic groups and C_4 lineage representation, a further seven selected grass species were analysed extending the list to 25 grass species. This extended species list encompassed seven independent C_4 lineages with at least three independent C_4 lineages represented in each C_4 decarboxylation subtype (Table 7.1). Also, the extended species list contained a total of seven C_3 species distributed well within the BEP and PACMAD clades in the reconstructed phylogenetic tree (Fig. 7.1). *Panicum milioides*, which is one of the very few C_3-C_4 intermediate species present in the grass family, was also included in the extended species list.

7.2.2 Extended species list: did the results change?

During the development of the plasmodesmata quantification method where only two representative species each from the C_3 and C_4 grasses were compared (Chapter 3), it was

Table 7.1 Photosynthetic type, taxonomic group (subfamily and tribe), and C_4 lineage representation of the 25 grass species examined.

Grass species	Photosynthetic type	Subfamily	Tribe	C_4 lineage*
Oryza sativa cultivar Kitaake	C_3, BEP	Ehrhartoideae	Oryzeae	Not applicable
Triticum aestivum cultivar Yecora 70	C_3, BEP	Pooideae	Triticeae	Not applicable
Hordeum vulgare cultivar Yagan	C_3, BEP	Pooideae	Triticeae	Not applicable
Brachypodium distachyon	C_3, BEP	Pooideae	Brachypoideae	Not applicable
Alloteropsis semialata	C_4 PCK, PACMAD	Panicoideae	Paniceae	*Alloteropsis*
Alloteropsis cimicina	C_4 NAD-ME, PACMAD	Panicoideae	Paniceae	*Alloteropsis*
Echinochloa frumentacea	C_4 NADP-ME, PACMAD	Panicoideae	Paniceae	*Echinochloa*
Echinochloa esculenta	C_4 NADP-ME, PACMAD	Panicoideae	Paniceae	*Echinochloa*
Panicum bisulcatum	C_3, PACMAD	Panicoideae	Paniceae	C_3 sister to MPC
Thyridolepis mitchelliana	C_3, PACMAD	Panicoideae	Paniceae	Closely-related C_3 to *Paraneurachne*
Panicum miliaceum	C_4 NAD-ME, PACMAD	Panicoideae	Paniceae	MPC
Panicum coloratum	C_4 NAD-ME, PACMAD	Panicoideae	Paniceae	MPC
Urochloa panicoides	C_4 PCK, PACMAD	Panicoideae	Paniceae	MPC
Panicum maximum	C_4 PCK, PACMAD	Panicoideae	Paniceae	MPC
Setaria viridis cultivar A10	C_4 NADP-ME, PACMAD	Panicoideae	Paniceae	MPC
Panicum antidotale	C_4 NADP-ME, PACMAD	Panicoideae	Paniceae	MPC
Cenchrus ciliaris	C_4 NADP-ME, PACMAD	Panicoideae	Paniceae	MPC
Zea mays cultivar B73	C_4 NADP-ME, PACMAD	Panicoideae	Andropogoneae	Andropogoneae
Sorghum bicolor cultivar Rooney	C_4 NADP-ME, PACMAD	Panicoideae	Andropogoneae	Andropogoneae
Paspalum dilatatum	C_4 NADP-ME, PACMAD	Panicoideae	Paspaleae	*Paspalum*
Steinchisma laxa	C_3, PACMAD	Panicoideae	Paspaleae	C_3 sister to *Steinchisma*
Panicum milioides	C_3-C_4 intermediate	Panicoideae	Paspaleae	*Steinchisma*
Leptochloa fusca	C_4 NAD-ME, PACMAD	Chloridoideae	Cynodonteae	Chloridoideae
Chloris gayana	C_4 PCK, PACMAD	Chloridoideae	Cynodonteae	Chloridoideae
Astrebla lappacea	C_4 NAD-ME, PACMAD	Chloridoideae	Cynodonteae	Chloridoideae

*According to (GPWGII, 2012).
MPC = Melinidinae, Panicinae, and Cenchrinae
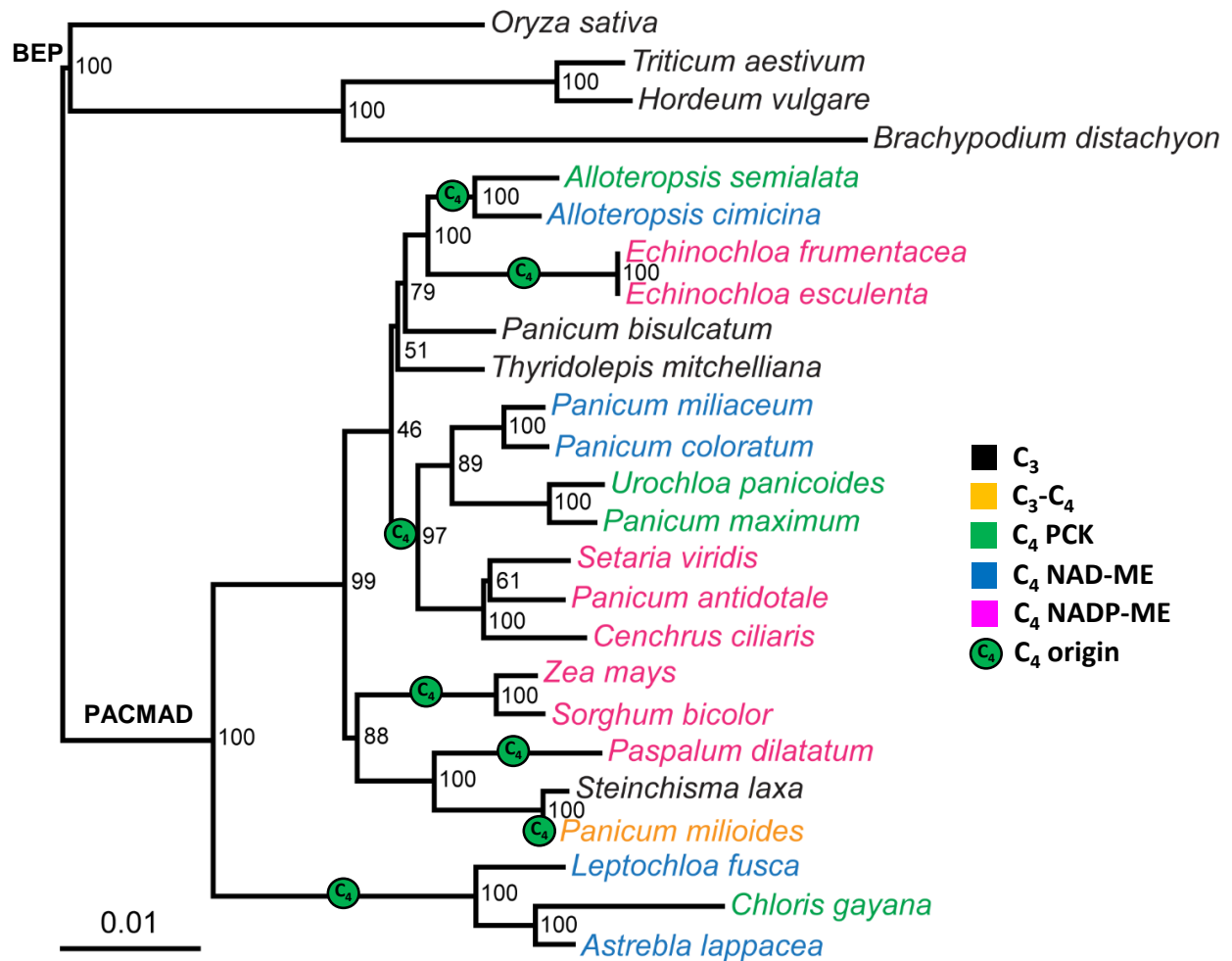
Figure 7.1 Phylogenetic tree of the C_3 and C_4 grass species examined in this study generated using sequences from ndhF and rbcL chloroplast genes. Species names are colour-coded according to photosynthetic types: black, C_3; orange, C_3-C_4 intermediate; green, C_4 PCK; blue, C_4 NAD-ME; magenta, C_4 NADP-ME. The seven independent evolutionary origins of C_4 photosynthesis according to (GPWGII, 2012) are indicated with green circles at the midpoint of the branches. Note that *Panicum milliodes*, a.k.a. *Steinchisma hians*, although technically C_3-C_4 intermediate (Duvall et al., 2003) was categorised as C_4 in (GPWGII, 2012). Support value at internal nodes is the percentage of non-parametric bootstrap replicates that support the bipartition. Scale bar indicates substitutions per site.

initially thought that plasmodesmata density is greater at mesophyll-bundle sheath cell interfaces and between mesophyll cells in C_4 species than in C_3 species. This led to the suggestion that increased in leaf plasmodesmata density may not be related to C_4 biochemistry. However, looking at more species revealed that plasmodesmata density between mesophyll cells does not differ overall between C_3 species and C_4 species (Chapter 4). The updated results showed that plasmodesmata density between mesophyll cells and plasmodesmata density at mesophyll-
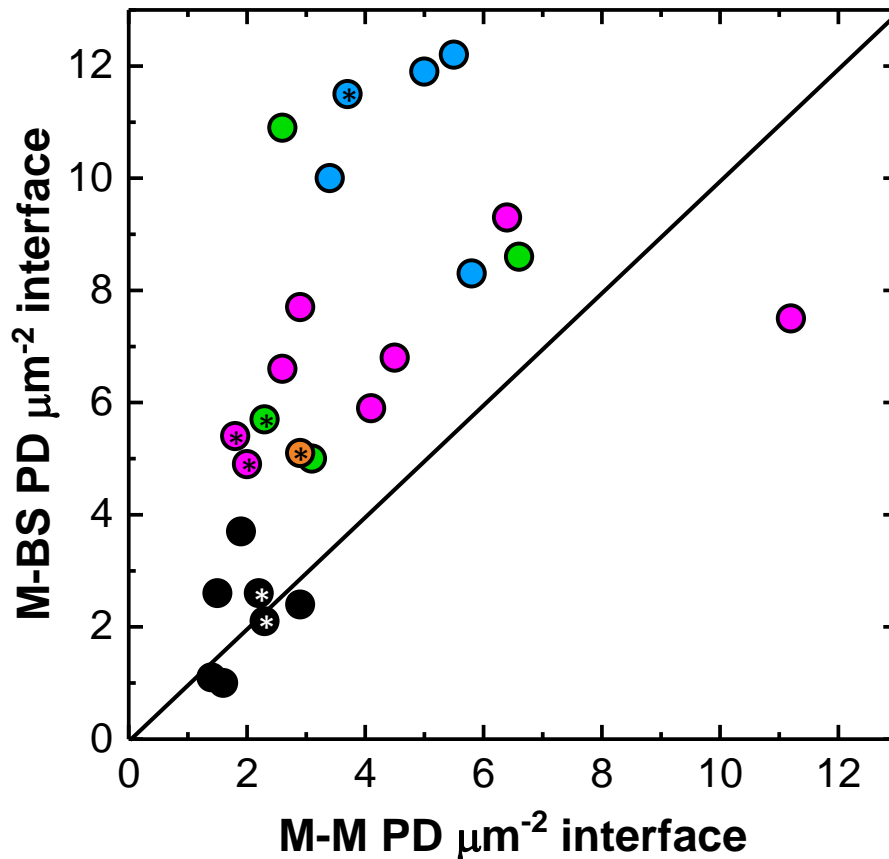
Figure 7.2 Plasmodesmata (PD) densities on the mesophyll-mesophyll (M-M) and mesophyll-bundle sheath (M-BS) cell wall interfaces of the 25 grass species examined. The seven additional species are marked with an asterisk. Colour-coding is as described in Figure 7.1. The outlier at the far right is *Zea mays* var. B73, a highly domesticated C_4 species.

bundle sheath cell interfaces are not correlated (Fig. 7.2).

Addition of seven more grass species to the 18 grass species described in Chapter 4 did not alter the plasmodesmata density results. In fact, the plasmodesmata densities obtained from the additional species aligned with the plasmodesmata density value range of their respective photosynthetic types (Fig. 7.2). Within the C_4 species, NAD-ME subtype still had the greatest plasmodesmata density between the mesophyll and bundle sheath cells, NADP-ME had the least, and PCK had the largest variability. Results also showed that irrespective of phylogenetic origin, either within BEP or PACMAD clade, all C_3 species had less plasmodesmata at mesophyll- bundle sheath cell interfaces compared to C_4 species (Fig. 7.2). Interestingly, the C_3-C_4 intermediate
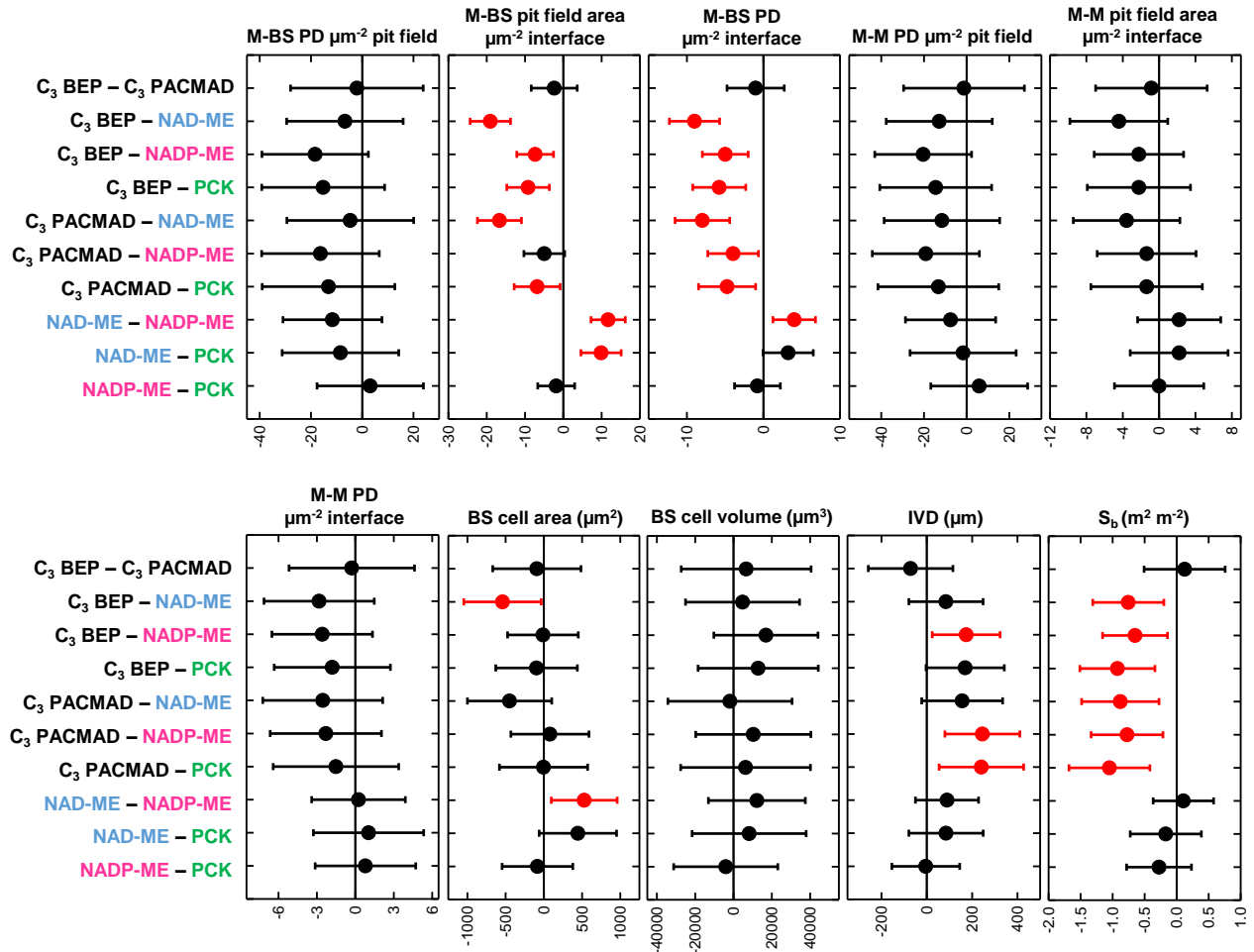
Figure 7.3 Mean trait difference among photosynthetic types according to *post-hoc* Tukey test. In red are statistically significant mean trait difference at *P*-value < 0.05. BS, bundle sheath; IVD, interveinal distance; S_b, bundle sheath surface area per unit leaf area; M, mesophyll.

species, *Panicum milioides*, had plasmodesmata density at mesophyll-bundle sheath cell interfaces within the C_4 range (Fig. 7.2). The importance of this result is discussed in Section 7.2.3.

The key parameters involved in the quantification of plasmodesmata density and other anatomical traits thought to have large influence in the evolution of C_4 photosynthesis are enumerated in Figure 7.3. In this figure, means comparisons according to Tukey test (*P*-value < 0.05) among photosynthetic types for each trait were plotted. Results showed that traits such as pit field area and plasmodesmata density per mesophyll-bundle sheath cell interface area, but not per mesophyll-mesophyll cell interface area, were significantly different when C_3 species and C_4 species were compared (Fig. 7.3). These results corroborated the initial finding from Chapter 4

that greater plasmodesmata density between mesophyll and bundle sheath cells in leaves is required for C_4 photosynthesis. Meanwhile, bundle sheath surface area per leaf area (S_b) and, to a lesser extent, interveinal distance, but not bundle sheath cell size, were statistically different between C_3 species and C_4 species. The implications of these results are discussed in Section 7.2.4.

7.2.3 Evolution of symplastic connections to the bundle sheath in C_4 leaves

Results from quantification of plasmodesmata density in 25 grass species (Figs. 7.2 and 7.3) suggests that increased plasmodesmata density between mesophyll and bundle sheath cells is a requirement for C_4 photosynthesis, which perfectly fits in the C_4 evolution pyramid (Fig. 7.4). The C_4 evolution pyramid was first proposed by Sage (2004) and enumerates the five major steps required for a C_3 plant to evolve an efficient C_4 photosynthesis based on anatomical and biochemical characterization of C_3, C_3-C_4 intermediate, and C_4 species within the dicot lineages, *Flaveria* and *Heliotropium* (Sage et al., 2012). Preceding the proto-Kranz condition, which involves enlargement of bundle sheath and development of more bundle sheath organelles, is a foliar anatomical preconditioning step, such as having close venation and gene duplication. Once these suitable anatomical characteristics are achieved, the evolution of a photorespiratory CO_2 pump follow, where glycine decarboxylase is lost in the mesophyll cell and consequently expressed almost exclusively in the bundle sheath cell. This phase is where the evolution of C_3-C_4 intermediate occurs and the first phase of biochemical modification. Once the photorespiratory CO_2 pump is in place, the next phase is the establishment of a C_4 cycle, which involves cell-specific expression of C_4 enzymes into either the mesophyll or bundle sheath. Finally, optimisation of the regulatory and kinetic properties of the C_4 enzymes as well as modification of the Kranz anatomy ensure maximum efficiency of the C_4 pathway. Consistent with these proposed C_4 evolutionary phases, close venation and increased bundle sheath cell size were reported as leaf anatomical attributes of C_4 photosynthesis in grasses (Christin et al., 2013).

Integrating the plasmodesmata density data obtained from grasses into the proposed C_4 evolution pyramid, the C_3-C_4 intermediate *P. milioides* is positioned along the photorespiratory CO_2 pump step or the C_3-C_4 intermediate evolution phase (Fig. 7.4). From the plasmodesmata density quantification results obtained from the extended study (Fig. 7.2), *P. milioides* had mesophyll-

124
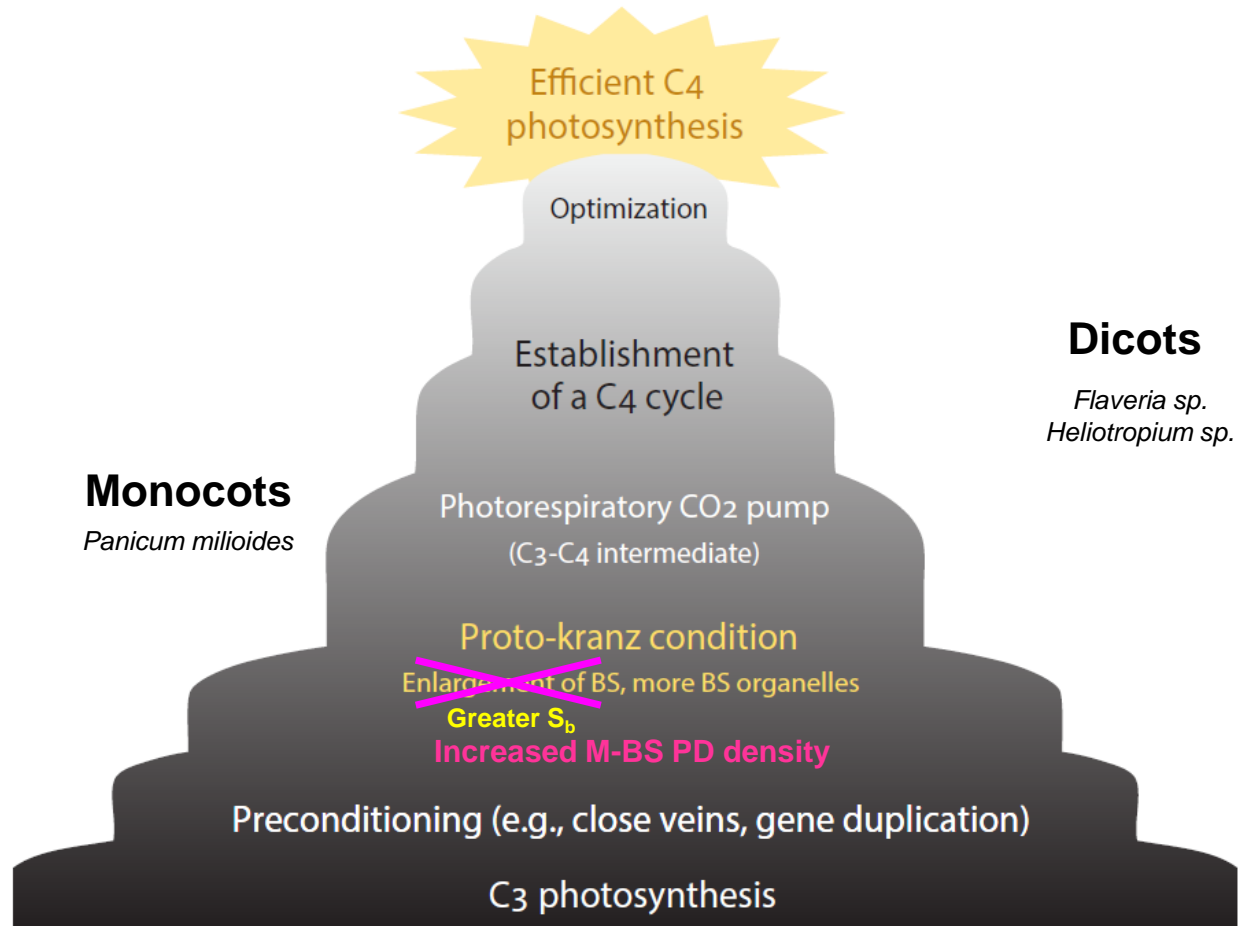
Figure 7.4 A conceptual model proposing the five major phases of C_4 evolution with modification to integrate data from plasmodesmata quantification and anatomical measurements performed in grasses. As discussed in the main text, the five stages are (1) foliar anatomical preconditioning, (2) evolution of the proto-Kranz anatomy, (3) photorespiratory CO_2 pump or the evolution of the C_3-C_4 intermediate, (4) establishment of a C_4 metabolic cycle, and (5) optimization phase, in which Kranz anatomy and leaf biochemistry are modified to maximize the efficiency of the C_4 pathway. S_b, bundle sheath surface area per leaf area; M, mesophyll; BS, bundle sheath; PD, plasmodesmata. Modified from Sage et al. (2012).

bundle sheath plasmodesmata density within the C_4 range. One of the potential implications of this result is that the evolutionary step of increased plasmodesmal numbers at the interfaces of mesophyll-bundle sheath cells preceded that of the photorespiratory pump. The presence of more plasmodesmata connection will enable the rapid flux of glycine from the mesophyll cells to the bundle sheath cells. Moreover, previous reports (Brunkard et al., 2013; Wang et al., 2017) also suggested that chloroplast development and function are strongly coordinated with plasmodesmata function and formation in the bundle sheath. Taking these into consideration, it

is very likely that increased plasmodesmata density at the mesophyll-bundle sheath cell interfaces co-evolved with increased chloroplasts in the bundle sheath and therefore, would occurred as part of the proto-Kranz condition in the C_4 evolution pyramid (Figure 7.4).

7.2.4 Bundle sheath cell size and the evolution of C_4 photosynthesis

In addition to plasmodesmata density, three-dimensional leaf stacks generated from PEA-CLARITY can also be used to measure bundle sheath cell size, both as area and volume. Because it is a volumetric image, orthogonal sectioning can be performed resulting to three different leaf sectional views: transverse, paradermal and longitudinal. Cell area is directly measured from the transverse section of the leaf while cell volume is a product between cell area and cell length, which can be measured from either the paradermal or longitudinal leaf projections (Fig. 4.5). These measurements were done for all the 25 grass species. Measurements revealed that in terms of bundle sheath cell length, *Triticum aestivum* (wheat), which is a C_3 species, had the longest bundle sheath cells while the shortest bundle sheath cells were found within the members of the C_4 species (Table 4.S2). For some C_4 species, the short bundle sheath cell was compensated by larger bundle sheath cell area, and thus appear as short, stout cells in paradermal view (Fig. 4.5). In Figure 7.3, where means for traits such as bundle sheath cell area, bundle sheath cell volume, interveinal distance, and S_b were compared among photosynthetic types, results showed that bundle sheath cell area and bundle sheath cell volume were not statistically different between C_3 species and C_4 species. Contrary to previous reports (Christin et al., 2013; Sage et al., 2012), this means that the enlargement of bundle sheath cell is not necessary to achieve efficient C_4 photosynthesis (Fig. 7.4).

Besides large bundle sheath cell size, short interveinal distance or the distance between bundle sheaths was also considered to be an anatomical enabler of C_4 photosynthesis from both monocot (Christin et al., 2013) and dicot (Sage et al., 2012) studies. However, from the extended study, means comparisons between C_3 species and each of the C_4 subtypes revealed that interveinal distance of C_3 species was not significantly different from that of C_4 species from the NAD-ME subtype (Fig. 7.3). This result indicates that interveinal distance is not a characteristic that can be used to distinguish C_3 species from all C_4 species.

In addition to bundle sheath cell size and interveinal distance, S_b or bundle sheath surface area per leaf area was also measured in the extended study. S_b is a physiological parameter used to estimate bundle sheath conductance to CO_2 diffusion with first estimates ranging between 0.6 m^2

m^{-2} and 3.1 m^2 m^{-2} (Apel and Peisker, 1978; Brown and Byrd, 1993). S_b was obtained by dividing measurement of bundle sheath tissue perimeter by interveinal distance (Pengelly et al., 2010). This parameter considers not only the bundle sheath cell size but also the size of the vasculature and the distance between bundle sheaths. Results from means comparisons revealed that S_b can strictly differentiate C_3 species and C_4 species (Fig. 7.3), where C_3 species had S_b value of 1 and C_4 species had S_b value of 2 (Table 4.S2). Based on these results, an increase in S_b appears to be a better C_4 leaf anatomy index than large bundle sheath cell size or short interveinal distance. Therefore, from the C_4 evolution pyramid, enlargement of bundle sheath as part of the proto-Kranz condition step should be replaced with greater S_b (Fig. 7.4).

7.2.5 Drivers of plasmodesmata development in grasses

To determine whether phylogeny dictates the differences in plasmodesmata densities observed in the 25 grass species examined, phylogenetic test using Spearman's rho was performed. Spearman's rho is a non-parametric test used to measure the strength of association between two variables, where the value of 1 means a perfect positive correlation and the value of -1 means a perfect negative correlation. Results from the extended study revealed very little to no association between phylogenetic distance between species and quantitative distance between plasmodesmata traits (Table 7.2). This lack of strong correlation, which was also seen in other leaf traits examined (Table 7.2), suggests that C_4 leaf anatomy is not solely reliant on phylogeny. Rather it appears that biochemistry is the main influence governing the differences in foliar anatomy observed in grasses particularly plasmodesmata density, where members of the same photosynthetic category had similar anatomical attributes (Figs. 7.2 and 7.3).

7.3 Does plasmodesmata density between mesophyll and bundle sheath cells responds to changes in photosynthetic capacity in C_4 species?

A significant achievement of this work was the development of a new plasmodesmata quantification method. This method combines the PEA-CLARITY technique with scanning electron microscopy to localize, capture, and quantify plasmodesmata connection at the

Table 7.2 Spearman's rank correlation rho between trait difference and phylogenetic distance of the 25 grass species examined.

Leaf traits	All species		BEP only		PACMAD only		C_3 only		C_4 only	
	rho	*p*-value	rho	*p*-value	rho	*p*-value	rho	*p*-value	rho	*p*-value
M-BS PD per µm^2 pit field	-0.08	0.190	-0.31	0.564	-0.02	0.733	-0.18	0.429	-0.01	0.931
M-BS Pit field area per interface area	+0.14	0.013	-0.03	0.956	-0.08	0.239	+0.28	0.217	-0.09	0.280
M-BS PD per µm^2 interface	**+0.20**	**0.000**	-0.14	0.803	-0.06	0.427	-0.12	0.607	-0.04	0.655
M-M PD per µm^2 pit field	-0.25	0.665	+0.79	0.059	+0.01	0.888	-0.02	0.935	-0.07	0.393
M-M Pit field area per interface area	+0.03	0.586	-0.14	0.803	+0.11	0.106	-0.17	0.452	+0.13	0.119
M-M PD per µm^2 interface	+0.13	0.020	-0.20	0.700	**+0.32**	**0.000**	+0.20	0.383	**+0.31**	**0.000**
BS cell area	-0.10	0.086	-0.14	0.803	-0.10	0.161	-0.18	0.432	-0.20	0.019
BS cell volume	+0.14	0.014	-0.49	0.356	-0.10	0.158	-0.18	0.432	-0.15	0.082
IVD	+0.13	0.021	+0.83	0.058	-0.09	0.180	+0.00	0.998	-0.19	0.028
S_b	**+0.32**	**0.000**	-0.44	0.381	**+0.23**	**0.001**	-0.18	0.426	**+0.46**	**0.000**

Correlation test was run using R Studio. Significant results at *p*-value < 0.01 are in bold. BS, bundle sheath; S_b, bundle sheath surface area per unit leaf area; M, mesophyll; PD, plasmodesmata.

mesophyll-bundle sheath cell interfaces and mesophyll-mesophyll cell interfaces within pieces of leaf tissue without resorting to serial sectioning. The new method is accurate, more robust, and relatively faster than the conventional transmission electron microscopy combined with serial sectioning. In addition to plasmodesmata density survey in 25 grass species, the new method developed here was also applied to investigate the response of plasmodesmata formation in C_4 grasses to changes in photosynthetic capacity. The idea behind this study is prompted by a publication which reported that there is a close correlation between mesophyll-bundle sheath cell plasmodesmata density and photosynthetic capacity in C_4 grasses (Sowiński et al., 2007). To address this, two independent experiments were performed using the C_4 model species, *Setaria viridis* and *Zea mays*.

7.3.1   Environmental perturbation of photosynthetic capacity using different growth light intensities

Despite the importance of plasmodesmata in facilitating transport between mesophyll cells and bundle sheath cells in C_4 plants, there is only one report on the effects of growth irradiance on plasmodesmata density in C_4 grass leaves. This was the work of Sowiński and colleagues in 2007. Their study reported that there was a proportional increase in mesophyll-bundle sheath plasmodesmata density with increasing light intensity across all C_4 subtypes, the magnitude of which was species-specific and that the difference in mesophyll-bundle sheath plasmodesmata density between low light-grown plants and high light-grown plants was directly correlated with photosynthetic rate (Sowiński et al., 2007). However, transmission electron microscopy-based plasmodesmata density quantification was used in the study, which is inherently challenging and potentially highly inaccurate (discussed in Chapter 1). Also, the use of Gunning constant (Gunning, 1978) for plasmodesmata density calculations may not be appropriate for leaves, where plasmodesmata are so highly clustered in pit fields (Figs. 3.4 and 4.2). To overcome these problems and provide more robust quantification, the new plasmodesmata quantification method was used to reinvestigate the response of plasmodesmata formation in C_4 grasses, *S. viridis* and *Z. mays*, to growth irradiance (Chapter 5). Results showed that the effect of growth irradiance on mesophyll-bundle sheath plasmodesmata density is not only species-dependent, which is consistent with the conclusions reached in the previous study (Sowiński et al., 2007), but also plant age-dependent. However, contrary to the previous conclusion (Sowiński et al., 2007), there is not a tight link found between plasmodesmata density and photosynthetic capacity in both *S. viridis* and *Z. mays* (Fig. 5.8). Given that light affects a spectrum of plant processes, the differences in mesophyll-bundle sheath plasmodesmata density observed between low light plants and high light plants could potentially be a pleiotropic effect rather than a direct effect of changes in CO_2 assimilation rate.

7.3.2   Perturbation of C_4 metabolism by knocking down PEP carboxylase gene

To look at the implication of impaired photosynthetic capacity to plasmodesmata development at the mesophyll-bundle sheath cell interfaces in leaves of C_4 species, a more targeted approach is

required. Coincidentally, our laboratory had generated transgenic C_4 plants with impaired photosynthetic capacity by knocking down the gene encoding the C_4-associated PEPC. These plants were made primarily to allow estimation of the bundle sheath conductance to CO_2 diffusion in C_4 plants, which happens to be a parameter where plasmodesmata density is an important determinant (Jenkins et al., 1989). PEP carboxylase or PEPC is localized to the cytosol of the mesophyll cell and catalyses the first carboxylation step of the C_4 photosynthetic pathway (Fig. 1.1). As described in Chapter 6, RNA interference or RNAi was used to target the cytosolic C_4-associated PEPC isoform in *Setaria viridis*. In brief, conserved PEPC amino acid sequences obtained from multiple sequence alignment (Figure 6.S1) were inserted into the vector pStargate facilitating the formation of a hairpin RNAi specific to the C_4-associated PEPC (Fig. 6.S2). This resulted in *S. viridis* plants with low CO_2 assimilation rate (Figs. 6.2 and 6.4). Plasmodesmata density quantification performed in leaves of these plants revealed increased plasmodesmata density at the mesophyll-bundle sheath cell interfaces largely driven by an increase in pit fields (Fig. 6.8, Table 6.2). A strong negative correlation between changes in CO_2 assimilation rate and mesophyll-bundle sheath plasmodesmata density from impaired PEPC gene expression was demonstrated in *S. viridis* (Chapter 6). This could have been due to cellular "sensing" of low metabolite gradients or equally, a pleiotropic effect of such a severe inhibition of C_4 photosynthesis. Given the numerous origins of C_4 photosynthesis in grasses and considering the species-specific effects of light in Chapter 5, it is still too early to say if this relationship holds true for all the C_4 grasses or what the mechanism may be.

7.4 Functional significance of increased plasmodesmata density in C_4 leaves

7.4.1 Plasmodesmata functional analysis

It is well known that the number of plasmodesmata does not always reflect the degree of their functionality because of the dynamically complex behaviour of plasmodesmata *in vivo* (van Bel and Oparka, 1995). Thus, functional assays are necessary to further the work described in this thesis. In this thesis, plasmodesmata quantification consistently showed that C_4 species had more symplastic connections (up to 12 times more) at the mesophyll-bundle sheath cell interfaces than their C_3 counterparts (Fig. 7.2). In an attempt to see whether greater plasmodesmata density

results in faster symplastic transport, fluorescent dye feeding experiment was performed using leaves of *Oryza sativa* (rice, C_3 species) and *Setaria viridis* (C_4 species).

Previous studies had shown that cleavage of 5,6-carboxyfluorescein diacetate (CFDA) via esterase activity within the living cells results in a highly polar, fluorescent 5,6-CF molecule (Botha et al., 2008; Wright et al., 1996). This molecule cannot cross cell membranes and therefore, can only travel symplastically via plasmodesmata. The vascular tracer Texas red, on the other hand, served as an apoplastic control for it can only move through the xylem (Botha et al., 2008). Using blue LED light and appropriate filters, CFDA uptake in leaves can be monitored in real time (Fig. 7.5).

Ideally when leaves are fed with CFDA solution from the tip, the uptake is initiated via the phloem and CF is transported through the adjacent vascular parenchyma cells to the bundle sheath cells and mesophyll cells. The approximate transport rate through plasmodesmata can then be estimated by sectioning leaves at different times after the start of dye feeding. Preliminary results from the comparative experiment showed that CF travelled faster in *S. viridis* leaves than in rice leaves. However, because the leaf tip was cut across the whole leaf width, the cut also exposed the mesophyll cells and bundle sheath cells which can serve as entry points for CFDA, hence making precise estimation of transport rate via plasmodesmata difficult. This is also true for the base-fed leaves where CFDA uptake is initiated from the xylem. Perhaps one way to circumvent this would be to create entry points from the leaf surface by sanding it and then monitoring the uptake from there. However, for a more targeted approach (i.e., starting from a single cell), other methods that can be explored include biolistic bombardment using GFP-expressing plasmids (Oparka et al., 1999) or the use of photo-activated fluorescent tracer caged compounds (Ellis-Davies, 2007; Liesche and Schultz, 2012; Liesche and Schulz, 2015; Shigeri et al., 2001). Caging technology involves the encapsulation of biomolecules of interest such as peptides and proteins with caged compounds, which are light-sensitive probes, rendering the former functionally inactive (Ellis-Davies, 2007; Liesche and Schultz, 2012; Liesche and Schulz, 2015). When introduced into a cell, the biomolecule of interest can only be released from encapsulation via photolysis where, upon exposure to a specific wavelength of light, the caged compound is cleaved (Ellis-Davies, 2007). Both methods can target a single cell which can serve as the point of origin from where symplastic transport rate of the peptides, proteins, or GFP-expressing plasmids can be monitored and quantified real time under a fluorescence microscope.
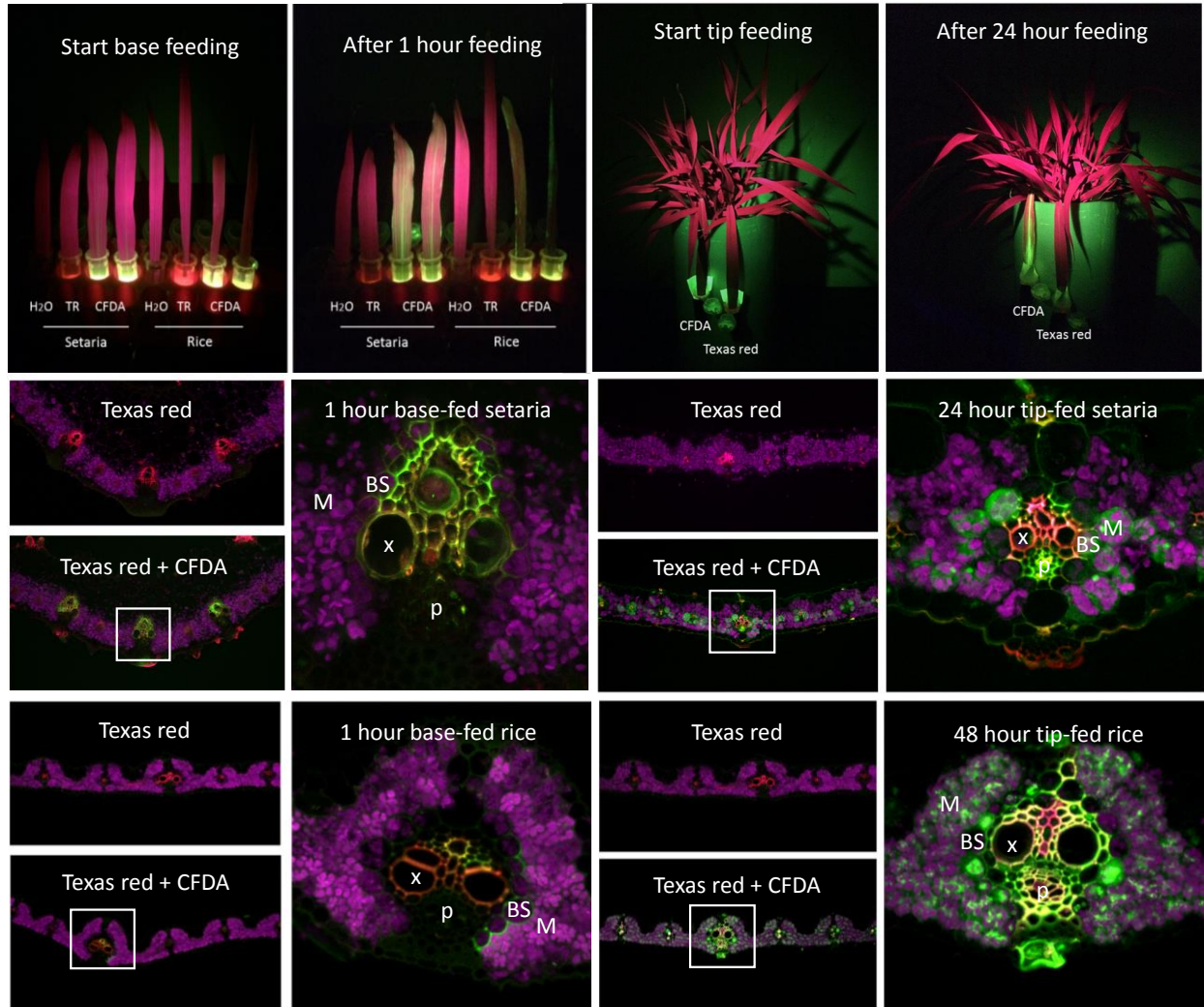
Figure 7.5 Fluorescent dye feeding in leaves of rice and *Setaria viridis* using 5,6-carboxyfluorescein diacetate (CFDA, symplastic) and Texas red (TR, apoplastic). Blue LED light and filtered glasses allowed real-time visualization of CFDA uptake in leaves (top panels). Hand-cut transverse sections were obtained from dye-fed leaves and examined under laser confocal fluorescence microscope. CF molecules (green fluorescence) formed after non-fluorescent CFDA is cleaved by esterase in a living cell (xylem in base-fed, phloem in tip-fed). CF molecules are then presumably transported to the bundle sheath cells and mesophyll cells via plasmodesmata. On the other hand, apoplastic Texas red (red fluorescence) showed compartmentalized uptake in the xylem for both base-fed and tip-fed leaves. Chlorophyll fluorescence is shown in purple. White boxed areas correspond to the regions magnified on the adjacent right. M-mesophyll cell, BS-bundle sheath cell, x-xylem, p-phloem.

7.4.2 Implication of plasmodesmata density difference between C_3 and C_4 species to creating a functional C_4 rice

To further emphasize the importance of having numerous plasmodesmata between the mesophyll and bundle sheath cells in C_4 photosynthesis, plasmodesmatal flux of C_3 leaves and C_4 leaves was estimated using the measured mesophyll-bundle sheath plasmodesmata density in combination with photosynthetic measurement (described in Chapter 3). This calculation, however, assumes that all the plasmodesmata present are functional and are able to perform dual transport of C_4 acids and C_3 compounds between mesophyll cells and bundle sheath cells. Results implied that in the case of C_4 rice, increasing the plasmodesmata density between the mesophyll and bundle sheath cells to support the expected increase in metabolite flux after the C_4 photosynthetic pathway was installed would be necessary to fully realize photosynthetic efficiency (Chapter 3, Table 2). Moreover, proposed C_4 evolution pyramid (Fig. 7.4) inferred that increased mesophyll-bundle sheath plasmodesmata density should happen concurrently with anatomical modifications such as increased S_b and induced chloroplast development in the bundle sheath. Although it is yet to be shown experimentally, the use of NADP-ME as the C_4 biochemical model for the creation of C_4 rice (Kajala et al., 2011) could also mean that suberization of the bundle sheath cell wall might be required for a functional C_4 rice. Unfortunately, the genes responsible for C_4 leaf anatomy including plasmodesmata development are yet to be discovered and this clearly poses a challenge for future research.

7.4.3 Discovering plasmodesmata developmental genes

The 12-fold greater plasmodesmata densities between mesophyll and bundle sheath cells in C_4 species compared to C_3 species is a clear indication of differential regulation of plasmodesmata developmental genes in C_4 plants. The next step now is to find out what are these plasmodesmata developmental genes. However, this task is not an easy feat given the complexities involved in the formation, structure, and regulation of plasmodesmata (Ehlers and Kollmann, 2001), and would entail combining detailed developmental studies with excellent molecular biology and bioinformatics. On a positive note though, around ten genes with functions potentially involved in symplastic transport have recently been found from genome-wide gene-tree/species-tree reconciliation analysis done in grasses (Emms et al., 2016) and would provide a good starting point.

133

7.5 Final outlook

Not until the genes involved in plasmodesmata development are discovered, allowing potential manipulation of plasmodesmata frequency and structure, will the role of leaf plasmodesmata in C_4 photosynthesis be fully realized. For now, empirical and comparative quantifications of plasmodesmata density between C_3 species and C_4 species present invaluable information towards better understanding of the role of the symplast in metabolite transport in plants. Numerical values generated from this work can be used for modelling studies of both C_3 and C_4 pathways. Novel anatomical findings from this work challenge previous statements regarding the evolution of C_4 leaf anatomy and consequently open new avenues of investigation and thinking. The method developed here also opens up exciting opportunities to study plant cells and tissues in 3D. Hopefully, the wealth of information generated from this work would be useful in achieving the goal of increasing food and biofuel production for future demands.

REFERENCES

_____

Andersen, K.S., Bain, J.M., Bishop, D.G., Smillie, R.M., 1972. Photosystem II activity in agranal bundle sheath chloroplasts from *Zea mays*. Plant Physiology 49, 461-466.

Apel, P., Peisker, M., 1978. Influence of high oxygen concentrations on the CO_2 compensation concentration in C_4 plants. Kulturpflanze 26, 99-103.

Bassham, J.A., Benson, A.A., Calvin, M., 1950. The path of carbon in photosynthesis: VIII. The role of malic acid. Journal of Biological Chemistry 185, 781-787.

Beebe, D.U., Russin, W.A., 1999. Plasmodesmata in the phloem-loading pathway, in: van Bel, A.J.E., van Kesteren, W.J.P. (Eds.), Plasmodesmata: structure, function, role in cell communication, Berlin; New York; Springer-Verlag, pp. 261-293.

Beebe, D.U., Turgeon, R., 1991. Current perspectives on plasmodesmata: structure and function. Physiologia Plantarum 83, 194-199.

Benitez-Alfonso, Y., Faulkner, C., Pendle, A., Miyashima, S., Helariutta, Y., Maule, A., 2013. Symplastic intercellular connectivity regulates lateral root patterning. Developmental Cell 26, 136-147.

Berry, J.A., Downton, W.J.S., Tregunna, E.B., 1970. The photosynthetic carbon metabolism of *Zea mays* and *Gomphrena globosa*: the location of the CO_2 fixation and the carboxyl transfer reactions. Canadian Journal of Botany 48, 777-786.

Björkman, O., Gauhl, E., 1969. Carboxydismutase activity in plants with and without β-carboxylation photosynthesis. Planta 88, 197-203.

Borner, G.H.H., Sherrier, D.J., Weimar, T., Michaelson, L.V., Hawkins, N.D., MacAskill, A., Napier, J.A., Beale, M.H., Lilley, K.S., Dupree, P., 2005. Analysis of detergent-resistant membranes in *Arabidopsis*. Evidence for plasma membrane lipid rafts. Plant Physiology 137, 104-116.

Botha, C., Cross, R., 1997. Plasmodesmatal frequency in relation to short-distance transport and phloem loading in leaves of barley (*Hordeum vulgare*). Phloem is not loaded directly from the symplast. Physiologia Plantarum 99, 355-362.

Botha, C.E.J., 1992. Plasmodesmatal distribution, structure and frequency in relation to assimilation in C_3 and C_4 grasses in southern Africa. Planta 187, 348-358.

Botha, C.E.J., Aoki, N., Scofield, G.N., Liu, L., Furbank, R.T., White, R.G., 2008. A xylem sap retrieval pathway in rice leaf blades: evidence of a role for endocytosis? Journal of Experimental Botany 59, 2945-2954.

Botha, C.E.J., Evert, R.F., 1988. Plasmodesmatal distribution and frequency in vascular bundles and contiguous tissues of the leaf of *Themeda triandra*. Planta 173, 433-441.

Botha, C.E.J., van Bel, A.J.E., 1992. Quantification of symplastic continuity as visualised by plasmodesmograms: diagnostic value for phloem-loading pathways. Planta 187, 359-366.

Brown, R.H., Byrd, G.T., 1993. Estimation of bundle sheath cell conductance in C_4 species and O_2 insensitivity of photosynthesis. Plant Physiology 103, 1183-1188.

Brunkard, J.O., Runkel, A.M., Zambryski, P.C., 2013. Plasmodesmata dynamics are coordinated by intracellular signaling pathways. Current Opinion in Plant Biology 16, 614-620.

Burch-Smith, T., C. Zambryski, P., 2016. Regulation of plasmodesmal transport and modification of plasmodesmata during development and following infection by viruses and viral proteins. In: Kleinow T. (eds) Plant-Virus Interactions. Springer, Cham.

Burton, R., Gidley, M., B Fincher, G., 2010. Heterogeneity in the chemistry, structure and function of plant cell walls. Nature Chemical Biology 6, 724–732.

Cantrill, L.C., Overall, R.L., Goodwin, P.B., 1999. Cell-to-cell communication via plant endomembranes. Cell Biology International 23, 653-661.

Christin, P.-A., Osborne, C.P., Chatelet, D.S., Columbus, J.T., Besnard, G., Hodkinson, T.R., Garrison, L.M., Vorontsova, M.S., Edwards, E.J., 2013. Anatomical enablers and the evolution of C_4 photosynthesis in grasses. Proceedings of the National Academy of Sciences of the United States of America 110, 1381-1386.

Chung, K., Wallace, J., Kim, S.-Y., Kalyanasundaram, S., Andalman, A.S., Davidson, T.J., Mirzabekov, J.J., Zalocusky, K.A., Mattis, J., Denisin, A.K., 2013. Structural and molecular interrogation of intact biological systems. Nature 497, 332-337.

Cilia, M.L., Jackson, D., 2004. Plasmodesmata form and function. Current Opinion in Cell Biology 16, 500-506.

Crawford, K.M., Zambryski, P.C., 1999. Plasmodesmata signaling: many roles, sophisticated statutes. Current opinion in plant biology 2, 382-387.

Dengler, N.G., Dengler, R.E., Donnelly, P.M., Hattersley, P.W., 1994. Quantitative leaf anatomy of C_3 and C_4 grasses (Poaceae): bundle sheath and mesophyll surface area relationships. Annals of Botany 73, 241-255.

Duvall, M.R., Saar, D.E., Grayburn, W.S., Holbrook, G.P., 2003. Complex transitions between C_3 and C_4 photosynthesis during the evolution of Paniceae: a phylogenetic case study emphasizing the position of *Steinchisma hians* (Poaceae), a C_3-C_4 intermediate. International Journal of Plant Sciences 164, 949-958.

Edwards, G.E., Furbank, R.T., Hatch, M.D., Osmond, C.B., 2001. What does it take to be C_4? Lessons from the evolution of C_4 photosynthesis. Plant Physiology 125, 46-49.

Edwards, G.E., Kanai, R., Black, C.C., 1971. Phosphoenolpyruvate carboxykinase in leaves of certain plants which fix CO_2 by the C_4-dicarboxylic acid cycle of photosynthesis. Biochemical and Biophysical Research Communications 45, 278-285.

Edwards, G.E., Lee, S.S., Chen, T.M., Black, C.C., 1970. Carboxylation reactions and photosynthesis of carbon compounds in isolated mesophyll and bundle sheath cells of *Digitaria sanguinalis* (L.) Scop. Biochemical and Biophysical Research Communications 39, 389-395.

Ehlers, K., Kollmann, R., 1996. Formation of branched plasmodesmata in regenerating *Solanum nigrum*-protoplasts. Planta 199, 126-138.

Ehlers, K., Kollmann, R., 2001. Primary and secondary plasmodesmata: structure, origin, and functioning. Protoplasma 216, 1-30.

Ellis-Davies, G.C.R., 2007. Caged compounds: photorelease technology for control of cellular chemistry and physiology. Nature methods 4, 619-628.

Emms, D.M., Covshoff, S., Hibberd, J.M., Kelly, S., 2016. Independent and parallel evolution of new genes by gene duplication in two origins of C_4 photosynthesis provides new insight into the mechanism of phloem loading in C_4 species. Molecular Biology and Evolution 33, 1796-1806.

Evert, R.F., Eschrich, W., Heyser, W., 1977. Distribution and structure of the plasmodesmata in mesophyll and bundle-sheath cells of *Zea mays* L. Planta 136, 77-89.

Evert, R.F., Eschrich, W., Heyser, W., 1978. Leaf structure in relation to solute transport and phloem loading in *Zea mays* L. Planta 138, 279-294.

Evert, R.F., Russin, W.A., Bosabalidis, A.M., 1996. anatomical and ultrastructural changes associated with sink-to-source transition in developing maize leaves. International Journal of Plant Sciences 157, 247-261.

Farquhar, G.D., Ehleringer, J.R., Hubick, K.T., 1989. Carbon isotope discrimination and photosynthesis. Annual Review of Plant Physiology and Plant Molecular Biology 40, 503-537.

Faulkner, C., Akman, O.E., Bell, K., Jeffree, C., Oparka, K., 2008. Peeking into pit fields: a multiple twinning model of secondary plasmodesmata formation in tobacco. The Plant Cell 20, 1504-1518.

Faulkner, C.R., Oparka, K.J., 2016. Plasmodesmata. eLS.

Fernandez-Calvino, L., Faulkner, C., Walshaw, J., Saalbach, G., Bayer, E., Benitez-Alfonso, Y., Maule, A., 2011. Arabidopsis plasmodesmal proteome. PLOS ONE 6, e18880.

Furbank, R.T., 2011. Evolution of the C_4 photosynthetic mechanism: are there really three C_4 acid decarboxylation types? Journal of Experimental Botany 62, 3103-3108.

Furbank, R.T., 2016. Walking the C_4 pathway: past, present, and future. Journal of Experimental Botany 67, 4057-4066.

Furbank, R.T., Hatch, M.D., 1987. Mechanism of C_4 photosynthesis: the size and composition of the inorganic carbon pool in bundle sheath cells. Plant Physiology 85, 958-964.

Gamalei, Y.V., Pakhomova, M.V., 1982. Distribution of plasmodesmata and parenchyma transport of assimilates in the leaves of several dicots. Sov. Plant Physiol 28, 649-661.

Giannoutsou, E., Sotiriou, P., Apostolakos, P., Galatis, B., 2013. Early local differentiation of the cell wall matrix defines the contact sites in lobed mesophyll cells of *Zea mays*. Annals of Botany 112, 1067-1081.

GPWGII, 2012. New grass phylogeny resolves deep evolutionary relationships and discovers C_4 origins. New Phytologist 193, 304-312.

Guenoune-Gelbart, D., Elbaum, M., Sagi, G., Levy, A., Epel, B.L., 2008. Tobacco mosaic virus (TMV) replicase and movement protein function synergistically in facilitating TMV spread by lateral diffusion in the plasmodesmal desmotubule of *Nicotiana benthamiana*. Molecular Plant-Microbe Interactions 21, 335-345.

Gunning, B.E.S., 1976. Introduction to plasmodesmata, in: Gunning, B.E.S., Robards, A.W. (Eds.), Intercellular communication in plants: studies on plasmodesmata, Springer Berlin Heidelberg, pp. 1-12.

Gunning, B.E.S., 1978. Age-related and origin-related control of the numbers of plasmodesmata in cell walls of developing *Azolla* roots. Planta 143, 181-190.

Gunning, B.E.S., Robards, A.W., 1976. Plasmodesmata and symplastic transport, in: Wardlaw, I.E., Passioura, J. (Eds.), Transport and transfer processes in plants, Academic Press, New York, pp. 15-41.

Guseman, J.M., Lee, J.S., Bogenschutz, N.L., Peterson, K.M., Virata, R.E., Xie, B., Kanaoka, M.M., Hong, Z., Torii, K.U., 2010. Dysregulation of cell-to-cell connectivity and stomatal patterning by loss-of-function mutation in *Arabidopsis* CHORUS (GLUCAN SYNTHASE-LIKE 8). Development 137, 1731-1741.

Haberlandt, G., 1904. Physiologische pflanzenanatomie, 3, neubearb, und verm. aufl. ed. W. Engelmann, Leipzig :.

Han, X., Hyun, Tae K., Zhang, M., Kumar, R., Koh, E.J., Kang, B.H., Lucas, William J., Kim, J.Y., 2014. Auxin-callose-mediated plasmodesmal gating is essential for tropic auxin gradient formation and signaling. Developmental Cell 28, 132-146.

Hatch, M.D., 1971. The C_4-pathway of photosynthesis. Evidence for an intermediate pool of carbon dioxide and the identity of the donor C_4-dicarboxylic acid. Biochemical Journal 125, 425-432.

Hatch, M.D., 1987. C_4 photosynthesis: a unique blend of modified biochemistry, anatomy and ultrastructure. Biochimica et Biophysica Acta (BBA) - Reviews on Bioenergetics 895, 81-106.

Hatch, M.D., Kagawa, T., 1976. Photosynthetic activities of isolated bundle sheath cells in relation to differing mechanisms of C_4 pathway photosynthesis. Archives of Biochemistry and Biophysics 175, 39-53.

Hatch, M.D., Osmond, C.B., 1976. Compartmentation and transport in C_4 photosynthesis, in: Stocking, C.R., Heber, U. (Eds.), Transport in Plants III. Springer Berlin Heidelberg, pp. 144-184.

Hatch, M.D., Slack, C.R., 1966. Photosynthesis by sugar-cane leaves: a new carboxylation reaction and the pathway of sugar formation. Biochemical Journal 101, 103-111.

Hattersley, P.W., Browning, A.J., 1981. Occurrence of the suberized lamella in leaves of grasses of different photosynthetic types. I. In parenchymatous bundle sheaths and PCR ("Kranz") sheaths. Protoplasma 109, 371-401.

Henderson, S., Caemmerer, S., Farquhar, G., 1992. Short-term measurements of carbon isotope discrimination in several C_4 species. Functional Plant Biology 19, 263-285.

Hepler, P.K., 1982. Endoplasmic reticulum in the formation of the cell plate and plasmodesmata. Protoplasma 111, 121-133.

Hesketh, J.D., 1963. Limitations to photosynthesis responsible for differences among species. Crop Science 3, 493-496.

Hodge, A.J., McLean, J.D., Mercer, F.V., 1955. Ultrastructure of the lamellae and grana in the chloroplasts of *Zea mays* L. The Journal of Biophysical and Biochemical Cytology 1, 605-614.

Hu, J., Shibata, Y., Voss, C., Shemesh, T., Li, Z., Coughlin, M., Kozlov, M.M., Rapoport, T.A., Prinz, W.A., 2008. Membrane proteins of the endoplasmic reticulum induce high-curvature tubules. Science 319, 1247-1250.

Hughes, L., Hawes, C., Monteith, S., Vaughan, S., 2014. Serial block face scanning electron microscopy—the future of cell ultrastructure imaging. Protoplasma 251, 395-401.

Jenkins, C.L.D., Furbank, R.T., Hatch, M.D., 1989. Mechanism of C_4 photosynthesis: a model describing the inorganic carbon pool in bundle sheath cells. Plant Physiology 91, 1372-1381.

Johnson, G.N., 2011. Physiology of PSI cyclic electron transport in higher plants. Biochimica et Biophysica Acta (BBA) - Bioenergetics 1807, 384-389.

Kagawa, T., Hatch, M.D., 1974. C_4-acids as the source of carbon dioxide for calvin cycle photosynthesis by bundle sheath cells of the C_4-pathway species *Atriplex spongiosa*. Biochemical and Biophysical Research Communications 59, 1326-1332.

Kajala, K., Covshoff, S., Karki, S., Woodfield, H., Tolley, B.J., Dionora, M.J.A., Mogul, R.T., Mabilangan, A.E., Danila, F.R., Hibberd, J.M., Quick, W.P., 2011. Strategies for engineering a two-celled C_4 photosynthetic pathway into rice. Journal of Experimental Botany 62, 3001-3010.

Kanai, R., Edwards, G.E., 1999. The biochemistry of C_4 photosynthesis., in: Sage, R.F., Monson, R.K. (Eds.), C_4 Plant Biology, Academic Press, London., pp. 49–87.

Karpilov, Y.S., 1960. The distribution of radioactive carbon 14 amongst the products of photosynthesis of maize. Trudy Kazansk Sel'shokoz Institute 41, 15-24.

Knox, J.P., Benitez-Alfonso, Y., 2014. Roles and regulation of plant cell walls surrounding plasmodesmata. Current Opinion in Plant Biology 22, 93-100.

Knox, K., Wang, P., Kriechbaumer, V., Tilsner, J., Frigerio, L., Sparkes, I., Hawes, C., Oparka, K., 2015. Putting the squeeze on plasmodesmata: a role for reticulons in primary plasmodesmata formation. Plant Physiology 168, 1563-1572.

Kromdijk, J., Głowacka, K., Leonelli, L., Gabilly, S.T., Iwai, M., Niyogi, K.K., Long, S.P., 2016. Improving photosynthesis and crop productivity by accelerating recovery from photoprotection. Science 354, 857-861.

Laetsch, W.M., 1974. The C_4 syndrome: a structural analysis. Annual Review of Plant Physiology 25, 27-52.

Lazzaro, M.D., Thomson, W.W., 1996. The vacuolar-tubular continuum in living trichomes of chickpea (*Cicer arietinum*) provides a rapid means of solute delivery from base to tip. Protoplasma 193, 181-190.

Leegood, R.C., 2008. Roles of the bundle sheath cells in leaves of C_3 plants. Journal of Experimental Botany 59, 1663-1673.

Levy, A., Erlanger, M., Rosenthal, M., Epel, B.L., 2007. A plasmodesmata-associated β-1, 3-glucanase in Arabidopsis. The Plant Journal 49, 669-682.

Liesche, J., Schultz, A., 2012. Quantification of plant cell coupling with three-dimensional photoactivation microscopy. Journal of Microscopy 247, 2-9.

Liesche, J., Schulz, A., 2015. Quantification of plant cell coupling with live-cell microscopy, in: Heinlein, M. (Ed.), Plasmodesmata: Methods and Protocols. Springer New York, pp. 137-148.

Lin, H., Karki, S., Coe, R.A., Bagha, S., Khoshravesh, R., Balahadia, C.P., Ver Sagun, J., Tapia, R., Israel, W.K., Montecillo, F., de Luna, A., Danila, F.R., Lazaro, A., Realubit, C.M., Acoba, M.G., Sage, T.L., von Caemmerer, S., Furbank, R.T., Cousins, A.B., Hibberd, J.M., Quick, W.P., Covshoff, S., 2016. Targeted knockdown of GDCH in rice leads to a photorespiratory-deficient phenotype useful as a building block for C_4 rice. Plant and Cell Physiology 57, 919-932.

Long, Stephen P., Marshall-Colon, A., Zhu, X.-G., 2015. Meeting the global food demand of the future by engineering crop photosynthesis and yield potential. Cell 161, 56-66.

López-Calcagno, P.E., Fisk, S., Brown, K.L., Bull, S.E., South, P.F., Raines, C.A., 2018. Overexpressing the H-protein of the glycine cleavage system increases biomass yield in glasshouse and field-grown transgenic tobacco plants. Plant Biotechnology Journal, 1-11.

Majeran, W., van Wijk, K.J., 2009. Cell-type-specific differentiation of chloroplasts in C_4 plants. Trends in Plant Science 14, 100-109.

Martens, H.J., Roberts, A.G., Oparka, K.J., Schulz, A., 2006. Quantification of plasmodesmatal endoplasmic reticulum coupling between sieve elements and companion cells using fluorescence redistribution after photobleaching. Plant Physiology 142, 471-480.

Maule, A., Faulkner, C., Benitez-Alfonso, Y., 2012. Plasmodesmata "in communicado". Frontiers in Plant Science 3.

Maule, A.J., 2008. Plasmodesmata: structure, function and biogenesis. Current Opinion in Plant Biology 11, 680-686.

Maule, A.J., Benitez-Alfonso, Y., Faulkner, C., 2011. Plasmodesmata – membrane tunnels with attitude. Current Opinion in Plant Biology 14, 683-690.

Mertz, R.A., Brutnell, T.P., 2014. Bundle sheath suberization in grass leaves: multiple barriers to characterization. Journal of Experimental Botany 65, 3371-3380.

Mongrand, S., Morel, J., Laroche, J., Claverol, S., Carde, J.-P., Hartmann, M.-A., Bonneu, M., Simon-Plas, F., Lessire, R., Bessoule, J.-J., 2004. Lipid rafts in higher plant cells: purification and characterization of triton X-100-insoluble microdomains from tobacco plasma membrane. Journal of Biological Chemistry 279, 36277-36286.

Mongrand, S., Stanislas, T., Bayer, E.M.F., Lherminier, J., Simon-Plas, F., 2010. Membrane rafts in plant cells. Trends in Plant Science 15, 656-663.

Moss, D.N., 1962. The limiting carbon dioxide concentration for photosynthesis. Nature 193, 587.

Munekage, Y.N., Taniguchi, Y.Y., 2016. Promotion of cyclic electron transport around photosystem I with the development of C_4 photosynthesis. Plant and Cell Physiology 57, 897-903.

Nelson, R.S., van Bel, A.J.E., 1998. The mystery of virus trafficking into, through and out of vascular tissue, in: Behnke, H.D., Esser, K., Kadereit, J.W., Lüttge, U., Runge, M. (Eds.), Progress in botany: genetics cell biology and physiology ecology and vegetation science. Springer Berlin Heidelberg, Berlin, Heidelberg, pp. 476-533.

Nicolas, W.J., Grison, M.S., Trépout, S., Gaston, A., Fouché, M., Cordelières, F.P., Oparka, K., Tilsner, J., Brocard, L., Bayer, E.M., 2017. Architecture and permeability of post-cytokinesis plasmodesmata lacking cytoplasmic sleeves. Nature Plants 3, 17082.

O'Brien, T., Carr, D., 1970. A suberized layer in the cell walls of the bundle sheath of grasses. Australian Journal of Biological Sciences 23, 275-288.

Olesen, P., 1975. Plasmodesmata between mesophyll and bundle sheath cells in relation to the exchange of C_4-acids. Planta 123, 199-202.

Oparka, K.J., Roberts, A.G., 2001. Plasmodesmata. A not so open-and-shut case. Plant Physiology 125, 123-126.

Oparka, K.J., Roberts, A.G., Boevink, P., Cruz, S.S., Roberts, I., Pradel, K.S., Imlau, A., Kotlizky, G., Sauer, N., Epel, B., 1999. Simple, but not branched, plasmodesmata allow the nonspecific trafficking of proteins in developing tobacco leaves. Cell 97, 743-754.

Orfila, C., Knox, J.P., 2000. Spatial regulation of pectic polysaccharides in relation to pit fields in cell walls of tomato fruit pericarp. Plant Physiology 122, 775.

Ort, D.R., Merchant, S.S., Alric, J., Barkan, A., Blankenship, R.E., Bock, R., Croce, R., Hanson, M.R., Hibberd, J.M., Long, S.P., Moore, T.A., Moroney, J., Niyogi, K.K., Parry, M.A.J., Peralta-Yahya, P.P., Prince, R.C., Redding, K.E., Spalding, M.H., van Wijk, K.J., Vermaas, W.F.J., von Caemmerer, S., Weber, A.P.M., Yeates, T.O., Yuan, J.S., Zhu, X.G., 2015. Redesigning photosynthesis to sustainably meet global food and bioenergy demand. Proceedings of the National Academy of Sciences 112, 8529-8536.

Overall, R.L., 1999. Substructure of plasmodesmata, in: van Bel, A.J.E., Van Kesteren, W.P. (Eds.), Plasmodesmata: structure, function, role in cell communication. Springer Berlin Heidelberg, pp. 129-148.

Overall, R.L., Wolfe, J., Gunning, B.E.S., 1982. Intercellular communication in *Azolla* roots: I. Ultrastructure of plasmodesmata. Protoplasma 111, 134-150.

Palmer, W.M., Martin, A.P., Flynn, J.R., Reed, S.L., White, R.G., Furbank, R.T., Grof, C.P.L., 2015. PEA-CLARITY: 3D molecular imaging of whole plant organs. Scientific Reports 5, 13492.

Parry, M.A.J., Andralojc, P.J., Scales, J.C., Salvucci, M.E., Carmo-Silva, A.E., Alonso, H., Whitney, S.M., 2013. Rubisco activity and regulation as targets for crop improvement. Journal of Experimental Botany 64, 717-730.

Pengelly, J.J.L., Sirault, X.R.R., Tazoe, Y., Evans, J.R., Furbank, R.T., von Caemmerer, S., 2010. Growth of the C_4 dicot *Flaveria bidentis*: photosynthetic acclimation to low light through shifts in leaf anatomy and biochemistry. Journal of Experimental Botany 61, 4109-4122.

Peskan, T., Westermann, M., Oelmüller, R., 2000. Identification of low-density Triton X-100-insoluble plasma membrane microdomains in higher plants. European Journal of Biochemistry 267, 6989-6995.

Pollard, M., Beisson, F., Li, Y., Ohlrogge, J.B., 2008. Building lipid barriers: biosynthesis of cutin and suberin. Trends in Plant Science 13, 236-246.

Prendergast, H., Hattersley, P., Stone, N., 1987. New structural/biochemical associations in leaf blades of C_4 grasses (Poaceae). Functional Plant Biology 14, 403-420.

Raffaele, S., Bayer, E., Lafarge, D., Cluzet, S., German Retana, S., Boubekeur, T., Leborgne-Castel, N., Carde, J.-P., Lherminier, J., Noirot, E., Satiat-Jeunemaître, B., Laroche-Traineau, J., Moreau, P., Ott, T., Maule, A.J., Reymond, P., Simon-Plas, F., Farmer, E.E., Bessoule, J.-J., Mongrand, S., 2009. Remorin, a solanaceae protein resident in membrane rafts and plasmodesmata, impairs *Potato virus X* movement. The Plant Cell 21, 1541-1555.

Ray, D.K., Mueller, N.D., West, P.C., Foley, J.A., 2013. Yield trends are insufficient to double global crop production by 2050. PLOS ONE 8, e66428.

Rhoades, M.M., Carvalho, A., 1944. The function and structure of the parenchyma sheath plastids of the maize leaf. Bulletin of the Torrey Botanical Club 71, 335-346.

Rizal, G., Thakur, V., Dionora, J., Karki, S., Wanchana, S., Acebron, K., Larazo, N., Garcia, R., Mabilangan, A., Montecillo, F., Danila, F., Mogul, R., Pablico, P., Leung, H., Langdale, J.A., Sheehy, J., Kelly, S., Quick, W.P., 2015. Two forward genetic screens for vein density mutants in sorghum converge on a cytochrome P450 gene in the brassinosteroid pathway. The Plant Journal 84, 257-266.

Robards, A.W., 1976. Plasmodesmata in higher plants, in: Gunning, B.E.S., Robards, A.W. (Eds.), Intercellular communication in plants: studies on plasmodesmata. Springer Berlin Heidelberg, pp. 15-57.

Robards, A.W., Lucas, W.J., 1990. Plasmodesmata. Annual Review of Plant Physiology and Plant Molecular Biology 41, 369-419.

Robinson-Beers, K., Evert, R., 1991a. Fine structure of plasmodesmata in mature leaves of sugarcane. Planta 184, 307-318.

Robinson-Beers, K., Evert, R.F., 1991b. Ultrastructure of and plasmodesmatal frequency in mature leaves of sugarcane. Planta 184, 291-306.

Roy, S., Watada, A.E., Wergin, W.P., 1997. Characterization of the cell wall microdomain surrounding plasmodesmata in apple fruit. Plant Physiology 114, 539.

Ruan, Y.-L., Llewellyn, D.J., Furbank, R.T., 2001. The control of single-celled cotton fiber elongation by developmentally reversible gating of plasmodesmata and coordinated expression of sucrose and K^+ transporters and expansin. The Plant Cell 13, 47-60.

Russin, W.A., Evert, R.F., 1985. Studies on the leaf of *Populus deltoides* (Salicaceae): ultrastructure, plasmodesmatal frequency, and solute concentrations. American Journal of Botany 72, 1232-1247.

Russin, W.A., Evert, R.F., Vanderveer, P.J., Sharkey, T.D., Briggs, S.P., 1996. Modification of a specific class of plasmodesmata and loss of sucrose export ability in the sucrose export defective1 maize mutant. The Plant Cell 8, 645-658.

Sage, R.F., 2004. The evolution of C_4 photosynthesis. New Phytologist 161, 341-370.

Sage, R.F., Sage, T.L., Kocacinar, F., 2012. Photorespiration and the evolution of C_4 photosynthesis. Annual Review of Plant Biology 63, 19-47.

Sage, T.L., Sage, R.F., 2009. The functional anatomy of rice leaves: implications for refixation of photorespiratory CO_2 and efforts to engineer C_4 photosynthesis into rice. Plant and Cell Physiology 50, 756-772.

Seagull, R.W., 1983. Differences in the frequency and disposition of plasmodesmata resulting from root cell elongation. Planta 159, 497-504.

Sharkey, T.D., 1988. Estimating the rate of photorespiration in leaves. Physiologia Plantarum 73, 147-152.

Shigeri, Y., Tatsu, Y., Yumoto, N., 2001. Synthesis and application of caged peptides and proteins. Pharmacology & Therapeutics 91, 85-92.

Slack, C.R., Hatch, M.D., Goodchild, D.J., 1969. Distribution of enzymes in mesophyll and parenchyma-sheath chloroplasts of maize leaves in relation to the C_4-dicarboxylic acid pathway of photosynthesis. Biochemical Journal 114, 489-498.

Slewinski, T.L., Baker, R.F., Stubert, A., Braun, D.M., 2012. Tie-dyed2 encodes a callose synthase that functions in vein development and affects symplastic trafficking within the phloem of maize leaves. Plant Physiology 160, 1540-1550.

Smertenko, A., Assaad, F., Baluška, F., Bezanilla, M., Buschmann, H., Drakakaki, G., Hauser, M.-T., Janson, M., Mineyuki, Y., Moore, I., Müller, S., Murata, T., Otegui, M.S., Panteris, E., Rasmussen, C., Schmit, A.-C., Šamaj, J., Samuels, L., Staehelin, L.A., Van Damme, D., Wasteneys, G., Žárský, V., 2017. Plant cytokinesis: terminology for structures and processes. Trends in Cell Biology 27, 885-894.

Sowiński, P., Bilska, A., Barańska, K., Fronk, J., Kobus, P., 2007. Plasmodesmata density in vascular bundles in leaves of C_4 grasses grown at different light conditions in respect to photosynthesis and photosynthate export efficiency. Environmental and Experimental Botany 61, 74-84.

Sowiński, P., Rudzińska-Langwald, A., Kobus, P., 2003. Changes in plasmodesmata frequency in vascular bundles of maize seedling leaf induced by growth at sub-optimal temperatures in relation to photosynthesis and assimilate export. Environmental and Experimental Botany 50, 183-196.

Tangl, E., 1879. ober offene Kommunikation zwischen den Zellen des Endosperms einiger Samen. Jb Wiss Bot 12, 170-190.

van Bel, A.J.E., Oparka, K.J., 1995. On the validity of plasmodesmograms*. Botanica Acta 108, 174-182.

van Bel, A.J.E., van Kesteren, W.J.P., Papenhuijzen, C., 1988. Ultrastructural indications for coexistence of symplastic and apoplastic phloem loading in *Commelina benghalensis* leaves. Planta 176, 159-172.

Vatén, A., Dettmer, J., Wu, S., Stierhof, Y.-D., Miyashima, S., Yadav, S.R., Roberts, C.J., Campilho, A., Bulone, V., Lichtenberger, R., Lehesranta, S., Mähönen, A.P., Kim, J.-Y., Jokitalo, E., Sauer, N., Scheres, B., Nakajima, K., Carlsbecker, A., Gallagher, K.L., Helariutta, Y., 2011. Callose biosynthesis regulates symplastic trafficking during root development. Developmental Cell 21, 1144-1155.

Voeltz, G.K., Prinz, W.A., Shibata, Y., Rist, J.M., Rapoport, T.A., 2006. A class of membrane proteins shaping the tubular endoplasmic reticulum. Cell 124, 573-586.

von Caemmerer, S., Furbank, R., 2003. The C_4 pathway: an efficient CO_2 pump. Photosynthesis Research 77, 191-207.

Wang, P., Khoshravesh, R., Karki, S., Tapia, R., Balahadia, C.P., Bandyopadhyay, A., Quick, W.P., Furbank, R.T., Sage, T.L., Langdale, J.A., 2017. Re-creation of a key step in the evolutionary switch from C_3 to C_4 leaf anatomy. Current Biology 27, 3278-3287.

White, R.G., Barton, D.A., 2011. The cytoskeleton in plasmodesmata: a role in intercellular transport? Journal of Experimental Botany 62, 5249-5266.

Whitney, S.M., Birch, R., Kelso, C., Beck, J.L., Kapralov, M.V., 2015. Improving recombinant Rubisco biogenesis, plant photosynthesis and growth by coexpressing its ancillary RAF1 chaperone. Proceedings of the National Academy of Sciences 112, 3564-3569.

Woo, K.C., Anderson, J.M., Boardman, N.K., Downton, W.J.S., Osmond, C.B., Thorne, S.W., 1970. Deficient photosystem II in agranal bundle sheath chloroplasts of C_4 plants. Proceedings of the National Academy of Sciences 67, 18-25.

Wright, K.M., Horobin, R.W., Oparka, K.J., 1996. Phloem mobility of fluorescent xenobiotics in *Arabidopsis* in relation to their physicochemical properties. Journal of Experimental Botany 47, 1779-1787.

Xie, B., Wang, X., Zhu, M., Zhang, Z., Hong, Z., 2011. CalS7 encodes a callose synthase responsible for callose deposition in the phloem. The Plant Journal 65, 1-14.

Zhu, X.G., Long, S.P., Ort, D.R., 2010. Improving photosynthetic efficiency for greater yield. Annual Review of Plant Biology 61, 235-261.